HYPERSONIC BOUNDARY LAYERS

by

John Erwin LaGraff

St. Catherine's College

BODLEIAN LIBRARY OXFORD
DEPOSITED THESIS
24 vii 70

A Thesis submitted for the Degree of Doctor of Philosophy at the University of Oxford, Department of Engineering Science.

Hilary Term 1970

"For anything which is not deduced from phenomena ought to be called a hypothesis, and hypotheses of this kind, ... have no place in experimental philosophy."

Sir Isaac Newton -- from a letter
to Prof. Cotes, London 1713.

ABSTRACT

The design, instrumentation, and calibration of the Oxford University Hypersonic Gun Tunnel is described. The calibration included the determination of the working section Mach Number, total temperature, total pressure, and unit Reynolds Number. The performance was compared with theoretical estimates.

Measurements of boundary layer transition on the outside surface of a hollow cylinder model using shadowgraph and surface pitot techniques are described. Transition experiments on the model in various European wind tunnels are compared and a correlation based on nozzle wall boundary layer aerodynamic noise radiation is discussed.

Heat transfer measurements on the surface of a 10° total angle sharp cone and a flat plate were made and compared with theoretical predictions. Transition location based on changes in the heat transfer rate was determined for the two models and compared with the hollow cylinder results. Effects of model wall curvature were shown to be present and were correlated by the ratio of boundary layer thickness to wall radius of curvature.

A fine hot wire constant temperature anemometer probe was developed and used to measure fluctuation levels through the transitional boundary layer of a flat plate. Strong fluctuation intensities were found within the boundary layer upstream of the region where transition begins based on mean surface heat transfer measurements. These fluctuations appeared to be due to large turbulent eddies generated near the model leading edge and were initially located in the boundary layer at a y/δ location consistent with compressible stability theory.

TABLE OF CONTENTS

	Page
Abstract	i
Acknowledgements	iv
List of Symbols	vi
List of Figures	x
PART I - THE GUN TUNNEL	
1 - Introduction	1
2 - General Description of Gun Tunnel	5
2.1 Driver & Shock Tube Barrel	5
2.2 Hypersonic Expansion Nozzle	6
2.3 Working Section & Dump Tank	9
2.4 Gun Tunnel Air Control System	9
2.4.1 High Pressure Air Supply System	
2.4.2 Vacuum System	
2.5 Diaphragm Development	12
2.5.1 Primary Diaphragms	
2.5.2 Secondary Diaphragms	
2.6 Piston Development	15
3 - Gun Tunnel Instrumentation	18
3.1 Electronic Instrumentation	18
3.1.1 Cathode Ray Oscilloscope	
3.1.2 U.V. Galvanometer Chart Recorder	
3.1.3 Galvanometer Amplifiers	
3.1.4 D.C. Amplifiers	
3.1.5 Filters	
3.2 Heat Transfer Measurements	21
3.2.1 Gauge Construction	
3.2.2 Gauge Calibration	
3.2.3 Heat Transfer Data Reduction	
3.2.4 Stagnation Point Heat Transfer	
3.2.5 Analogue Circuit Calibration	
3.3 Flow Visualization	32
3.3.1 Schlieren Techniques	
3.3.2 Shadowgraph Techniques	
3.4 Pressure Measurements	34
3.4.1 Transducer Calibration	
3.4.2 Pitot Pressure	
3.4.3 Static Pressure	
3.4.4 Reservoir Pressure	
4 - Shock Tube Calibration	39
4.1 Shock Velocity Measurements	39
4.2 Wave System Analysis & Piston Motion	41
4.3 Barrel Pressure History	48
5 - Working Section Calibration	53
5.1 Running Time Tests	53
5.2 Mach Number Measurements	55
5.2.1 Pitot Probe Tests	
5.2.2 Static Pressure Tests	
5.2.3 Other Tests	
5.3 Total Temperature Measurements	57
5.3.1 Thermocouple Probe	
5.3.2 Hot Film Probe	
5.3.3 Pressure Record Analysis	
5.4 Condensation Tests	64

Page

6 - Gun Tunnel Simulation Capabilities 66

7 - Conclusions - Part I 68

PART II

8 - Introduction 70

9 - Hollow Cylinder Transition 75
 9.1 The Model 76
 9.2 Gun Tunnel Transition Results 77
  9.2.1 Shadowgraph Tests
  9.2.2 Surface Pitot Tests
 9.3 Transition Tests in Other Facilities 83
 9.4 Correlation Theories 85
  9.4.1 Aerodynamic Noise
  9.4.2 Noise-Transition Correlations
  9.4.3 Correlation of Multi-Source Data

10 - Heat Transfer Measurements 100
 10.1 The Models 100
  10.1.1 Sharp Leading Edge Flat Plate
  10.1.2 10^{o} Cone
 10.2 Heat Transfer Results and Theoretical Comparisons 103
  10.2.1 Test Conditions
  10.2.2 Heat Transfer Results
  10.2.3 Theoretical Comparisons
 10.3 Transition Results 111

11 - Boundary Layer Fluctuations 121
 11.1 Experimental Apparatus 122
  11.1.1 The Model
  11.1.2 Fine Wire Probes
  11.1.3 Electronic Instrumentation
 11.2 Hot Wires in Supersonic Flow 133
 11.3 Experimental Results and Discussion 137
  11.3.1 Fluctuation Profiles
  11.3.2 The Critical Layer
  11.3.3 Boundary Layer Breakdown and Transition

12 - Conclusions - Part II 156

List of References 160

Appendix I 172

ACKNOWLEDGEMENTS

The author wishes to express his appreciation to his supervisor, Dr. D.L. Schultz, for making possible the opportunity to come to Oxford to undertake this research program and especially for his enthusiastic encouragement and support and many helpful suggestions throughout the duration of the program.

The author wishes to express his indebtedness to his many colleagues in the Department of Engineering Science for many fruitful discussions and suggestions, but in particular to Dr. T.V. Jones and also to Dr. J.P. Batham for his many significant contributions to the operational development of the Gun Tunnel and instrumentation during the course of his D. Phil. studies.

The completion of the program would not have been possible without the strong, competent support of members of the technical staff too numerous to list. Special acknowledgement must go, however, to Mr. Kevin Grindrod for his meticulous machining efforts throughout the program and to Mr. John L. Allen for his enthusiastic support in all phases of the experimental program and in the preparation of the drawings and the assemblage of the final manuscript. The support of Mr. G.N. Roger and the staff of the Electronics Workshop was invaluable in the development of much of the instrumentation. The services of the Department's library, photographic, and general office staff are also acknowledged along with the typing services of Mrs. M. Matheson.

To his many colleagues in other research centers, the author also wishes to express gratitude for making available their considerable developmental experience with gun tunnels and for their cooperation with the comparative transition experiments of Chapter 9. Special mention should go to Mr. J.L. Stollery and his associates in the Aeronautics Department of Imperial College; Mr. Roy Hawkins, and co-workers, of Rolls Royce, Bristol Engines Division; Dr. R.A. East of the University of Southampton; Dr. L. Davies and staff of the Aerodynamics Department, N.P.L.; and Dr. B. Lemcke of the Aeronautical Research Institute of Sweden (FFA).

The support of the Ministry of Technology and their research establishments in financing and monitoring the research described in this thesis under agreement number (AT/2057/023/SRA) is great appreciated.

Finally, the author wishes to express his appreciation to his wife Susan, on whom the real burden of the D. Phil. ultimately fell, for her support and forbearance during this austere period.

LIST OF SYMBOLS

Some symbols, defined explicitly in the context of their application in a single situation in the thesis, are not listed here. Where multiple definitions are sometimes given for the symbols listed below, the appropriate meaning is clear from the usage in the text. In general a double subscript is an abbreviated way of writing the ratio of conditions at the first subscript to the second (e.g. $P_{41}' \equiv P_4/P_1$). When the words Gun Tunnel are written as a proper noun, the Oxford Gun Tunnel described in Part I is being referred to. When lower case letters are used, gun tunnels in general are being discussed (or another specific gun tunnel). Whenever possible in this thesis, dimensionless units are used. In Part I, where dimensional units are used, both British and S.I. units are usually given for general usefulness in future Gun Tunnel programs. In Part II the units are often mixed because of the use of S.I. units for the Gun Tunnel calibration from Part I and the use of British units for the model construction and many of the experimental measurements.

A	area
a	speed of sound
b	model leading edge thickness
C	capacitance
c	specific heat
c_f	skin friction coefficient
$\bar{c}_f$	mean skin friction coefficient
c_i	amplification rate
c_p	specific heat at constant pressure
c_r	disturbance phase velocity

D	diameter; coefficient of diffusion
e'	instantaneous hot wire voltage fluctuation
h	altitude; heat transfer coefficient $\frac{\dot{q}}{T_r - T_w}$
H	enthalpy
H_D	enthalpy of dissociation
I	current
k	thermal conductivity
L	length; Lewis Number, $k/\rho cD$
M	Mach Number, u/a
m	mass
$\dot{m}$	mass flow rate
Nu	Nusselt Number, hD/k
P	pressure
P_{t_2}	pitot pressure
Pr	Prandtl Number, $c\mu/k$
$\dot{q}$	heat transfer rate
r	radius; specific resistivity; recovery factor
r_m	mean model radius of curvature between leading edge and X_{t_b}
R	electrical resistance; gas constant
Re	Reynolds Number, $\rho ux/\mu$
Re_t	transition Reynolds Number, $(u/\nu)_e x_t$
St_e	Stanton Number, $\dot{q}/\rho_e u_e c_{p_e}(T_r - T_w)$
s	entropy
T	temperature
T_r	recovery temperature
$\bar{T}_w$	wire mean temperature
t	time
u	velocity
u_p	piston velocity

x_t	distance to transition point
x_{t_b}	distance to begin transition
x_{t_e}	distance to end transition
x	distance; distance in flow direction
Δx_t	$(x_{t_e} - x_{t_b})$
y	distance normal to flow direction
α	thermal coefficient of resistivity;
	disturbance wave number (2π/wave length)
β	$(\rho c k)^{\frac{1}{2}}$
γ	ratio of specific heats
δ	boundary layer velocity thickness ($.99u_e$)
δ^*	boundary layer displacement thickness (equa. (9.4.4)
δ_b	boundary layer thickness at begin transition
η	Ψ_1/Ψ_2
μ	coefficient of viscosity; also $\{(\gamma-1)/(\gamma+1)\}^{\frac{1}{2}}$
θ	momentum thickness (equa. 9.4.3)
ν	kinematic viscosity (μ/ρ)
π	pressure ratio across shock wave, P_{n+1}/P_n
ρ	density
σ	tensile strength
τ	running time
τ_w	wall shear stress
Ψ	ratio of cone to flat plate transition Re

Subscripts and Superscripts

b	conditions at back face of piston
c	conditions at critical layer; test section circumference
e	conditions at outer edge of boundary layer
f	conditions at front face of piston

G	thin film gauge conditions
p	peak conditions behind 1st reflected shock wave from piston
R	first reflected shock wave conditions
s	incident shock wave conditions; stagnation point conditions
t	stagnation (total) conditions at 30 msec. after start of run
w	model wall conditions; wire conditions
o	room temperature (or reference) conditions
1	initial barrel conditions
2	conditions behind incident shock wave
3	conditions behind contact surface (or piston)
4	initial driver conditions
5	conditions behind 1st reflected shock wave
∞	free stream conditions
*	conditions at nozzle throat; conditions at reference temperature T*
$\overline{(\ )}$	refers to mean quantities
$(\ )'$	instantaneous fluctuating quantity

LIST OF FIGURES

PART I

Fig. 1.1 Gun Tunnel Operation

Fig. 2.1 General View Gun Tunnel from Driver

Fig. 2.2 Oxford University Hypersonic Gun Tunnel

Fig. 2.3 Nozzle Dimensions

Fig. 2.4 Gun Tunnel Mach 7 Contoured Nozzle

Fig. 2.5 Contoured Nozzle Notation

Fig. 2.6(a) Working Section

(b) Nozzle Exit and Pitot

Fig. 2.7 Air Flow Sketch Diagram

Fig. 2.8(a) Air Control Panel

(b) Compressors

Fig. 2.9 Diaphragm Natural Bursting Pressure

Fig. 2.10 Aluminium Diaphragm Bursting Pressure

Fig. 2.11 Gun Tunnel Piston

Fig. 2.12 Nylon Piston (43 Grams)

Fig. 3.1 Gun Tunnel Instrumentation

Fig. 3.2(a) Pitot Probe with Hemisphere Heat Gauge Adaptor

(b) Static Pressure Ring

Fig. 3.3 Heat Transfer Analogue Circuit Arrangement

Fig. 3.4 Thin Film Gauge Pulse Calibration Circuit

Fig. 3.5 Thin Film Gauge Calibration (Gauge SP1)

Fig. 3.6 Stagnation Point Heating

Fig. 3.7 Heat Transfer Analogue Circuit

Fig. 3.8 Analogue Calibration

Fig. 3.9 Schlieren Geometry

Fig. 3.10 Transducer Calibration

Fig. 3.11 Typical Pressure Traces

Fig. 4.1 Gun Tunnel Shock Velocity

Fig. 4.2 M_s vs P_{51} & T_{51} - Ideal Shock Tube Theory - Air

Fig. 4.3 x - t Diagram Detail

Fig. 4.4 Gun Tunnel x - t Diagram

Fig. 4.5 Reservoir Pressure Record - Effect of Piston Mass and P_{41}

Fig. 4.6 Reservoir Pressure Recovery

Fig. 4.7 Peak Pressure (P_p) Measurements

Fig. 5.1 Theoretical Running Time Based on Mass Flow Rate

Fig. 5.2 Gun Tunnel Running Time

Fig. 5.3 Mach 7 Contoured Nozzle Calibration, Re/cm = 1.75×10^5

Fig. 5.4 Mach 7 Contoured Nozzle Calibration, Re/cm = 3.4×10^5

Fig. 5.5 Contoured Nozzle Mach Number Symmetry Tests

Fig. 5.6 University of Southampton Total Temperature Probe

Fig. 5.7 Total Temperature Probe Output

Fig. 5.8 Total Temperature Probe Output

Fig. 5.9 Total Temperature Probe Output

Fig. 5.10 Gun Tunnel Temperature History

Fig. 5.11 Gun Tunnel Total Temperature

Fig. 5.12 Stagnation Point Thin Film Anemometer Output Voltage

Fig. 5.13 Stagnation Point Thin Film Calibration Gauge 1

Fig. 5.14 Detailed Pressure Analysis

Fig. 5.15 Gun Tunnel Total Temperature

Fig. 5.16 Flat Plate Static Pressure

Fig. 5.17 Equilibrium Condensation Temperature - Air

Fig. 6.1 Flow Velocity

Fig. 6.2 Sutherland Viscosity Relation - Air

Fig. 6.3 Free Stream Unit Reynolds Number

Fig. 6.4 Maximum Free Stream Unit Reynolds Number

Fig. 6.5 Free Flight Unit Reynolds Number

Fig. 6.6 Gun Tunnel Free Flight Reynolds Number Simulation Region

PART II

Fig. 9.1 3" Hollow Cylinder Model
Fig. 9.2 Standard Hollow Cylinder Transition Model
Fig. 9.3 Hollow Cylinder Shadowgraph
Fig. 9.4 Hollow Cylinder Transition Reynolds Number
Fig. 9.5 Microdensitometer Boundary Layer Profiles
Fig. 9.6 Boundary Layer Pitot Profiles
Fig. 9.7 Surface Pitot Pressure
Fig. 9.8 Turbulent Pitot Profiles
Fig. 9.9 Laminar Pitot Profiles
Fig. 9.10 Hollow Cylinder Transition on a Common Model
Fig. 9.11 Pate and Schueler Correlation
Fig. 9.12 Hollow Cylinder Data - Nagel Correlation
Fig. 10.1 Flat Plate Heat Transfer Model (No. 1)
Fig. 10.2 10° Cone Heat Transfer Model
Fig. 10.3 Flat Plate Surface Heat Transfer - I
Fig. 10.4 Flat Plate Surface Heat Transfer - II
Fig. 10.5 Flat Plate Surface Heat Transfer - III
Fig. 10.6 10° Cone Surface Heat Transfer - I
Fig. 10.7 10° Cone Surface Heat Transfer - II
Fig. 10.8 10° Cone Surface Heat Transfer - III
Fig. 10.9 10° Cone Surface Heat Transfer - IV
Fig. 10.10 Transition Reynolds Number
Fig. 10.11 10° Cone Heat Transfer Traces
Fig. 10.12 Effect of Model Curvature on Transition Location
Fig. 10.13 Ratio of End Transition Point Between Cone and Planar Model
Fig. 11.1 Flat Plate Hot Wire Traversing Mechanism
Fig. 11.2 Hot Wire Probe Tip

Fig. 11.3	Hot Wire Anemometer Bridge Connections
Fig. 11.4	Half Wave Integrator
Fig. 11.5	Hot Wire Signal Analysis - I
Fig. 11.6	Hot Wire Signal Analysis - II
Fig. 11.7	Hot Wire Total Output
Fig. 11.8	Flat Plate Hot Wire Profiles - I
Fig. 11.9	Flat Plate Hot Wire Profiles - II
Fig. 11.10	Flat Plate Boundary Layer Thickness
Fig. 11.11	Mean Wire Convected Heat Transfer
Fig. 11.12	Peak Fluctuation Location
Fig. 11.13	Peak Fluctuation Height in Laminar Boundary Layers
Fig. 11.14	Typical Hot Wire Output Near Peak y/δ
Fig. 11.15	Flat Plate Hot Wire Output

LIST OF TABLES

		Page
Table 1(a)	Contoured Nozzle Co-ordinates with Turbulent Boundary Layer Corrections	8a
(b)	Nozzle Co-ordinates (contd.)	8b
Table 2	Gun Tunnel Operational Diaphragms	14
Table 3	Thin Film Gauge Calibration Factors	26
Table 4	Analogue Calibration Factors	31
Table 5	Summary of Shock & Piston Velocity Measurements	44
Table 6	Peak Pressure Measurement & Theory	51
Table 7	Working Section Mach Number	56
Table 8	Shock Wave Entropy Rise	63
Table 9	Transition Test Facilities	84
Table 10	Transition Results Summary	112

PART ONE - THE GUN TUNNEL

CHAPTER ONE

INTRODUCTION

The hypersonic gun tunnel is basically a simple shock tube fitted with a hypersonic expansion nozzle at the downstream end of the tube. The shock processed gas in the shock tube provides the necessary source of gas to act as a reservoir to drive the nozzle. The gun tunnel differs from a conventional reflected shock tunnel only in the presence of a free sliding piston (in the former) placed in the barrel downstream of the diaphragm station. As with a shock tube, the mode of operation of a gun tunnel can best be described by a simple x - t wave diagram (Fig. 1.1). The bursting of the primary diaphragm permits the high pressure driver gas to expand and accelerate the piston. The accelerating piston causes compression waves to propagate into the barrel gas. These waves gradually coalesce and form a shock wave which continues down the barrel at a supersonic velocity compared with the sound speed in the undisturbed barrel gas. This wave thus increases its separation from the piston with time. The light piston would in theory approach the velocity of the ideal contact surface in normal shock tube flow. The shock wave on reaching the end of the barrel, reflects and propagates back upstream until striking the piston. This step increase in force on the front face of the piston produces an acceleration in a direction opposite to the piston velocity and after some time causes the piston to cease its forward motion and even reverse direction. During this time the shock wave will have experienced multiple reflections between the

FIG.1.1

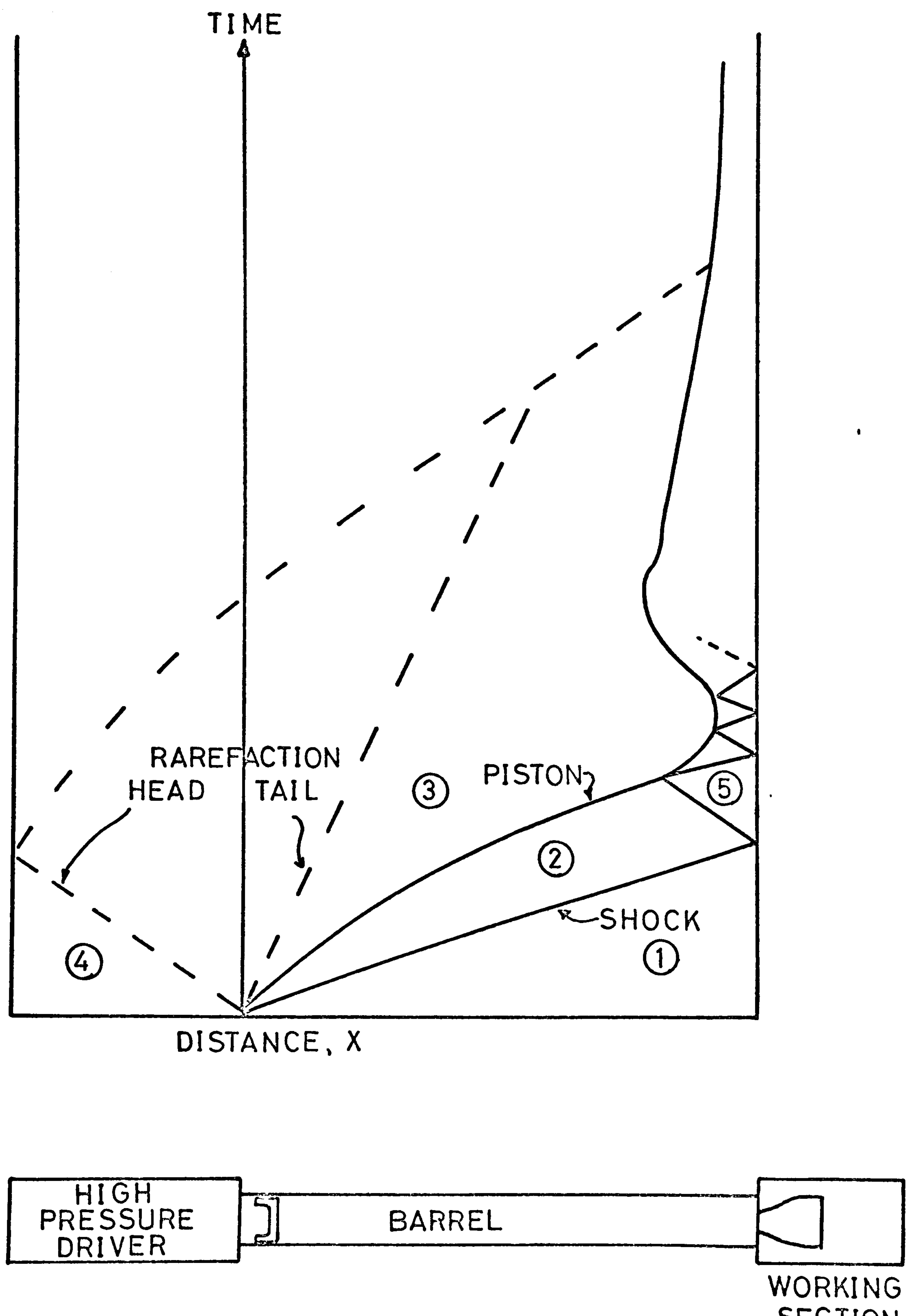

GUN TUNNEL OPERATION

piston and the end wall until it has weakened into a sound wave. The shock compressed gas is relatively slowly expelled through the throat entrance of the nozzle as the piston approaches the end wall in dynamic equilibrium. The time period between when the piston oscillations and shock reflections decay and when the piston arrives at the end wall is usually considered the steady running time of the gun tunnel. The diaphragm burst also sets up an expansion wave system similar to that in a shock tube. The arrival of this wave system at the back face of the piston can also limit the test time by causing a pressure drop in the compressed barrel gas.

Early theoretical evaluation of the potential performance of the gun tunnel concept of operation predicted very high temperatures and pressures compared with conventional reflected shock tunnel performance (Refs. 1-4). It was also suggested that running times an order of magnitude greater than shock tunnels could be expected due to the presence of a piston to separate the cold expanded driving gas from the hot driven gas. The longer running time and to some extent the higher pressure predictions have been realized in the practical operation of gun tunnels. In every practical situation,however, it has proved quite impossible to achieve the high temperatures of the theoretical predictions. This was due in part to the divergence of the actual multiple shock reflection behaviour from that assumed in the original theories. The primary limitation, however, proved to be the design of pistons to operate at the high diaphragm pressure ratios needed to produce strong shocks. The high pressure ratios imply both a very high piston kinetic energy and a relatively low barrel pressure ahead of the piston. The piston therefore grossly overshoots its equilibrium pressure position near the end of the barrel to produce the very high peak pressure required to remove its kinetic energy in a short distance. The resulting high acceleration loadings usually caused destructive failure of the piston.

The gun tunnel was therefore seen to be best used as a low enthalpy shock tunnel with high Reynolds Number simulation capabilities (high pressure, low temperature) and long running times which eased many instrumentation requirements compared to shock tunnels. Many research groups have devoted great efforts into gun tunnel operational development in the past 10-15 years, most notably R.A.R.D.E. (Fort Halstead), Imperial College and the University of Southampton (Refs. 1, 5-9). Although the first gun tunnel in operation was at NASA-Ames, this facility was a heavy piston type and experienced structural failures in attempts to achieve high temperatures. This was soon abandoned and it remained for the groups mentioned above to develop the first comprehensive range of experiments which lead to a more complete understanding of gun tunnel operation. Later, other groups became active in the field of gun tunnel development and in many cases were able to make significant contributions to the understanding of gun tunnel real performance. The following references include some of the important contributed papers from most of the groups involved with gun tunnel research but is by no means comprehensive (Refs. 6, 10-24). It is seen that gun tunnel operation has been extended to total pressures greater than 680 atmospheres (Refs. 20, 22). Although most total temperature operation of gun tunnels is below 2000°K, careful piston design (Ref. 12) and preheating of the barrel gas (Ref. 24) has allowed operation somewhat above this value.

The purpose of Part I of this thesis is to describe in some detail the design and operation of the Oxford University Hypersonic Gun Tunnel which has been in operation at the Department of Engineering Science since mid-1967. This includes a mechanical description of the Gun Tunnel including diaphragm development. The development of general instrumentation and instrumentation techniques used in Part II of the thesis is also discussed. The calibration of the shock compression heater with estimates of piston motion was performed and comparisons with some theoretical estimates of performance made. A calibration of the flow conditions in the working section was carried out with emphasis on Mach number and total temperature determination.

CHAPTER TWO

GENERAL DESCRIPTION OF GUN TUNNEL

2.1 Driver and Shock Tube Barrel

A general view of the Gun Tunnel is shown in Fig. 2.1. This is a view taken from the driver end looking downstream along the barrel toward the working section at the far end. The double diaphragm assembly can be seen in the foreground in an extracted position. The arrangement of the high pressure driver, barrel and working section is shown schematically in Fig. 2.2. The high pressure vessel which serves as the driver consists of a single piece cylindrical barrel of 6 inches (15.24 cm) internal diameter and 20 feet (6.56 m) in length. This vessel has been hydraulically tested to 510 atmospheres and designed for compressed gas operation to 374 atmospheres.

The driver pressure is sealed from the driven barrel by two metal diaphragms. A sectional view of this double diaphragm assembly is shown in Ref. 25. Two diaphragms are employed to permit driver pressure operation above the natural bursting pressure of a single diaphragm with an intermediate pressure maintained between the two diaphragms. The bursting point is then precisely set in both pressure and time by the sudden venting to atmosphere of the intermediate pressure between the two diaphragms. The compression on the 'O' ring seals of the double diaphragm assembly is maintained by a pressure differential arising from the location of the two upstream 'O' rings. The two transition blocks upstream of each diaphragm are unconstrained axially to allow easy replacement and removal of diaphragms and to ensure complete compression of the 'O' rings into their dovetail grooves when

FIG. 2.1

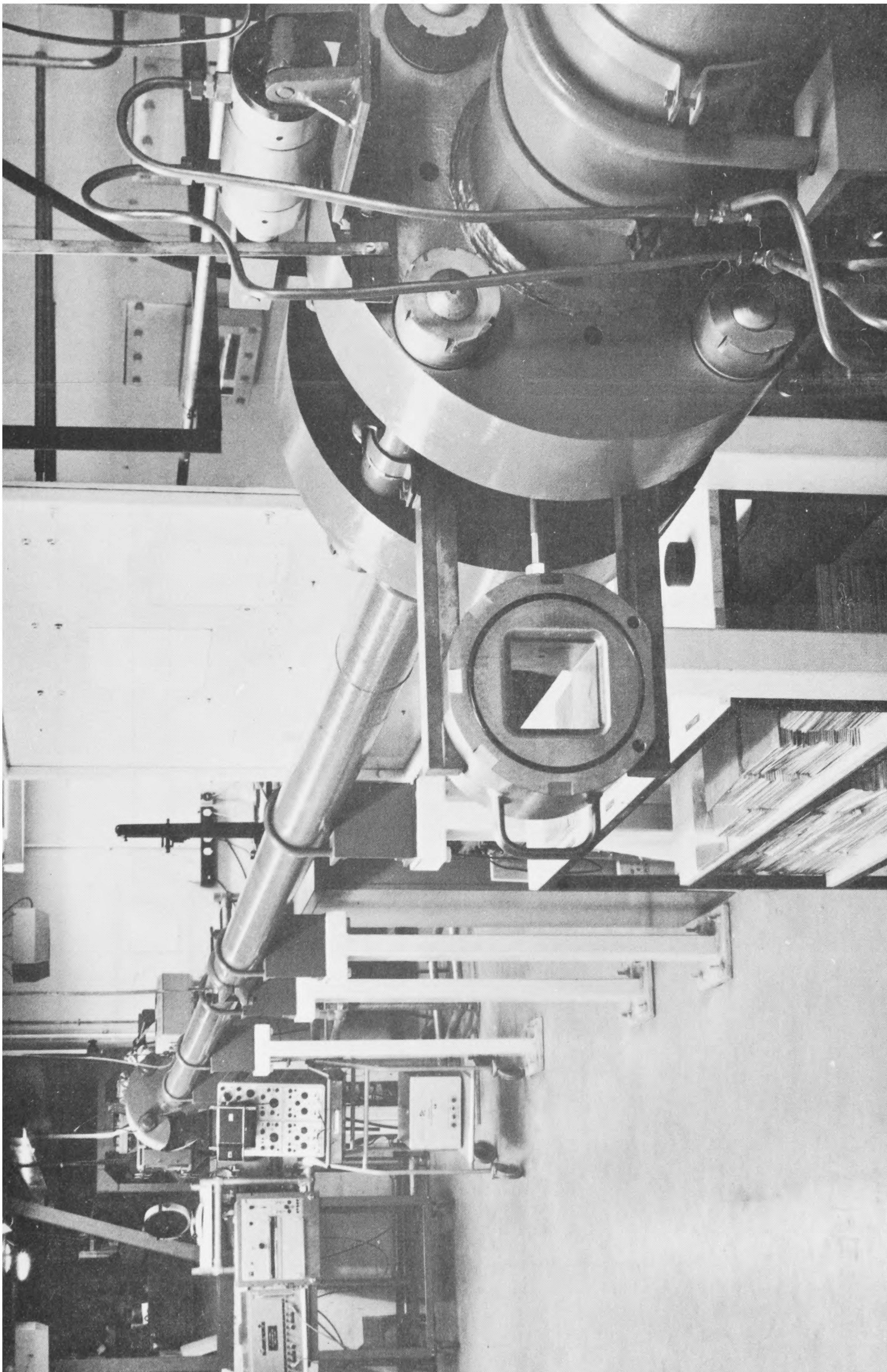

GENERAL VIEW GUN TUNNEL FROM DRIVER

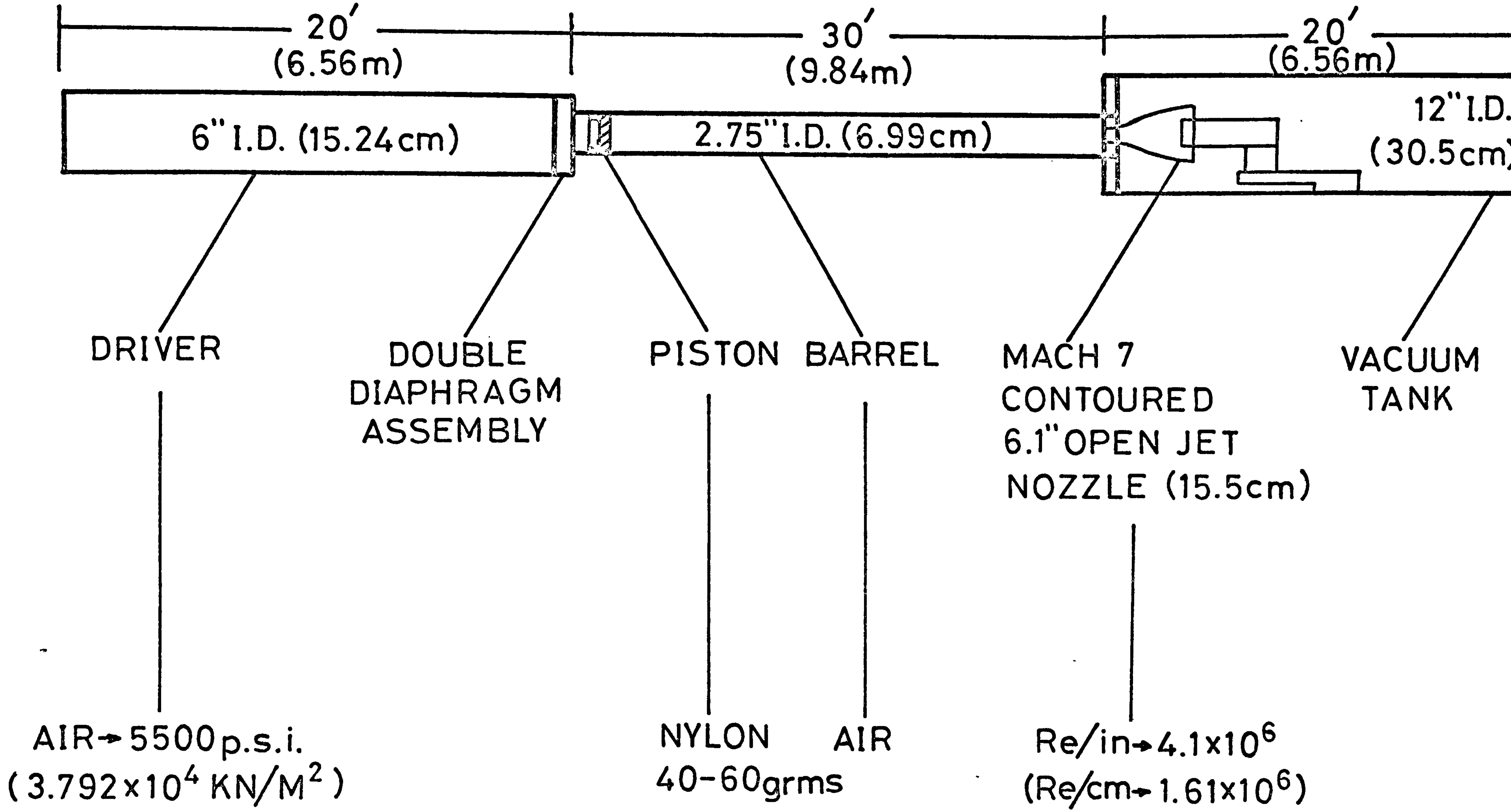

OXFORD UNIVERSITY HYPERSONIC GUN TUNNEL

FIG.2.2

pressure is applied. The cross-section of the transition blocks downstream of each diaphragm is 89 x 89 mm square to ensure symmetrical petalling of the diaphragms. Further details of diaphragm design will be discussed in Section 2.5.

The barrel, or driven tube, downstream of the diaphragms is made up of two equal length sections to form a total length of 30 feet (9.84 m) with a bore diameter of 2.75 inches (6.99 cm). The internal diameter has been accurately bored and honed to a tolerance of ± .002 inches (± .05 mm). The internal diameter of the downstream end of the barrel is about .0035 inches (.089 mm) larger than the upstream end. The entire internal surface of the barrel has been hardened and plates by a 'Kanigen' process. The barrel is fitted with three removable instrumentation ports on the top-dead-center sidewall at $1\frac{3}{8}$ inches (3.49 cm), 6 inches (15.24 cm) and 18 inches (45.7 cm) from the downstream end of the barrel.

2.2 Hypersonic Expansion Nozzle

There are several dimensional constraints which must be considered in nozzle design for the existing Gun Tunnel configuration. The exit plane diameter has an upper limit of the dump tank diameter. The upper limit of the nozzle throat size is constrained by the necessity to maintain a nearly solid wall for perfect normal shock reflection. The minimum area ratio of barrel to throat has been set as 25 (Ref. 26). This may be a somewhat arbitrary limit and may be revised downward if care is taken to measure any changes in flow conditions caused by imperfect shock reflection. The minimum size for the throat (and thus the exit plane for a given Mach number) is set only by the minimum size test core that one can accept for a model of interest. Some of these dimensional constraints can be viewed more clearly in Fig. 2.3 for a range of moderate hypersonic Mach Numbers.

There are many experimental situations where a parallel test stream with very small axial gradients of test conditions is desired. A general discussion of the limitations of conical nozzles can be found in Refs. 27 and 28. In view of these limitations, a Mach 7 contoured expansion nozzle was designed and fabricated for use with the Gun Tunnel. A sectional view of this nozzle is shown in Fig. 2.4. The overall length is about 29 inches (73.6 cm) and the nozzle exit diameter is 6.1 inches (15.5 cm). The throat diameter was made to be 0.55 inches (1.4 cm) giving an area ratio between the barrel and throat of 25. The stainless steel throat section was made as a separate insert to facilitate its replacement in case of damage or for a change in nozzle area ratio. Operation of the nozzle off its design Mach Number would lead to some degradation in performance, however. The aluminium mandrel is shown in position to act as a form for the winding of the fibreglass reinforced epoxy resin nozzle shell. It was of course removed when the nozzle was installed. The initial length of the nozzle expansion was made of steel to allow the static pressure to fall below an atmosphere for the highest reservoir pressure operating conditions by the time the epoxy part of the wall was reached.

The co-ordinates of the contoured Mach 7 expansions were calculated by a computer program developed at the Bristol Engines Division of Rolls Royce Ltd. and kindly made available by Mr. R. Hawkins and Mr. R. Hurd. The computer yields the inviscid co-ordinates X, Y as well as including an estimate

FIG. 2.3

NOZZLE DIMENSIONS

BARREL DIAMETER 2.75" ($A=5.93\ IN^2$)
[6.98cm, $38.2\,cm^2$]
A^* = THROAT AREA

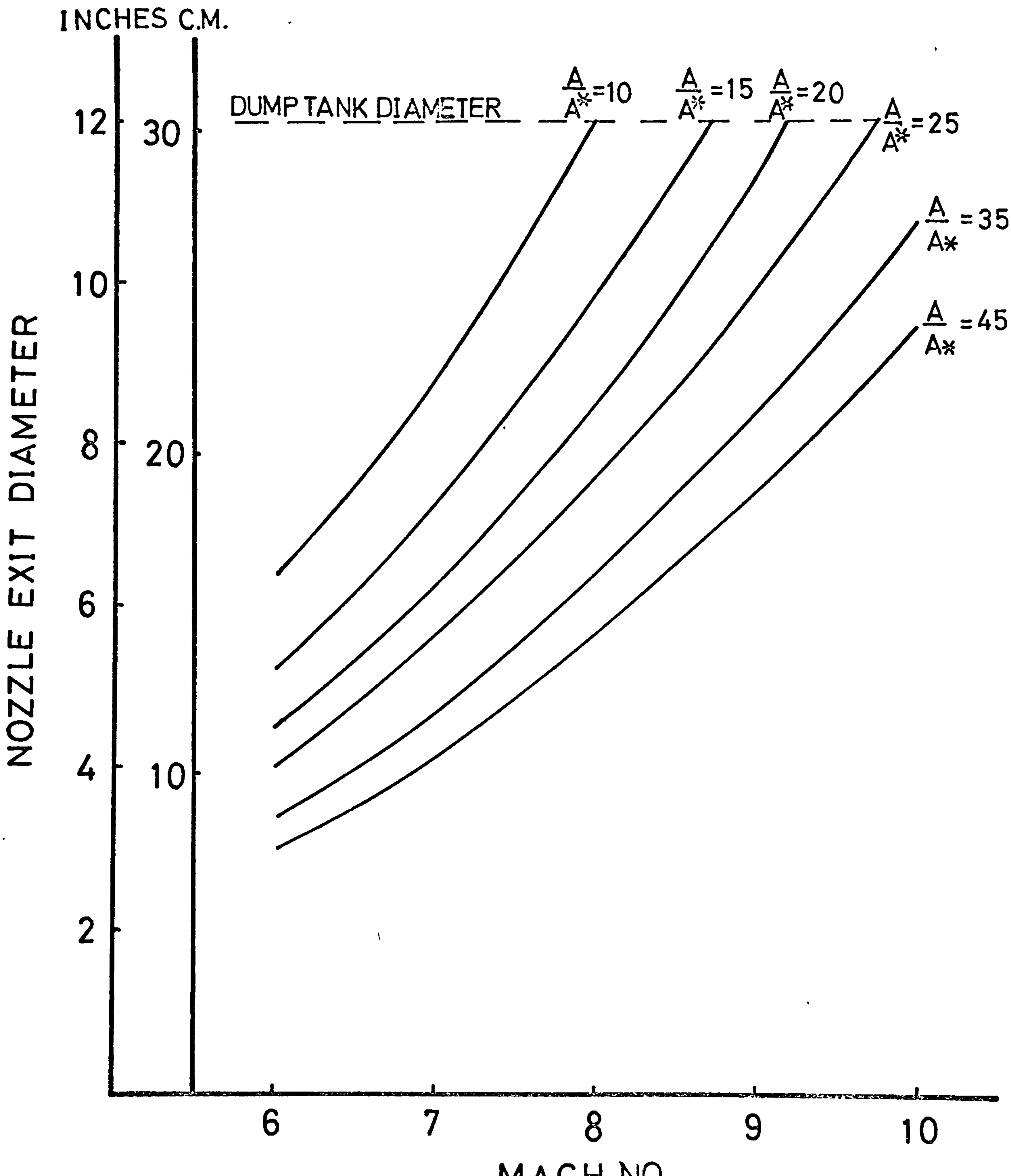

FIG.2.4

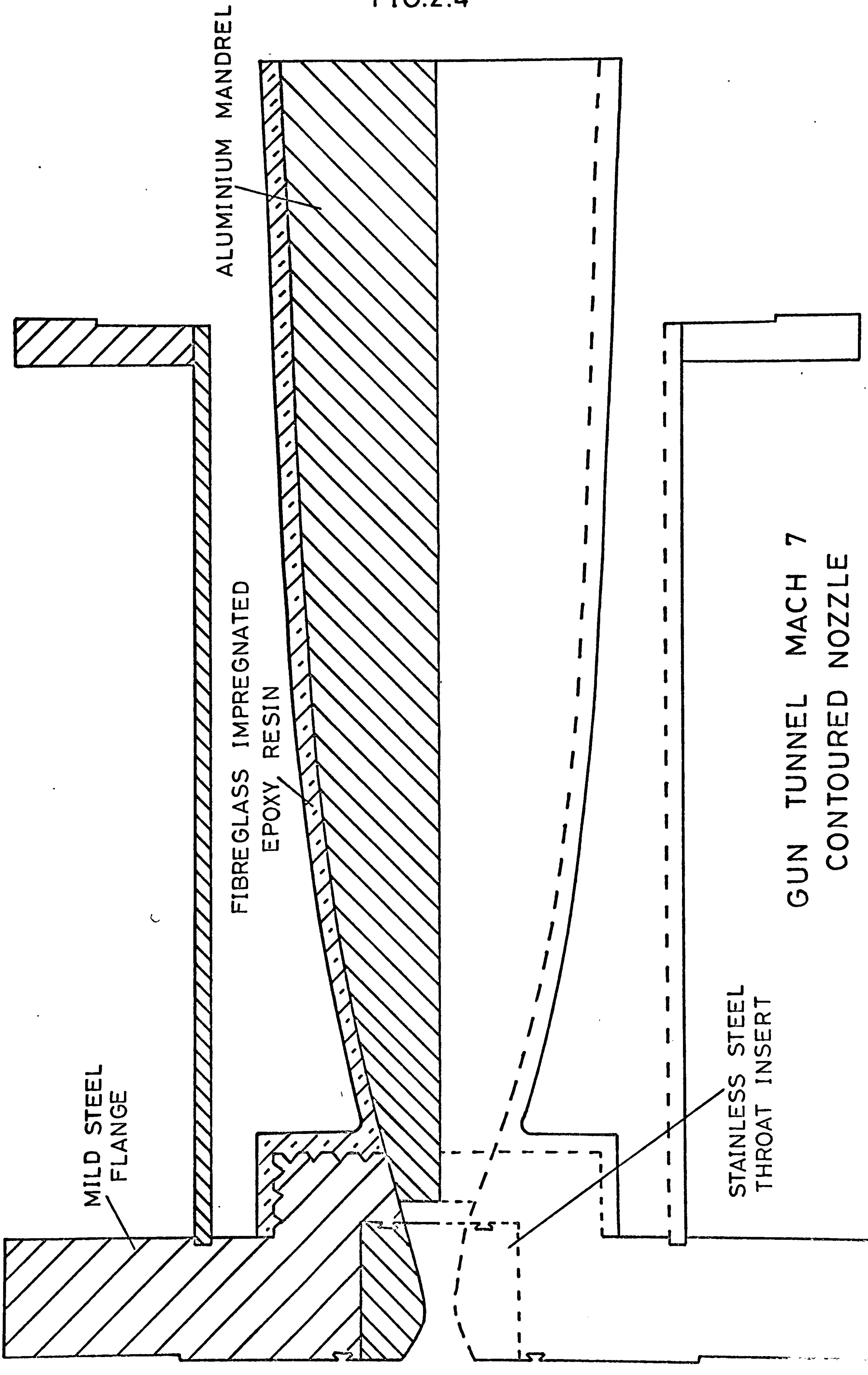

ALUMINIUM MANDREL
FIBREGLASS IMPREGNATED
EPOXY RESIN
MILD STEEL
FLANGE
STAINLESS STEEL
THROAT INSERT
GUN TUNNEL MACH 7
CONTOURED NOZZLE

of the local compressible turbulent boundary layer displacement thickness δ^*. This estimate is based on a correlation of several adiabatic wall compressible turbulent displacement thickness expressions as outlined in a paper by Stratford and Beaver (Ref. 29). The δ^* estimate must be made for a particular operating reservoir condition. The definition of the terms calculated by the program is illustrated in Fig. 2.5. The computer output of these terms is listed in Tables 1 (a,b) for a Mach 7 axially symmetric nozzle with a total pressure of 204.2 atmospheres and a total temperature of 700°K. The length dimensions are in inches. Operation off the design reservoir conditions does not introduce great errors as the displacement thickness has only a $-\frac{1}{5}$ power law dependence on Reynolds Number. The nozzle length can be shortened depending on the degree of flow divergence and the Mach Number loss one is willing to tolerate. The computer program also produced a listing of the actual corrected co-ordinates in any convenient ΔX separation interval.

Using the computed co-ordinates with the boundary layer corrections, two-dimensional plates of the nozzle profile were formed on a precision milling machine. The internal profile of the throat section and the external profile of the aluminium mandrel were then cut using profile copying lathes. The contour of the short wall length of the mild steel flange was direct cut to the proper co-ordinates on a standard lathe. With the mandrel in place as shown in Fig. 2.4, the epoxy-fibreglass laminate was wrapped as shown by the Industrial Reinforced Plastics Company of Bristol. Mandrel extraction then left the completed nozzle profile with joining errors of less than .001 inches (25 μ).

FIG. 2.5

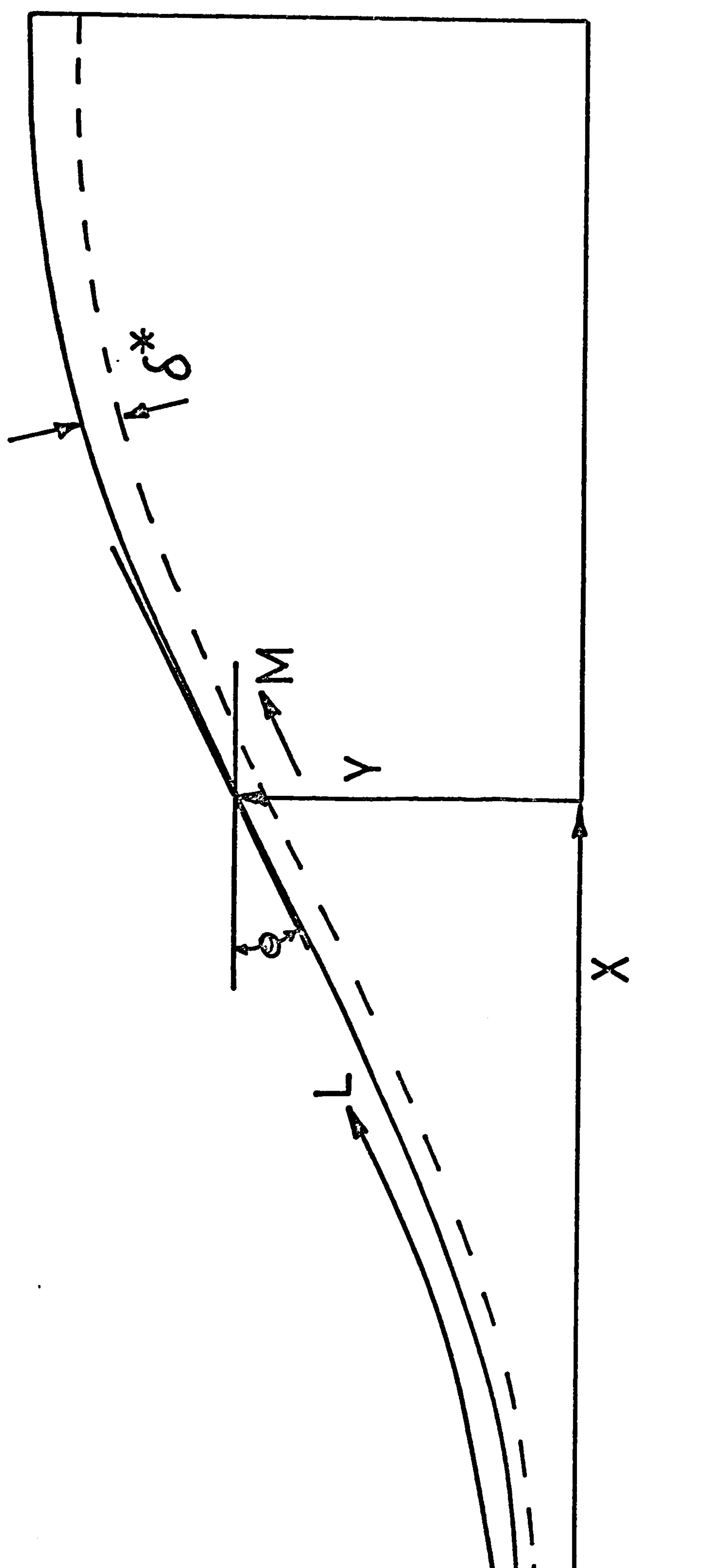

CONTOURED NOZZLE NOTATION

Table 1a

CONTOURED NOZZLE CO-ORDINATES WITH TURBULENT BOUNDARY LAYER CORRECTION

MACH 7.00 AXIALLY SYMMETRIC
TOTAL PRESSURE 204.20 ATMOSPHERES
TOTAL TEMPERATURE 700.00 KELVIN

UNCORRECTED CO-ORDINATES X, Y, (INCHES)

X	Y	M	DELTA-STAR
-5.50000-1	2.75000-1	1.00000+0	0.00000+0
0.00000+0	2.75000-1	1.03023+0	1.22627-3
3.43027-2	2.75217-1	1.07512+0	1.20127-3
4.22015-2	2.75330-1	1.08537+0	1.19719-3
5.12009-2	2.75478-1	1.09738+0	1.19263-3
6.13811-2	2.75685-1	1.11129+0	1.18772-3
7.28208-2	2.75960-1	1.12660+0	1.18382-3
8.55907-2	2.76320-1	1.14373+0	1.18060-3
9.97631-2	2.76785-1	1.16273+0	1.17847-3
1.15409-1	2.77376-1	1.18381+0	1.17761-3
1.32594-1	2.78118-1	1.20702+0	1.17849-3
1.51381-1	2.79037-1	1.23251+0	1.18144-3
1.71840-1	2.80162-1	1.26039+0	1.18694-3
1.93978-1	2.81528-1	1.29076+0	1.19533-3
2.17870-1	2.83170-1	1.32372+0	1.20716-3
2.43534-1	2.85125-1	1.39987+0	1.19136-3
2.70988-1	2.87430-1	1.39776+0	1.24620-3
3.00223-1	2.90119-1	1.43770+0	1.27206-3
3.31218-1	2.93238-1	1.48308+0	1.30159-3
3.63924-1	2.96827-1	1.53005+0	1.33803-3
3.98263-1	3.00910-1	1.57985+0	1.38099-3
4.34131-1	3.05525-1	1.63243+0	1.43091-3
4.71375-1	3.10689-1	1.68769+0	1.48819-3
5.09803-1	3.16420-1	1.74546+0	1.55316-3
5.49203-1	3.22718-1	1.80553+0	1.62610-3
5.89295-1	3.29566-1	1.86762+0	1.70711-3
6.29797-1	3.36944-1	1.93139+0	1.79615-3
6.70340-1	3.44812-1	1.99642+0	1.89289-3
7.10652-1	3.53105-1	2.06230+0	1.99711-3
7.50461-1	3.61757-1	2.12859+0	2.10843-3
7.89467-1	3.70725-1	2.19479+0	2.22593-3
8.27689-1	3.79940-1	2.26063+0	2.34972-3
8.65062-1	3.89422-1	2.32581+0	2.47901-3
9.02039-1	3.99190-1	2.39037+0	2.61488-3
9.39029-1	4.09403-1	2.45447+0	2.75775-3
9.77045-1	4.20266-1	2.51869+0	2.91045-3
1.01715+0	4.32121-1	2.58377+0	3.07591-3
1.06076+0	4.45395-1	2.65073+0	3.25884-3
1.10953+0	4.60578-1	2.72068+0	3.46537-3
1.16481+0	4.78197-1	2.79449+0	3.70104-3
1.22820+0	4.98649-1	2.87283+0	3.97365-3
1.30043+0	5.22269-1	2.95573+0	4.28787-3
1.38224+0	5.49112-1	3.04285+0	4.64986-3
1.47288+0	5.78241-1	3.13297+0	5.05977-3
1.57182+0	6.11388-1	3.22497+0	5.51882-3
1.67794+0	6.65950-1	3.31760+0	6.02542-3

Table 1b

NOZZLE CO-ORDINATES (Continued)

X	Y	M	DELTA-STAR
1.79129+0	6.81986-1	3.41073+0	6.58230-3
1.91460+0	7.21158-1	3.50555+0	7.20446-3
2.09065+0	7.77843-1	3.62983+0	8.11195-3
2.31660+0	8.46812-1	3.77293+0	9.30615-3
2.57234+0	9.20716-1	3.91832+0	1.07038-2
2.85112+0	9.98814-1	4.06148+0	1.22848-2
3.15029+0	1.01862+0	4.20085+0	1.40450-2
3.46808+0	1.16941+0	4.33597+0	1.59810-2
3.80377+0	1.21032+0	4.46659+0	1.80963-2
4.15792+0	1.32094+0	4.59300+0	2.04011-2
4.52845+0	1.40678+0	4.71496+0	2.28864-2
4.91571+0	1.47170+0	4.83279+0	2.55578-2
5.32054+0	1.55103+0	4.94666+0	2.84300-2
5.74010+0	1.63113+0	5.05659+0	3.14800-2
6.17735+0	1.70129+0	5.16294+0	3.47392-2
6.62923+0	1.77156+0	5.26552+0	3.81835-2
7.09816+0	1.84682+0	5.36479+0	4.18349-2
7.58277+0	1.91194+0	5.46072+0	4.56853-2
8.08313+0	1.98874+0	5.55336+0	4.97366-2
8.59878+0	2.04719+0	5.64280+0	5.39852-2
9.13027+0	2.10809+0	5.72911+0	5.84379-2
9.67598+0	2.16661+0	5.81229+0	6.30756-2
1.02383+1	2.22227+0	5.89252+0	6.79272-2
1.08131+1	2.27568+0	5.96978+0	7.29469-2
1.14051+1	2.32598+0	6.04409+0	7.81811-2
1.20086+1	2.37408+0	6.11554+0	8.35687-2
1.26285+1	2.41905+0	6.18406+0	8.91589-2
1.32606+1	2.46162+0	6.24982+0	9.49024-2
1.39075+1	2.50125+0	6.31268+0	1.00822-1
1.45669+1	2.53831+0	6.37279+0	1.06890-1
1.52395+1	2.57266+0	6.43007+0	1.13104-1
1.59249+1	2.60434+0	6.48453+0	1.19453-1
1.66220+1	2.63349+0	6.53625+0	1.25919-1
1.73313+1	2.66001+0	6.58511+0	1.32494-1
1.80515+1	2.68415+0	6.63123+0	1.39155-1
1.87829+1	2.70582+0	6.67451+0	1.45892-1
1.95245+1	2.72519+0	6.71501+0	1.52681-1
2.02760+1	2.74235+0	6.75272+0	1.59506-1
2.10371+1	2.75734+0	6.78760+0	1.66344-1
2.18066+1	2.77038+0	6.81978+0	1.73177-1
2.25845+1	2.78146+0	6.84921+0	1.79985-1
2.33699+1	2.79081+0	6.87602+0	1.86751-1
2.41624+1	2.79851+0	6.90031+0	1.93461-1
2.49613+1	2.80470+0	6.92217+0	2.00103-1
2.57662+1	2.80948+0	6.94169+0	2.06663-1
2.65763+1	2.81300+0	6.95888+0	2.13117-1
2.73913+1	2.81539+0	6.97373+0	2.19434-1
2.82095+1	2.81682+0	6.98586+0	2.25536-1
2.90323+1	2.81748+0	6.99440+0	2.31282-1
2.98565+1	2.81770+0	6.99920+0	2.36585-1

The photographs of Fig. 2.6 show the contoured nozzle assembly in place on the Gun Tunnel. Fig. 2.6b shows clearly the exit plane of the nozzle and illustrates the configuration of the free jet type test section.

2.3 Working Section and Dump Tank

The location and configuration of the working section-dump tank assembly can best be seen by reference to Figs. 2.2 and 2.6 (a,b). This assembly is made up of three sections including the nozzle assembly for a total length of about 20 feet (6.56 m). The internal diameter of the section is 12 inches (30.5 cm). The entire dump tank assembly is mounted on rollers which permit the section to be moved downstream by means of hydraulic rams. The separation is made at the flange at the beginning of the nozzle assembly (far left of Fig. 2.6a) to allow access to the end of the gun barrel to retrieve the piston after a run and to replace the secondary diaphragm (see Section 2.5) which isolates the initial barrel pressure from the working section vacuum. The working section includes two 10 inch (25.4 cm) diameter schlieren quality windows for flow photography. Downstream of the windows are two removable plates on tee-sections for model mounting and instrumentation lead-throughs. Since the dump tank section has been pressure tested to only five atmospheres, steps were taken to prevent the over-pressures which would result from piston failures. A flat plate resting on a vertical port downstream in the dump tank maintains a vacuum seal but will lift clear from any over-pressure in the dump tank.

2.4 Gun Tunnel Air Control System

2.4.1 High Pressure Air Supply System

The high pressure operation of the Gun Tunnel driver and

FIG. 2.6

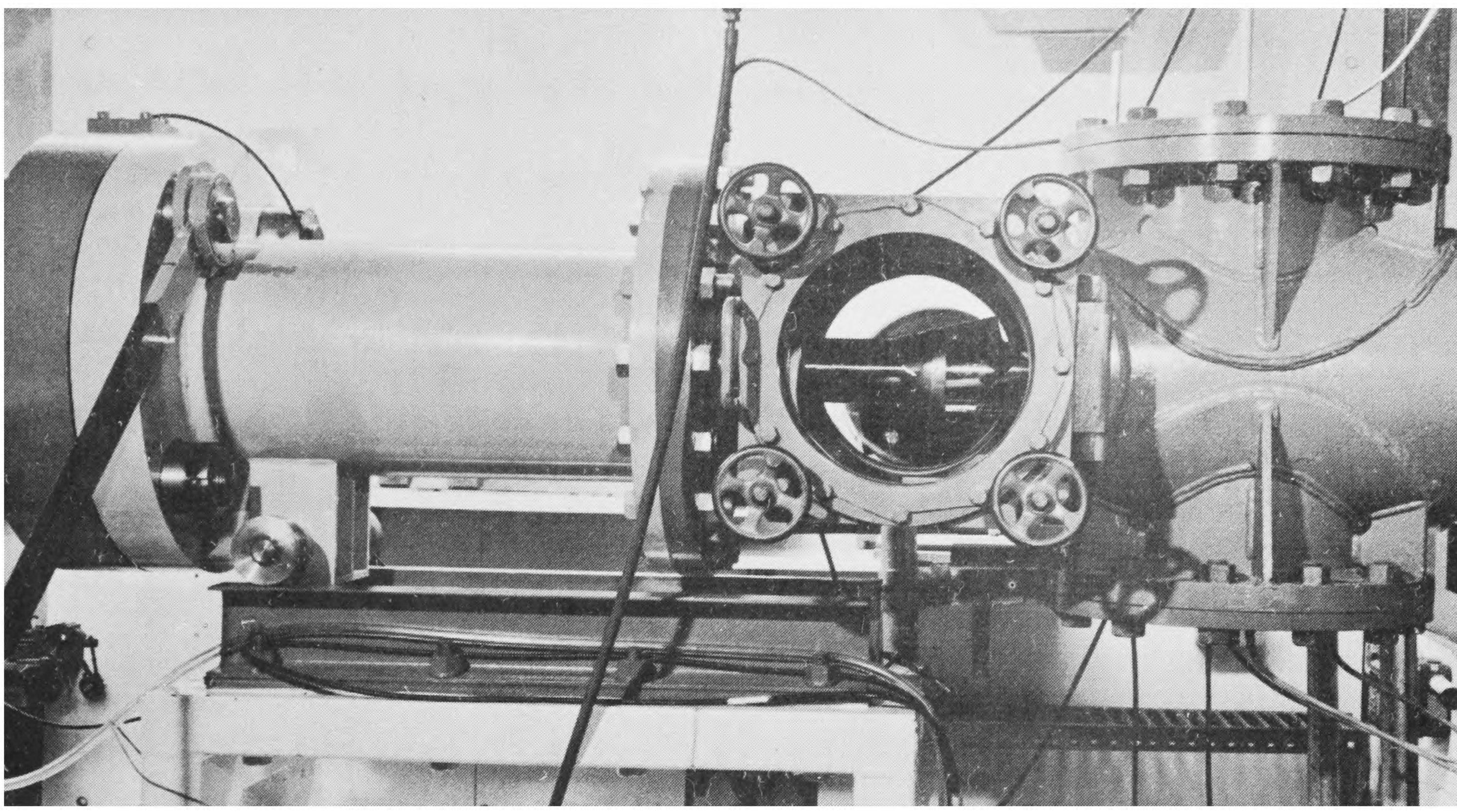

WORKING SECTION

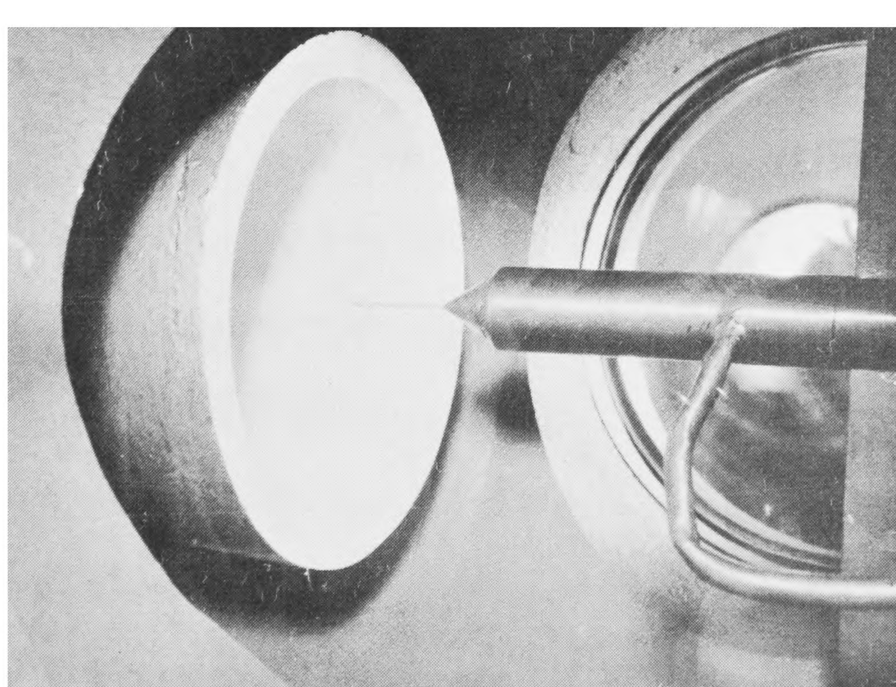

NOZZLE EXIT AND PITOT

its large volume dictates the need for a considerable capacity of high pressure air supply. This is provided by an air compressor and storage combination which has been installed to supply the Gun Tunnel. There are two Corblin diaphragm type air compressors which supply the system. The first machine is a Type A2CV250 two stage compressor with a maximum discharge pressure of 250 atmospheres. The second compressor is a Type B2C1000 single stage machine with an output pressure capability of 1000 atmospheres although in this case it has been set to a limit of 374 atmospheres. The second machine is operated in series with the first when pressures greater than 250 atmospheres are needed. A schematic diagram of the compressor installation and the air line connections to the Gun Tunnel room is shown in Fig. 2.7. The two compressors are shown in Fig. 2.8b. Further details of the compressor design and operation can be found in the manufacturer's operating manual. The pumping rate of each compressor is 4.4 standard cubic feet per minute (7.64 cubic meters per hour). This pumping rate requires about one hour to raise the driver pressure by 68 atmospheres. An air storage capacity of 60 cubic feet (1.7 cubic meters) has been built into the system for pressures up to 250 atmospheres. This allows much faster recycling times for Gun Tunnel operation up to this pressure with the air storage bottles being recharged at a slower rate. Operation frequency at pressures above 250 atmospheres is limited by the pumping speed.

The various parts of the air supply system are separated by up to six floor levels in the building. All air inter-connections are made with AMINCO stainless steel tubing and

FIG. 2.7

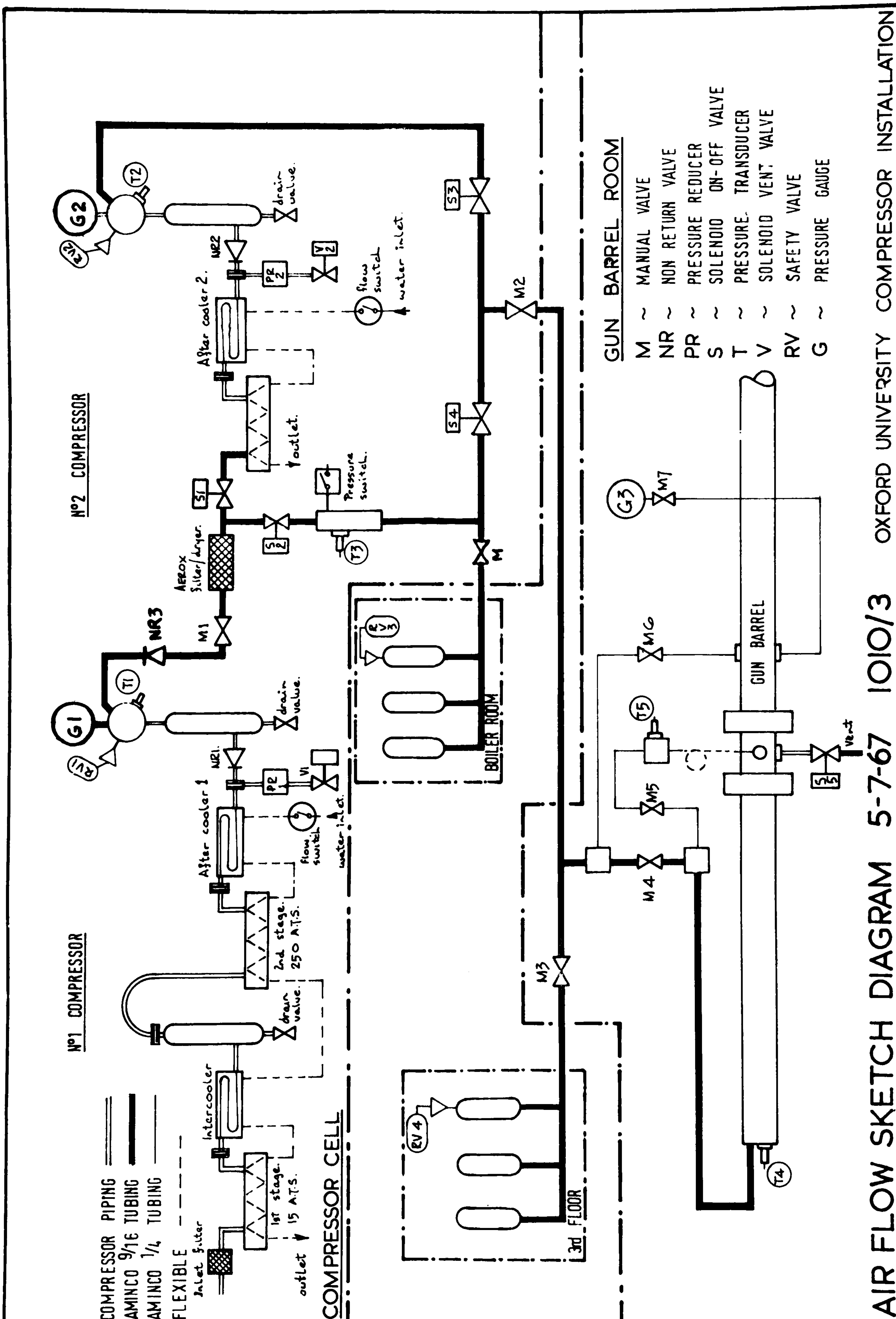

AIR FLOW SKETCH DIAGRAM 5-7-67 1010/3 OXFORD UNIVERSITY COMPRESSOR INSTALLATION
COMPRESSOR PIPING
AMINCO 9/16 TUBING
AMINCO 1/4 TUBING
FLEXIBLE
COMPRESSOR CELL
Nº1 COMPRESSOR
Nº2 COMPRESSOR
BOILER ROOM
3rd FLOOR
GUN BARREL ROOM
M ~ MANUAL VALVE
NR ~ NON RETURN VALVE
PR ~ PRESSURE REDUCER
S ~ SOLENOID ON-OFF VALVE
T ~ PRESSURE TRANSDUCER
V ~ SOLENOID VENT VALVE
RV ~ SAFETY VALVE
G ~ PRESSURE GAUGE
Inlet filter
outlet
1st stage. 15 A.T.S.
Intercooler
drain valve
2nd stage. 250 A.T.S.
After cooler 1
After cooler 2.
flow switch
water inlet
Aerox filter/dryer.
Pressure switch.
GUN BARREL
vent
G1
G2
G3
T1
T2
T3
T4
T5
RV1
RV2
RV3
RV4
NR1
NR2
NR3
PR1
PR2
V1
V2
M
M1
M2
M3
M4
M5
M6
M7
S1
S2
S3
S4
S5

FIG 2.8

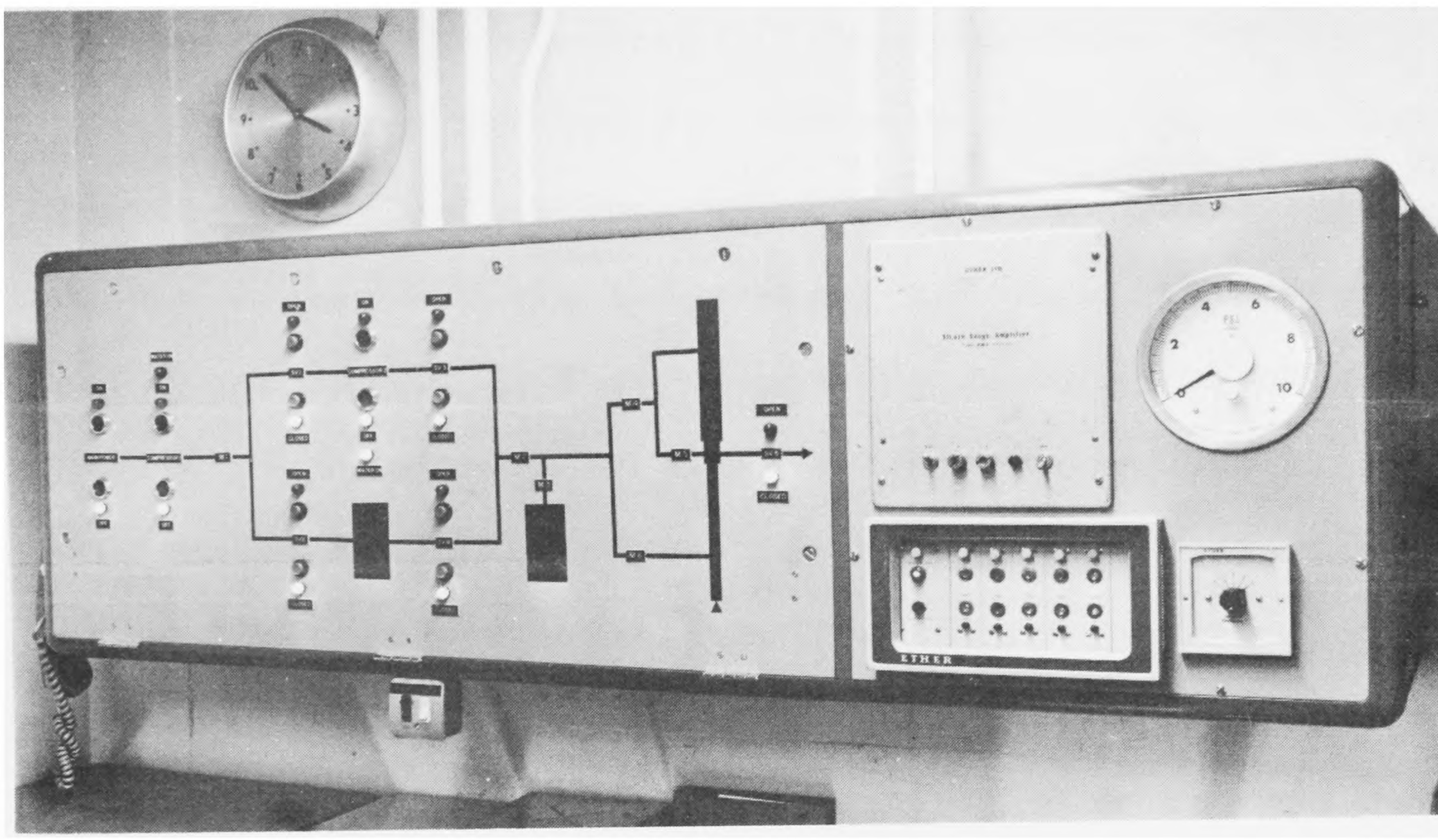

AIR CONTROL PANEL

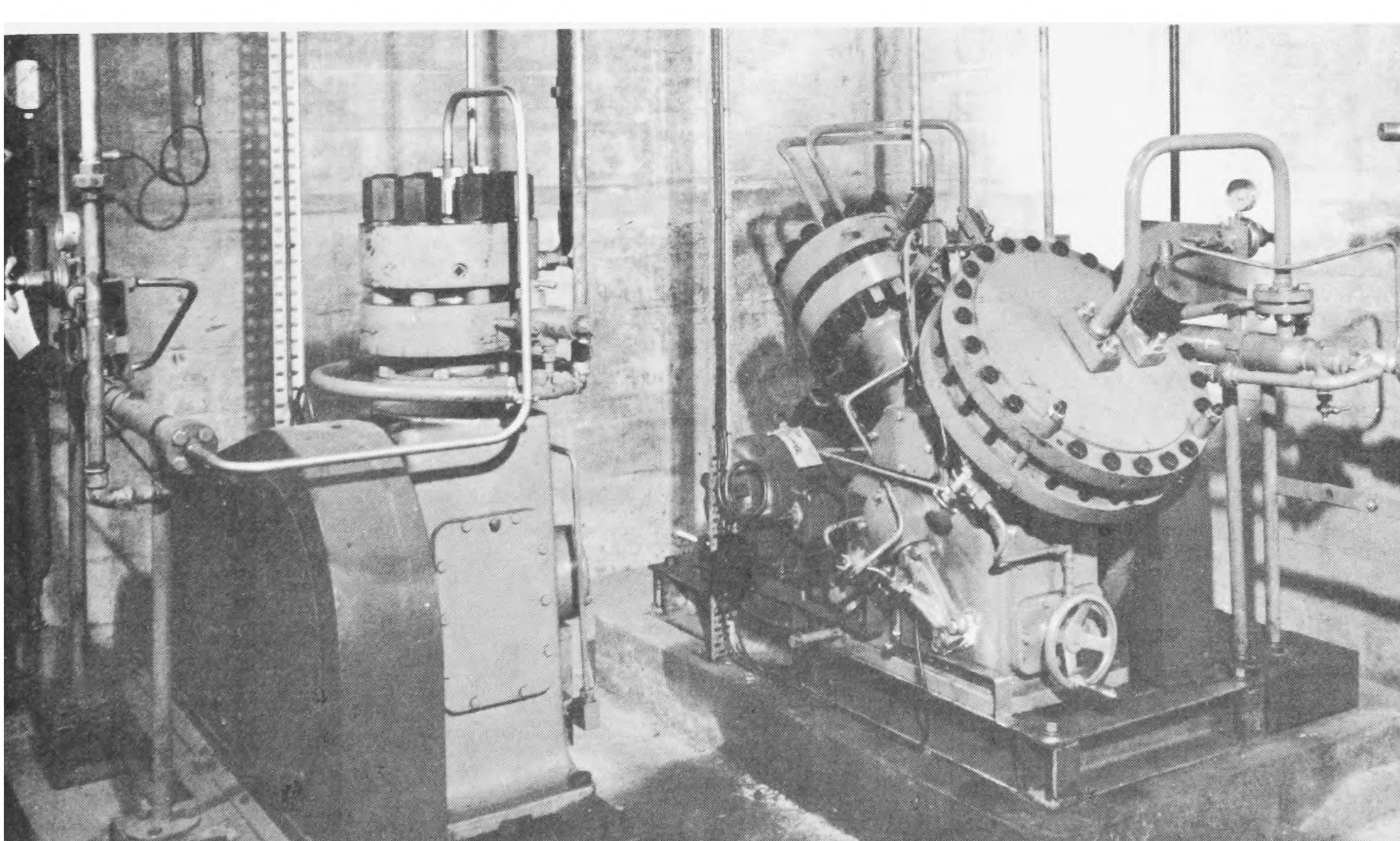

COMPRESSORS

couplings tested up to 1360 atmospheres. The compressors and electrical solenoid air valves are controlled from the Gun Tunnel room by the panel shown in Fig. 2.8a. Schematics of the electrical interconnections of the panel are shown in Ref. 25. These circuits provide interlocking relay connections which prevent improper operation of the system. There are several pressure relief valves and other safety devices to provide for compressor shut-off due to over-pressure or other malfunction. This allows unattended operation of the compressor system. A five channel strain gauge pressure transducer system allows the remote monitoring of pressures at locations shown in Fig. 2.7. Air purity is preserved by the diaphragm type design of the compressors which prevents oil cross-contamination. Inlet and air line particle filters along with air line chemical moisture and oil vapour absorption filters maintain the purity of the air.

Details of the pressure and vacuum connections to the Gun Tunnel are shown in Ref. 25. The manual pressure valves are AMINCO non-rotating stem valves designed for 1360 atmosphere operation and capable of precise flow regulation. This enables accurate pressures to be set in the driver and the barrel with Budenberg Standard Test Gauges to monitor the pressure. The intermediate pressure between the primary diaphragms is set by equilibration with the driver pressure during the driver charging sequence with M5 being closed at a pressure halfway to the final driver level. The pressure in this section is monitored by a strain gauge transducer, and read on the main control panel.

2.4.2 Vacuum System

A vacuum pumping system has been installed on the working section-dump tank to provide the low pressures required to start a hypersonic nozzle. In general the working section pressure must be lowered to a value below the steady static pressure of the expanded nozzle flow at the exit plane (see Ref. 30). A schematic of the vacuum system connection is included in Ref. 25. The vacuum pump is a single stage Leybold S60 rotary type with a pumping speed of 60 cubic meters per hour and an ultimate pressure limit of 20 microns Hg. Pump down time to the normal operating level of 0.5 mm Hg. is 10 minutes. A Genevac thermocouple vacuum gauge monitors the vacuum. A vent valve to atmosphere is provided because the normal post-run pressure in the dump tank is sub-atmospheric. All electrical controls for the vacuum system are operated from the Gun Tunnel control room.

2.5 Diaphragm Development

2.5.1 Primary Diaphragms

Detailed discussions of shock wave diaphragm techniques including analysis of actual bursting pressures of various materials can be found in the standard shock tube texts such as Refs. 31-34. The main requirements of performance for diaphragms in the Gun Tunnel was found to be the ability to open cleanly and fully when suddenly exposed to a pressure above the natural bursting pressure. Clean bursting is desirable to avoid damage to the barrel and piston from high speed metal particles breaking loose from a bursting diaphragm. Full opening of the diaphragms is essential if run to run variations in reservoir pressure due to changing area restrictions at the diaphragm station are to be avoided. These two requirements can best be controlled in the present Gun Tunnel arrangement by scribing the diaphragms. The double diaphragm assembly as described in Section 2.1 has a square cross-section downstream of each diaphragm and all diaphragms have been tested with milled grooves on their downstream facing side. These machined slots are cut with a square cross-section tool and are located in positions corresponding to the diagonals of the diaphragm assembly square section.

The results of some natural bursting pressure tests on various materials in the Gun Tunnel are shown in Fig. 2.9. Photographs of some $\frac{1}{8}$ inch aluminium diaphragms before and after bursting are shown in Ref. 25. This clearly shows the fully opened ideal bursting performance of the Gun Tunnel diaphragms. Tests run on unscribed aluminium diaphragms produced irregular tearing, incomplete opening and (in the case of the downstream diaphragm) a complete shearing off of a large section of metal.

An approximate method of predicting the bursting pressure of unscribed diaphragms was suggested in Ref. 34. The expression is given as

$$P = \frac{(4)(x)(f_{ULT})}{D} \qquad (2.5.1)$$

where D is the diameter of the hemispherical shape the diaphragm is assumed to acquire during loading and x is the material thickness. The thickness x was assumed invariant up to the point where the ultimate yield stress f_{ULT} is reached. Comparison of this prediction for the TYPE BS-1470-1C aluminium used in the bursting tests is made in Fig. 2.10 where the thickness is taken as that remaining after the grooves are machined and D is taken as 3.5 inches. The prediction is quite good for zero (or very small) groove depths. The bursting strength is seen to fall off quite

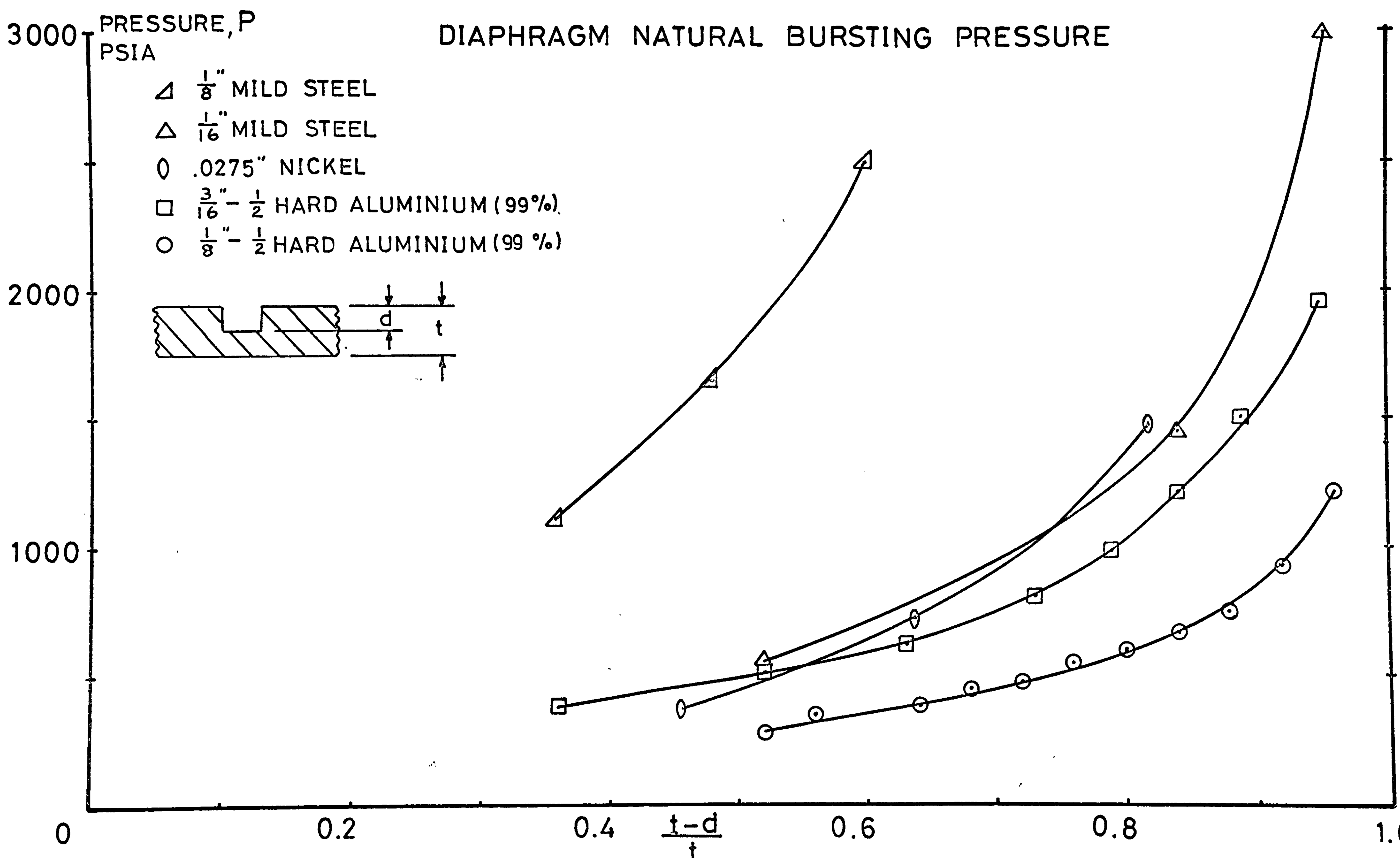

DIAPHRAGM NATURAL BURSTING PRESSURE
PRESSURE, P
PSIA
3000
2000
1000
0
0.2
0.4
0.6
0.8
1.0
$\frac{t-d}{t}$
$\frac{1}{8}$" MILD STEEL
$\frac{1}{16}$" MILD STEEL
.0275" NICKEL
$\frac{3}{16}$" – $\frac{1}{2}$ HARD ALUMINIUM (99%)
$\frac{1}{8}$" – $\frac{1}{2}$ HARD ALUMINIUM (99 %)
d
t

FIG.2.9

ALUMINIUM DIAPHRAGM BURSTING PRESSURE

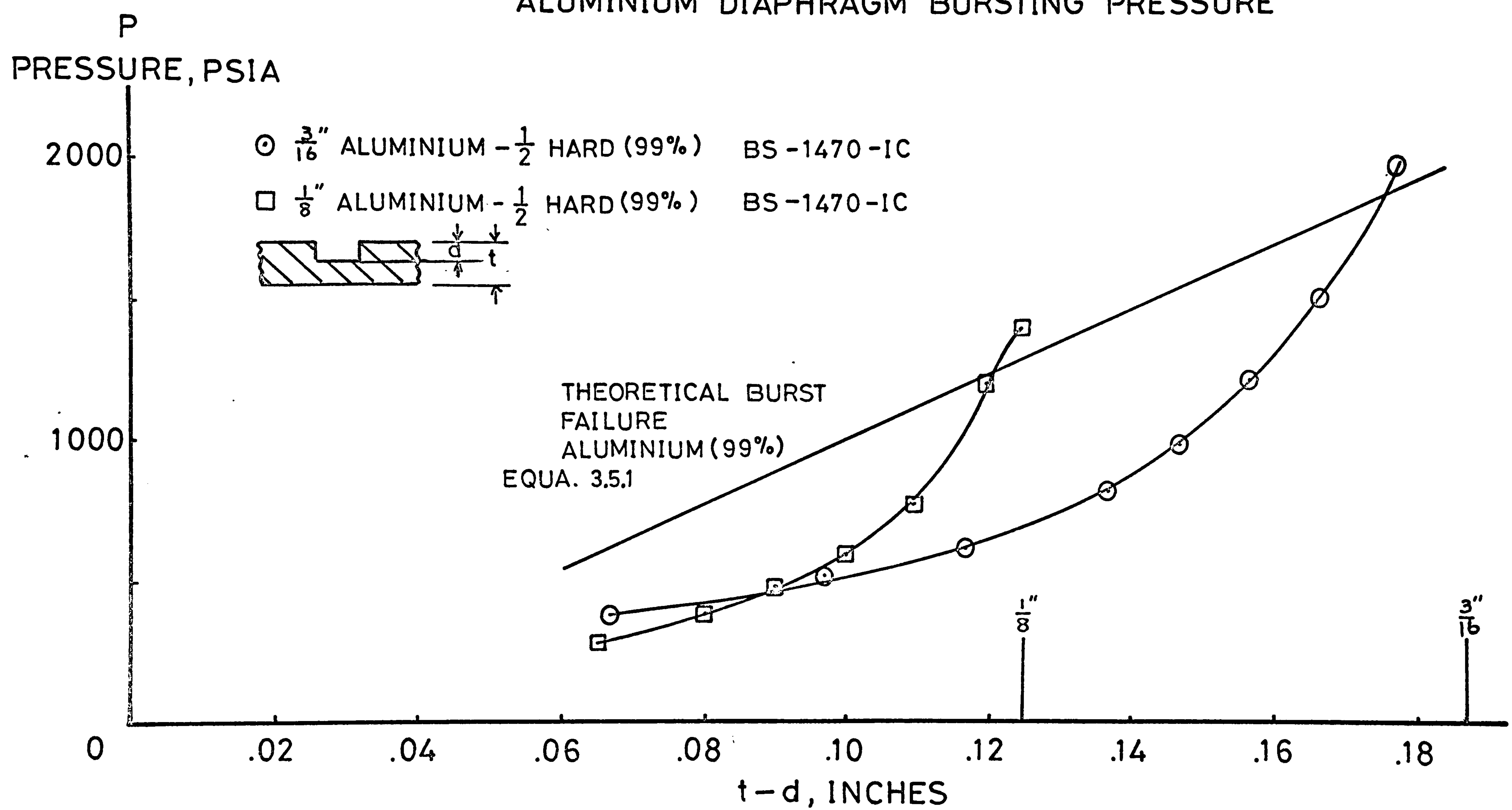

FIG.2.10

rapidly, however, as the groove depth is increased and acts as a source of stress concentration.

Another aspect of diaphragm performance which became a matter of operational concern in the Gun Tunnel was the stiffness or resistance to bending of the hinge of the petals of a diaphragm which had burst. There were certain conditions in which the petals of a set of diaphragms, although opening completely and otherwise performing normally, subsequently folded back closed (or facing upstream) due to the strong counterflow produced by the rearward travelling shock wave off the decelerating piston. This event, although occurring late in the time scale of the run and thus having no effect on the running conditions, introduced physical problems of diaphragm extraction after the run. This problem was alleviated somewhat by using diaphragms with a total thickness greater than would normally be necessary for a given pressure operation and grooving them more deeply. The lower limit in pressure at which diaphragms could be operated by deepening the grooves would be set by the point where the aerodynamic forces of the expanding driver gas would not be sufficient to completely open the petals. The resistance to bending is of course dependent on total material thickness and is not affected by groove depth. Table 2 describes the diaphragms used regularly for each range of driving pressures.

TABLE 2

(Gun Tunnel Operational Diaphragms)

(See Fig. 2.10 notation) (inches)

P_4, PSIA	MATERIAL	t	d	t - d
600	AL	.125	.040	.085
900	AL	.125	.030	.095
1200	AL	.125	.012	.113
1600	AL	.187	.040	.147
2000	AL	.187	.030	.157
2500	AL	.187	.020	.167
3000	STEEL	.125	.055	.070

2.5.2 Secondary Diaphragms

The main property required of the secondary diaphragm was to provide a seal at the nozzle entrance between the vacuum of the working section and the initial pressure P_1 in the gun barrel. This seal ideally must burst cleanly when the incident shock arrives at the end wall. Obstruction of the nozzle entry and the release of loose particles by the secondary diaphragm should also be kept to a minimum. Adhesive backed PVC and Mylar (Melinex) tape were tested in the Gun Tunnel. Adhesive backing had the advantage of simplifying the diaphragm mounting and sealing procedure. Of the two types of tape tested, the Mylar (3M Co. Ltd., Scotch Brand 56) tape proved the most satiafactory on all aspects of performance. A single thickness of .002 inches was capable of holding in excess of 50 psia. Multiple thicknesses could be used to restrain higher barrel pressures. Diaphragm opening was complete with the excess material adhering to the inlet of the throat after the run. At total temperatures in excess of 1000°K, some charring and vapourization of the material took place. Evidence of model damage due to high speed particles released by the diaphragm burst was slight. Ref. 35 contains a description of similar experience in another gun tunnel.

2.6 Piston Development

The mechanical requirements which constrain gun tunnel piston design are mutually opposing with the results that the final design is often an empirically determined compromise. To withstand the high accelerations of the starting process and the high peak pressures and deceleration associated with the piston motion at the downstream end of the barrel, the piston must be physically robust. It can be seen, however, from the analysis of Section 4.3 that piston mass in general must be as light as possible. The material must also be capable of being machined with some precision and capable of holding these dimensions over a long period. The closeness of the fit is also a compromise. A loose fit may allow excessive cold driver gas to leak past the piston during the run and reduce the temperature of the driven gas ahead of the piston. A very tight fit can cause overheating of the piston surface in contact with the wall from frictional heating. The frictional forces can also reduce the final speed of the piston with a corresponding reduction in reservoir conditions.

One material which meets these requirements for a wide range of operating conditions is nylon. Extensive tests have been carried out in the Gun Tunnel on pistons fabricated from a hard machining grade Type 66 nylon obtained from the G.H. Bloore Co. Ltd. Dimensional stability tests on two nearly identical pistons (one pure Type 66 nylon and the other Type 66 with a graphite and molybdenum disulfide impregnate) maintained in a controlled atmosphere room for two weeks showed a superior performance for the impregnated nylon. Changes in piston size of only $(10^{-4})\%$ were measured during this time period for this nylon. The impregnated nylon was also claimed to have a superior surface wear resistance by the manufacturers. For the preceding reasons the impregnated nylon was used almost exclusively for the pistons tested. Fig. 2.11 shows the general design of the piston with dimensions for three different sizes (and strengths). Piston A can be used up to driver pressures of 200 atmospheres

GUN TUNNEL PISTON

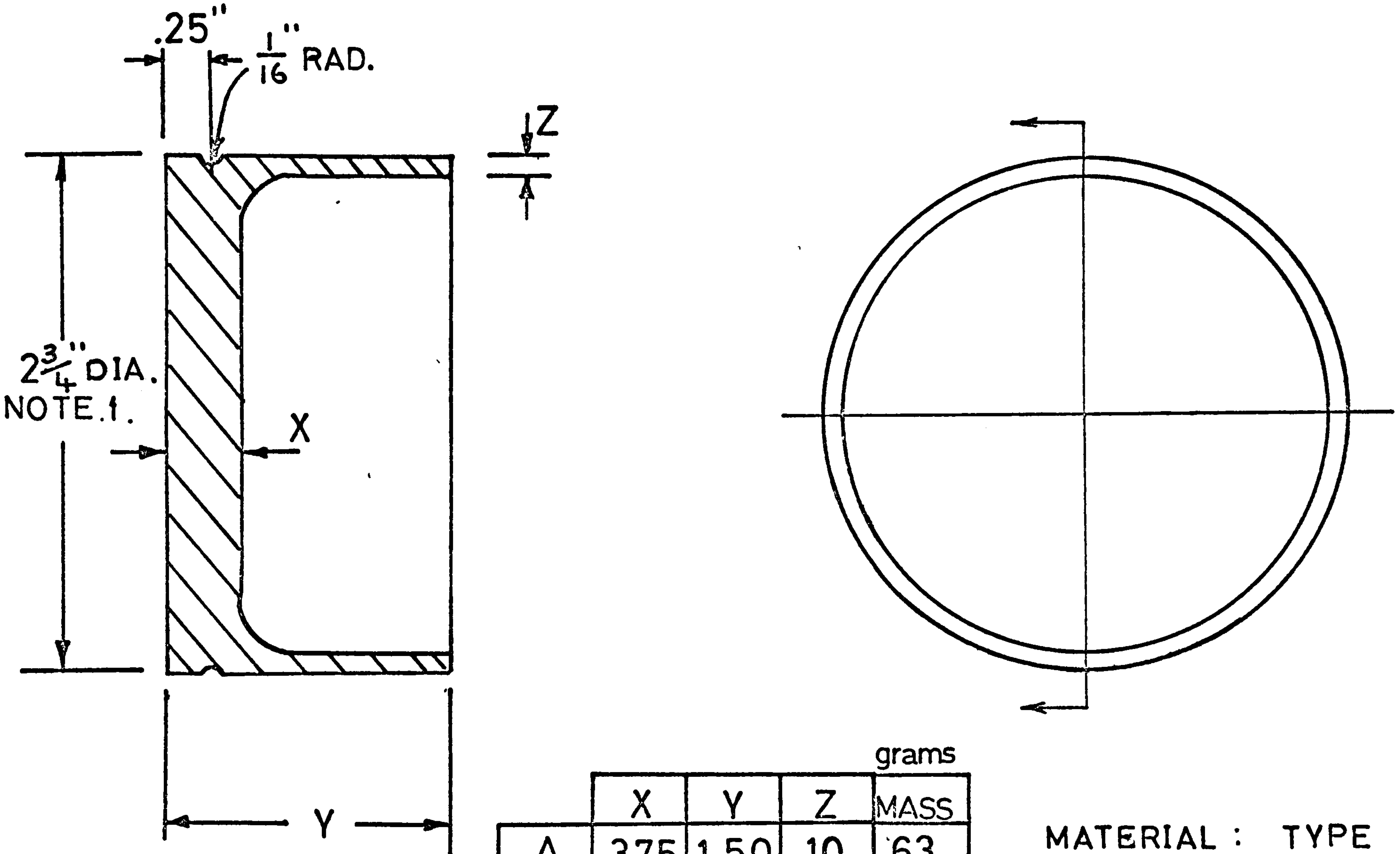

NOTE .1. FINAL CUT TO PRECISION
FIT IN GUN BARREL

	X	Y	Z	MASS (grams)
A	.375	1.50	.10	63
B	.250	1.25	.08	43
C	.187	.75	.08	29

ALL DIMENSIONS INCHES

MATERIAL : TYPE 66 NYLON (WITH GRAPHITE AND MOLYBDENUM DI-SULFIDE IMPREGNATE)

FIG.2.11

and diaphragm pressure ratios of 50. There is some exchange in performance limits possible such as lowering the driver pressure and increasing the pressure ratio. Pressure ratios up to 150 have been tried without serious degradations of the piston from the higher temperatures. Piston C has been tested up to total pressures of 100 atmospheres and diaphragm pressure ratios of 50. The selection of a piston for operation below the extremes of capabilities tested was a matter of deciding how much pressure overshoot and reservoir pressure fluctuation was acceptable for a particular test and how much risk of piston failure one was willing to tolerate. For modest pressure performance tests piston life of 50-100 runs was not unusual. A photograph of two impregnated nylon pistons (B) is shown in Fig. 2.12.

High diaphragm pressure ratios in excess of 200 usually involve a transition to piston materials such as aluminium alloys (see Refs. 6 and 10). Lemcke's analysis (Ref. 12) has shown that the pertinent parameter in piston design was the ratio of the material density to the square root of the tensile strength $\rho/(\sigma)^{\frac{1}{2}}$. This must be minimized and it is found that a nylon type plastic gives the best value. Lemcke has used 'Makrolon' which, while similar to nylon, has superior elastic and temperature resistance properties. Through careful design, Lemcke has constructed pistons of this material which have operated up to pressure ratios of 1400 and driver pressures of 300 atmospheres.

FIG. 2.12

NYLON PISTON (43 GRAM)

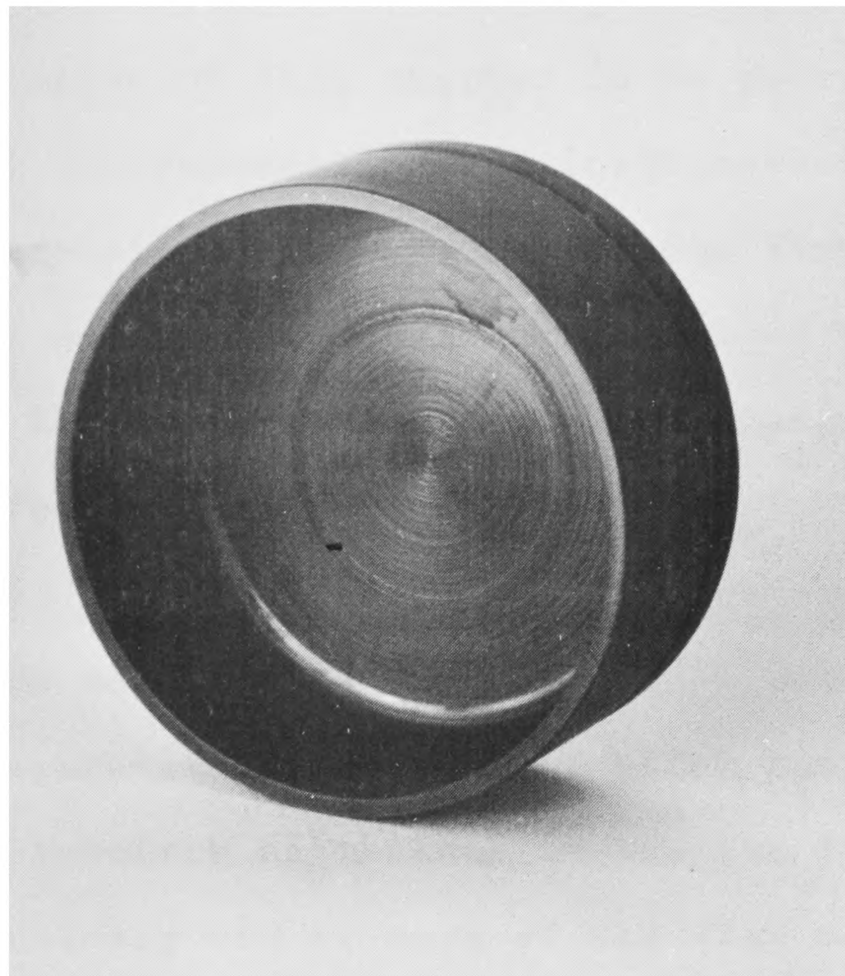

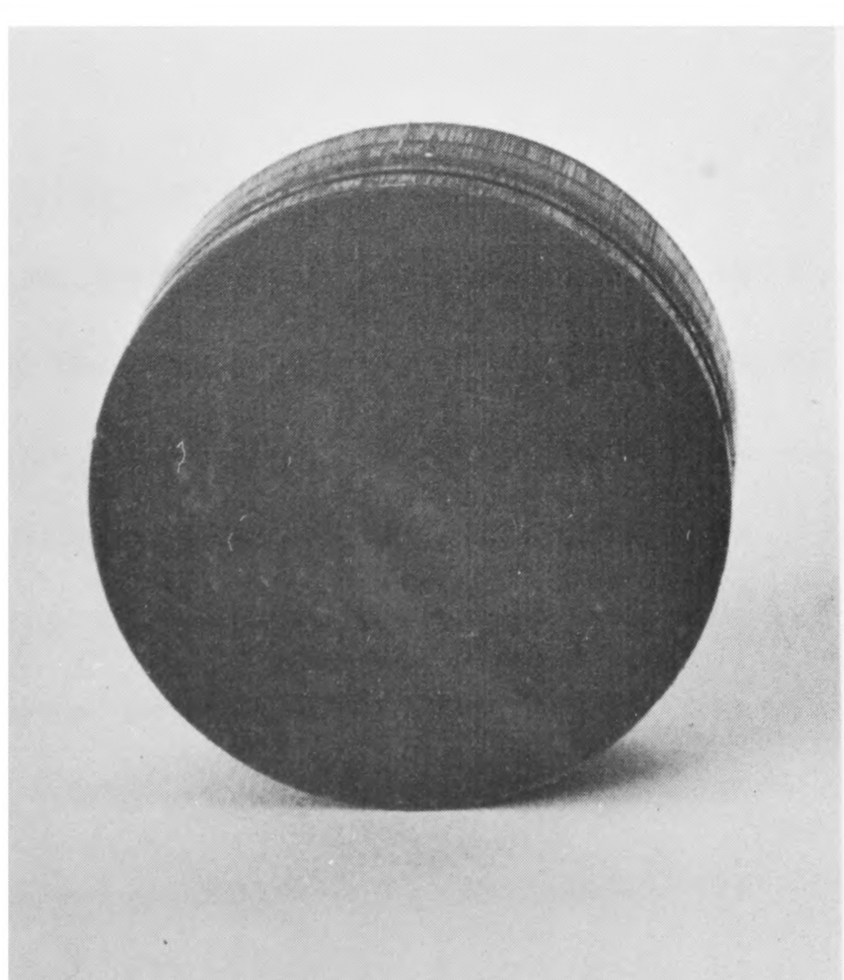

CHAPTER THREE

GUN TUNNEL INSTRUMENTATION

The purpose of this chapter is to describe in some detail the general instrumentation and instrumentation techniques which were developed for use on the Gun Tunnel calibration experiments and on the research program of Part II. In some cases this involved the adaptation of standard commercial equipment for operation in the Gun Tunnel time scale and environment. In other cases special instrumentation has been designed and constructed for Gun Tunnel use. In all cases the instrumentation is capable of being applied to a wide variety of research situations in the Gun Tunnel. The ability to make routinely one or more of the flow measurements described in the following sub-sections would contribute to the successful completion of nearly any general research program undertaken in the Gun Tunnel. More specialized instrumentation is described in other sections in connection with a particular measurement.

3.1 Electronic Instrumentation

The measurement of events in any short duration shock driven facility usually involves the use of some type of transducer capable of producing an electrical signal which can be related to the parameter being monitored. It is then necessary to bring this signal in an appropriate form to recording devices which have been synchronized with the event. A permanent record can then be made of the transient phenomenon for analysis at some later time. This section describes the recording equipment and associated electronics which have been in use on the Gun Tunnel. Fig. 3.1 is a schematic diagram of a typical Gun Tunnel

FIG.3.1

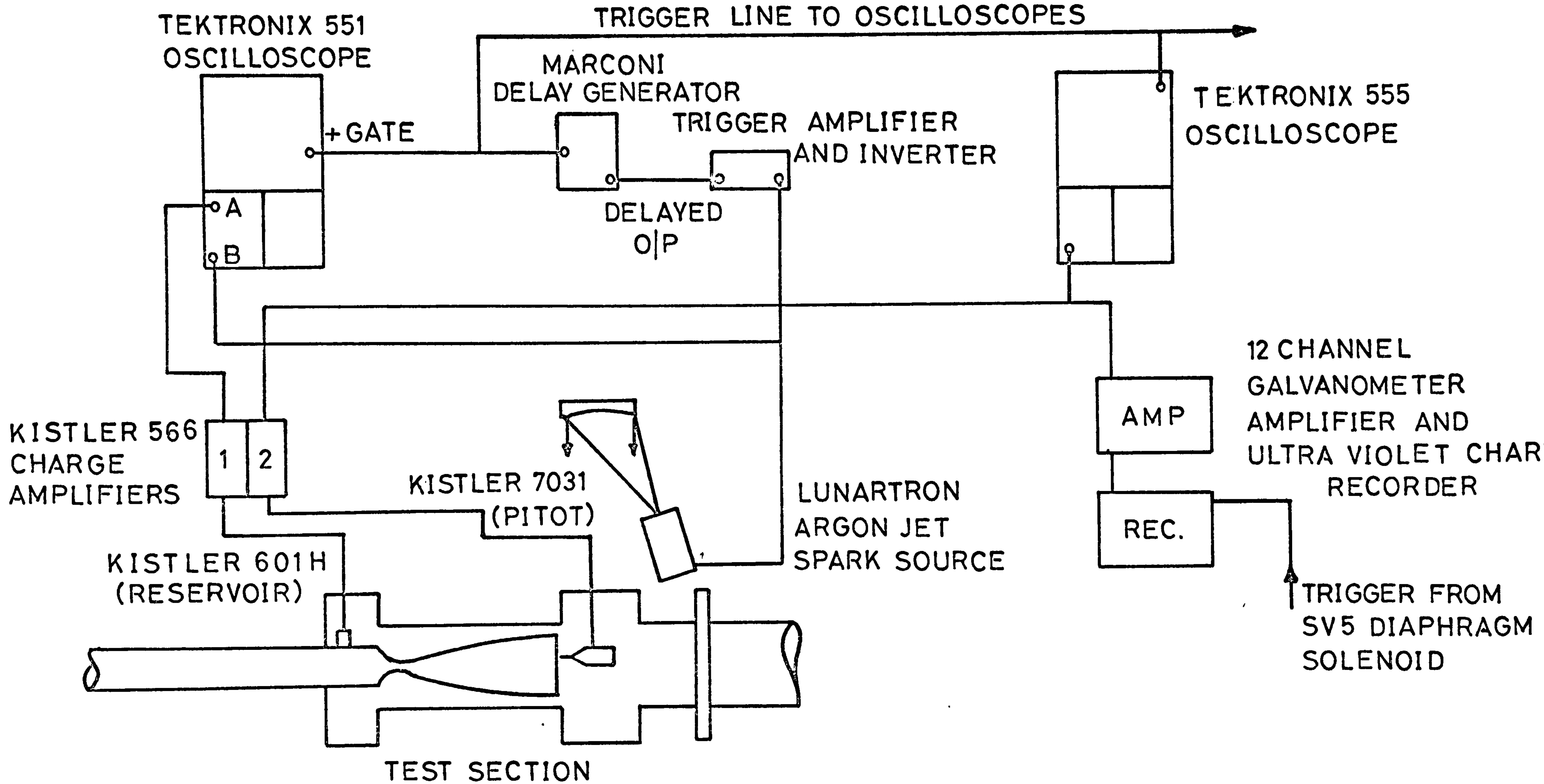

GUN TUNNEL INSTRUMENTATION

instrumentation arrangement including the connections for event synchronization. A more complete description of the electronic equipment developed for this research program, including circuit schematics and frequency response tests, can be found in Ref. 25.

3.1.1 Cathode Ray Oscilloscopes

The oscilloscope is the most versatile piece of equipment available for data acquisition on the Gun Tunnel. It is easily synchronized with the flow as shown in Fig. 3.1 where the output from a pressure transducer in the gun barrel internally triggers an oscilloscope. The gated output of this oscilloscope can then be used to trigger other oscilloscopes either with or without some delay placed in the line. With interchangeable plug-in units, a wide range of signals can be directly applied to the oscilloscope inputs. There were available for the Gun Tunnel experiments one Type 555 and three Type 551 Tektronix dual beam oscilloscopes along with one Tektronix Type 535 single beam unit. Each beam could be fitted with dual trace plug-ins bringing the number of data channels to twenty. The CRT traces were recorded on Polaroid Land cameras mounted on Teleford Type A adaptors. Each oscilloscope channel was frequently calibrated using a square wave generator during the course of the program.

3.1.2 UV Galvanometer Chart Recorder

A S.E. Laboratories Type SE2100 ultra violet galvanometer chart recorder was sometimes used to record Gun Tunnel data. This unit could accommodate up to 25 galvanometers although for the present tests it was fitted with 12 channels. The galvanometers had a frequency response of 0-3 KHz. The deflection sensitivity was only 300 mV/cm and the input impedance 40 ohms.

Therefore,low output impedance preamplifiers were generally required to drive the galvanometers. The maximum recording speed of the UV sensitive chart was 10 feet per second. Because of the finite time required to establish a steady rate of paper feed, the chart was usually started by a signal from the diaphragm solenoid (SV5) to allow a few tenths of a second to come to speed (see Fig. 3.1).

3.1.3 Galvanometer Amplifiers

The need to provide a variable gain, low output impedance source to drive the galvanometers was discussed in the last sub-section. A circuit was designed and constructed especially for operation with the UV galvanometers. The circuit was designed to provide a continuously variable voltage gain of 100 to 1000 with a frequency response of d.c. to greater than 10 KHz. Although the amplifier was designed for operation with the galvanometer unit, it could equally well be used as a high gain source for other data recording devices. A total of twelve amplifier channels were constructed by the Electronics Workshop of the Department of Engineering Science and mounted in a single self-contained unit.

3.1.4 D.C. Amplifiers

During the development of the analogue heat transfer circuits discussed below in Section 3.2 it was decided that there was a need for high gain d.c. amplifiers with a range of pre-set calibrated gain settings. Such a circuit was designed and constructed in the Electronics Workshop. This had a range of switchable gain settings ranging from unity to 1000. The feedback was adjusted to give a nearly constant bandwidth operation over all gain settings thus minimizing gain losses due to filtering effects on high frequency components of the signal. The 10KΩ output impedance was sufficient for operation with the oscilloscopes also.

3.1.5 Filters

It was often desirable to be able to suppress unwanted frequency components of a signal. Such filtering is usually directed toward removing high frequency noise or low frequency and d.c. components. Simple RC low pass and high pass filters were constructed and are described in Ref. 25.

3.2 Heat Transfer Measurements

A fundamental measurement to be able to make in hypersonic flow research is the instantaneous surface heat transfer rate. A considerable body of experience has been accumulated in recent years on the techniques for heat transfer measurements in short duration impulse driven hypersonic facilities. These techniques are well documented in the literature (see Refs. 36-40). This section describes some of the particular techniques which have been used on the Gun Tunnel experiments and would be applicable in general to a wide range of heat transfer programs.

3.2.1 Gauge Construction

The thin film resistance thermometers used in the Gun Tunnel experiments have been formed using Hanovia Bright Platinum 05-X paint. This paint consists of a suspension of platinum and gold compounds in volatile oils and solvents which can be applied with a fine brush or inking pen to a clean substrate. The substrate material was usually Pyrex glass or fused quartz. The paint was air dried before being placed in a well ventilated oven and baked near the softening temperature of the substrate for 30 minutes (650°C for Pyrex and quartz). This process could be repeated several times to build up the film thickness and lower the gauge resistance.

Electrical leads could then be fixed to the thin film gauge either by direct soldering (if great care was taken) or by applying a more robust conducting paint to the ends of the film and then soldering leads to this. Johnson, Matthey and Co. Ltd. Silver Preparation FSP410 and FSP409 has been used successfully for this purpose. This preparation was applied in two stages followed by baking. It was remarkably robust and leads could be easily soldered to it. The complete gauge was then usually securely mounted with casting epoxy resin in the test model or in an adapter which fits into the model. An adapter designed for a hemisphere stagnation point experiment with a thin film gauge in place is shown in Fig. 3.2a.

3.2.2 Gauge Calibration

The theory of thin film resistance thermometer response to an externally applied heat transfer rate is outlined in some detail in Refs. 36-38. Only the final results of the analysis are reported here along with the basic assumptions implied in the results. The analysis is basically one of relating the surface temperature history of the substrate to the instantaneous value of heat transfer rate to the surface. The surface temperature history was monitored by relating the resistance of the platinum film to its temperature

$$R = R_o(1 + \alpha\ [T - T_o]) \tag{3.2.1}$$

where α is the film's thermal coefficient of resistivity and R_o is the gauge resistance at T_o.

The primary assumption was that the presence of the film does not affect the surface temperature response of the substrate. Since the platinum films applied as described above have a thickness of the order of 0.1 microns and thus a

FIG. 3.2

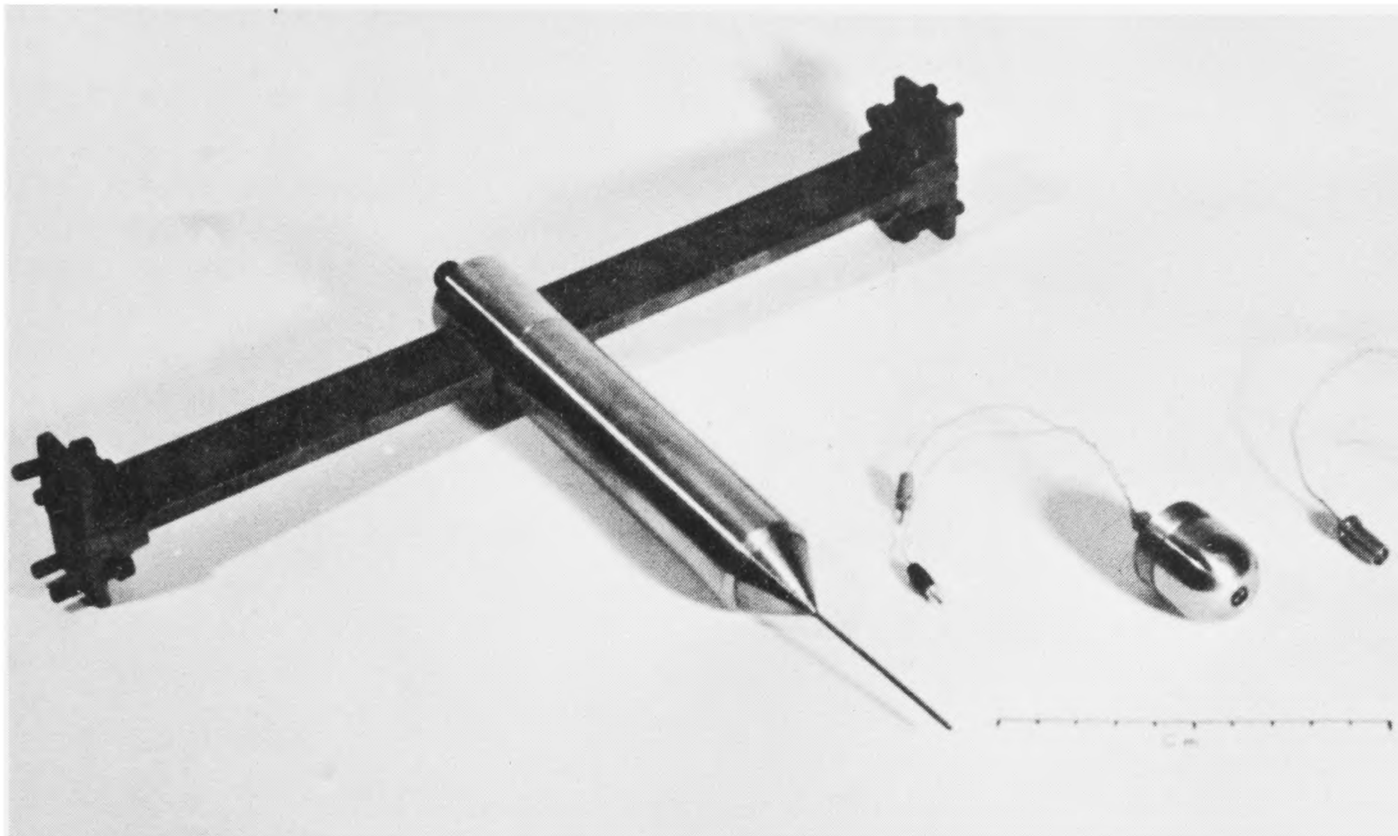

a) PITOT PROBE WITH HEMISPHERE HEAT GAUGE ADAPTER

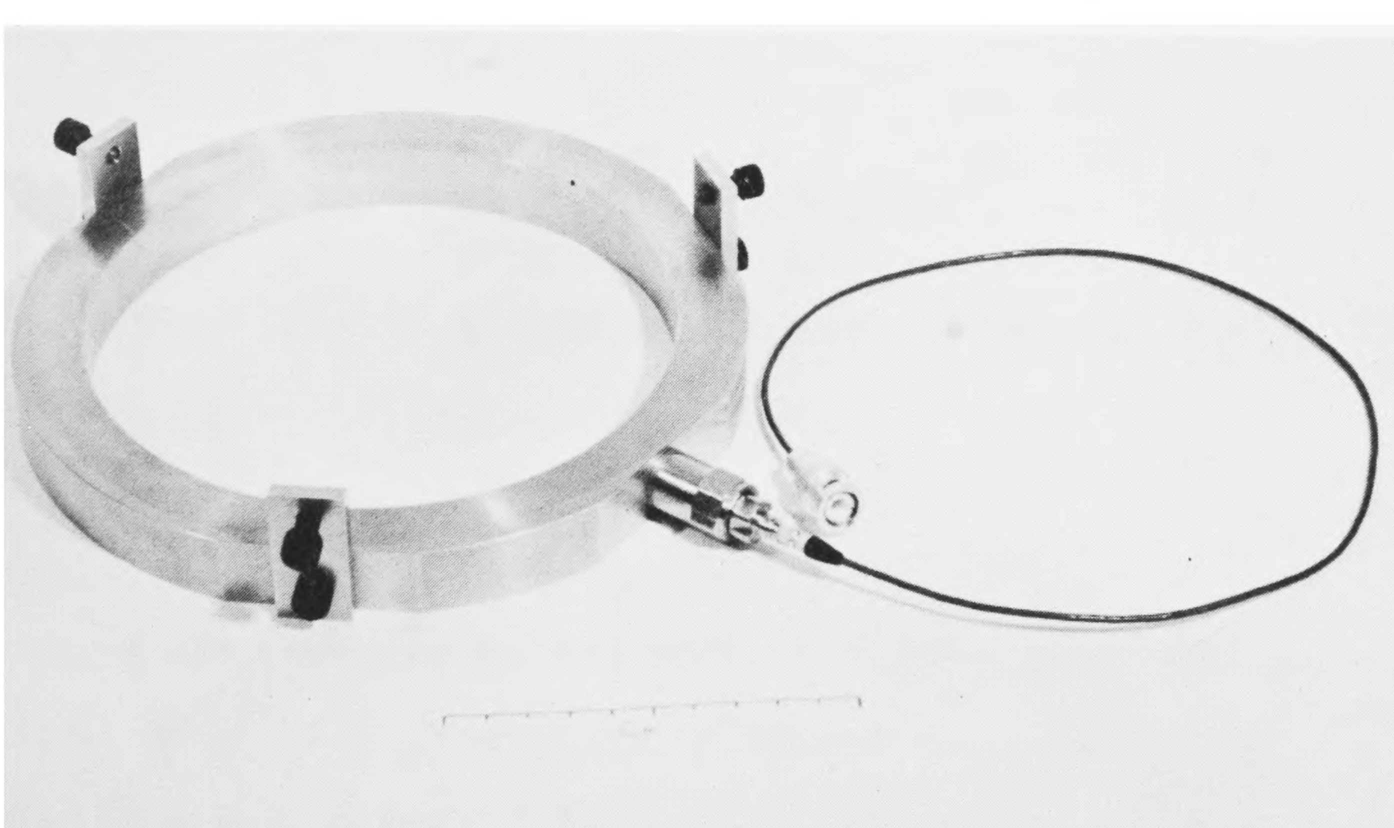

b) STATIC PRESSURE RING

negligible heat capacity, this assumption is usually satisfied for all but very short times (< 10 μsec). The other main assumption was that the dimensions of the substrate were such that a one-dimensional transient heat diffusion analysis was valid throughout the time scale of the experiment. The situation is then one of solving the one-dimensional heat diffusion equation

$$\frac{\partial T}{\partial t} \doteq \frac{k}{\rho c} \frac{\partial^2 T}{\partial x^2} \tag{3.2.2}$$

with the Fourier rate equation

$$\dot{q} = k \frac{\partial T}{\partial x} \tag{3.2.3}$$

as one of the boundary conditions at the surface (X = 0). The properties ρ, c, and k refer to the substrate density, specific heat and conductivity respectively. The solution from Ref. 38 for the surface temperature history T(t) is given as

$$T(t) = \frac{1}{\sqrt{\pi \rho c k}} \int_0^t \frac{\dot{q}(\tau)}{\sqrt{t - \tau}} \, d\tau . \tag{3.2.4}$$

For a step function $\dot{q}$ applied to the surface at t = 0, (3.2.4) can be integrated to yield,

$$T(t) = \frac{2}{\sqrt{\pi \rho c k}} \dot{q} \sqrt{t} + T_o . \tag{3.2.5}$$

Assuming that the series resistance in the gauge electrical circuit (Fig. 3.3) was large compared with the gauge resistance and using (3.2.1), (3.2.5) can be written in terms of gauge voltage history V(t),

$$\dot{q}_o = \frac{\sqrt{\pi \rho c k}}{2 V_o \alpha} \frac{[V(t) - V_o]}{\sqrt{t}} \tag{3.2.6}$$

where V_o is the film voltage drop before the application of $\dot{q}$.

FIG.3.3.

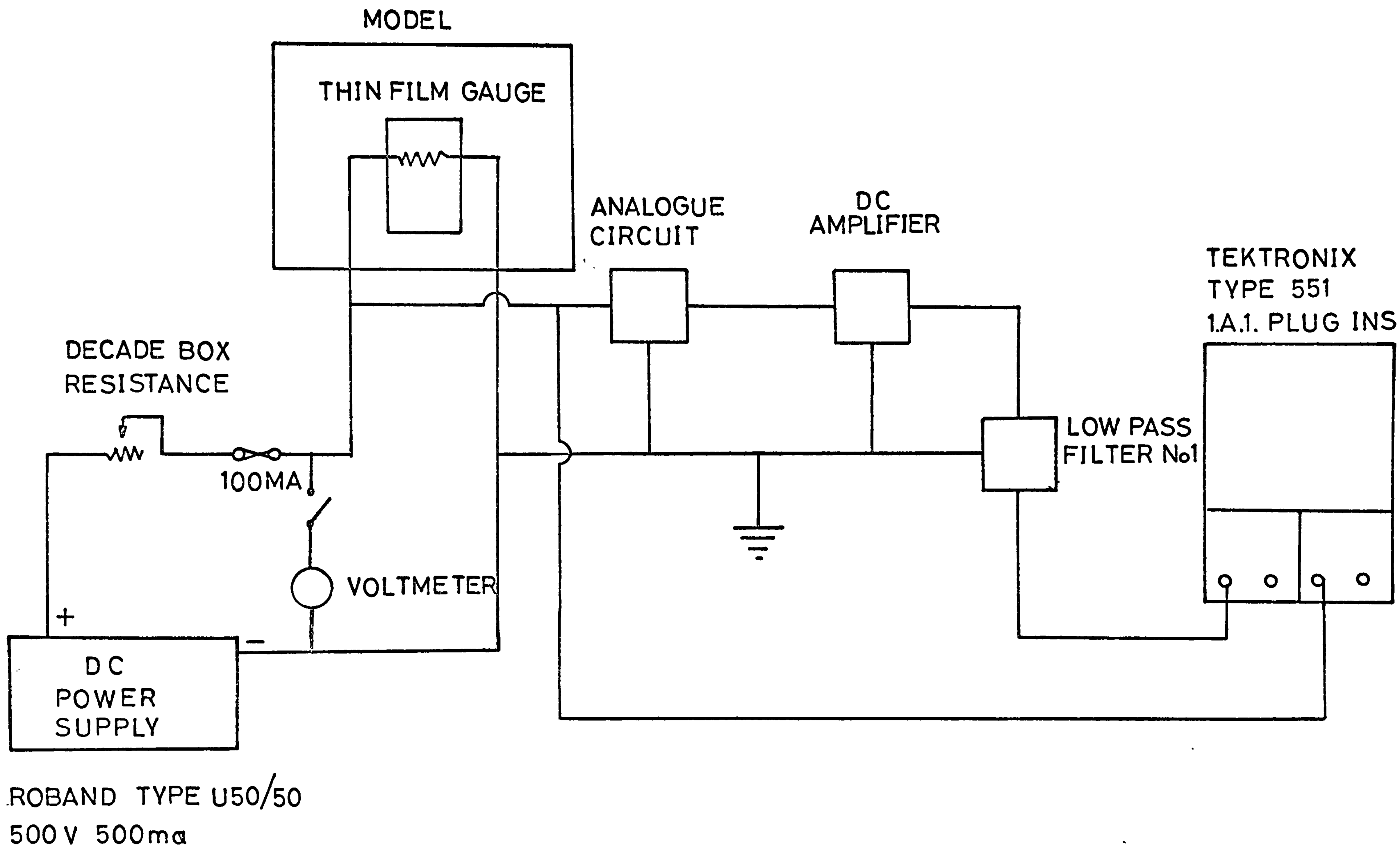

HEAT TRANSFER ANALOGUE CIRCUIT ARRANGEMENT
(ONE CHANNEL)

The more general situation in Gun Tunnel experiments has $\dot{q} = \dot{q}(t)$. In this case, (3.2.4) becomes,

$$\dot{q}(t) = \frac{\sqrt{\rho c k}}{2\alpha\sqrt{\pi}V_o}\left[\frac{2V(t)}{\sqrt{t}} + \int_o^t \frac{V(t) - V(\tau)}{(t-\tau)^{3/2}}\right] d\tau \qquad (3.2.7)$$

using the same assumptions relating gauge voltage and temperature as used to derive (3.2.6).

Before a thin film gauge can be used to obtain heat transfer rates, the constants of the gauge (α, ρ, c, k) appearing in (3.2.7) must be evaluated for each gauge. One method for obtaining a lumped value for these constants relies on the simplified constant $\dot{q}$ expression (3.2.6). A constant $\dot{q}$ pulse is applied to the film by passing a short current pulse through the gauge using the balanced bridge circuit shown in Fig. 3.4. The effective heat transfer rate to the film is then given by

$$\dot{q} = \frac{I_o^2 R}{A} \qquad (3.2.8)$$

where A is the gauge active surface area. The values of the circuit components were selected to give a nearly constant current during the pulse test. The out-of-balance bridge voltage was monitored on an oscilloscope as a record of the film response to the heating (Fig. 3.5a). This voltage history is then replotted against $\sqrt{t}$ (Fig. 3.5b). The slope of this graph along with (3.2.6) and (3.2.8) then gives the combined constants directly.

$$\frac{2\alpha}{\sqrt{\pi\rho c k}} = \frac{A(R + R_2)^4}{V_1^{\,3} R_2 R^2} \; \frac{\Delta V}{\sqrt{t}} \qquad (3.2.9)$$

This method has the disadvantage of requiring an accurate measurement of the film surface area.

Some research groups which have accumulated much experience

FIG. 3.4

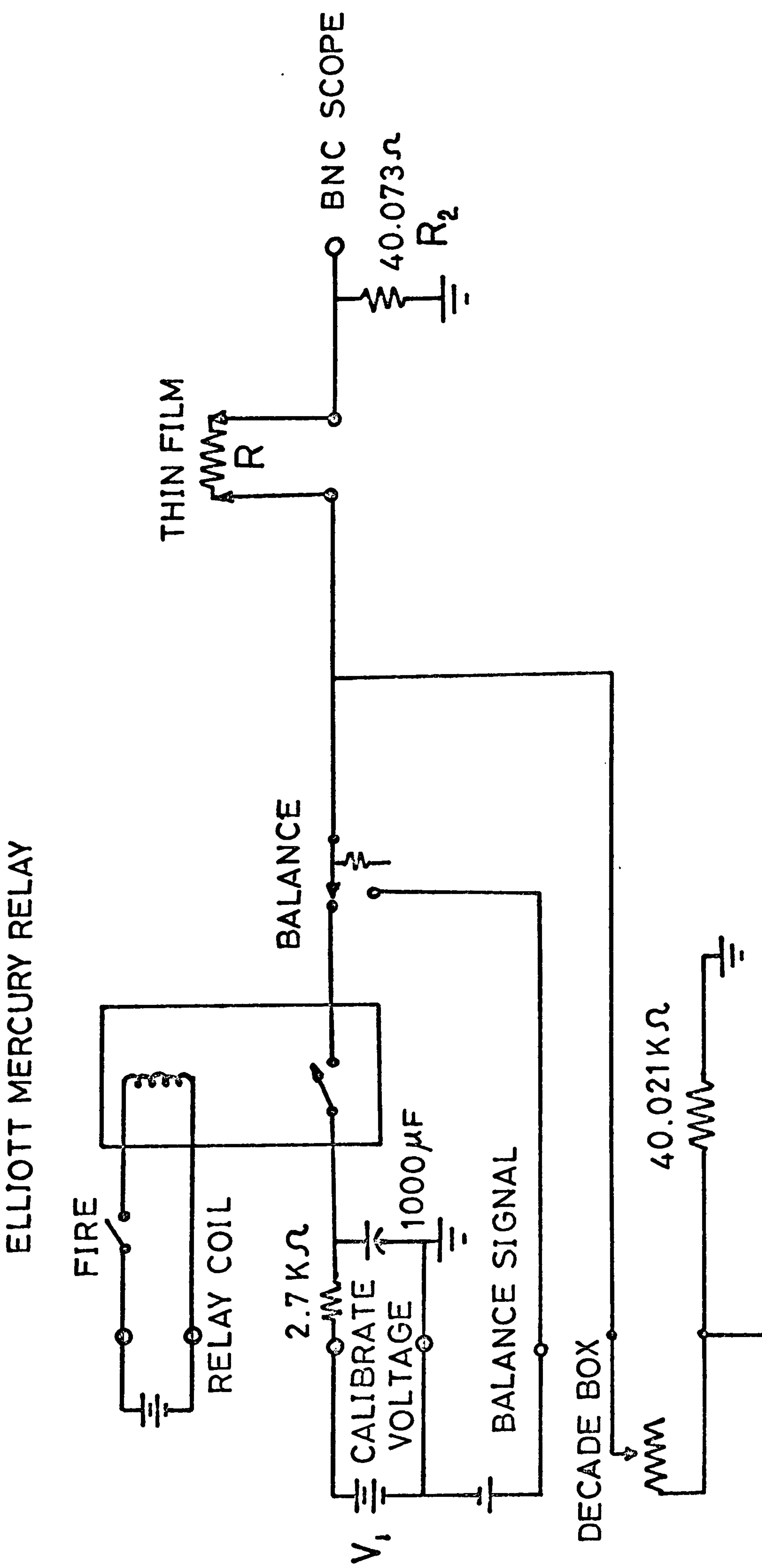

THIN FILM GAUGE PULSE CALIBRATION CIRCUIT

FIG. 3.5

THIN FILM GAUGE CALIBRATION
GAUGE SPI (HANOVIA 05-X ON PYREX)

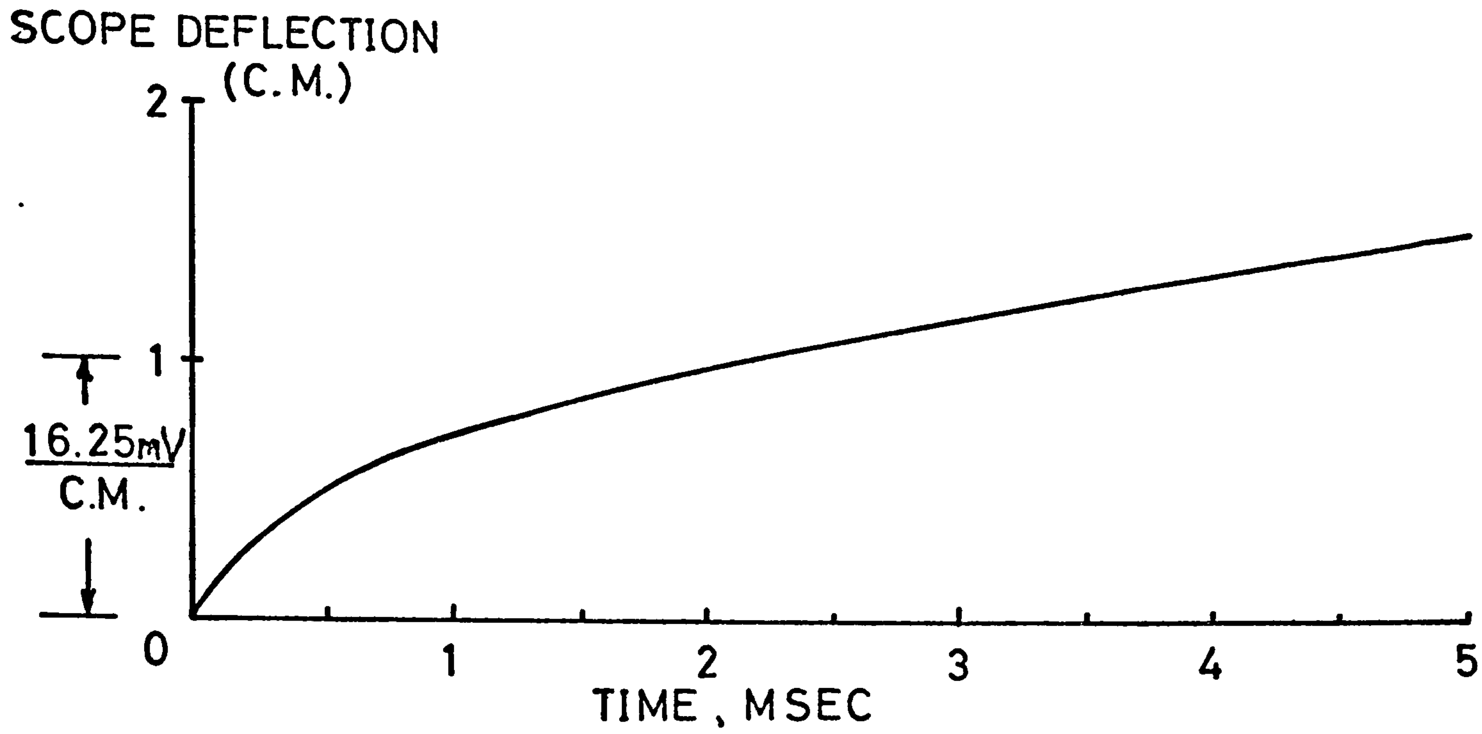

a) FILM RESPONSE TO CURRENT PULSE

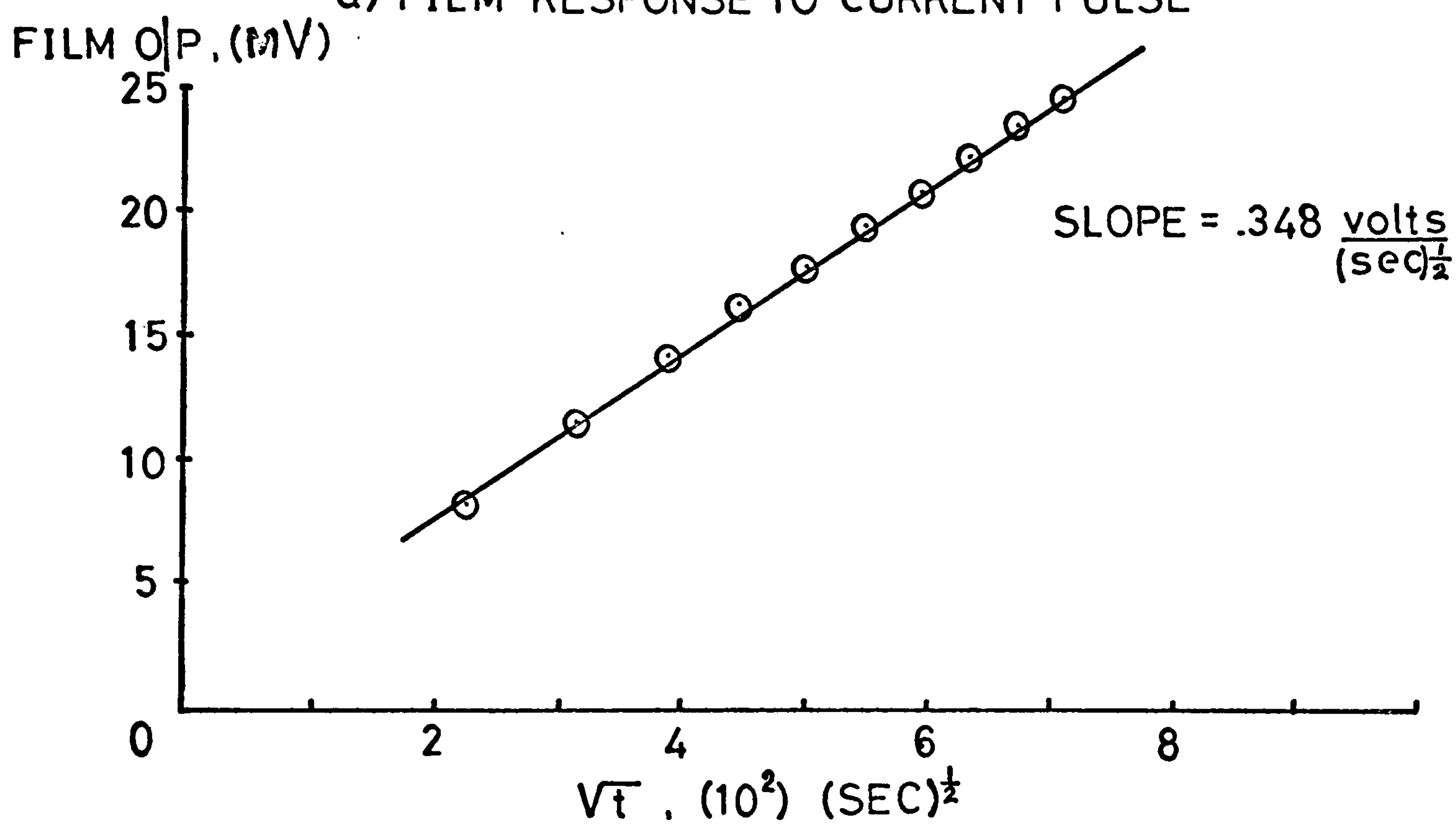

b) FILM O|P VS. √t

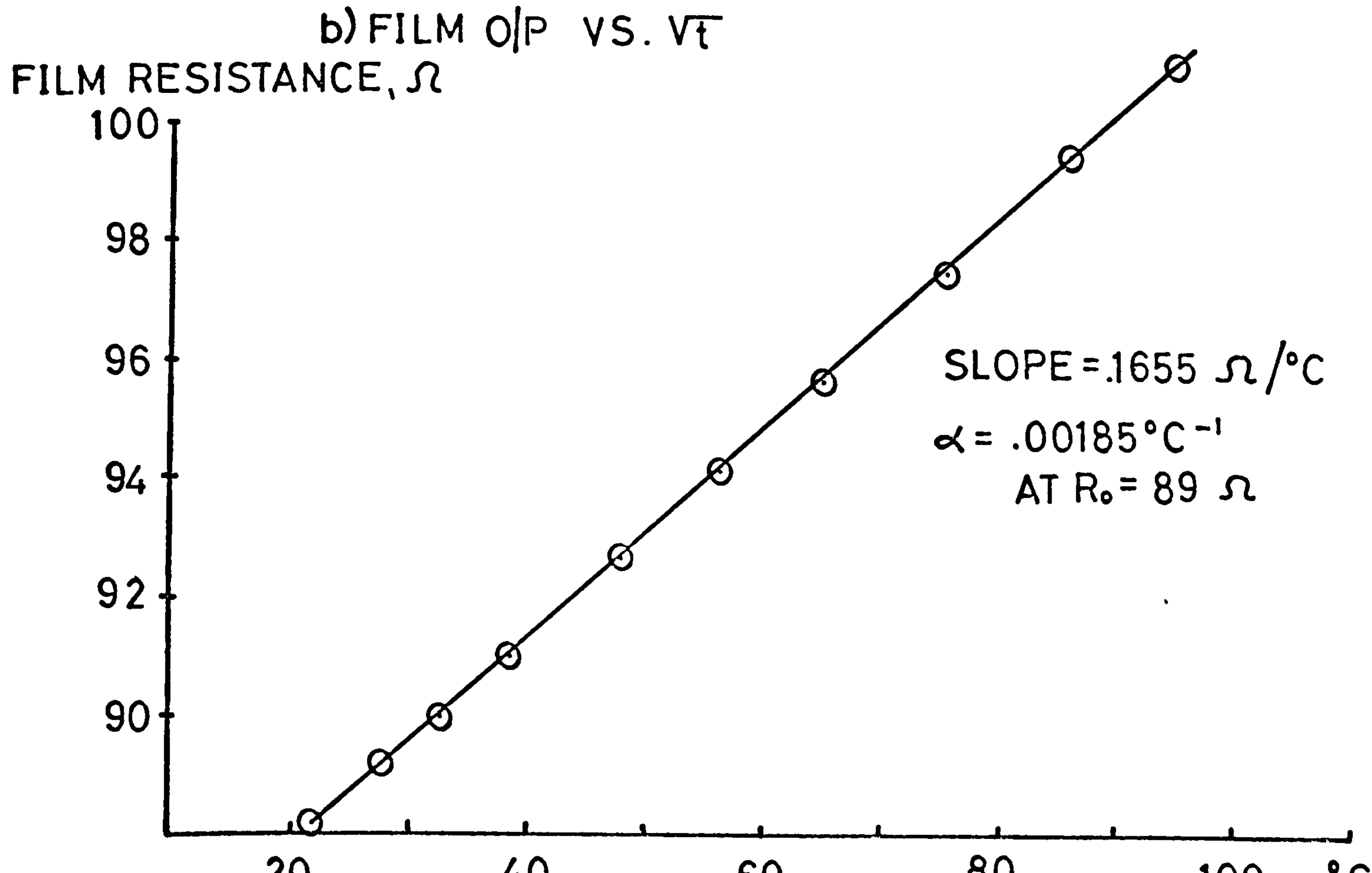

C) ALPHA CALIBRATION

in the calibration and use of thin film heat transfer gauges have noted that most of the variation in the calibration factor

$$\alpha/\sqrt{\rho c k}$$

between different gauges arises from variations in α alone (see Refs. 41-43). A precise measurement of α in a distilled water or oil bath experiment would then be sufficient to define the calibration factor by assuming bulk values for substrate ρ, c and k. It is usually preferable to verify the bulk properties of the substrate material by performing both the current pulse test and the α determination test at least once for a particular supply of material.

Fig. 3.5c shows a typical calibration of film resistance variation with temperature. This test was performed in a heated distilled water bath and shows good linearity. Some tests were performed in a silicon oil bath and indicated that this linearity exists up to 200°C. There is a slight variation of $(\rho c k)^{\frac{1}{2}}$ with temperature (Ref. 44), the value being about 5% higher at 50°C than at room temperature. Under most operating conditions of the Gun Tunnel tests and gauge calibrations, the film temperatures were well below this temperature. Ref. 37 shows that with a surface heat transfer of 20 watts/cm^2, the surface temperature rise on Pyrex is 32°C in 40 msec. The pulse calibration situation in Fig. 3.5 with V_1 = 6.2 volts, produced a film temperature increase of 7.4°C in 5 msec.

The results of the calibration tests on gauge SP1 are listed below in Table 3 along with some values of $(\rho c k)^{\frac{1}{2}}$ for Pyrex (borosilicate) found by other groups. This gauge consisted of 2 coats of Hanovia 05-X platinum film on the end of a $\frac{1}{8}$ inch Pyrex rod. The gauge surface area was 9.96×10^{-3} cm^2.

TABLE 3

Thin Film Gauge Calibration Factors
Pyrex

GAUGE OR REFERENCE	$\alpha/\sqrt{\rho c k}$ $\left(\frac{cm^2}{watt(sec)^{\frac{1}{2}}}\right)$	α $(^{o}C)^{-1}$	$\sqrt{\rho c k}$ $\left(\frac{cal}{(sec)^{\frac{1}{2}}\ {}^{o}C(cm)^2}\right)$
SP1	.01133	.00185	.0389
Ref. 36			.0366
Ref. 37			.0330
Ref. 38			.0348
Ref. 40			.0344
Ref. 41			.0363

A modification of the current pulse film calibration technique has been developed by Skinner (Ref. 45) which involves pulsing the film both in still air (or vacuum) and in a fluid such as water. This method has the advantage of eliminating the need for knowing the gauge surface area provided that the properties ($\rho c k$) of the fluid are known accurately. Another method of dynamically calibrating thin film gauges has been described by Softley (Ref. 36). This involves calibrating the films in a shock tube where the wall heat transfer rate is accurately known.

3.2.3 Heat Transfer Data Reduction Program

The numerical integration of equation (3.2.7) would be very tedious if performed manually. The data reduction for all the Gun Tunnel heat transfer experiments has involved the use of a computer program to perform the integration of (3.2.7). This program was developed at the National Physical Laboratory and used previously on the Oxford University KDF-9 computer by Jones (Ref. 47). The program is listed in Ref. 25. The program input requires the oscilloscope (or other data recorder) deflection and sensitivity at any desired time interval frequency along with the film and substrate calibration constants. The output then gives the instantaneous heat transfer rate at each time interval. A sample data input tape and data print-out sheet are included in Ref. 25.

3.2.4 Stagnation Point Heat Transfer

A hemisphere (r = 1.27 cm) model was constructed and fitted with a calibrated thin film gauge at the stagnation point (Fig. 3.2a). Measurements of stagnation point heat transfer were made to check out the heat transfer measurement techniques described in this section. The well established theory of hypersonic stagnation point heat transfer due to Fay and Riddell (Ref. 48) was used to compare the results. This theory gives the following expression for equuilibrium heat transfer rate to a hemisphere.

$$\dot{q} = .763(\rho\mu)_w^{.1}(\rho\mu)_s^{.4}\left[1 + (L^{.52} - 1)\frac{H_D}{H_S}\right]\left[\frac{H_s - H_w}{(Pr)^{.6}}\right]\left(\frac{du_e}{dx}\right)_s^{\frac{1}{2}} \tag{3.2.10}$$

Crabtree (Ref. 49) arrived at a simplified form of this expression which he found to be accurate to better than 4% for $H_w/H_s > 0.1$. This expression is given below (3.2.11) along with some of the assumptions implied,

$$\dot{q} = 1.12\left(\frac{P_s}{T^*}\right)^{\frac{1}{2}}\left(\frac{\mu_*}{r}\right)^{\frac{1}{2}}\left(\frac{T_s}{R}\right)^{\frac{1}{4}}(H_s - H_w) \tag{3.2.11}$$

where s refers to stagnation point conditions and * to conditions at a reference enthalpy $H_* = .5(H_s - H_w)$. The assumptions included a modified Newtonian flow approximation for the stagnation point velocity gradient,

$$\left(\frac{du_e}{dx}\right)_s = \frac{1}{r}\left(\frac{2P_s}{\rho_s}\right)^{\frac{1}{2}} \quad \text{for } M >> 1$$

as well as Prandtl No. (Pr) = .71 and zero dissociation (L = 1) for $T_t < 1500^{\circ}K$. The Sutherland viscosity relation was also implied. The symbols R and r in (3.2.11) refer to the gas constant and hemisphere radius respectively. It was also assumed that

$$(H_s - H_w) = C_p^* \,(T_s - T_w)$$

for the temperature range of interest.

The theoretical stagnation point heat transfer rates for a range of flow conditions appropriate to the Gun Tunnel are shown in Ref. 25. A computer analysis of the temperature response of the stagnation point film for nearly identical Gun Tunnel runs is shown in Fig. 3.6a as $\dot{q}$ vs time from the start of the run for the flow condition listed in the figure. A comparison of measured heat transfer rates at different total temperatures with the theory (3.2.11) is shown in Fig. 3.6b.

3.2.5 Analogue Circuit Calibration

The reduction of thin film temperature response to heat transfer values can be quite tedious if a large number of measurements are involved despite the use of a digital computer program to perform the integration of (3.2.7). Meyer (Refs. 50 and 51) has taken advantage of the direct analogy between the one-dimensional heat diffusion equation (3.2.2) and the equation for one-dimensional diffusion of current through a medium with distributed capacity C per unit volume and resistivity R,

FIG. 3.6

STAGNATION POINT HEATING

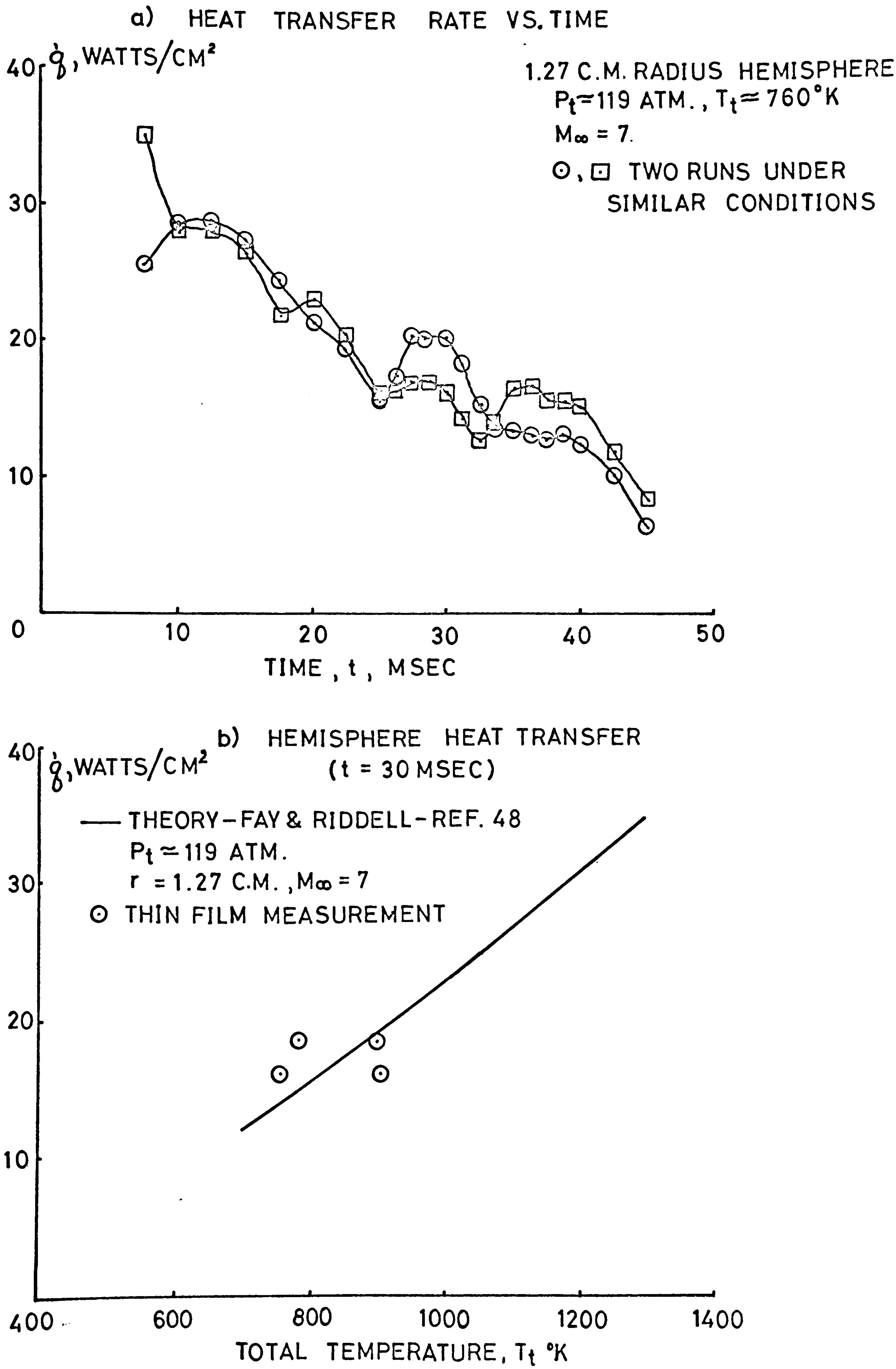

$$\frac{\partial V}{\partial t} = \frac{1}{RC}\frac{\partial^2 V}{\partial y^2} \qquad (3.3.12)$$

where V is the potential, to produce $\dot{q}$ directly. Meyer has suggested using a T-section electrical analogue stage

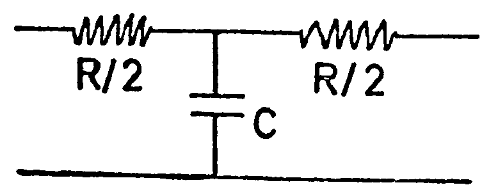

with a time constant RC fast enough for the type of experiment being considered. The number of stages used was then adjusted to make the network appear infinite to an input signal for the total duration of the experiment. Meyer suggested a criterion for the number of stages (n) required for an accuracy of 2% which was given as

$$n^2 = \frac{t}{RC\ (.2)} \qquad (3.2.13)$$

where t is the total time of the test.

HEAT TRANSFER ANALOGUE CIRCUIT
FIG. 3.7

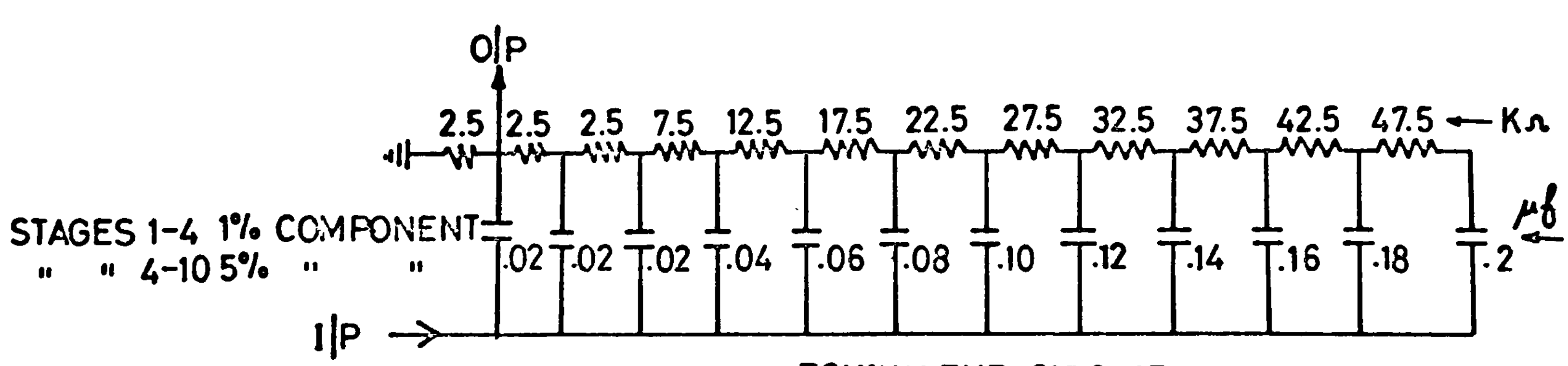

EQUIVALENT CIRCUIT

The electrical analogue circuit built for use on the Gun Tunnel experiments is shown in Fig. 3.7. Using a stage time constant of 100 μ seconds and a total running time of 50 msecs., the number of stages required from (3.2.13) would be 50. To reduce the actual number of stages used, Meyer (Ref. 51) suggested that the stage values of R and C be lumped together producing arithmetically increasing values for each successive stage. This maintains the short time constant of the input stage and the overall time constant of the network for long times. The input voltage signal from the rate of change of film temperature thus produces at the analogue output a signal proportional to the heat transfer at the front face of the model substrate. Twelve analogue channels were constructed for use in the research program.

A typical circuit arrangement for using the analogue network for the direct reading of heat transfer is shown in Fig. 3.3. High gain d.c. amplifiers are usually needed to record the analogue output due to the large signal loss through the network. An expression relating analogue output voltage (V_o) to the heat transfer is given as approximately

$$q = \frac{2\sqrt{\rho c k}}{\sqrt{RC}\;\alpha} \; \frac{V_o}{E_o}. \qquad (3.2.14)$$

where E_o is the steady state voltage across the thin film. Under typical operating conditions in the Gun Tunnel experiments, this gave a sensitivity of about 60 microvolts/watt/cm^2. In practice, the analogue transfer function $2/\sqrt{RC}$ value had to be calibrated, especially when some stages have been lumped together. This calibration was performed by measuring both the film response and the analogue output for an actual run in the Gun Tunnel working section with the circuit arrangements as shown in Fig. 3.3. These outputs are shown for a typical case in Fig. 3.8(a and b). The film output voltage (which is the analogue input signal) was analysed as in Section 3.2.3 to produce the heat transfer values (Fig. 3.8c). Comparing the analogue output with the computed $\dot{q}$ yielded calibrated value of $2/\sqrt{RC}$ in (3.2.14) assuming the previously calibrated values of the gauge constant $(\rho c k)^{\frac{1}{2}}/\alpha$. The films for this

FIG. 3.8

ANALOGUE CALIBRATION

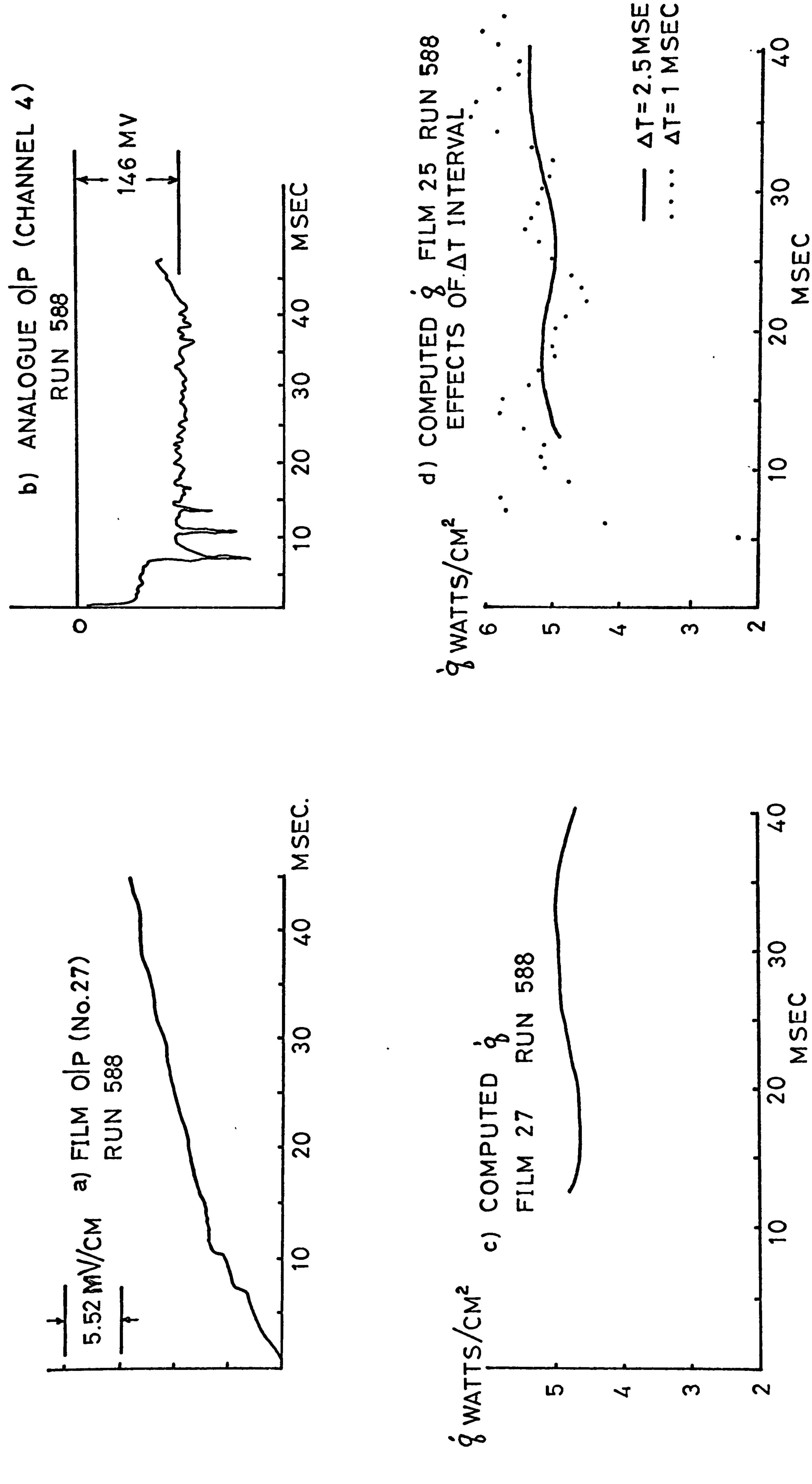

calibration test were constructed at the N.P.L. and mounted on the 10° cone designed for the experimental program discussed in Chapter 10. The value of $(\rho ck)^{\frac{1}{2}}$ for the quartz substrate has been established by the N.P.L. as .0398 cal/$^{\circ}$C(cm)^{2} (sec)$^{\frac{1}{2}}$ for the particular supplier they use. The term α was measured at Oxford for each film by a distilled water bath experiment. The actual output voltage of the analogue was determined from theoscilloscope trace accounting for the presence of the d.c. amplifier and low pass filter in the line. The precise value of amplifier gain was measured for each channel using a 2.5 KΩ terminated 250 Hz sine wave source and a rms voltmeter. The low frequency (25 Hz) line drop of the low pass filter was also determined for each filter channel. A summary of the calibrated values of $2/(RC)^{\frac{1}{2}}$ for each analogue channel is listed in Table 4.

TABLE 4

Analogue Calibration Factors

CHANNEL	$\frac{2}{(RC)^{\frac{1}{2}}}$	CHANNEL	$\frac{2}{(RC)^{\frac{1}{2}}}$
1	261	7	251
2	240	8	238
3	228	9	260
4	234	10	255
5	251	11	262
6	231	12	264

Fig. 3.8d shows the effects of the time interval selected for the readings of film voltage deflection for the computer input. Large low frequency variations in computed heat transfer rate is indicated by taking smaller time intervals. It thus should be pointed out that a realistic mean value of $\dot{q}$ should

be used when defining the analogue calibration factor.

3.3 Flow Visualization

The ability to obtain a photographic record of the flow environment in a wind tunnel is an important aspect of nearly all research programs. A qualitative appraisal of shock pattern and location, boundary layer state, and general flow steadiness contribute substantially to the understanding of experimental results. Quantitative analysis of boundary layer thickness and growth rate, flow separation location and length, shock stand-off distance, and flow field density changes is possible with detailed evaluation of flow photographs. The specific photographic apparatus which has been set up for Gun Tunnel experimental flow visualization is described in this section.

3.3.1 Schlieren Techniques

The detailed theory and design of schlieren systems for air flow analysis has been comprehensively described in the literature (see Refs. 52-55). The basic optical geometry and apparatus used for the simple double mirror, single pass schlieren system on the Gun Tunnel is shown in Fig. 3.9. The system is mounted on a horizontal plane intersecting the working section and producing a parallel light beam which fills the 10 inch working section windows. The mirrors were high optical quality front surface aluminized mirrors. Conventional schlieren optics are sensitive to components of the flow field density gradients which are perpendicular to the knife edge. The knife edge (along with the source slit) can be oriented in any direction desired. For most of the Gun Tunnel tests, where boundary layer and oblique shock visualization was important, the knife edge and source slit were arranged to be parallel to

SCHLIEREN GEOMETRY

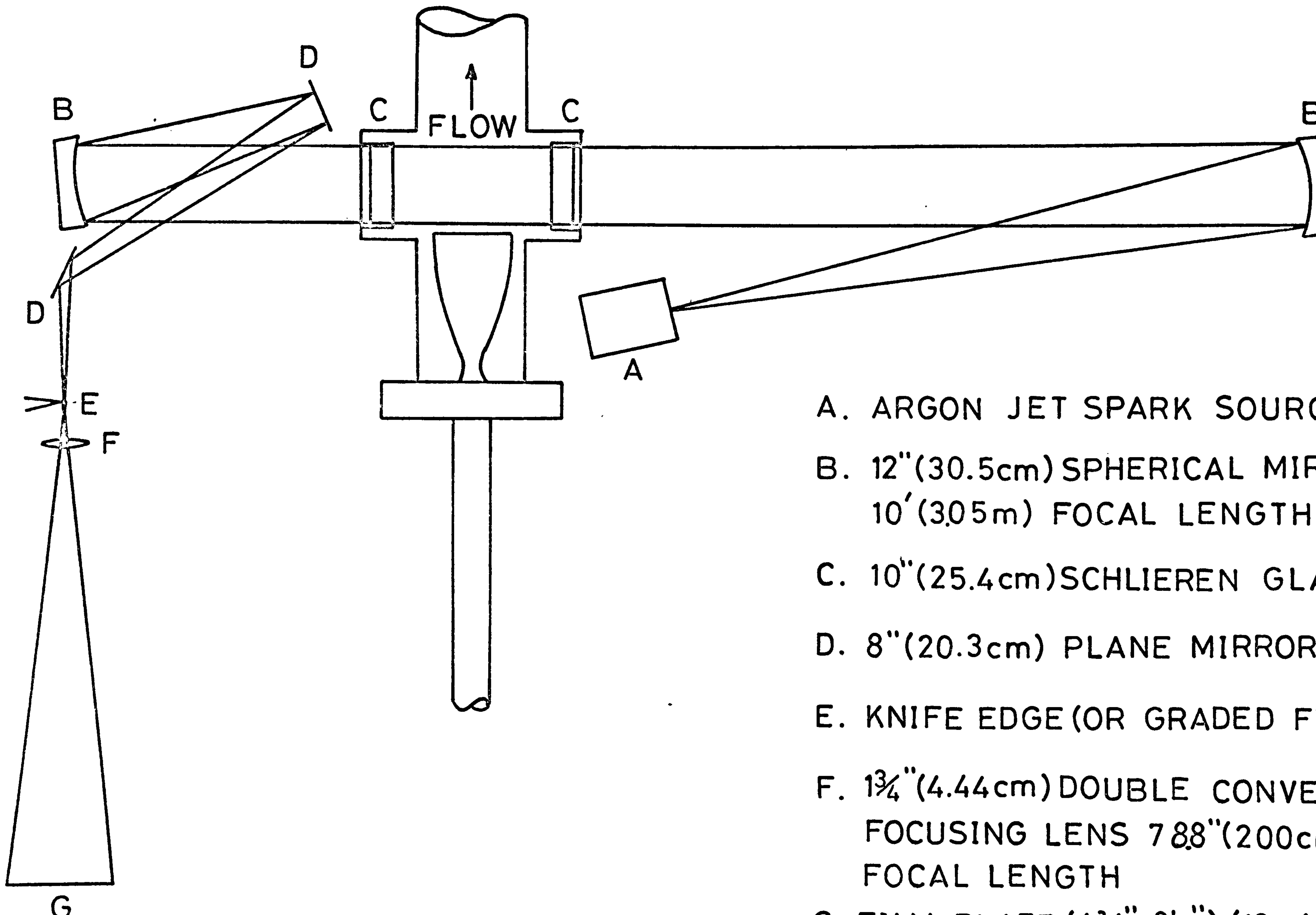

A. ARGON JET SPARK SOURCE

B. 12"(30.5cm) SPHERICAL MIRRORS
10'(3.05m) FOCAL LENGTH

C. 10"(25.4cm) SCHLIEREN GLASS

D. 8"(20.3cm) PLANE MIRRORS

E. KNIFE EDGE (OR GRADED FILTER)

F. 1¾"(4.44cm) DOUBLE CONVEX
FOCUSING LENS 78.8"(200cm)
FOCAL LENGTH

G. FILM PLATE (4¾"x6½") (12 x 16.5cm)

FIG. 3.9.

the flow direction. In some situations with strong density gradients (e.g. boundary layers) the range of the system was exceeded causing the source image to go completely on or off the knife edge with a resulting loss in sensitivity. This problem can be overcome by replacing the knife edge with a filter of graded optical density so that the source image is never completely cut off. Such filters, constructed by a photographic process at the N.P.L., have been used on many of the Gun Tunnel tests with much success.

The light source used in the schlieren system is a Lunatron Electronics Ltd., Argon Jet Light Source constructed to a design originating at the N.P.L. This unit uses a capacitive discharge through an Argon gas column to produce a very high intensity, short duration (.25 μsec) light source. A laminar Argon column was maintained by a flow rate of 3-4 standard cubic feet per hour. The Argon column served to increase the repeatability of the spark location and to constrain spatially the extent of the arc, thus helping to insure proper system alignment from run to run. The spark was focused on an adjustable slit on the front of the unit. The whole unit can be rotated to obtain any slit orientation desired. A tungsten lamp was included in the unit and focused on the slit to aid alignment procedures. The synchronization of the spark with the flow was achieved using a delay generator coupled to the reservoir pressure transducer as shown in Fig. 3.1. A special amplifier was built to match the spark triggering requirements with the delay generator output signal.

3.3.2 Shadowgraph Techniques

The shadowgraph technique in which the parallel light beam through the working section is not refocused onto a knife edge, produces an image intensity which is proportional to the second derivative of the density (or refractive index) gradient with respect to distance in the flow. The system can be set up by merely removing the knife edge from the schlieren arrangement of Fig. 3.9 (focussed shadowgraph) or by placing the film plate at the second window C in Fig. 3.9 (direct shadowgraph). The latter method has been used most frequently on the Gun Tunnel experiments for operational simplicity. This method also produces a unity magnification which makes the direct reading of distances off the image plate easier. The shadowgraph is especially useful for detailed observation of boundary layers where, because of range limitations, much detail is lost with schlieren optics.

A typical direct shadowgraph of the boundary layer on a 3 inch (7.62 cm) diameter hollow cylinder in the Gun Tunnel is shown in Fig. 9.3. A useful feature of the shadowgraph is that with highly cooled hypersonic laminar boundary layers, the peak of the second derivative of the density is very near the outer edge of the boundary layer (Ref. 56) and produces a dark line on the shadowgraph at this point. This is clearly seen in Fig. 9.3. The disappearance of this well defined line indicates the onset of transition to a turbulent boundary layer and will be discussed further in Chapter 9.

3.4 Pressure Measurements

The ability to measure a wide range of transient pressure levels is a considerable advantage in designing research programs in the Gun Tunnel. They contribute to the understanding of Gun Tunnel operation and performance as well as to working section model surface pressure and boundary layer profile experiments. There are several types of commercial transducer with a sufficiently high natural frequency response for the Gun Tunnel time scale. The main types selected for use in all the Gun Tunnel experiments were Kistler quartz piezo-electric transducers. These offer the advantages of small physical dimensions, robust construction and linear output characteristics over a wide range of pressure levels. This linearity permits a transducer designed for operation to many hundreds of atmospheres to be successfully utilized down to pressures below one atmosphere. A Kistler Type 601H, 1000 atmosphere transducer was used in the barrel end to monitor reservoir pressure for each run. Kistler Type 7031, 250 atmosphere transducers were used on all working section measurements. The 7031 is acceleration compensated to reduce spurious signals due to transducer vibrations during the run. The transducer outputs were all analyzed using Kistler Type 566 high impedance charge amplifiers. This section describes some specific pressure measurement techniques and calibration procedures used on Gun Tunnel experiments.

3.4.1 Transducer Calibration

All Kistler quartz transducers are supplied from the manufacturers with an actual calibration curve. Nevertheless, it is usually desirable for research applications to perform a separate calibration on each gauge in the pressure range it is intended to be used in. This is especially important in the very low pressure end of operation. The reservoir transducer was tested up to 4000 psia on a dead weight hydraulic test stand. If great care is taken in providing very clean electrical connections between the transducer and the charge amplifier, the charge output signal will be very steady for many minutes, thus simplifying the signal reading procedure. The calibration curve for the 601H is shown in Fig. 3.10a. For low pressure calibration a special semidynamic calibration

FIG. 3.10

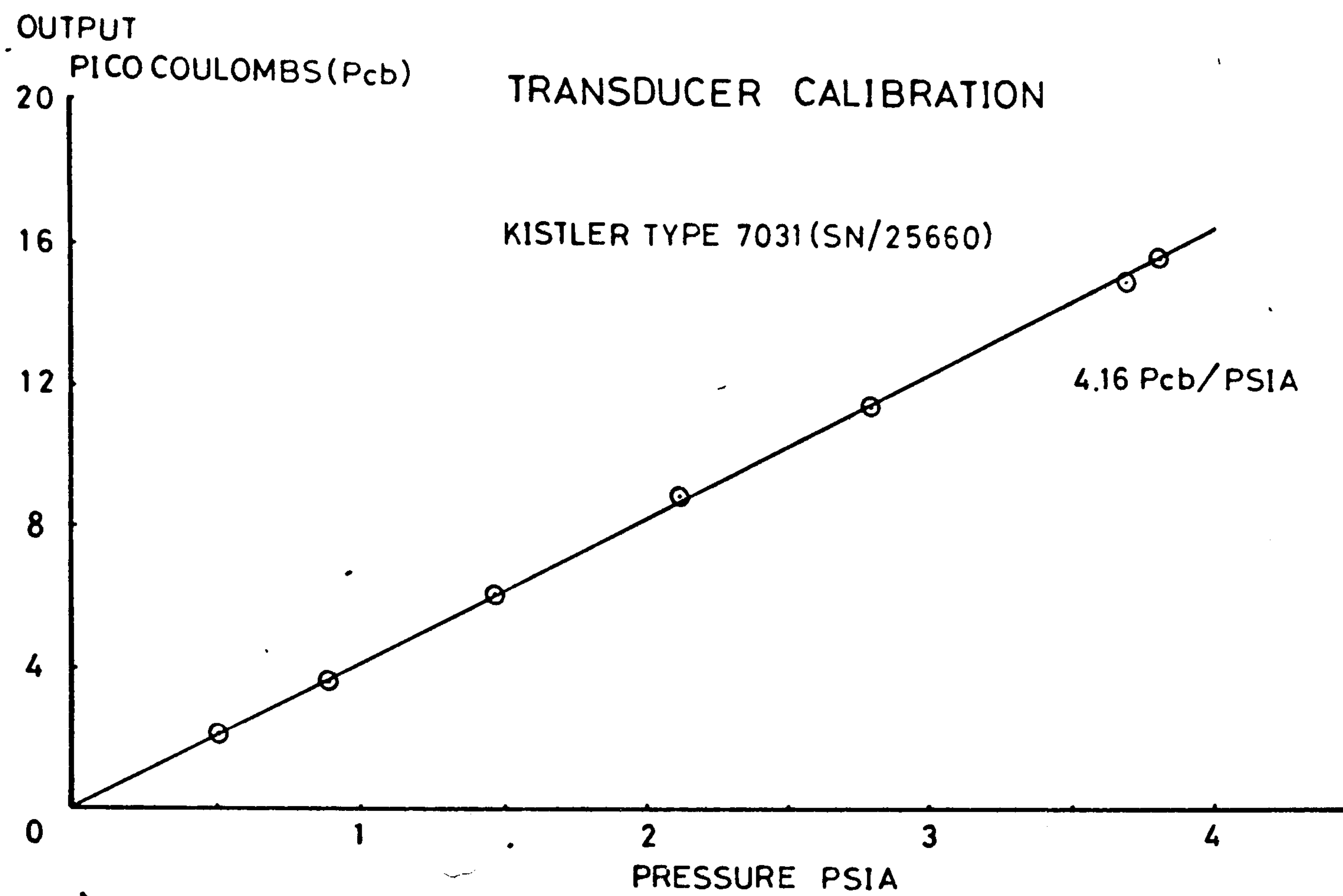
OUTPUT
PICO COULOMBS(Pcb)
TRANSDUCER CALIBRATION
KISTLER TYPE 7031(SN/25660)
4.16 Pcb/PSIA
20
16
12
8
4
0
1
2
3
4
PRESSURE PSIA

a)

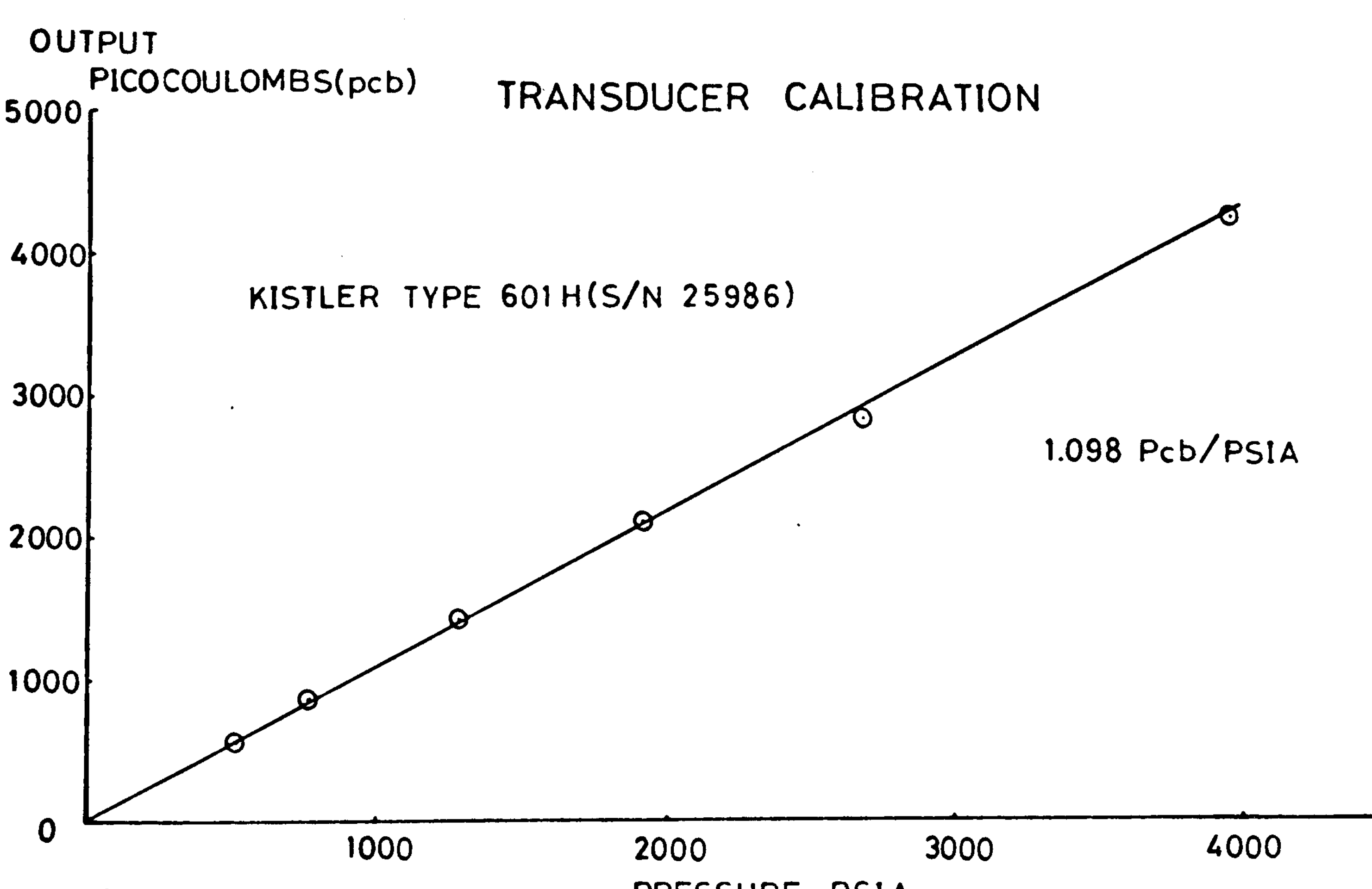
OUTPUT
PICOCOULOMBS(pcb)
TRANSDUCER CALIBRATION
KISTLER TYPE 601H(S/N 25986)
1.098 Pcb/PSIA
5000
4000
3000
2000
1000
0
1000
2000
3000
4000
PRESSURE PSIA

b)

rig has been constructed. This allows a fairly rapid application of pressure (of the order of 0.1 seconds) to the transducers starting from either a vacuum or a one atmosphere base line. Typical results for a Type 7031 are shown in Fig. 3.10b. This shows excellent linearity and a calibration factor quite close to that supplied by the manufacturers.

3.4.2 Pitot Pressure

Pitot pressure has been measured in both the free stream and through a model boundary layer. Fig. 3.2a shows a free stream pitot probe that was constructed for the calibration of the working section. Fig. 3.11b shows a typical pitot probe output from an unfiltered Type 7031 transducer. This is seen to follow the reservoir pressure (Fig. 3.11a) closely. For boundary layer profile work, .050 inch i.d. pitot tubing was flattened at the tip by clamping in a precision vice with a .015 inch shim inserted in the end to produce a rectangular shape.

There are two potential sources of error in using probes of this type. One is due to pressure leaks between the probe tip and the transducer face. This can be controlled if care is taken to maintain good seals on all joints in the system. The other source of error could be from frequency limitations of the system. The natural frequency of the transducer itself is quite high (50 KHz) and does not present a limitation on most Gun Tunnel experiments. The effective frequency response of the transducer may be limited by the geometry of the pressure cavity ahead of the transducer face. If the volume of this cavity is too large, it has been shown (Ref. 58) that the filling time may limit the response. At the pressure levels encountered in Gun Tunnel pitot measurements, this is generally not a problem if the volume is kept to a minimum. The type of

FIG 3.11

TYPICAL PRESSURE TRACES

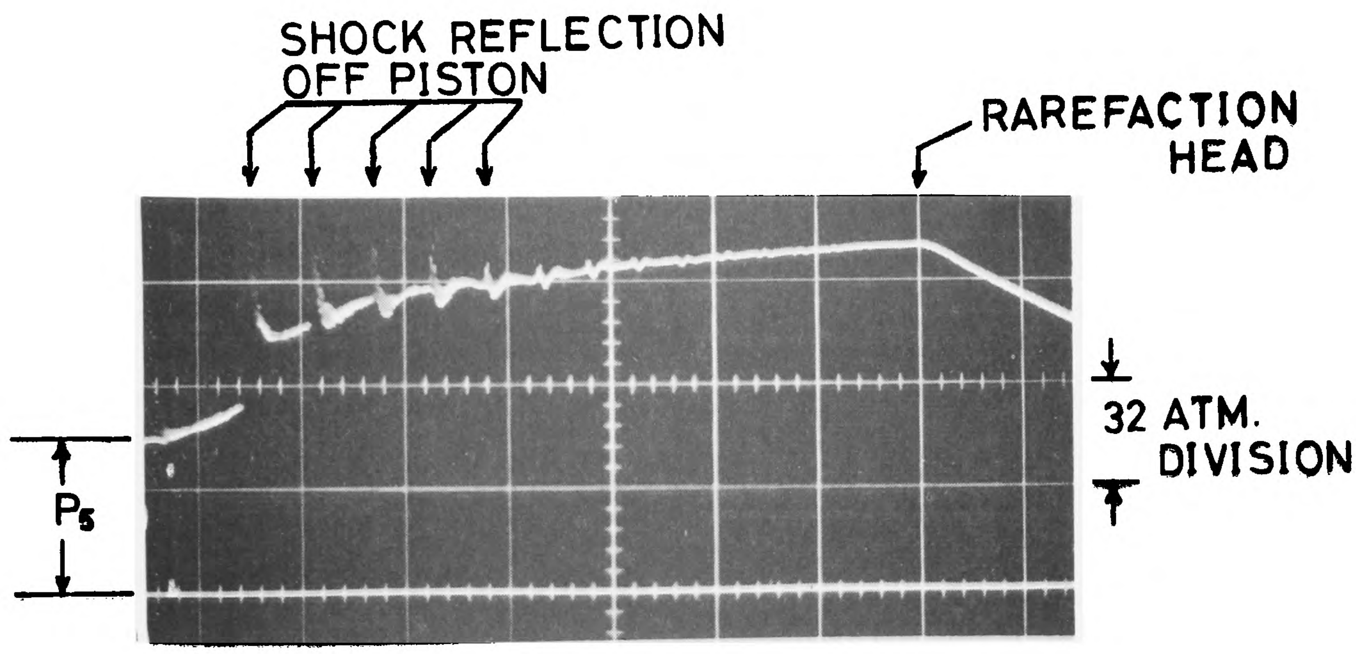

a) RESERVOIR

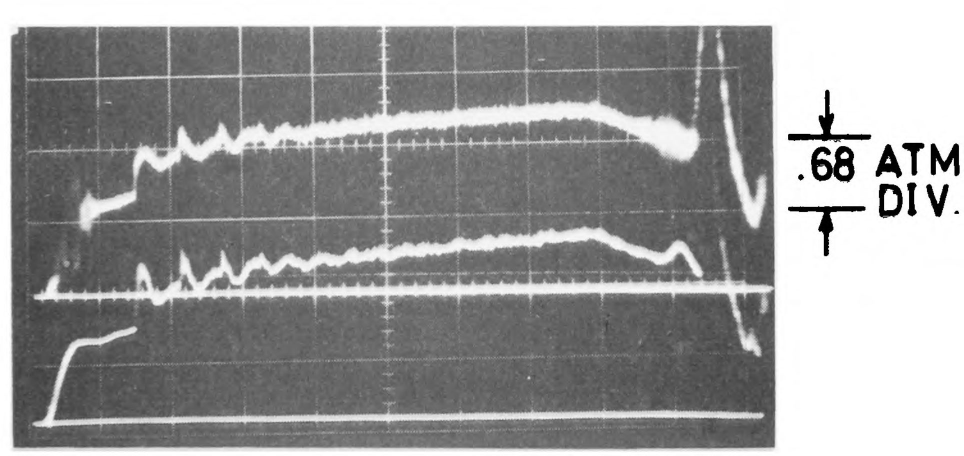

b) FREE STREAM PITOT

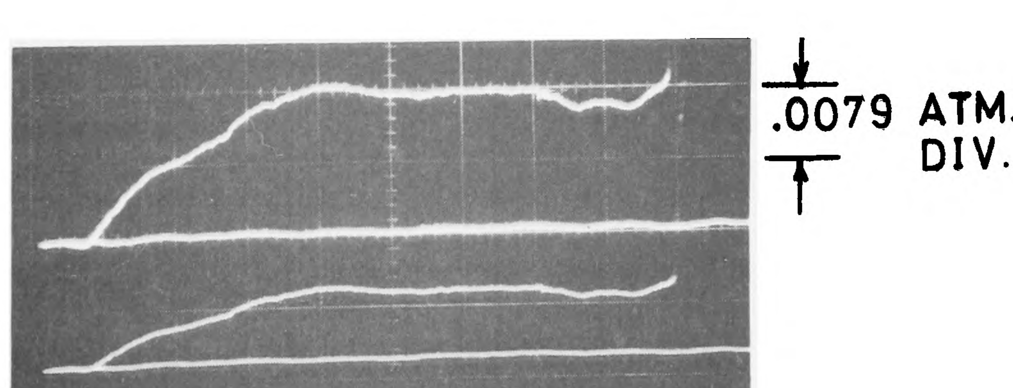

C) FLAT PLATE STATIC

frequency limitation described by Harper (Ref. 59) is more likely to be encountered if care is not taken in designing the transducer mounting. This limitation occurs when the cavity immediately in front of the transducer face is too small in height. Viscous forces then limit the rate at which the pressure from the tubing can equilibrate itself over the face of the transducer. For the 7031 size transducer in a pitot measurement, the height of the cavity should not be less than about .010 inches to prevent frequency limitations due to this effect.

3.4.3 Static Pressure

Because of the extremely low static pressures encountered in hypersonic flow experiments, great care must be taken in isolating transducers used in such experiments from tunnel vibrations. A method of suspending the transducers inside models on rubber bands has been developed by Batham (Ref. 57) for Gun Tunnel flat plate static pressure tests. This method effectively isolated the transducer from all but very low frequencies. The pressure was conducted by steel and plastic tubing from the static ports to the transducer adapter mounted internal to the model support. Details of the transducer mounting can be found in Ref. 57.

A typical flat plate static pressure trace is shown in Fig. 3.11c. This is for M = 7 and a total pressure of about 50 atmospheres. The static pressure level is about 0.0156 atmospheres and corresponds to around 100 millivolts for the maximum gain setting of the charge amplifier. The signal is completely unfiltered. The frequency response is seen to be somewhat low causing some lag in reaching equilibrium compared with the reservoir pressure. This effect is due entirely to volume fill time and is difficult to avoid for practical tube lengths at this low pressure. The response time is seen to be adequate, however, to read steady state pressure levels in the Gun Tunnel.

The wall static pressure at the nozzle exit was measured using a brass extension ring shown in Fig. 3.2b. Positioning screws assured accurate alignment with the nozzle wall. The transducer was mounted directly in the ring and consequently was not as well isolated from tunnel vibrations as in the flat plate tests. The output required filtering to produce accurately readable traces at the lowest pressure levels tested.

3.4.4 Reservoir Pressure

A port is provided in the barrel side wall $1\frac{3}{8}$ inches from the end wall. A type 601H quartz transducer was inserted in this to within $\frac{1}{2}$ inch of the wall. This allowed a record of the barrel end pressure (reservoir pressure) to be made for each run. A typical pressure trace is shown in Fig. 3.11a. Frequency response is no problem at this pressure level.

CHAPTER FOUR

SHOCK TUBE CALIBRATION

4.1 Shock Velocity Measurements

The relationship between the diaphragm pressure ratio (P_{41}) and the resulting incident shock speed ($M_s = U_s/a_1$) is given by the Taub equation for a constant area shock tube,

$$P_{41} = \frac{2\gamma_1 M_s^{\,2} - (\gamma_1 - 1)}{\gamma_1 + 1}\left\{1 - \frac{\gamma_4 - 1}{\gamma_1 + 1}\cdot\frac{a_1}{a_4}\left(M_s - \frac{1}{M_s}\right)\right\}^{-2\gamma_4/(\gamma_4 - 1)} \qquad (4.1.1)$$

where the subscripts refer to regions of the shock tube flow defined in Fig. 1.1 and 'a' is the sound speed of the gas. It was of interest to compare the ideal prediction with the actual performance with a piston in place. In this way it could be determined if the effects of piston mass and friction were appreciable. The incident shock velocity was measured by means of thin film heat transfer gauges (see Section 3.2) mounted flush with the barrel wall in the two instrumentation ports described in Section 2.1. These gauges, located 0.5 and 1.5 feet from the end wall, were used in conjunction with the pressure transducer in the barrel near the end wall (Section 3.4.4) to measure the passage of the shock wave and therefore the shock velocity when the time and distance between stations is considered. Each of the surface thin films was connected into a differentiating circuit (see Ref. 25) to make their response to a step change in heat transfer more easily located on an oscilloscope trace. The large amplitude, narrow width pulse produced by the shock front was useful for starting and stopping electronic counters as an alternative method of measuring shock velocity. Some directly measured values of shock velocity are plotted in Fig. 4.1 for a range of diaphragm pressure ratios of interest in Gun Tunnel operation. This is

FIG. 4.1

GUN TUNNEL SHOCK VELOCITY

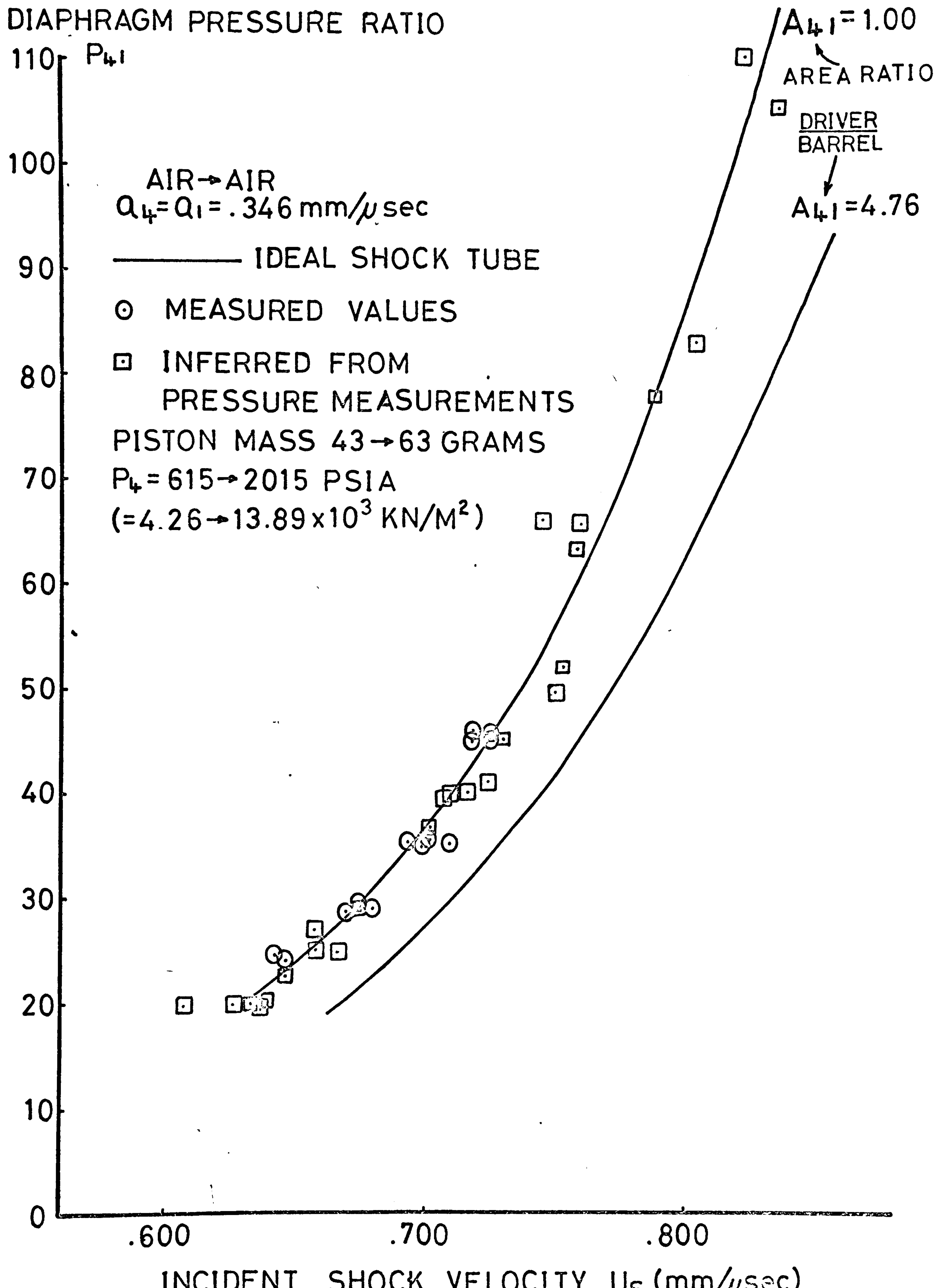

compared with the ideal constant area shock tube prediction of (4.1.1) for air driving air. Also included in Fig. 4.1 is the improved performance prediction due to an area convergence at the diaphragm station. This theory from Ref. 60 was computed using the curves of Ref. 34 for the actual driver to barrel area ratio of the Gun Tunnel. An alternative method of measuring the incident shock velocity is the indirect method of measuring shock pressure ratios and relating this to incident shock velocity. The ideal perfect gas assumptions have been shown (e.g. Ref. 32) to be valid for the low shock speeds encountered in the Gun Tunnel experiments. The shock relation used was the reflected pressure ratio P_{51} as is given in Ref. 33.

$$P_{51} = \left\{\frac{2\gamma M_s^2-(\gamma-1)}{\gamma+1}\right\}\left\{\frac{(3\gamma-1)M_s^2-2(\gamma-1)}{(\gamma-1)M_s^2+2}\right\} \qquad (4.1.2)$$

The reflected pressure was used because it could be more accurately measured under the conditions of the tests. Since (4.1.2) does not yield M_s as an explicit function of P_{51}, the expression was calculated and plotted to simplify analysis for P_{51}. The curve is reproduced here (Fig. 4.2) for reference.

The direct and inferred measurements of shock velocity are plotted in Fig. 4.1. They are seen to agree well with each other and to follow quite closely the trend predicted by ideal shock tube behaviour although the performance seems to be reduced by about 5% below what should be expected for the actual area ratio of the Gun Tunnel. Such a reduction in performance is normal for conventional shock tubes (Ref. 34) since deviations from the assumptions of perfect diaphragm burst and one-dimensional, inviscid, zero heat transfer flow implied in (4.1.1) are present even for the weak shock case.

M_s vs. P_{51} & T_{51}

IDEAL SHOCK TUBE THEORY-AIR

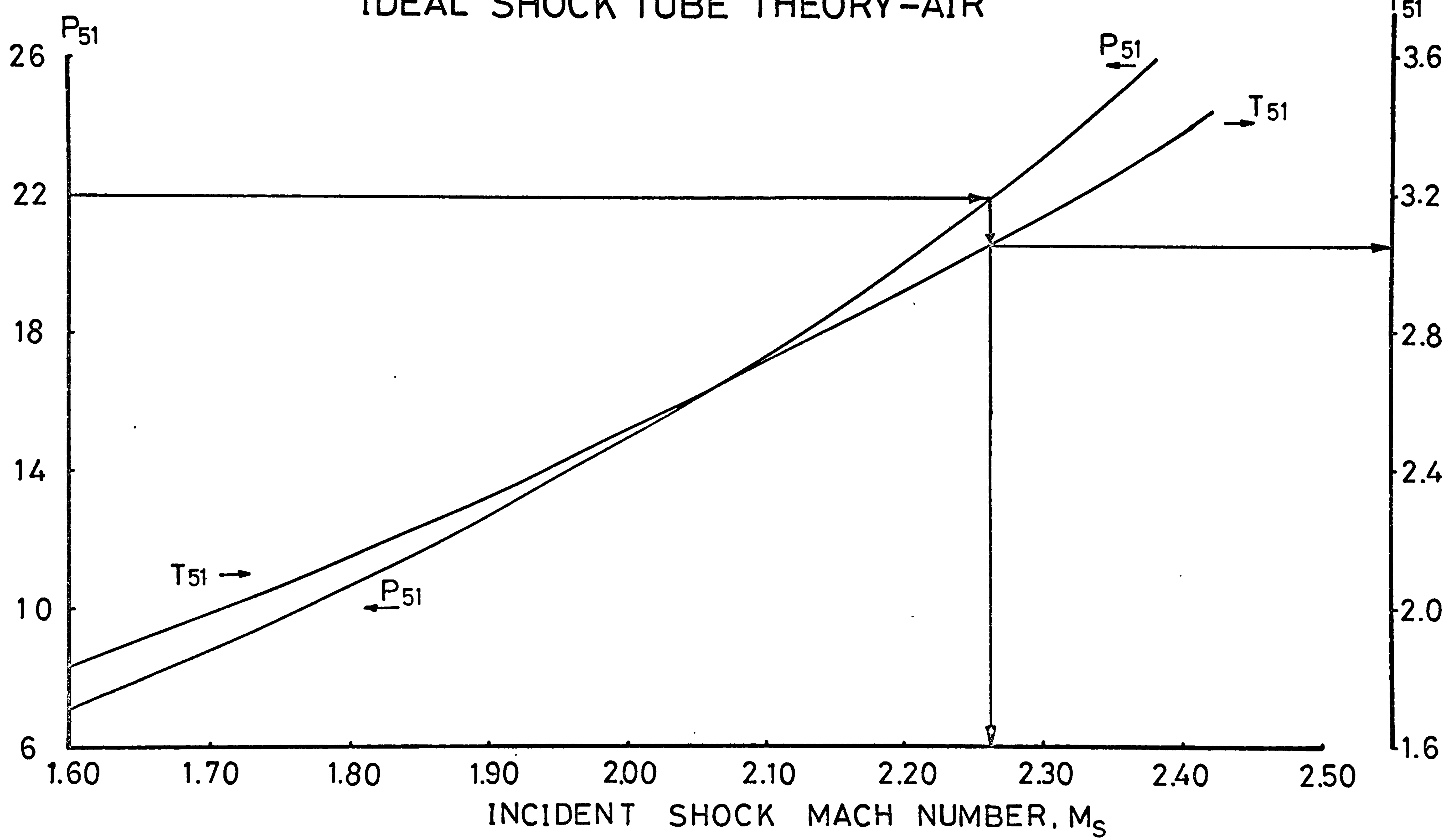

FIG. 4.2.

A similar slight loss in performance was reported by East (Ref. 7) in experiments in which the incident shock pressure ratio was measured and compared with theory for each diaphragm pressure ratio. A similar reduction was found both with and without a piston in place although the piston case produced a slightly lower shock strength for a given diaphragm pressure ratio in East's study.

4.2 Wave System Analysis and Piston Motion

The same barrel wall instrumentation arrangement as described in the previous section to measure incident shock velocity was modified slightly to follow the shock wave trajectory through several reflections. In addition, a microphone was fixed to the barrel near the diaphragm station to tie in all the measured time intervals to the origin in the x-t plane at diaphragm burst. The time between the diaphragm burst and the shock arrival at the pressure end station was very repeatable for a given diaphragm pressure ratio. The time between the bursts of the two primary diaphragms was not measurable on the time scale of the experiment. The results of the trajectory analysis for a single P_{41} condition and piston mass are shown in the detailed x-t diagram of Fig. 4.3. The measured time of arrival of the shock wave at the end wall gives an average incident shock velocity over the 30 foot length of barrel as 2270 ft/sec. Although the incident shock velocity was not measured for these particular experiments, the identical conditions plotted in Fig. 4.1 yielded an incident shock velocity near the end of the barrel of 2300 ft/sec (.700 mm/μsec). This agreement indicated that the effects of finite shock formation time and shock speed attenuation down the barrel were either very small

FIG. 4.3

X-t WAVE DIAGRAM DETAIL

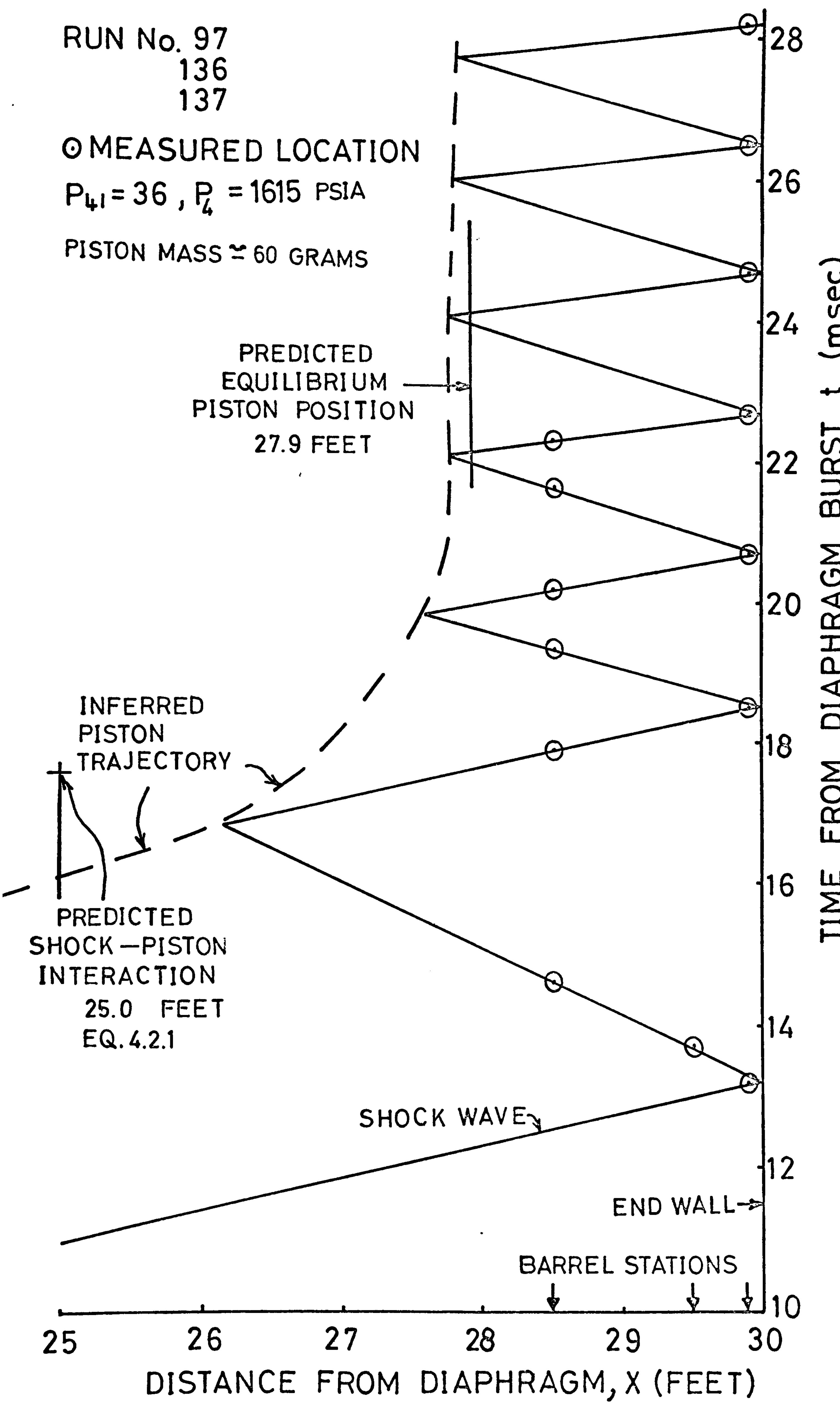

or self-cancelling. The measurement of the time intervals between each successive passage of the shock past the barrel stations enables the shock to be located in the x-t plane at discrete values of x. The assumption of constant shock velocity between reflections permits a linear extrapolation of shock location at points other than the barrel stations. The intersection of successive shock trajectories then locates the points of shock interaction with the piston and the end wall.

The point of the first shock-piston interaction is shown to be at 26.1 feet from the diaphragm station for the conditions of this series of tests. An analysis based on ideal shock tube relations and assuming the piston has instantaneously attained the velocity of the ideal contact surface (u_2), allows an expression to be derived which locates the first shock-piston interaction at a distance x_1 from the end wall

$$x_1 = \frac{u_R}{u_s} \cdot \frac{(u_s - u_2)}{(u_R + u_2)} (L_1) \tag{4.2.1}$$

where L_1 is the barrel length and u_R is the absolute reflected shock speed with respect to barrel fixed coordinates. The flow velocity behind the incident shock wave is given by ideal shock relations as

$$u_2 = \frac{2a_1}{\gamma+1} \left\{ M_s - \frac{1}{M_s} \right\} \tag{4.2.2}$$

and the absolute velocity of the reflected shock wave as

$$u_R = \frac{u_s[2 + \frac{2}{\gamma-1} P_{12}]}{\frac{\gamma+1}{\gamma-1} + P_{12}} \tag{4.2.3}$$

The incident shock pressure ratio P_{21} $(= \frac{1}{P_{12}})$ is given by

$$P_{21} = \frac{2\gamma M_s^2 - (\gamma - 1)}{\gamma + 1} \tag{4.2.4}$$

for ideal flow. Combining equations (4.2.1 - 4.2.4) and assuming the measured value of $M_s = 2$ (u_s = 2270 ft/sec) gives the ideal intersection point as x_1 = 25.0 feet. The time of this interaction is $t = x_1/u_2$ = 17.6 millisecs. The ideal interaction point is shown in Fig. 4.3. The actual performance of the Gun Tunnel is seen to be closely approximated by an ideal shock tube analysis provided that an actual incident shock velocity is used. Examining further the magnitude of non-ideal behaviour it is seen from the slope of the first reflected shock wave in Fig. 4.3 that the velocity of this wave is 1053 ft/sec. The ideal value for u_R from (4.2.3) is 1135 ft/sec for $M_s = 2$. The average value of piston velocity up to the point of shock interaction is 1540 ft/sec whereas the velocity of the ideal contact surface is given by (4.2.2) as 1420 ft/sec for $M_s = 2$. Whether this excess piston average velocity over the ideal contact surface velocity is a real phenomenon or simply within the scatter of the experiment and assumptions, is difficult to determine with certainty. It could be pointed out, however, that Stalker (Ref. 11) has observed a consistent excess of measured piston maximum velocity over the velocity of an ideal contact surface found using actual shock strengths. This velocity discrepancy produced a compression wave between the piston and the incident shock which could be measured as a steady rise in the pressure behind the first reflected shock off the wall. A similar pressure rise is detectable in the same region (P_5) of all tests on the Gun Tunnel (e.g. see Fig. 3.11a).

Several research groups have made very detailed measurements of actual piston trajectories in gun tunnels using microwave techniques (Refs. 5, 9-12). This technique permitted measurements of piston maximum velocity as well as the starting and stopping process of the piston. Table 5 lists some results of piston maximum velocity measurements for conditions generally similar to those in the present tests. Ideal contact surface velocity (u_2) based on an actual measurement of shock strength is included where given.

TABLE 5

Summary of Shock and Piston Velocity Measurements

SOURCE	P_{41}	PISTON MASS m (grams)	MEASURED M_s	IDEAL u_2 ft/sec	PISTON VELOCITY u_p ft/sec	MEASURED u_R ft/sec	IDEAL u_R ft/sec
PRESENT DATA	36	60	2.0	1420	1540	1053	1135
LEMCKE Ref.12	35	10	2.2	1650	1640 (EXTRA-POLATED)	-	-
MEYER Ref.10	40	100	-	-	1450	-	-
STOLLERY et. al. Ref. 5	33.7	60	-	-	1600	-	-
STALKER Ref.11	36	.03	-	908	1305	-	-
KAMIMOTO et. al. Ref.18	40	10	2.05	1480	1635	-	-

Several authors, beginning with Cox and Winter (Ref. 1), have considered the case of the theoretical motion of a free piston in a gun tunnel (e.g. Refs. 7, 10, 12). The approach of these theories involved the summation of all forces acting on the piston and equated this to the rate of change of momentum of the piston. This usually had the form

$$A(P_b - P_f) - f = \frac{m\, du_p}{dt} \qquad (4.2.5)$$

where P_b and P_f were the pressures on the back and front faces of the piston respectively and f was an assumed constant friction force. The solution of (4.2.5) involved expressing P_b and P_f in terms of piston velocity u_p ($= u_2$). The front face pressure was usually related to u_2 by the ideal shock tube relations (4.2.2) and (4.2.4). The back face pressure, however, required some varying assumptions concerning the nature of the driver expansion process for the different barrel configurations in each gun tunnel considered. When actual piston trajectory measurements were made, they were found to lag the zero friction solution of (4.2.5) for each particular gun tunnel geometry. Agreement was usually improved by including a relatively high friction term in the solution. This approach was not always adequate, however, and may have merely corrected in the proper direction for some causes of non-ideal behaviour not related to piston friction. Real shock tubes, in general, do not reproduce ideal shock tube flow and thus ideal shock tube theory could not be expected to describe adequately the motion of a piston. The results of Table 5 suggest, in fact, that consideration should be given to real shock tube performance when attempts are made to correlate piston velocities.

The inferred piston trajectory is based on the known piston position at at least three points with three additional points known to reasonable accuracy. The actual trajectory probably overshoots the final position shown in Fig. 4.3. This statement is based on continuous observations of piston trajectories reported in the literature (Refs. 10, 11, 17) and on the fact that the piston is heavier than that required for no-overshoot operation (see Ref. 16). The final equilibrium position of the piston can be estimated by computing the initial mass of the cold barrel gas and determining what volume this gas would occupy if compressed to the final observed reservoir pressure and temperature. For the conditions listed in Fig. 4.3, the length (ℓ) of this hot gas slug would be 2.1 feet and is shown to be quite close to the observed final position. The length is given by the approximate expression,

$$\ell = \frac{T_{t1}}{P_{41} P_{e4}} L . \tag{4.2.6}$$

A complete x-t wave diagram has been calculated for the Gun Tunnel conditions described in Fig. 4.3. This is shown in Fig. 4.4 along with the measured shock positions and inferred piston position discussed above. The location of the contact surface is based on the measured incident shock velocity and ideal shock tube expressions. The actual arrival of the rarefaction wave at the piston is shown as well as the projected point of arrival of the piston at the end wall based on the analysis of Section 5.1. The head of the rarefaction produced by the diaphragm burst travels into the undisturbed driver gas at the local speed of sound a_4. The time variant region of the expansion is bounded by the rarefaction head and tail. The equation of the tail is given by

$$x = (u_3 - a_3)t \tag{4.2.7}$$

and the equation of the head between its reflection off the driver end wall and intersection with the tail is given by

$$\frac{x}{L_4} = \frac{\gamma+1}{\gamma-1} \left(\frac{t\ a_4}{L_4}\right)^{\frac{3-\gamma}{\gamma+1}} - \frac{2}{\gamma-1} \left(\frac{t\ a_4}{L_4}\right) \tag{4.2.8}$$

FIG. 4.4

GUN TUNNEL X – t WAVE DIAGRAM

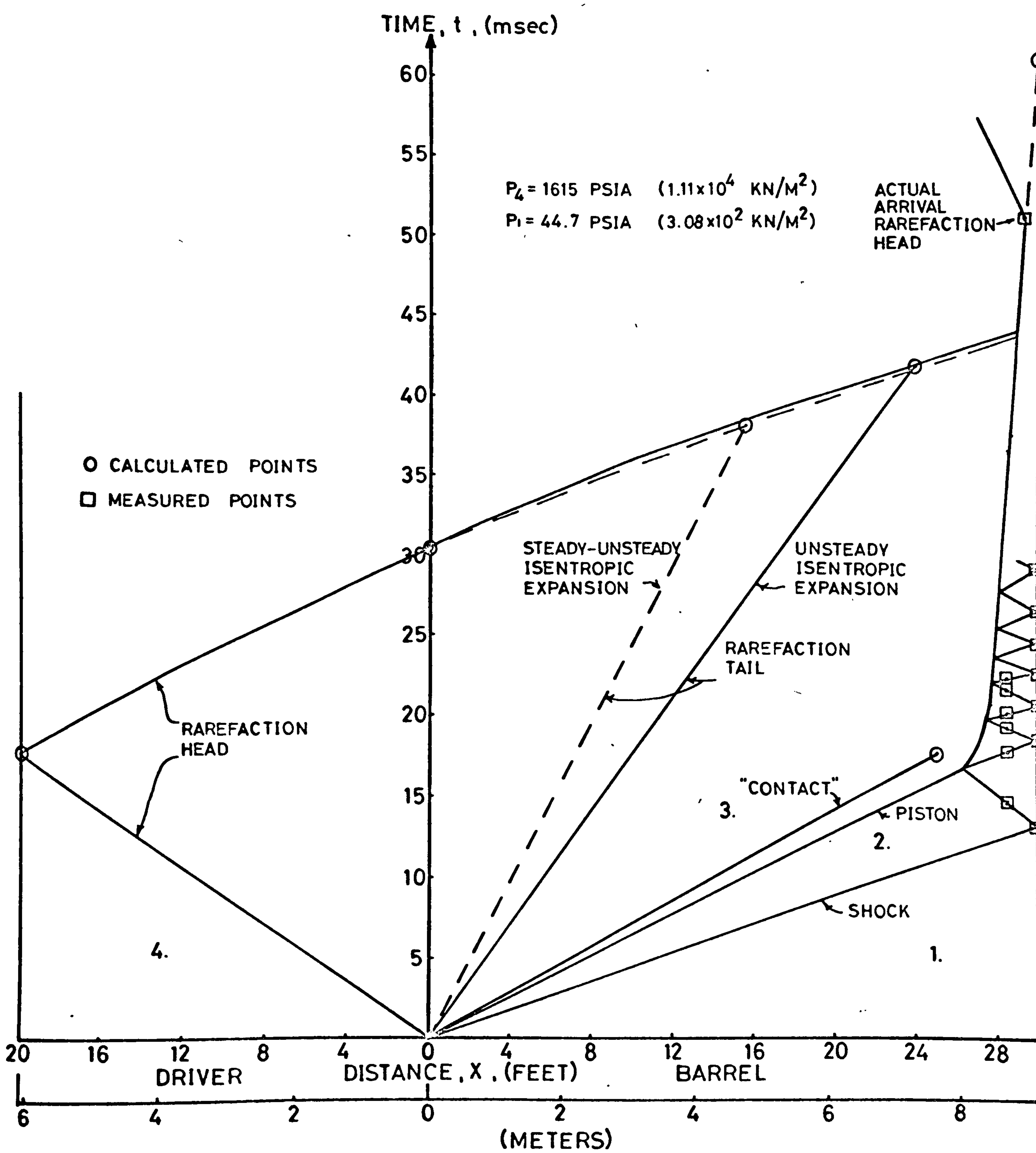

where L_4 is the driver length and perfect gas expansion ($\gamma_3 = \gamma_4$) is assumed. The intersection of the head with the tail can be found by combining (4.2.7) and (4.2.8) with an assumption relating a_3 and u_3 in an isentropic expansion. It is assumed that u_3 must equal u_2 for the condition of zero mass flow across an ideal contact surface. u_2 is found from (4.2.2) for the measured value of M_s. An expansion in a constant area shock tube is usually described as a steady isentropic one. In this case, the quantity

$$\frac{2}{(\gamma-1)} a + u$$

is conserved yielding the expression

$$\frac{a_3}{a_4} = 1 - \frac{(\gamma - 1)}{2} . \frac{u_3}{a_4} \tag{4.2.9}$$

for a_3. Flagg (Ref. 61) has suggested that the more likely type of expansion for a shock tube with a driver to barrel area ratio greater than unity is a steady expansion to sonic velocity followed by an unsteady expansion to final conditions. In this case a_3 is given by

$$\frac{a_3}{a_4} = \left(\frac{\gamma+1}{2}\right)^{\frac{1}{2}} - \left(\frac{\gamma-1}{2}\right) . \frac{u_3}{a_4} \quad . \tag{4.2.10}$$

The intersection of the expansion head and tail was then computed for both cases and included in Fig. 4.4. The velocity of the head after the intersection is given by

$$\nu_H = u_3 + a_3 \quad . \tag{4.2.11}$$

It is seen that although the intersection points are different for the two cases, the time of arrival of the rarefaction head at the piston is not appreciably different. It is also seen that the predicted arrival time is slightly earlier than the observed time. This may be due to unaccounted for effects of the transmission of the head through the diaphragm station. It has been suggested (Ref. 12) that the observed pressure drop could be caused by an expansion wave produced by the interaction of a rearward travelling shock wave with the area change at the diaphragm station. This shock wave has been observed (Ref. 11) and is seen to originate from the rapid deceleration of the piston near the end of the barrel. Insufficient quantitative information concerning the motion of this shock exists to enable an accurate prediction of its behaviour. It is therefore not possible in the present case (Fig. 4.4) to establish which phenomenon is the more likely cause of the pressure drop. It has been observed during tests on the Gun Tunnel, however, that the location of this pressure drop is quite insensitive to large changes in diaphragm pressure ratio and piston mass. This observation is more likely to be true for diaphragm-burst-produced expansions than for those produced by the rearward piston shock.

4.3 Barrel Pressure History

The reservoir side wall pressure is measured during each run at the instrumentation station nearest the downstream end of the barrel. This pressure station was mentioned in Section 4.2 in connection with its use to measure the timing of the shock reflection process. The main purpose of the pressure measurement, however, was to determine the level and duration of steady pressure from run to run. It was also of interest to be able to observe the details of the pressure variations with changing piston mass and diaphragm pressure ratio. Three typical reservoir pressure traces are shown in Fig. 4.5. The trace sweeps were initiated by the arrival of the incident

FIG. 4.5

RESERVOIR PRESSURE RECORD

EFFECT OF PISTON MASS AND P_{41}

5 MSEC/CM → $P_4 = 1575$ PSIA ($1.08 \times 10^4 \frac{KN}{M^2}$)

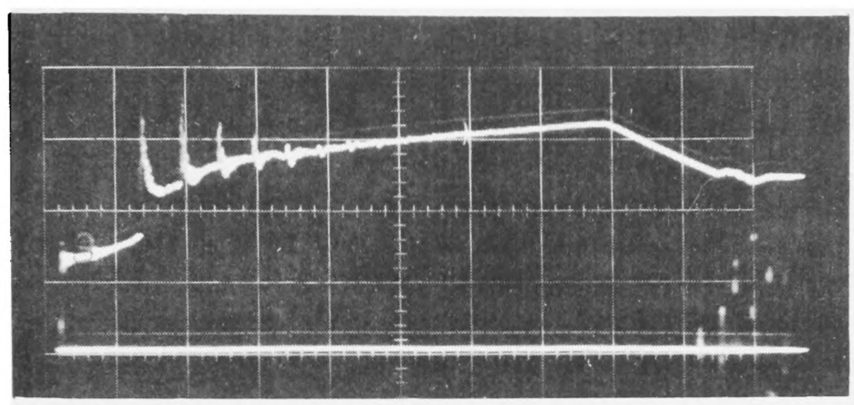

a) $P_{41} = 24.3$ M = 40 g

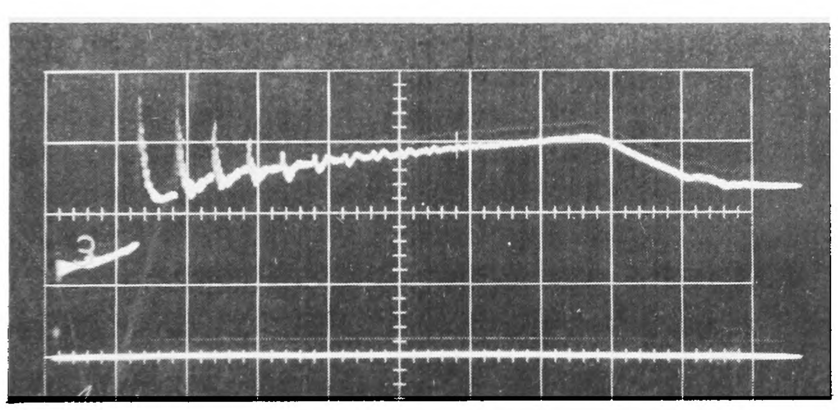

b) $P_{41} = 24.3$ M = 63 g

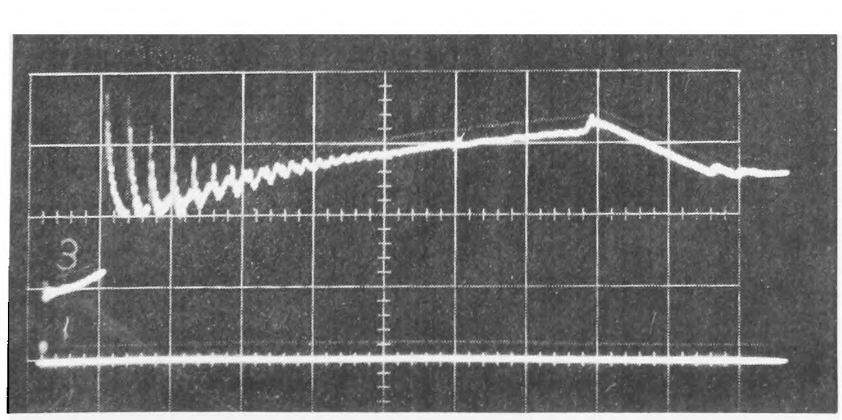

c) $P_{41} = 45.4$ M = 63 g

shock wave. The incident shock pressure (P_2) level can be seen as a faint white dot between the baseline and the reflected shock pressure (P_5) level. This pressure (P_5) rises slightly until the arrival of the shock wave reflected from the piston. A sharp jump in pressure is then seen followed immediately by a rapid expansion reducing the peak shock pressure to a level only slightly above the level immediately preceding the shock. This process is repeated for each successive reflected shock with the shock strength decreasing each time until decaying into a sound wave. The pressure then appears to rise very slowly (apparently under the influence of a weak compression wave system) until the arrival of the expansion wave which effectively terminates the useful portion of the run. For calibration purposes, the pressure level at 30 msecs. after the arrival of the incident shock is defined as the equilibrium total pressure (P_t) of the experiment. Some values of this measured pressure (P_t) normalized with respect to the driver pressure (P_4) are given in Fig. 4.6 for a wide range of driver pressures and driver pressure ratios (P_{41}). The ratio P_{t4} does not appear to be a strong function of P_{41}. It has been found by Hawkins (Ref. 26) that the ratio P_{t4} is primarily a function of the geometry of the transition section at the diaphragm station. According to Hawkins, a decrease in the driver/barrel area ratio or the insertion of a constricted area plate at the diaphragm produces a decrease in the final pressure ratio (P_{t4}). This can be observed qualitatively in the present experiments by referring to the diaphragms used for each P_4 in Table 2. Thicker diaphragms produced a greater area constriction and a decrease in P_{t4}. For a given diaphragm thickness, an increase in P_{41} produced a more complete diaphragm opening

RESERVOIR PRESSURE RECOVERY
(AT 30 M.SEC)

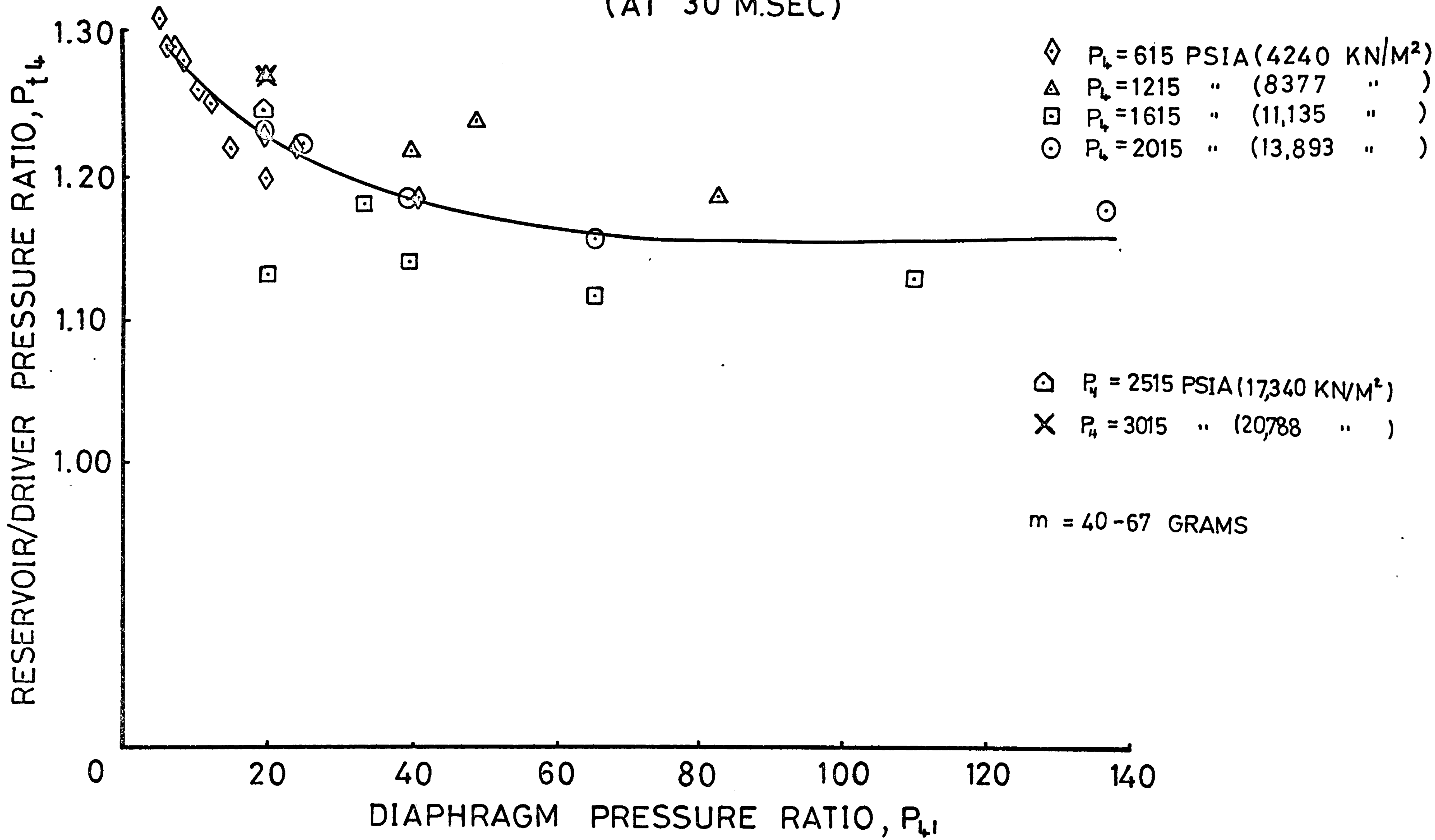

FIG. 4.6

and thus an increase in P_{t4}.

The amplitude, frequency, and duration of the pressure oscillations on the traces of Fig. 4.5 are seen to vary with the changing P_1 and piston mass (m). A theoretical analysis of the piston energy balance during the deceleration of the piston has been made by Stalker (Ref. 11) and Lemcke (Ref. 12). Their methods consisted essentially of assuming the piston kinetic energy was dissipated by isentropically compressing the barrel gas from P_5 to the peak pressure P_p. Lemcke also considered the work done bringing the gas behind the piston to rest isentropically. In terms of the symbols of this report, Lemcke's expression for peak pressure was given as

$$\frac{P_p}{P_s} = \left\{1 + P_{25}\left[\left(P_{t4} \cdot P_{42}\right)^{\frac{\gamma-1}{\gamma}} - 1\right] + \frac{\gamma-1}{2} \cdot \frac{m\ u^2}{P_1 A_1 L T_{51}}\right\}^{\frac{\gamma}{\gamma-1}} \qquad (4.3.1)$$

Several tests were conducted in which the piston mass and barrel pressure were varied for a constant driver pressure. The peak pressure behind the first shock reflection from the piston was measured. The pressure record on an UV recorder was used because of the greater accuracy in locating the peak pressure possible on this device compared with an oscilloscope trace. The conditions and results of these tests are listed below in Table 6 along with the computed value from (4.3.1). For the computation, a perfect gas was assumed and the piston velocity was assumed to be that of the flow behind the incident shock (u_2). Ideal shock tube relations were used for the actual calibrated value of shock speed. P_{t4} was taken from Fig. 4.6 as approximately 1.20.

TABLE 6

Peak Pressure Measurement and Theory (Ref. 12)

P_4 = 106.2 atmospheres

RUN	P_{41}	m GRAMS	M_s	P_p/P_5 (Exp.)	P_p/P_5 (4.3.1)
86	35.0	63	2.00	3.98	2.89
88	35.0	40	2.00	3.44	2.89
42	63.3	67	2.21	5.67	4.10
43	106.2	67	2.39	8.28	6.28
46	63.3	67	2.21	5.38	4.10
47	45.1	67	2.095	4.72	3.31
48	35.0	67	2.00	3.96	2.97
49	35.0	67	2.00	3.96	2.97

The theory is seen to underestimate the observed values of peak pressure. Meyer (Ref. 10) obtained similar results for his peak pressure measurements compared to Lemcke's theory although Lemcke's own data compared favourably with the theory. The power law functional dependence of peak pressure on piston kinetic energy basic to Lemcke's approach is substantiated for the present series of tests in Fig. 4.7. In this, the piston velocity is assumed proportional to shock speed for the small M_s range of the tests.

The frequency of the reflected shock disturbance on the pressure traces depends mainly on the equilibrium final position of the piston given by (4.2.6). This is a function of diaphragm pressure ratio (P_{41}) only since P_{t4} is nearly constant and the total temperature ratio (T_{t1}) is a function of P_{41} only. The rate of damping of the shock strength does not appear to vary appreciably for the conditions tested. The time for the shock

FIG. 4.7

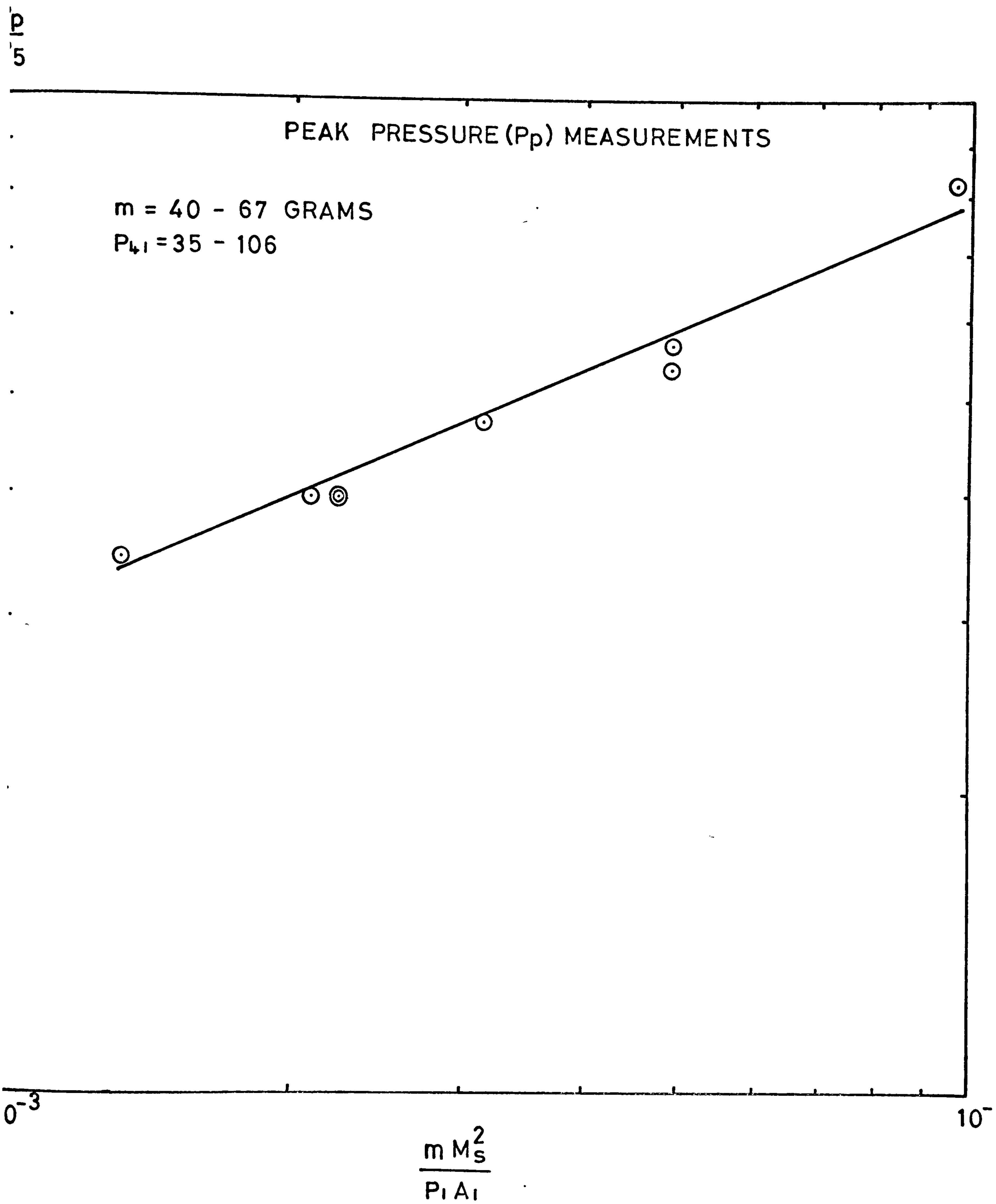
P
5
PEAK PRESSURE (Pp) MEASUREMENTS
m = 40 - 67 GRAMS
P41 = 35 - 106
0^-3
10^-2
m M_s^2 / P1 A1

strength to reduce to near unity qualitatively depends simply on the initial amplitude of the peak pressure.

Davies et. al. (Ref. 16) and East and Pennelegion (Ref. 62) have considered the possibility of adjusting the Gun Tunnel running conditions so as to produce a piston deceleration with no oscillations. This would involve adjusting the peak pressure (P_p) to equal the final equilibrium pressure (P_t). They have been able to approach this operating condition quite closely. To achieve the conditions of equilibrium observed in these two references on the larger gun tunnel of this report would require a piston much lighter than that found necessary for structural reasons.

CHAPTER FIVE

WORKING SECTION CALIBRATION

This section describes some experiments conducted to determine some of the flow properties in the working section of the Gun Tunnel. In some cases this involved direct measurements in the working section free stream, while in other cases, free stream flow parameters were inferred from measurements made in the barrel near the entrance to the nozzle throat. All tests referred to in this section were conducted with the open jet Mach 7 contoured nozzle in place. The physical configuration of the nozzle assembly has been described in Section 2.2.

5.1 Running Time Tests

It was seen in Section 4 that the quasi-steady region of the reservoir conditions could be effectively terminated by the arrival of an expansion wave at the nozzle entrance. It is also possible for the run to be terminated before the arrival of the expansion wave by the depletion of the hot compressed gas ahead of the piston. This mass flow running time limit (τ) can be theoretically approximated as the ratio of the initial mass of driven gas in the barrel to the mass flow rate through the nozzle throat. This time is then given as

$$\tau = \frac{m_1}{\dot{m}} = \frac{\rho_1 A_1 L_1}{\rho^* a^* A^*} \tag{5.1.1}$$

where (*) refers to conditions at the nozzle throat. Using isentropic nozzle flow expressions, (5.1.1) can be written in terms of reservoir conditions as

$$\tau = (T_t)^{\frac{1}{2}} \; \frac{P_1}{P_t} \cdot \frac{A_1}{A^*} \cdot \frac{L_1}{T_1} \; \frac{1}{\sqrt{\gamma R}\left(\frac{2}{\gamma+1}\right)^{\frac{1}{2}\,\frac{\gamma+1}{\gamma-1}}} \tag{5.1.2}$$

where R is the gas constant. This expression is plotted in Fig. 5.1 for various total temperatures and total pressure ratios (P_{t1}) assuming a perfect gas and using the dimensions of the Mach 7 nozzle assembly. It will be shown in Section 5.3 that the total temperature is a function of P_{t1} only. The running time can then be written as a unique function of total pressure ratio, only, for given nozzle and barrel dimensions. Using the actual calibrated relation between total temperature and total pressure ratio from Section 5.3, the expression relating running time and total pressure ratio is shown in Fig. 5.2. The measured running time defined as when the piston arrives at the end wall was determined from observations of the reservoir pressure record and/or of the free stream pitot trace. The agreement is seen to be quite good except at the higher pressure ratios (shorter times) where the assumptions of constant pressure and temperature introduce more appreciable errors.

A third possible cause of running time limitation is due to working section static pressure increases during the run. Such an increase can affect the nozzle pressure distribution and ultimately cause flow breakdown. Although shock tunnel running times are generally too short for this to be a problem, some workers (Refs. 6, 26, 63) have found the addition of a diffusor, similar to those used in continuous supersonic facilities, necessary in gun tunnel operation. This flow breakdown effect can also be aggravated by the blockage effects of large models. Although no diffusor has been used with the open jet Mach 7 nozzle in the current series of Gun Tunnel tests, no flow breakdown due to this effect has been observed for a wide range of model sizes. It appears that the pressure recovery

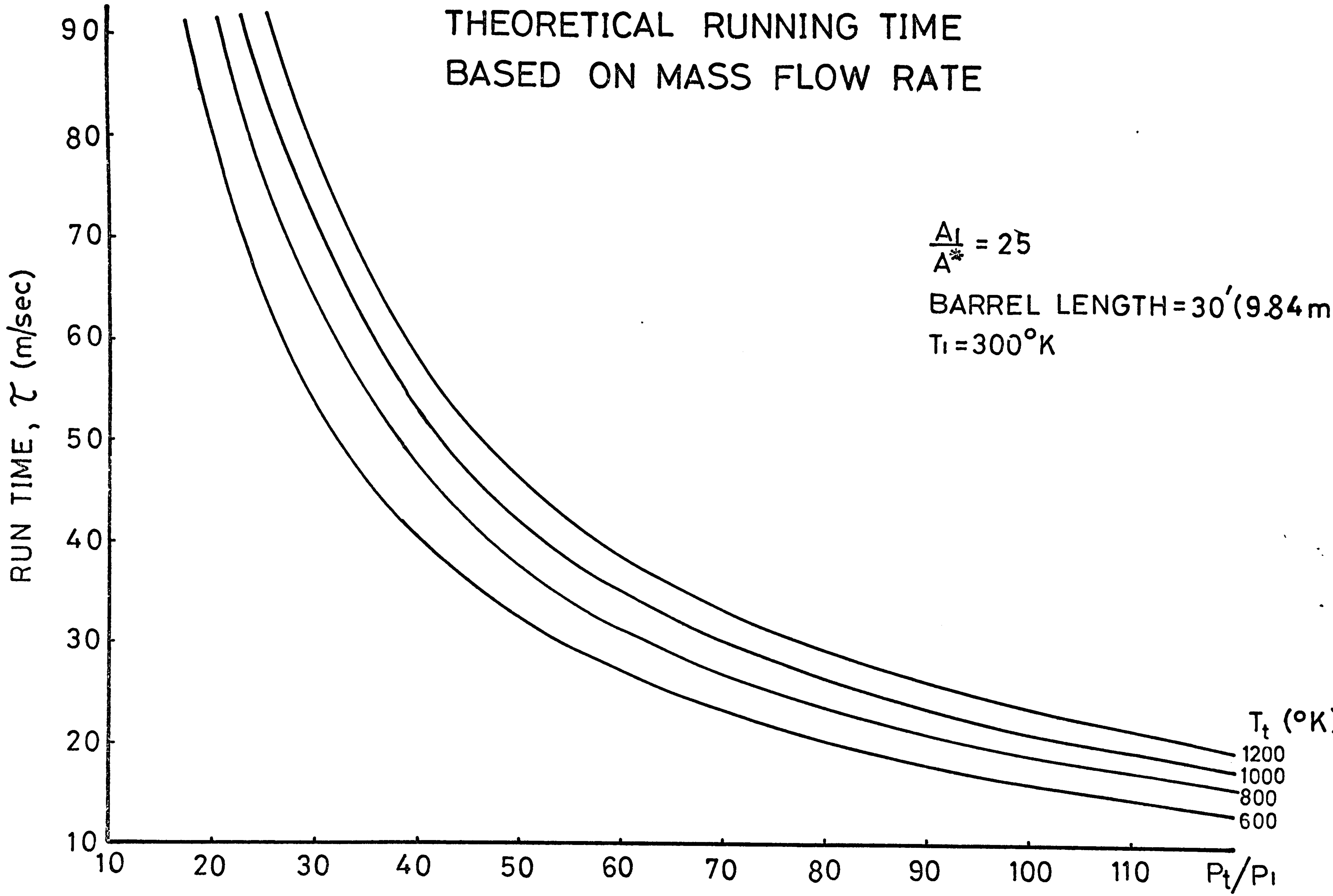
THEORETICAL RUNNING TIME
BASED ON MASS FLOW RATE
$\frac{A_1}{A^*} = 25$
BARREL LENGTH = 30′ (9.84 m)
$T_1 = 300°K$
RUN TIME, τ (m/sec)
P_t/P_1
T_t (°K)
1200
1000
800
600
90
80
70
60
50
40
30
20
10
10
20
30
40
50
60
70
80
90
100
110

FIG. 5.1

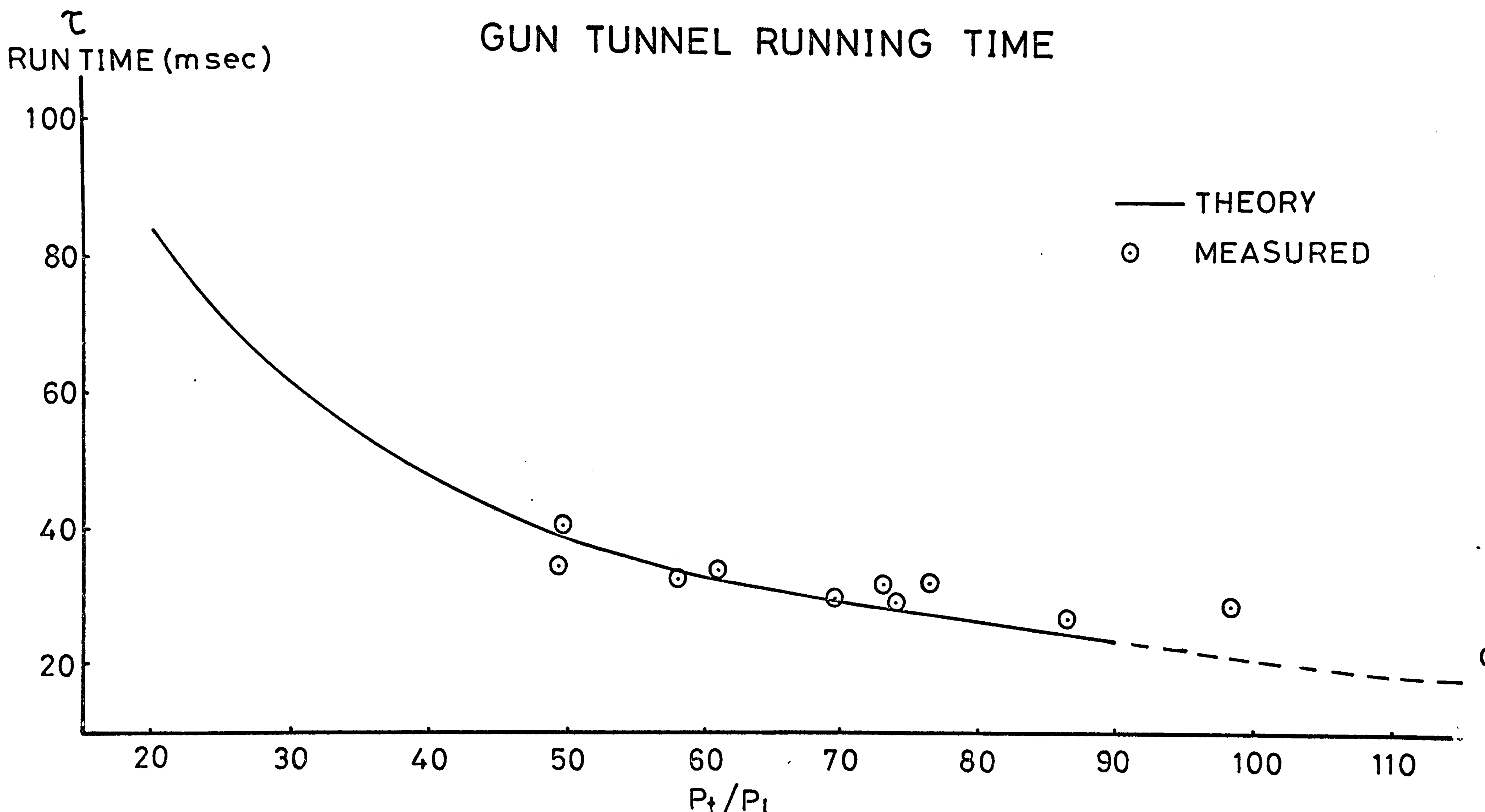
GUN TUNNEL RUNNING TIME
τ
RUN TIME (msec)
100
80
60
40
20
THEORY
MEASURED
20
30
40
50
60
70
80
90
100
110
P_t/P_1

FIG. 5.2

shock becomes fixed at some position downstream of the working section during the run.

5.2 Mach Number Measurement

5.2.1 Pitot Probe Tests

Working section flow uniformity has been calibrated for the Mach 7 contoured nozzle by using the pitot probe described in Section 3.4.2. The ratio of the pitot pressure to the reservoir pressure was used with the tables of Ref. 64 to define the flow Mach Number for isentropic nozzle flow. The measured Mach Number distribution across the vertical plane for three different axial locations near the nozzle exit is shown in Figs. 5.3 and 5.4 for two typical operating conditions. The Mach Number is seen to be very close to the nominal design value although there are some slight irregularities across the nozzle due perhaps to some non-uniformities in the machined nozzle co-ordinates. The Mach Number level and distribution is seen to be nearly independent of the free stream unit Reynolds Number. This would be expected from the weak dependence of turbulent layer growth rates on Reynolds Number. Although the test conditions of Figs. 5.3 and 5.4 are below the design Reynolds Number, the mean axial Mach Number gradients are very low (.007 and .0024 per cm. respectively). The measured nozzle wall boundary layer velocity thickness of about 0.55 inches agrees well with the computed value used in the nozzle design and listed in Table 1 if the cold wall nozzle displacement/velocity thickness ratio of 0.45 for Mach 7 from Ref. 65 is used.

The symmetry of the Mach Number distribution was checked for one test condition by making a pitot traverse in the horizontal plane at a point 5 inches from the nozzle exit plane.

FIG.5.3

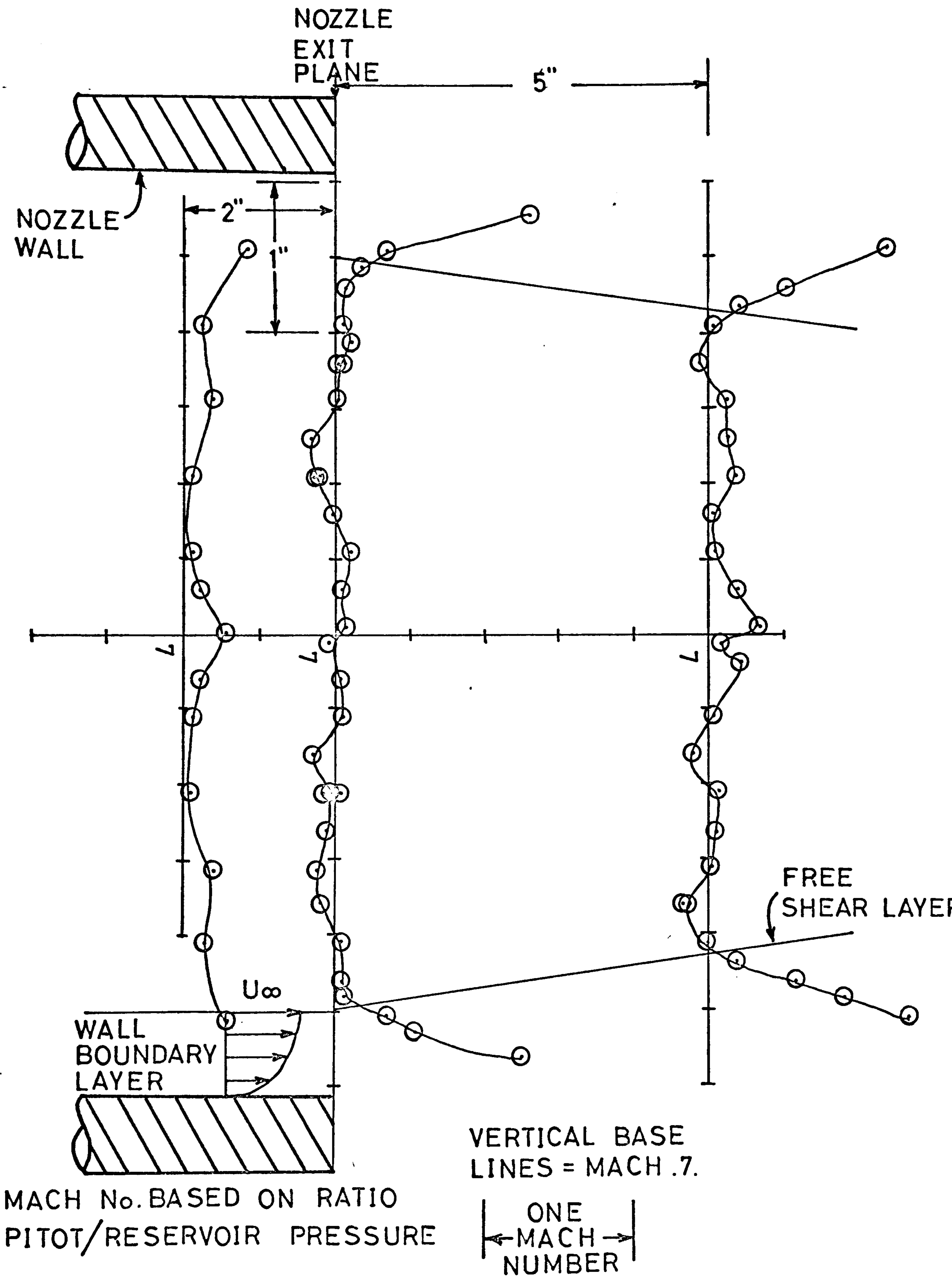

MACH.7. CONTOURED NOZZLE CALIBRATION

$Re/cm = 1.75\times10^{5}$, $T_t = 720\ ^{\circ}K$

FIG. 5.4

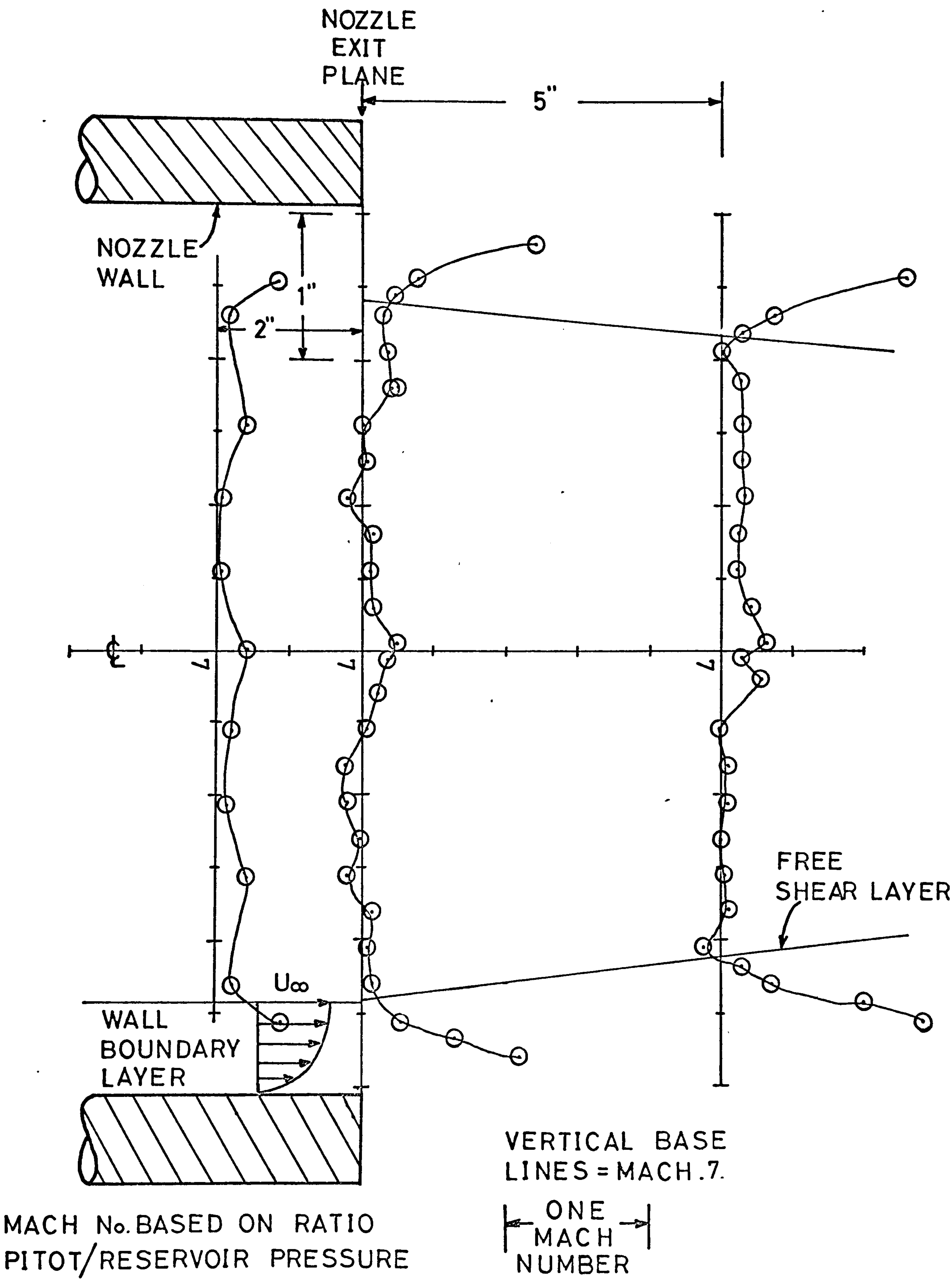

MACH.7. CONTOURED NOZZLE CALIBRATION

$Re/cm = 3.4 \times 10^5$, $T_t = 720°K$

The results of this test are plotted in Fig. 5.5 along with the vertical plane results for the same conditions.

5.2.2 Static Pressure Tests

Static pressure measurements were made in the working section to provide an alternative check on flow Mach Number. The static pressure was measured on a flat plate mounted on the nozzle centre line and on a static pressure ring extension on the end of the open jet nozzle. Both techniques were described in Section 3.4.3. The flat plate static port was 10.5 inches from the leading edge to avoid any leading edge effects. The measured static pressure was compared with the reservoir pressure for each test and the Mach number determined using the tables of Ref. 64 and the assumption of isentropic nozzle flow. The results are listed below in Table 7 for various unit Reynolds Numbers along with the pitot results of the previous section. Also included are estimates of the Mach Number from Batham (Ref. 57) in which simultaneous measurements of pitot pressure and static pressure were made to define the Mach Number using the Rayleigh pitot formula and thus making the assumption of isentropic flow unnecessary.

TABLE 7

Working Section Mach Number

$P_{41} = 20$, $T_t = 720^{\circ}K$

Re/cm	METHOD OF MEASUREMENT	M
1.75×10^5	PITOT/RESERVOIR	6.99
	F.P. STATIC/RESERVOIR	6.89
	STATIC RING/RESERVOIR	6.86
	F.P. STATIC/PITOT	6.74
3.4×10^5	PITOT/RESERVOIR	7.07
	F.P. STATIC/RESERVOIR	6.99
	STATIC RING/RESERVOIR	6.98
	F.P. STATIC/PITOT	7.00
5.64×10^5	PITOT/RESERVOIR	7.02
	F.P. STATIC/RESERVOIR	7.01
	F.P. STATIC/PITOT	6.96

FIG. 5.5

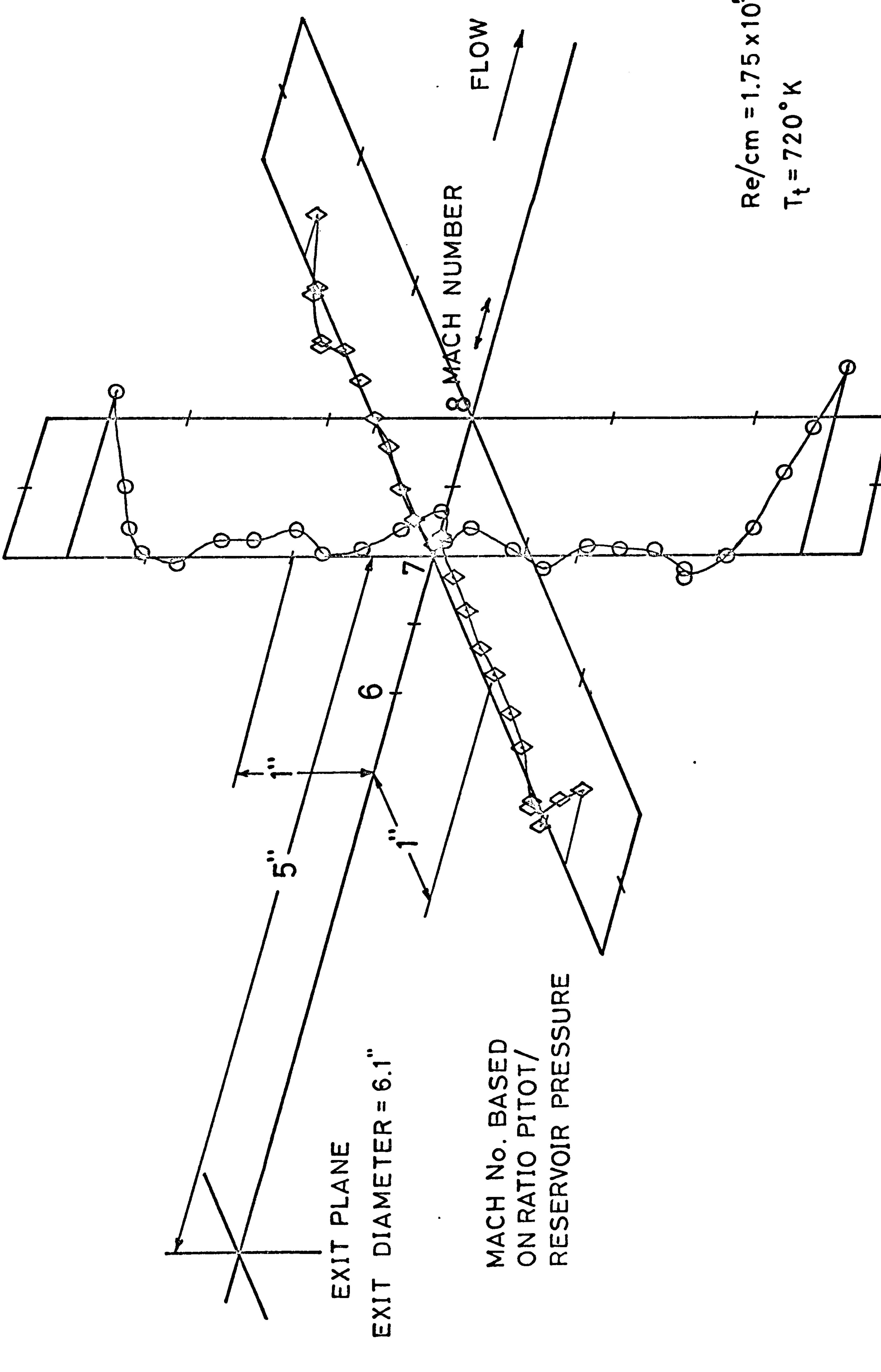

CONTOURED NOZZLE MACH NUMBER SYMMETRY TESTS

The various methods show fair agreement with the exception of the lowest unit Reynolds Number case where some deviation from isentropic flow may be indicated.

5.2.3 Other Tests

Crude estimates of flow Mach Number are possible from observations of shock wave positions in the flow. These estimates generally are not acceptable for any quantitative work but are nevertheless quite often useful as a first estimate.

A measurement of the shock detachment distance on a hemisphere model (shown in Ref. 25) provides a rough estimate of Mach = 6 using the data summarized in Ref. 66. The measurement of the Mach wave angle from the leading edge of a flat plate or hollow cylinder test in the Gun Tunnel (e.g. Fig. 9.3) also provides an estimate of flow Mach Number if it is assumed that the Mach wave is of vanishing strength. This method also gives a value of Mach Number of about 6. Slightly better accuracy is obtained if angle measurements are made on oblique attached shock waves. The shock wave angle on a 10° total angle cone was measured during a series of tests in the Gun Tunnel (see Chapter 10) and this gave a value of 6.5-7 for the Mach Number.

5.3 Total Temperature Measurements

One of the most important parameters to be measured in hypersonic flow facilities is the total temperature. This is especially difficult to measure in short duration, shock driven facilities because of the high temperatures involved and very short run times. In shock tunnels where this problem is most severe, the temperature is usually estimated from real gas shock wave analysis. The complex nature of the shock reflection process in gun tunnels makes such an analysis inadequate. Most gun tunnel research groups have undertaken experiments to estimate the total temperature. This is usually done either by indirect methods such as flow velocity measurements (Refs. 10, 19, 23, 67) and stagnation point heat transfer measurements (Ref. 13) or by direct measurements such as sodium line reversal (Ref. 68) and thermocouple probes (Ref. 69).

The methods used to estimate the stagnation temperature of the Oxford Gun Tunnel are described in this section. The methods involved direct measurements using a shielded thermocouple probe and a constant temperature, heated thin film probe. An indirect method based on a detailed analysis of the reservoir pressure record was included for comparison.

5.3.1 Thermocouple Probe

A rapid time response, shielded thermocouple stagnation temperature probe developed at the University of Southampton and described in Ref. 69 was made available by R.A. East for use on the Oxford Gun Tunnel. The theory of operation is described in Ref. 69 and details of the probe are shown in Fig. 5.6. The probe is operated in the nozzle free stream at several different known shield temperatures and the thermocouple output observed for each run. A null technique then establishes what value of shield temperature produces zero thermocouple output. This value is then assumed to be equal to the stagnation gas temperature inside the probe tip. The total temperature of the flow is then established by assuming that the recovery factor of the probe is nearly unity. The vent area was adjusted in the tests of Ref. 69 to make the assumption of unity recovery factor quite good.

Typical probe outputs are shown in Fig. 5.7 for two different flow conditions. The base lines represent the

UNIVERSITY OF SOUTHAMPTON TOTAL TEMPERATURE PROBE

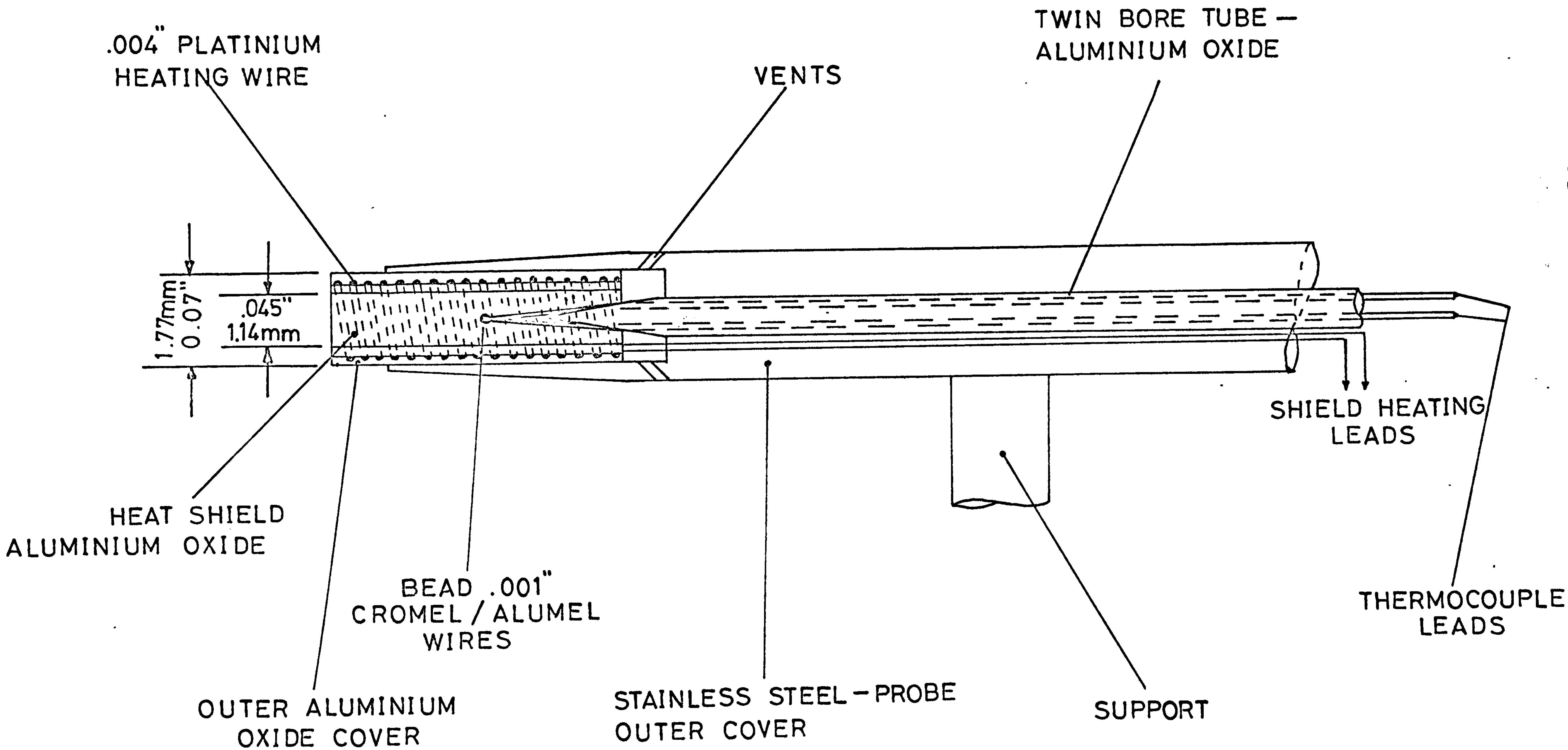

FIG. 5.6

FIG. 5.7

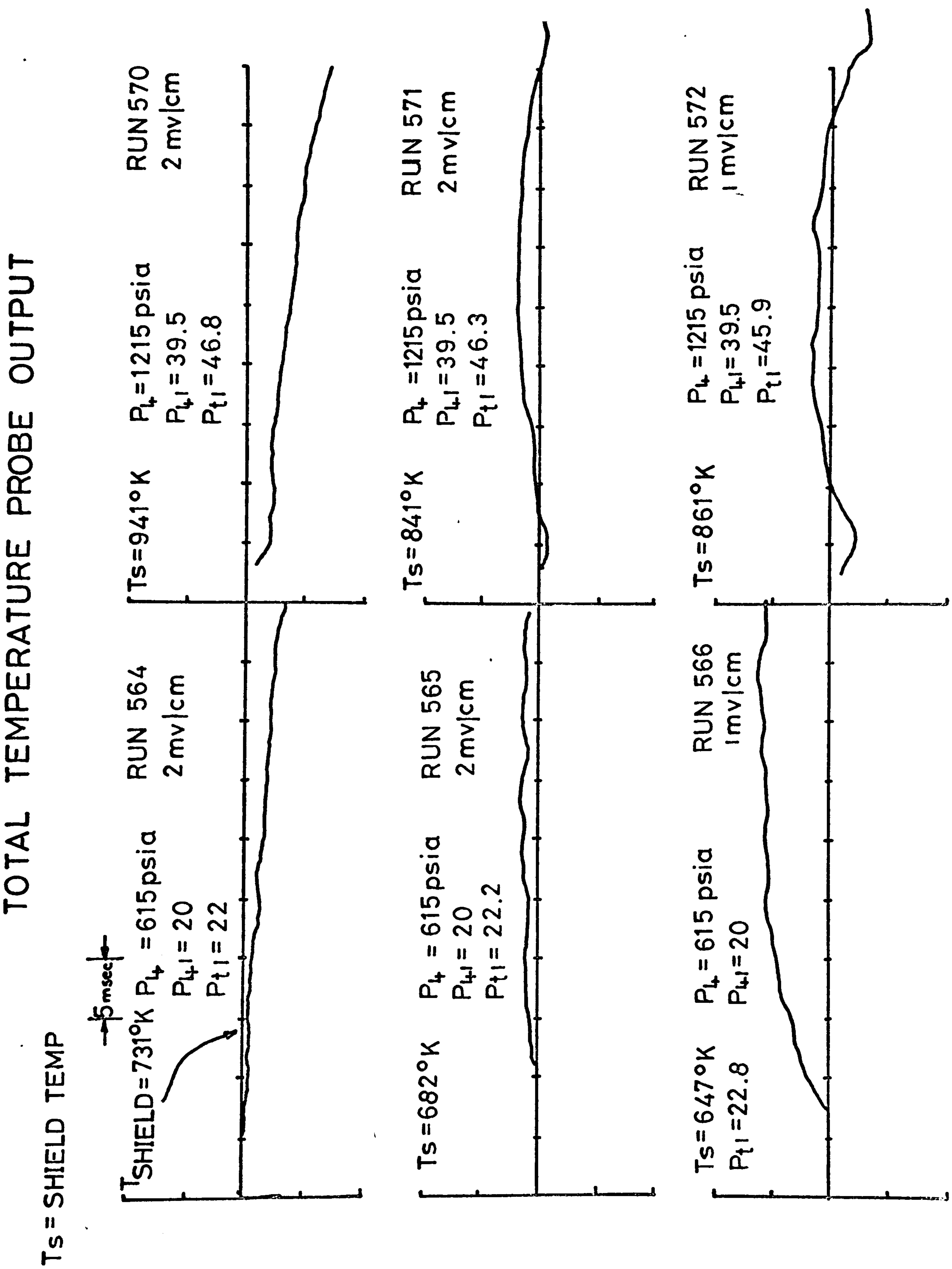

TOTAL TEMPERATURE PROBE OUTPUT
Ts = SHIELD TEMP
5 msec
T_SHIELD = 731°K
P4 = 615 psia
P41 = 20
Pt1 = 22
RUN 564
2 mv/cm
Ts = 941°K
P4 = 1215 psia
P41 = 39.5
Pt1 = 46.8
RUN 570
2 mv/cm
Ts = 682°K
P4 = 615 psia
P41 = 20
Pt1 = 22.2
RUN 565
2 mv/cm
Ts = 841°K
P4 = 1215 psia
P41 = 39.5
Pt1 = 46.3
RUN 571
2 mv/cm
Ts = 647°K
Pt1 = 22.8
P4 = 615 psia
P41 = 20
RUN 566
1 mv/cm
Ts = 861°K
P4 = 1215 psia
P41 = 39.5
Pt1 = 45.9
RUN 572
1 mv/cm

equilibrium probe output corresponding to the shield temperatures set before the run and monitored on a DVM with a typewriter printout. Thermocouple indicated temperatures during the run determined from a standard chromel/alumel calibration curve are compared with the preset shield temperature for two typical cases as a function of time in Figs. 5.8 and 5.9. The null points where the thermocouple temperature during the run equals the shield temperature are determined by linear interpolation for various times. The resulting Gun Tunnel total temperature time histories for three pressure ratios are shown in Fig. 5.10. The probe performance does not appear to be affected by changes in free stream unit Reynolds Number. The increased rate of cooling of the reservoir temperature with increasing total temperature is also apparent. The calibrated results of Gun Tunnel total temperature versus total pressure ratio P_{t1} are plotted in Fig. 5.11.

5.3.2 Hot Film Probe

A second method of direct total temperature measurement was employed to compare with the thermocouple probe. This involved the use of a thin film gauge mounted in the stagnation point of the hemisphere model shown in Fig. 3.2a. The thin film is set and maintained at an elevated temperature (resistance) by a DISA Type 55D01 Constant Temperature Anemometer Unit with high gain feedback circuitry. When the bridge voltage required to maintain the film temperature has stabilized, the probe is run in the tunnel and the feedback amplifier output signal required to maintain bridge balance is monitored. This feedback signal is proportional to the instantaneous heat transfer rate to or from the thin film during the run. The heat transfer rate is in turn proportional to the temperature differ-

FIG. 5.8

TOTAL TEMPERATURE PROBE OUTPUT

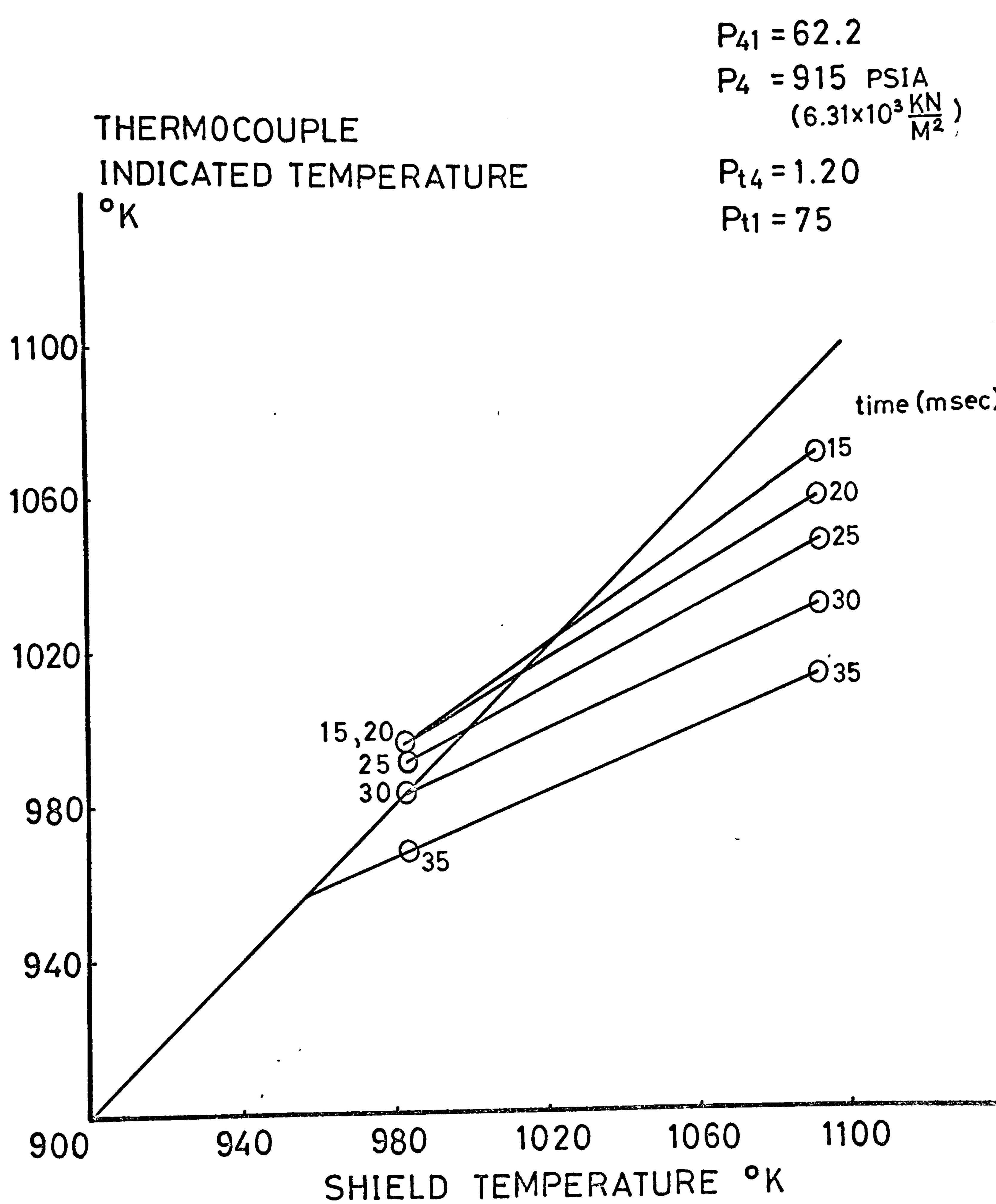

FIG. 5.9

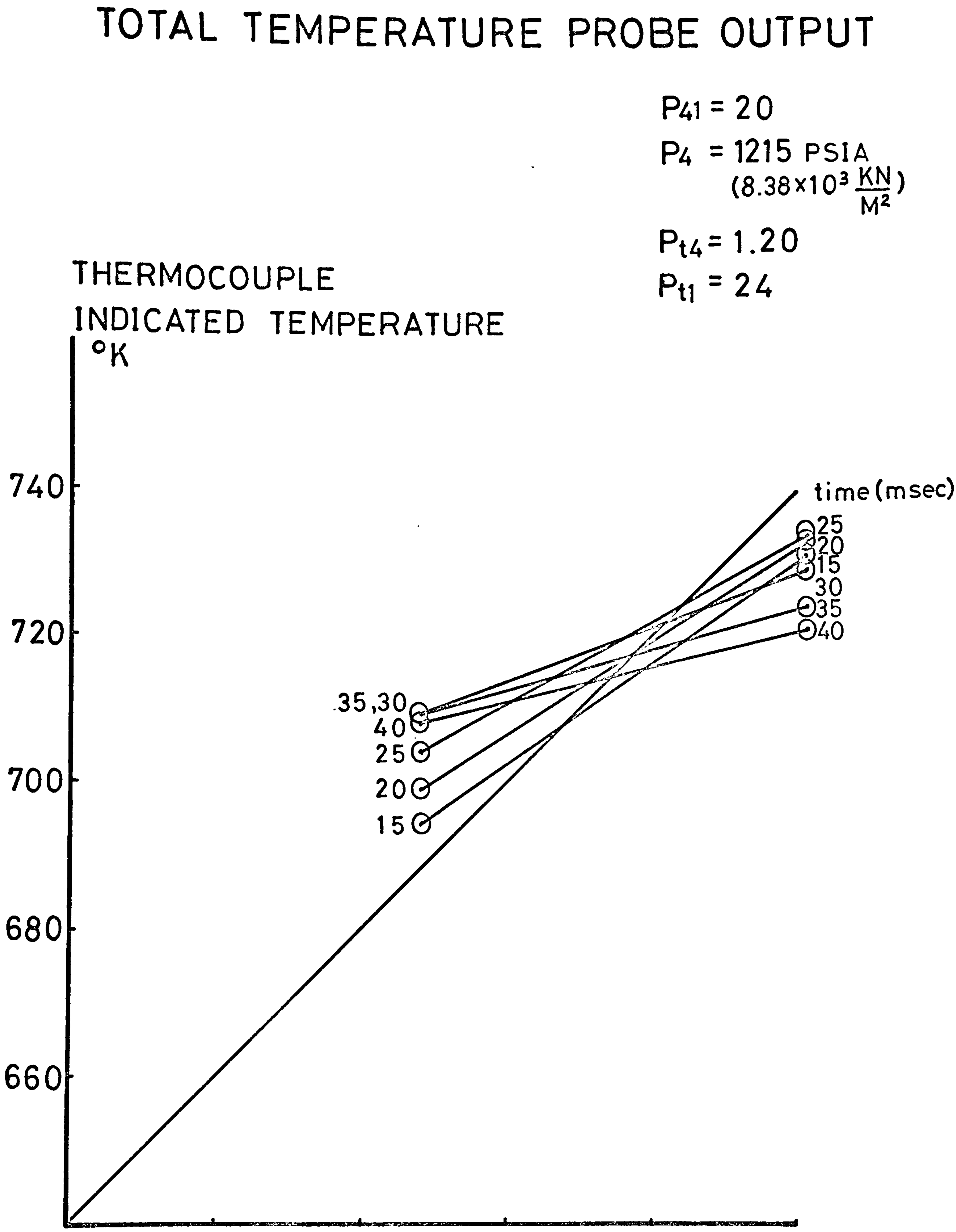
TOTAL TEMPERATURE PROBE OUTPUT
P41 = 20
P4 = 1215 PSIA
(8.38×10³ KN/M²)
Pt4 = 1.20
Pt1 = 24
THERMOCOUPLE
INDICATED TEMPERATURE
°K
740
720
700
680
660
640
660
680
700
720
740
SHIELD TEMPERATURE °K
time (msec)
25
20
15
30
35
40
35,30
40
25
20
15

FIG. 5.10

GUN TUNNEL TEMPERATURE HISTORY

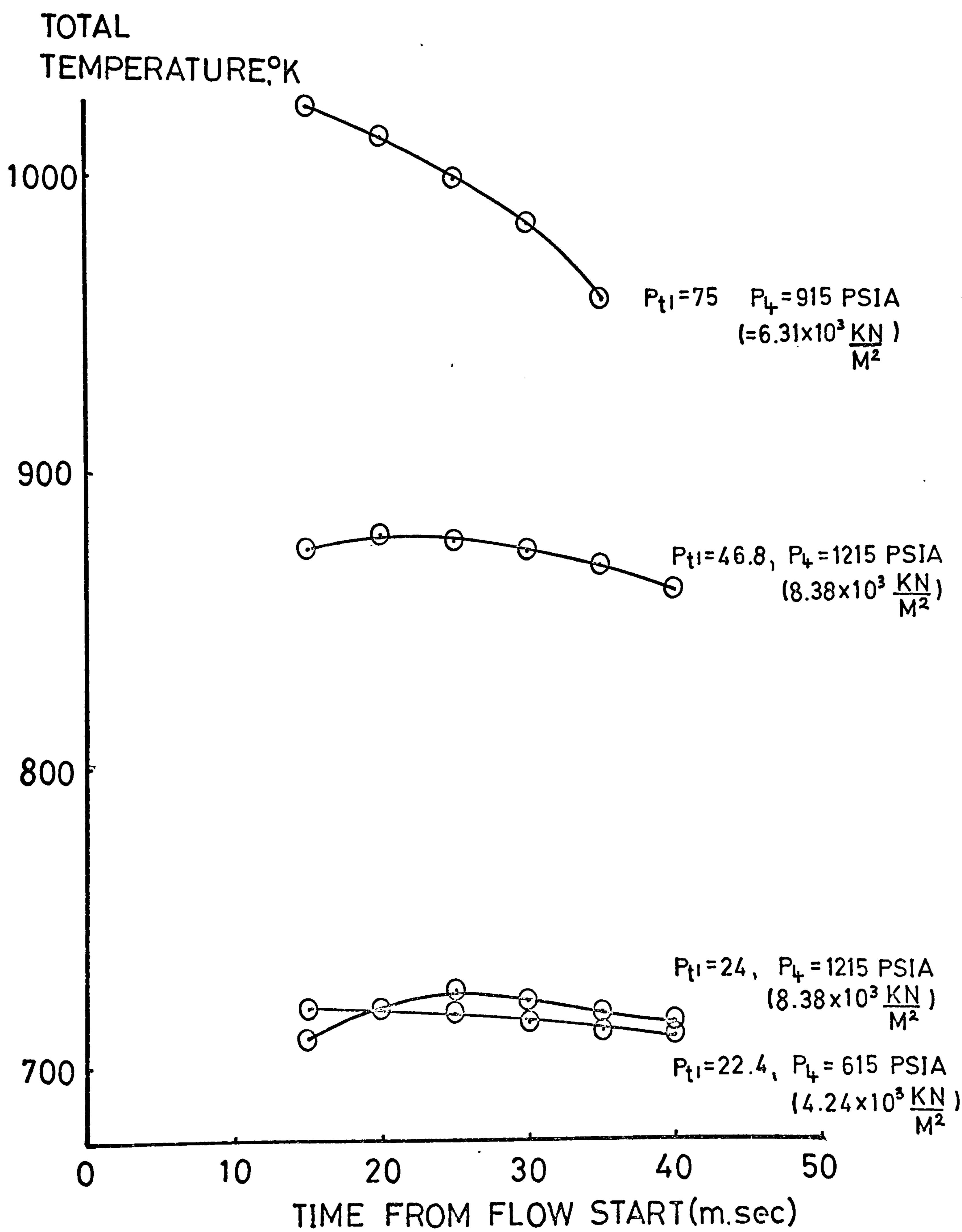

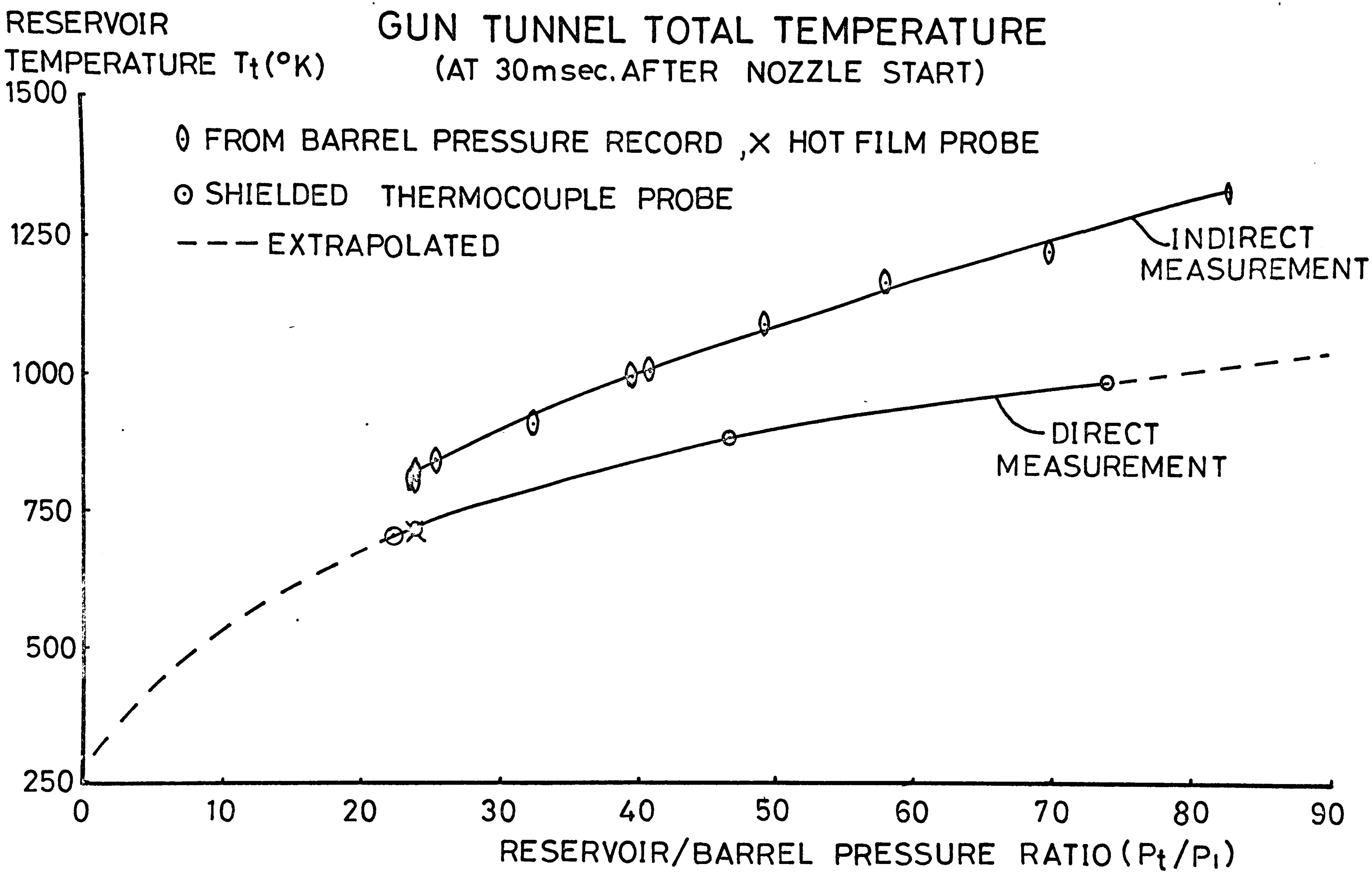
GUN TUNNEL TOTAL TEMPERATURE
(AT 30msec. AFTER NOZZLE START)
RESERVOIR
TEMPERATURE Tt (°K)
FROM BARREL PRESSURE RECORD , X HOT FILM PROBE
SHIELDED THERMOCOUPLE PROBE
- - - EXTRAPOLATED
INDIRECT MEASUREMENT
DIRECT MEASUREMENT
1500
1250
1000
750
500
250
0
10
20
30
40
50
60
70
80
90
RESERVOIR/BARREL PRESSURE RATIO (Pt/P1)

FIG.5.11

ence between the thin film and the stagnation temperature of the gas.

Anemometer output voltages for three settings of thin film resistance (plotted as the ratio of thin film hot resistance to its room temperature resistance, R_G/R_o) and a single Gun Tunnel operating condition are shown in Fig. 5.12. The output signal is taken at two times, one immediately following the first reflected shock wave and the other at 30 msec. after the beginning of the run. Fig. 5.12 also includes a typical anemometer output signal during a run to clarify where the measurements were taken. A linear interpolation was then used to define the film resistance at the null point where the film temperature equalled the stagnation temperature.

The main uncertainty in this method involves relating the thin film resistance to its temperature at the high temperature levels encountered. The resistance-temperature calibration at low temperatures can be determined in a conventional oil bath experiment. The calibration of the gauge used in these tests is shown in Fig. 5.13 up to 50°C. The slope is linear and equal to .0615 $\Omega/^\circ C$. Tests on other gauges in a silicon oil bath showed linearity continuing to 200°C. Even this is not adequate, however, for the 400°C level of these tests. To extend the calibration to these levels, advantage was taken of the reliability of predicting reflected shock temperatures from measured shock strengths and ideal shock wave relations. The determination of the resistance-temperature slope is summarized below.

$$P_{51} = 11.6 \quad \text{is measured}$$

$$\therefore \; T_5 = 653^\circ K \text{ from Fig. 4.2 and } T_o = 290^\circ K.$$

FIG. 5.12

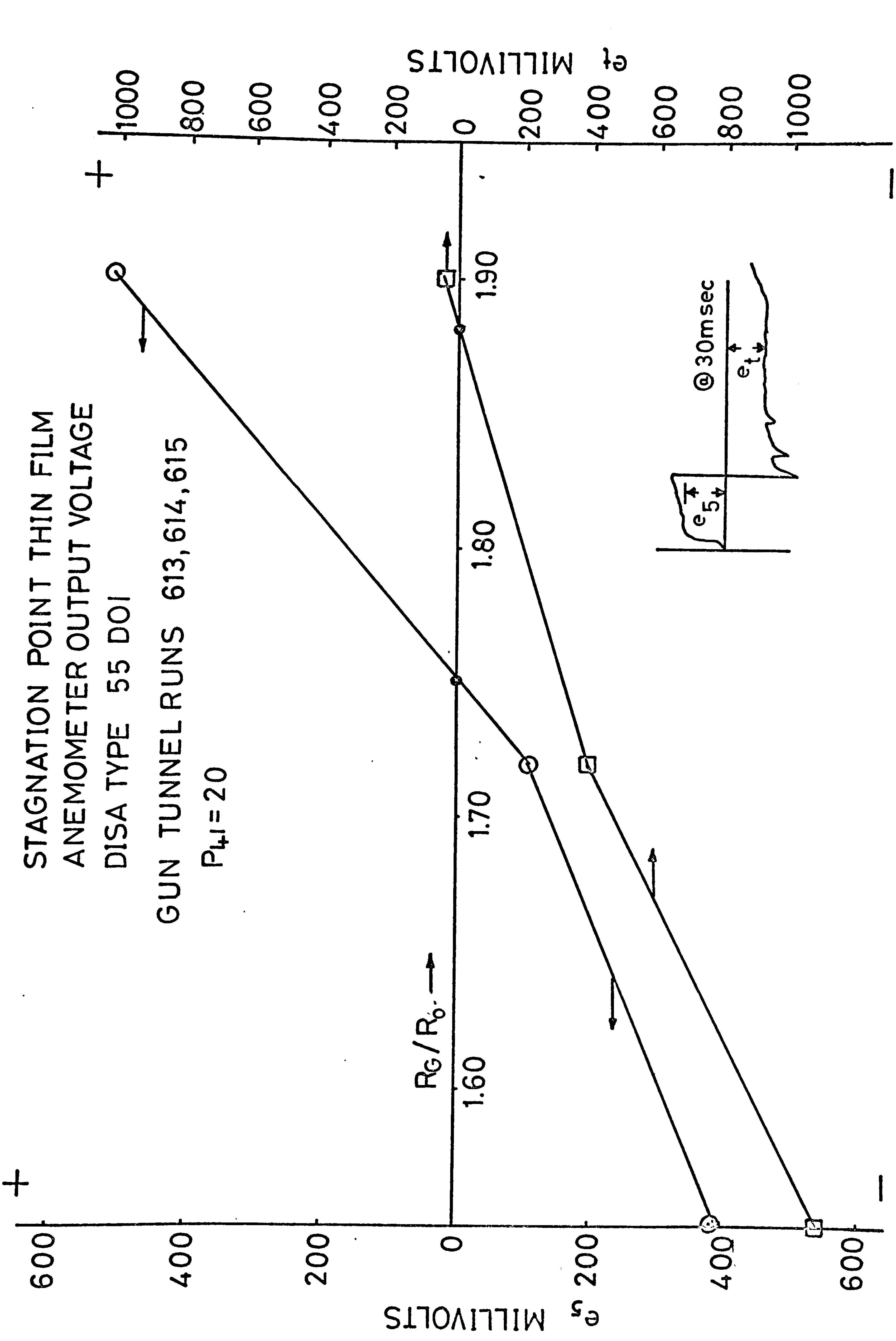

STAGNATION POINT THIN FILM
ANEMOMETER OUTPUT VOLTAGE
DISA TYPE 55 D01
GUN TUNNEL RUNS 613, 614, 615
$P_{41} = 20$
e_t MILLIVOLTS
e_5 MILLIVOLTS
R_G/R_o →
1.60
1.70
1.80
1.90
1000
800
600
400
200
0
@ 30msec
e_t
e_5
+
−

$$\underline{\Delta T} = T_5 - T_o = 653 - 290 = \underline{363^oK}$$

$$\frac{R_G}{R_o} = 1.75 \text{ at } e_5 \text{ null point}$$

$$\therefore R_G = 54.2\ \Omega \text{ since } R_o \cong 31\ \Omega \text{ from Fig. 5.13}$$

$$\underline{\Delta R} = R_G - R_o = \underline{23.2}\ \Omega$$

$$\underline{\text{SLOPE}} = \frac{\Delta R}{\Delta T} = \frac{23.2}{363} = \underline{.0639\ \Omega/^oC}$$

STAGNATION POINT
THIN FILM CALIBRATION
GAUGE. 1.
FIG. 5.13

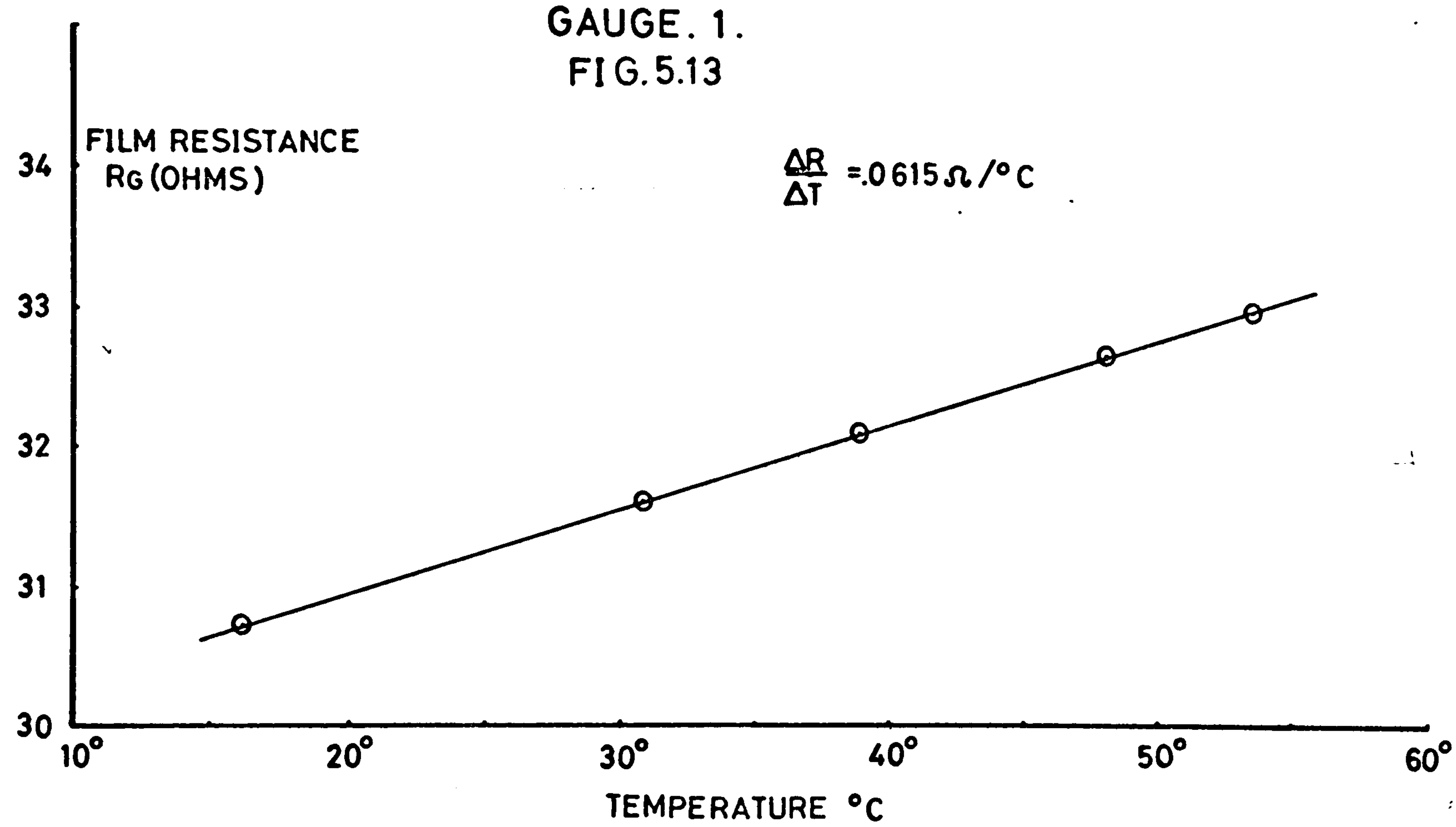

This slope is seen to agree quite well with the slope determined from the low temperature test in Fig. 5.13. The assumption of linearity holding to the total temperature levels is now more reasonable. The estimated total temperature using $R_G/R_o = 1.88$ from the e_t null point and using the high temperature mean slope is found to be 717^oK at the 30 msec. point. This is seen to agree quite well with the thermocouple determined total temperature in Fig. 5.11.

The calibration should ideally be extended to above the value of temperature it is desired to measure. Extending the temperature range of this type of probe would involve some additional precautions that the gauge, substrate, and gauge electrical connections will not be degraded by the high temperatures.

5.3.3 Pressure Record Analysis

It was mentioned in the introduction to Section 5.3 that the prediction of total temperature behind the first reflected shock wave from shock wave theory was fairly reliable. Shock wave theory was more difficult to apply to gun tunnel operation because of the added complication caused by the presence of the piston and the resulting multiple shock reflections. East (Ref. 7) has suggested an approach to this problem based on a detailed analysis of an actual reservoir pressure trace of a gun tunnel using both shock wave theory and isentropic gas relations. The actual pressure level is measured immediately before and after the passage of each successive shock wave and the temperature calculated from the appropriate flow relation. The relation between the temperature ratio and pressure ratio across a shock wave is given by

$$\frac{T_{n+1}}{T_n} = \frac{P_{n+1}}{P_n}\left\{\frac{\mu^2(P_{n+1}/P_n) + 1}{(P_{n+1}/P_n + \mu^2}\right\} \tag{5.3.1}$$

where $\mu^2 = (\gamma-1)/(\gamma+1)$. The adiabatic, isentropic relation is given simply by

$$\frac{T_{n+1}}{T_n} = \left(\frac{P_{n+1}}{P_n}\right)^{\frac{\gamma-1}{\gamma}} \quad . \tag{5.3.2}$$

A typical reservoir pressure record from the Gun Tunnel has been analysed using the approach outlined above. A sketch of the pressure trace along with the measured and calculated results is shown in Fig. 5.14 for $\gamma = 1.4$. Each shock reflection from the piston is followed by an isentropic

FIG. 5.14.

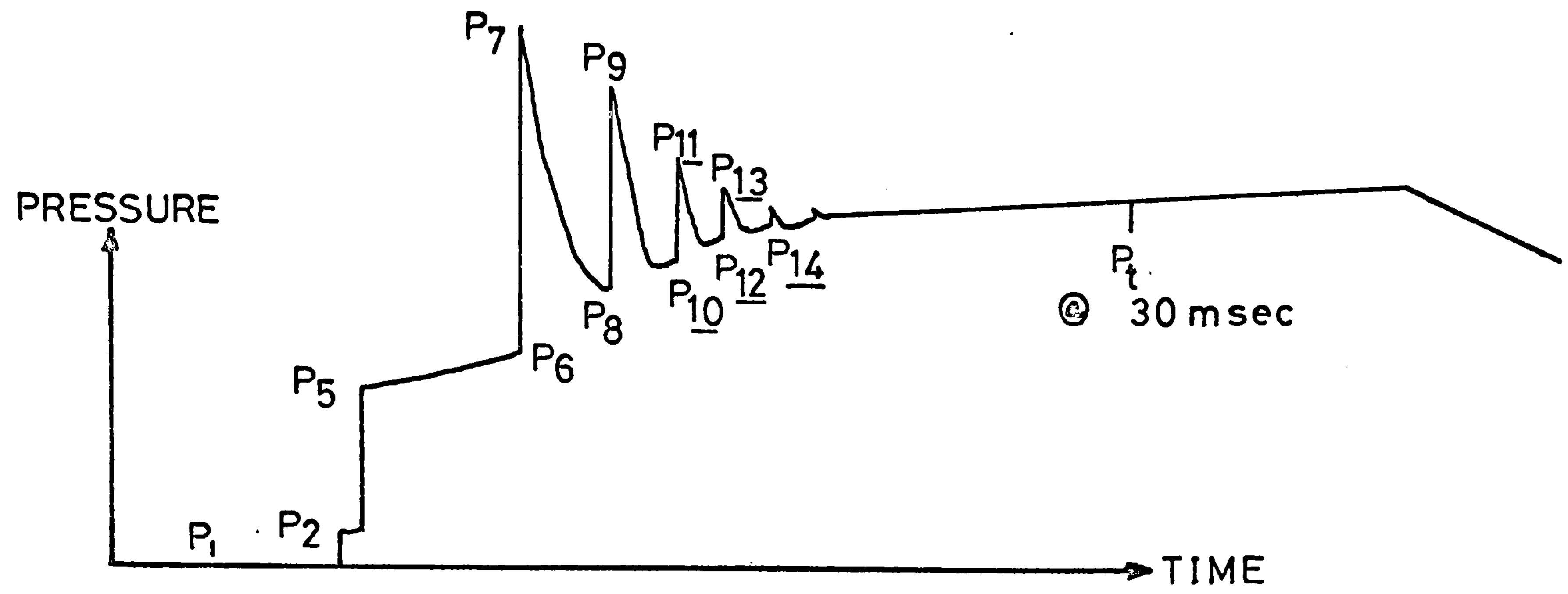

RUN No. 70 , P_4 = 1565 psia , γ=1.4

n	1	2	5	6	7	8	9	10	11	12	13	14	t
P_n psia	45	207	672	838	2425	1255	2060	1345	1770	1453	1685	1465	1640
T_n °K	296	506	758	809	1135	939	1090	966	1042	986	1030	988	1020

DETAILED PRESSURE TRACE

expansion. P_5 appears to be followed by a weak isentropic compression to P_6. After the expansion to P_{14}, the remainder of the compression to the final reservoir pressure is treated as isentropic. The final temperature (1020°K) at 't' can be compared with that calculated assuming an isentropic compression from the first reflected shock level P_5,

$$T_t = T_5 . \left(\frac{P_t}{P_5}\right)^{\frac{\gamma-1}{\gamma}} = 758\left(\frac{1640}{672}\right)^{.286} = 980^{\circ}\text{K}.$$

The difference is not too great implying that most of the entropy change is across the first two shock waves. That this is indeed the case can be verified from the expression relatingentropy change across shock waves to the shock pressure ratio from Ref. 32. This is given in non-dimensional form as

$$\frac{S_{n+1} - S_n}{R} = \frac{1}{\gamma-1} (\log)_e \left\{\pi \left[\frac{\mu^2\pi + 1}{\pi + \mu^2}\right]^{\gamma}\right\} \qquad (5.3.3)$$

where R is the gas constant and $\pi = P_{n+1}/P_n$. The non-dimensional entropy rise for the first four shock transitions are given below in Table 8.

TABLE 8

Shock Wave Entropy Rise

SHOCK	1 → 2	2 → 5	6 → 7	8 → 9
$S/_R$	.338	.152	.115	.0185

A comparison of the directly measured total temperatures with that predicted from the semi-empirical method outlined above was made using the simplification that the final temperature was reached via an isentropic compression from the first reflected shock region. This was made for a range of total pressure ratios using the actual measured shock strength to determine T_5. The calculated total temperature is plotted on Fig. 5.11. It appears to be some 10-15% higher than the directly measured values. This is reasonable, however, since the calculation method assumes adiabatic conditions which could not strictly be true for the high gas temperature and cold wall conditions of the test.

The directly measured value of total temperature has been used as the true Gun Tunnel temperature calibration in the calculation of the working section flow conditions. The temperature calibration of this Gun Tunnel is compared with the actual calibration of two gun tunnels of geometrically similar barrel dimensions in Fig. 5.15.

5.4 Condensation Tests

The operation of hypersonic aerodynamic facilities requires efforts to insure that the total temperature is adequately high to prevent liquefaction of the expanded working gas. In general, in shock heated facilities, this minimum temperature is easily exceeded. In some situations, however, it is desired to operate the facility at the minimum possible temperature; for example, when high Reynolds Numbers are sought. When operating at low temperatures, it is of interest to determine the actual point of onset of condensation for the Mach Number and total pressure at which the tests will be run.

Bowman (Ref. 70) has conducted a series of tests to determine the onset of condensation of nitrogen in the R.A.R.D.E. gun tunnel. Working section pitot pressure and static pressure were monitored as the total temperature was reduced. Bowman concluded that static pressure gave a more positive indication of the condensation point. In the tests of Ref. 70, it was

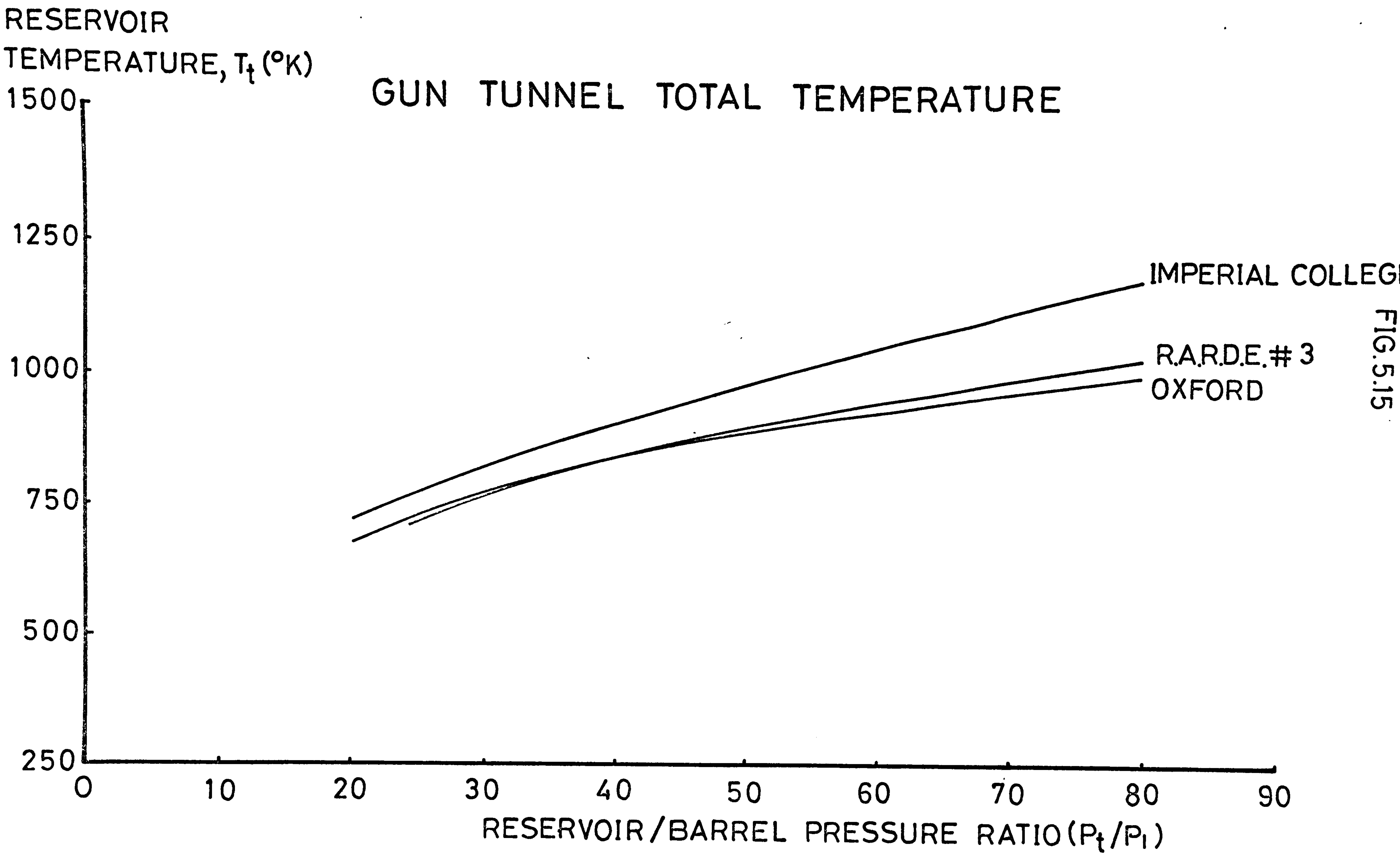
RESERVOIR
TEMPERATURE, T_t (°K)
GUN TUNNEL TOTAL TEMPERATURE
1500
1250
1000
750
500
250
0
10
20
30
40
50
60
70
80
90
IMPERIAL COLLEGE
R.A.R.D.E. # 3
OXFORD
RESERVOIR/BARREL PRESSURE RATIO (P_t/P_1)

FIG. 5.15

observed that a useful degree of supersaturation was possible at static pressures below about 10 mm of Hg.

A flat plate with a static pressure port was set up in the working section of the Oxford Gun Tunnel. The tests were run in the Mach 7 contoured nozzle at a fixed driver pressure. The barrel pressure was gradually increased for each run thus reducing the total temperature as determined from an extrapolation of the total temperature calibration curve of Fig. 5.11. The results are shown in Fig. 5.16. As in Ref. 70, the first indication of a rising static pressure is interpreted as the onset of condensation. Since in these tests air was the working gas, this was probably the effects of the oxygen condensing. This condensation point is compared with the equilibrium condensation curves for air from Ref. 71 and the results of the R.A.R.D.E. test at similar flow conditions in Fig. 5.17. It appears that an appreciable degree of supersaturation is possible in these conditions. The degree of supersaturation possible is probably dependent on the freedom of the gas from impurities such as water vapour, CO_2 and dust which can act as nucleation sites for condensation. Bowman (Ref. 70) also found the degree of supersaturation to be dependent on the static pressure level.

FIG.5.16

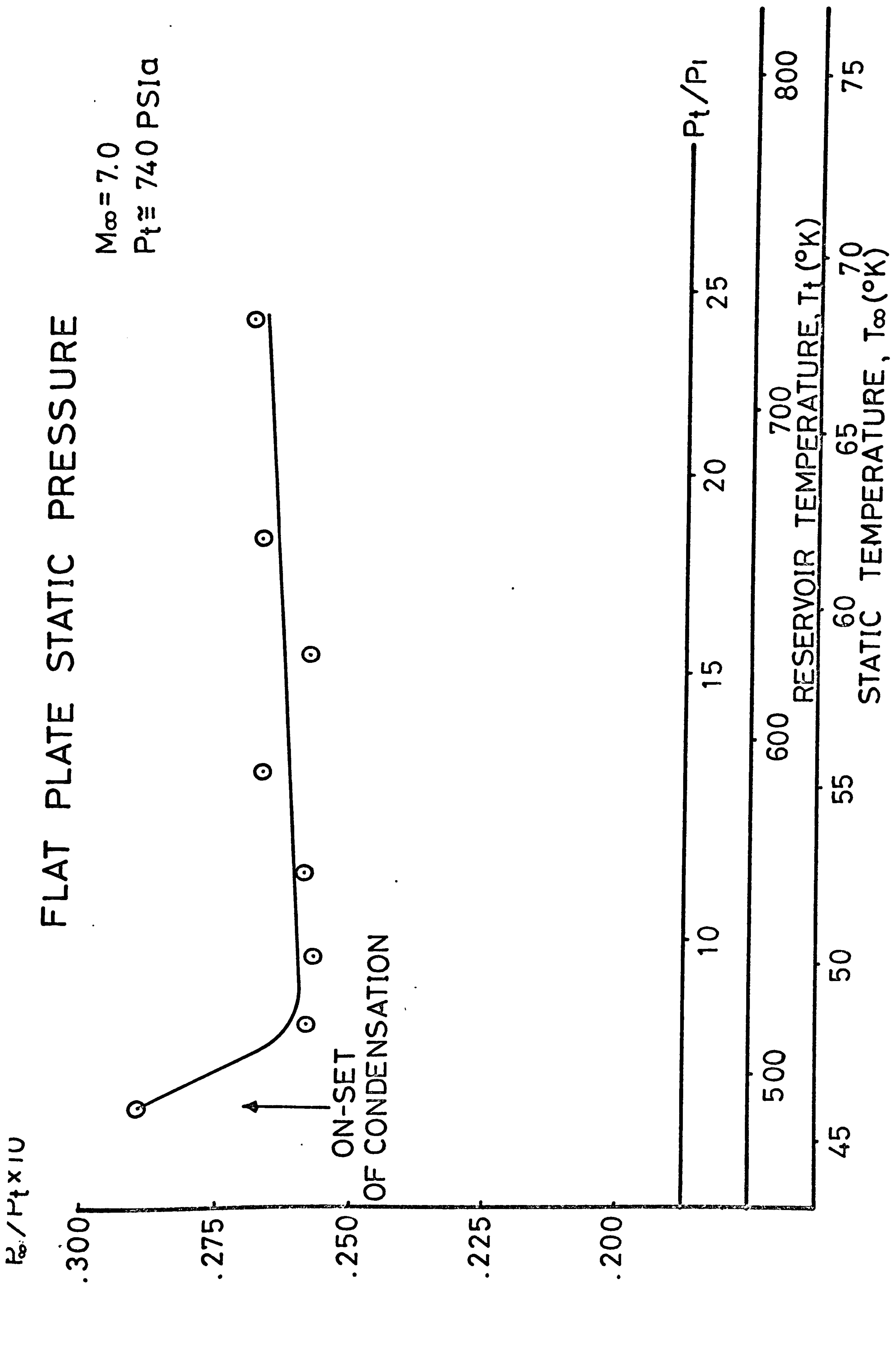

FLAT PLATE STATIC PRESSURE
M∞ = 7.0
Pt ≅ 740 PSIa
ON-SET OF CONDENSATION
P∞/Pt x 10
.300
.275
.250
.225
.200
Pt/P1
10
15
20
25
RESERVOIR TEMPERATURE, Tt (°K)
500
600
700
800
STATIC TEMPERATURE, T∞ (°K)
45
50
55
60
65
70
75

FIG. 5.17

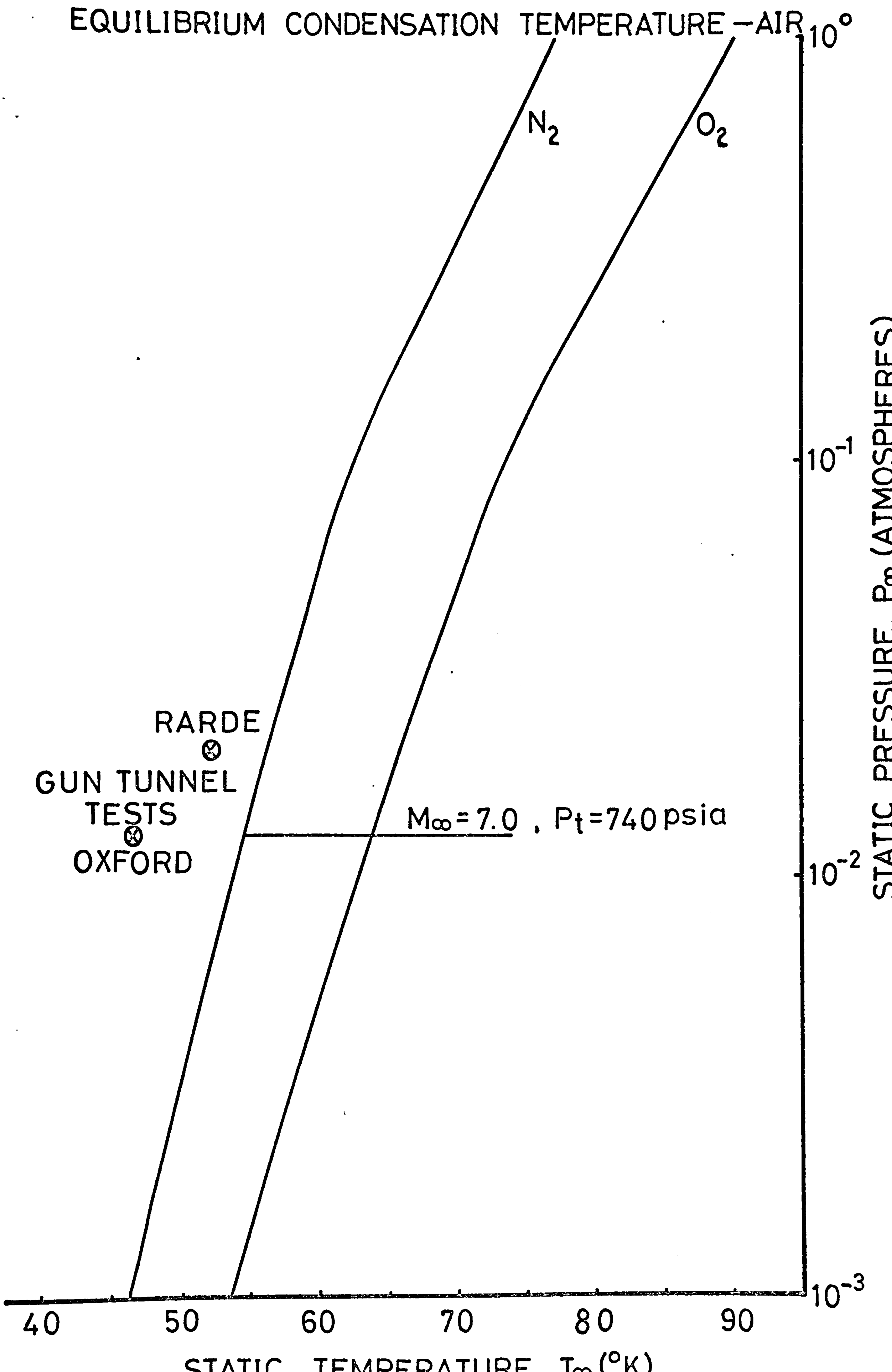
EQUILIBRIUM CONDENSATION TEMPERATURE – AIR
N2
O2
RARDE
GUN TUNNEL
TESTS
OXFORD
M∞ = 7.0 , Pt = 740 psia
10°
10⁻¹
10⁻²
10⁻³
STATIC PRESSURE, P∞ (ATMOSPHERES)
40
50
60
70
80
90
STATIC TEMPERATURE, T∞ (°K)

CHAPTER SIX

GUN TUNNEL SIMULATION CAPABILITIES

The complete wind tunnel duplication of a wide range of hypersonic vehicle flight conditions rapidly becomes prohibitive as the Mach Number increases and the flight altitude decreases. In the usual hypersonic aerodynamic facility test, only one or two of the important dimensionless parameters are duplicated. Thus a flight Reynolds Number can sometimes be duplicated by high density levels on scale models. Similarly, hypersonic Mach Numbers can be obtained by expanding the flow to very low static temperature levels. A very detailed discussion of the techniques of simulation and partial duplication of ambient conditions in hypersonic flight is included in a report by Hertzberg, et. al. (Ref. 72).

The somewhat limited total temperature range of the Gun Tunnel compared with shock tunnels limits the range of hypervelocities which can be duplicated (see Fig. 6.1). In some research situations, however, the flow Mach Number is the important parameter to duplicate. Changing the area ratio of the nozzle can produce a wide range of Mach Numbers although for a given total temperature this produces little increase in flow velocity. The upper Mach Number limit for a total temperature limit of 2000°K would be about 16 to exclude the possibility of flow condensation. Boundary layer studies require a duplication of flight Reynolds Numbers and these can be produced if the flow Mach Number and total temperature are kept moderately low. The unit Reynolds Number duplication capability of the Gun Tunnel has been calculated using a simplified expression for unit Reynolds Number given in terms of flow Mach Number, static temperature and static pressure.

FIG. 6.1

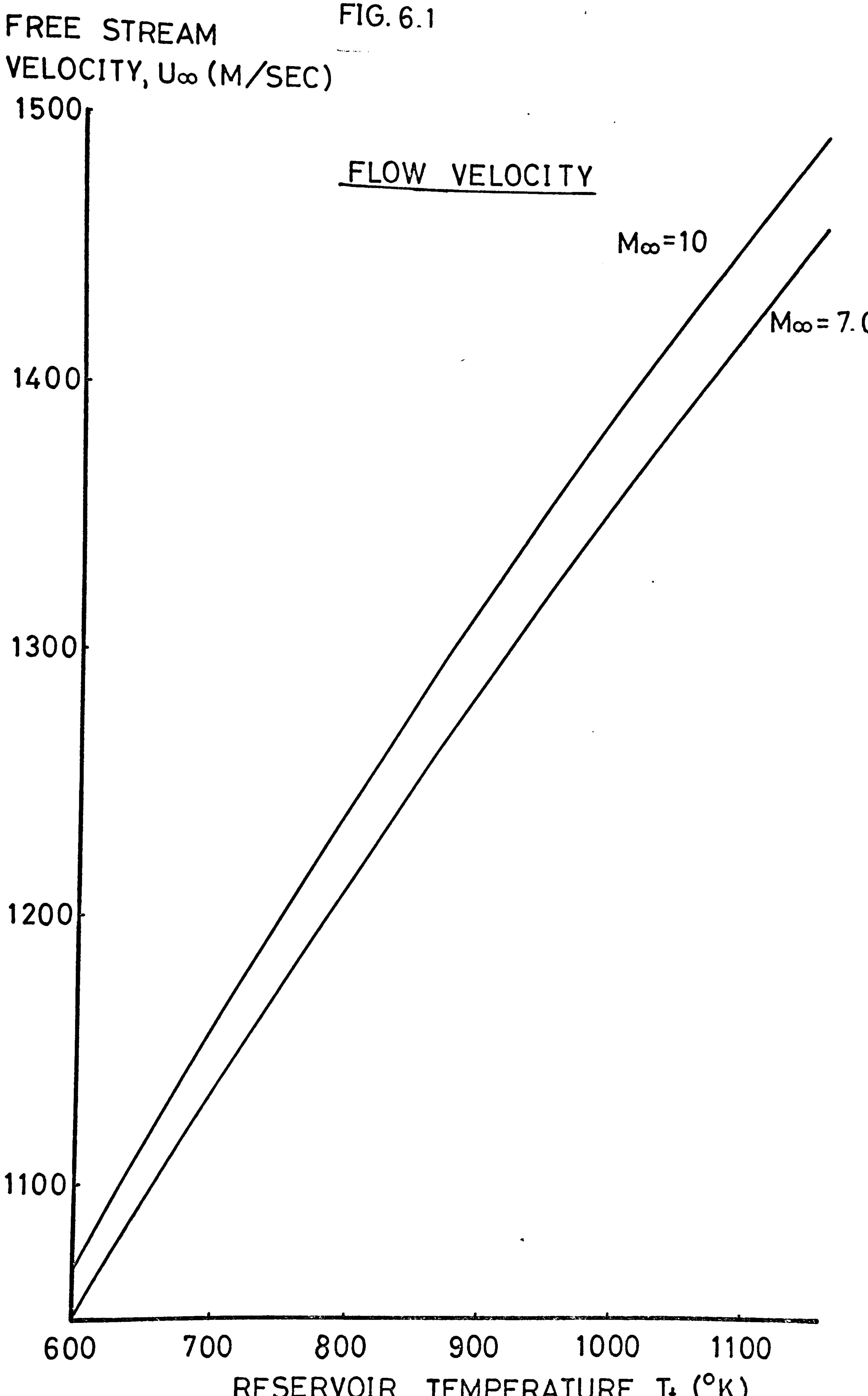

FREE STREAM
VELOCITY, U∞ (M/SEC)
1500
1400
1300
1200
1100
FLOW VELOCITY
M∞=10
M∞= 7.0
600
700
800
900
1000
1100
RESERVOIR TEMPERATURE, Tt (°K)

This expression assumes a Sutherland viscosity-temperature relation (Fig. 6.2) and an invariant gas constant (R) for air in the temperature range of interest. A value of 1.35 for γ is assumed as the value near the mean temperature of interest. The expression is given as

$$Re/cm = 4.78 \times 10^7 \ \frac{M_\infty \, (T_\infty + 110) P_\infty}{T_\infty^2} \tag{6.1}$$

where the static pressure P_∞ is in atmospheres. The unit Reynolds Number for the Mach 7 nozzle is given for a range of total temperatures over the total pressure range of the Gun Tunnel in Fig. 6.3. The maximum unit Reynolds Number capability of the Gun Tunnel is given in Fig. 6.4 for three Mach Numbers and a range of total temperatures. These values are bounded at the low temperature end by condensation limits and at the high temperature end by Gun Tunnel limitations.

The free flight unit Reynolds Number range versus flight Mach Number and geometric altitude was calculated using the standard atmosphere data of Ref. 73 and is plotted in Fig. 6.5. Using this data and the information on Figs. 6.3 and 6.4 it is possible to plot a map of the Gun Tunnel free flight Reynolds Number simulation regime (Fig. 6.6). This has been done assuming an arbitrary vehicle size of 10 meters and a test model size of 30 cm limited by the working section dimensions. The upper limit of altitude has been arbitrarily terminated at about 60 kilometers but could be extended by using lower driver pressures and static temperatures above the condensation limit.

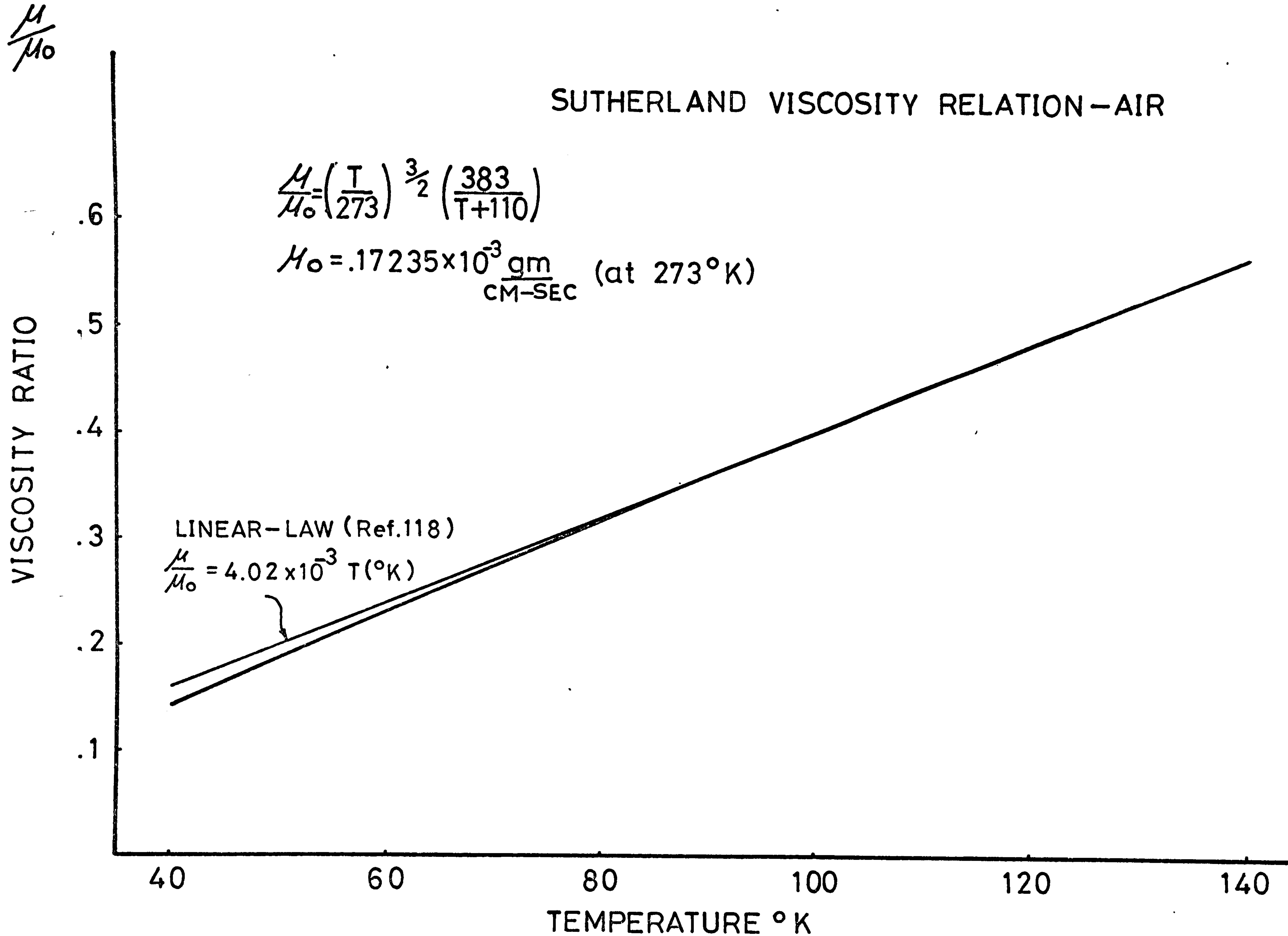
SUTHERLAND VISCOSITY RELATION-AIR
$\frac{\mu}{\mu_o}=\left(\frac{T}{273}\right)^{3/2}\left(\frac{383}{T+110}\right)$
$\mu_o=.17235\times10^{-3}\frac{gm}{CM-SEC}$ (at 273°K)
LINEAR-LAW (Ref.118)
$\frac{\mu}{\mu_o}=4.02\times10^{-3}\,T(°K)$
$\frac{\mu}{\mu_o}$
VISCOSITY RATIO
.6
.5
.4
.3
.2
.1
40
60
80
100
120
140
TEMPERATURE °K

FIG.6.2

FIG. 6.3

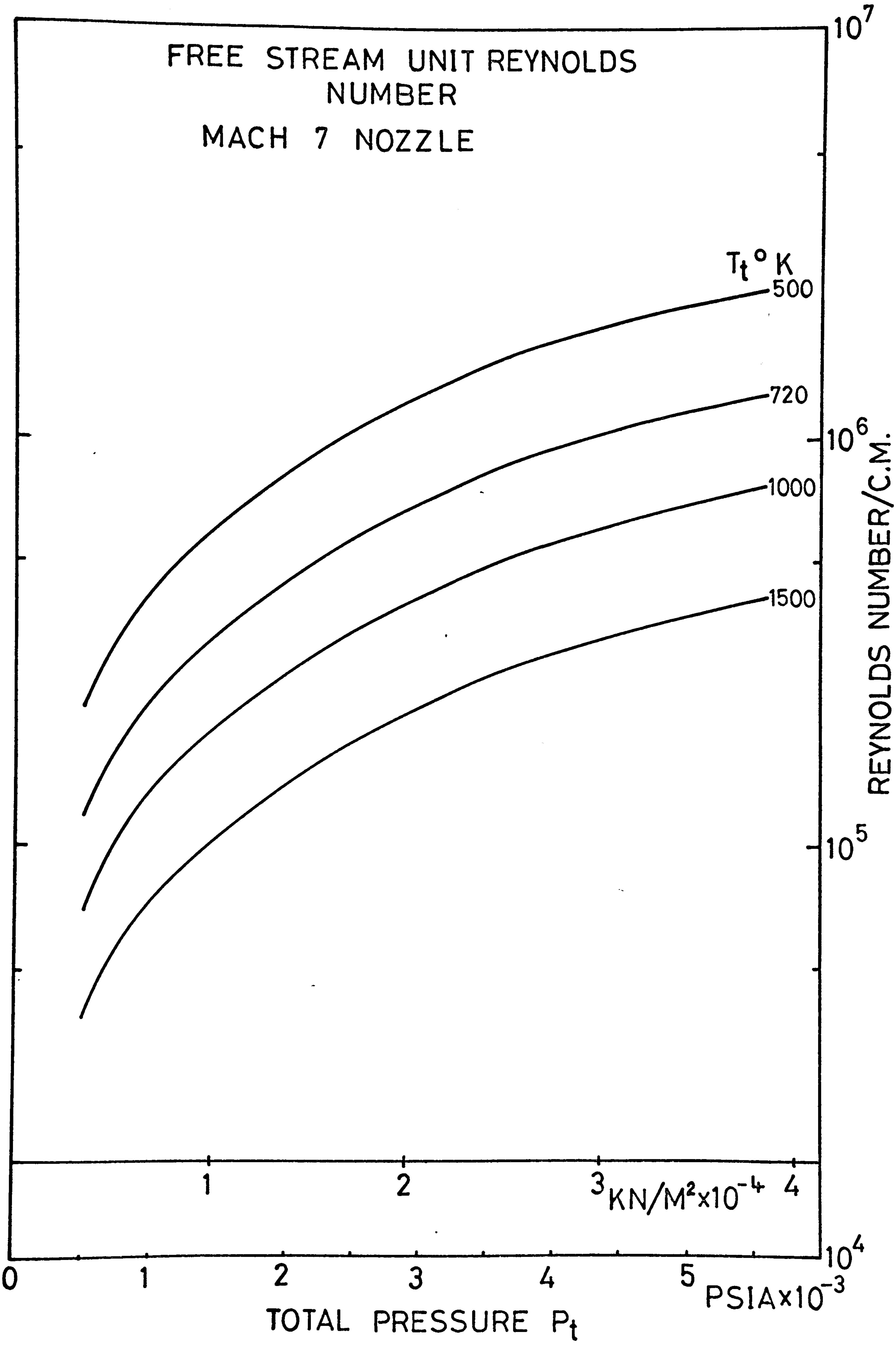
FREE STREAM UNIT REYNOLDS NUMBER
MACH 7 NOZZLE
Tt ° K
500
720
1000
1500
REYNOLDS NUMBER/C.M.
10^7
10^6
10^5
10^4
1
2
3 KN/M²x10^-4
4
0
1
2
3
4
5 PSIAx10^-3
TOTAL PRESSURE Pt

FIG. 6.4

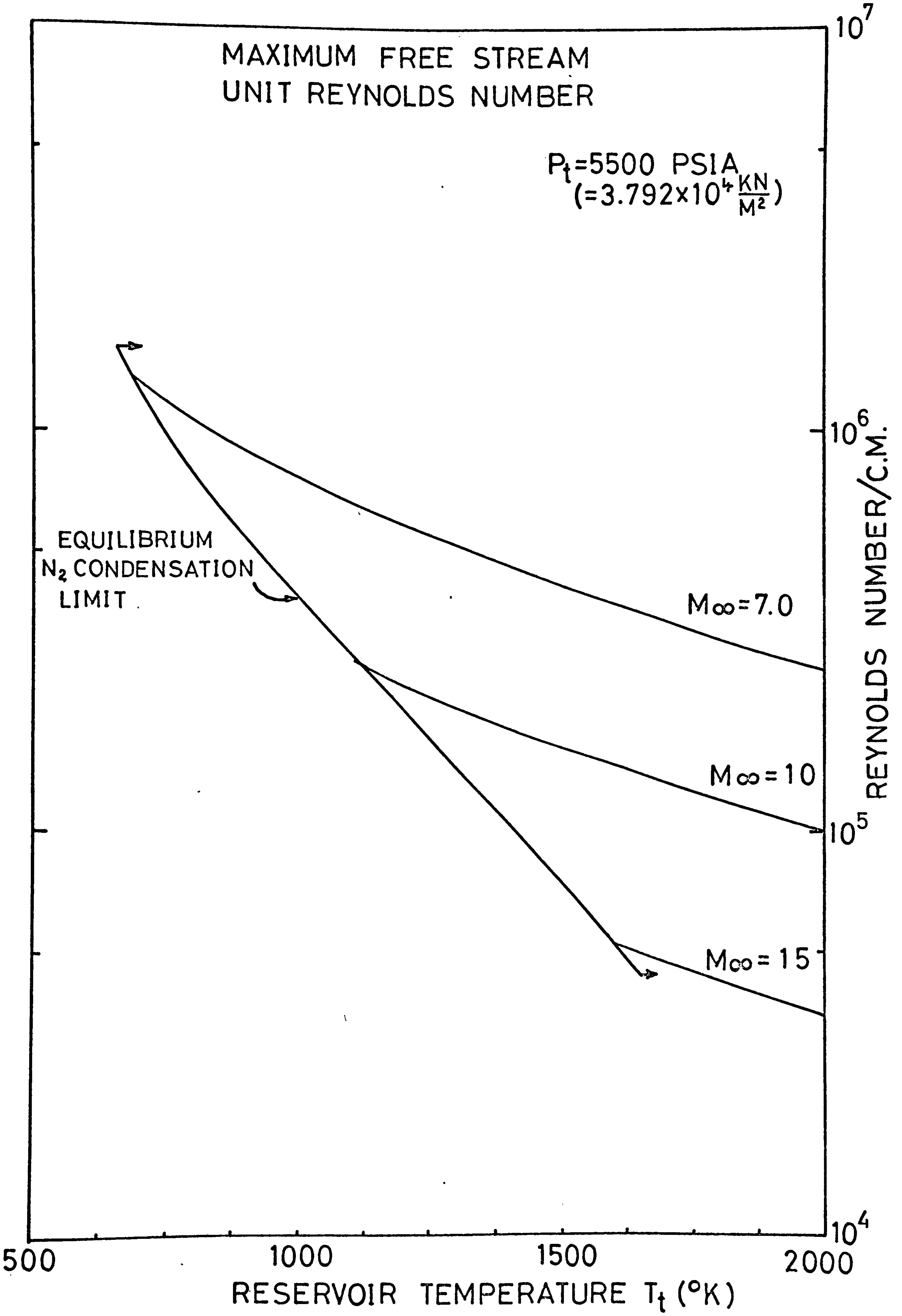
MAXIMUM FREE STREAM
UNIT REYNOLDS NUMBER
P_t=5500 PSIA
(=3.792×10⁴ KN/M²)
EQUILIBRIUM
N_2 CONDENSATION
LIMIT
M∞=7.0
M∞=10
M∞=15
10^7
10^6
10^5
10^4
REYNOLDS NUMBER/C.M.
500
1000
1500
2000
RESERVOIR TEMPERATURE T_t (°K)

FIG. 6.5.

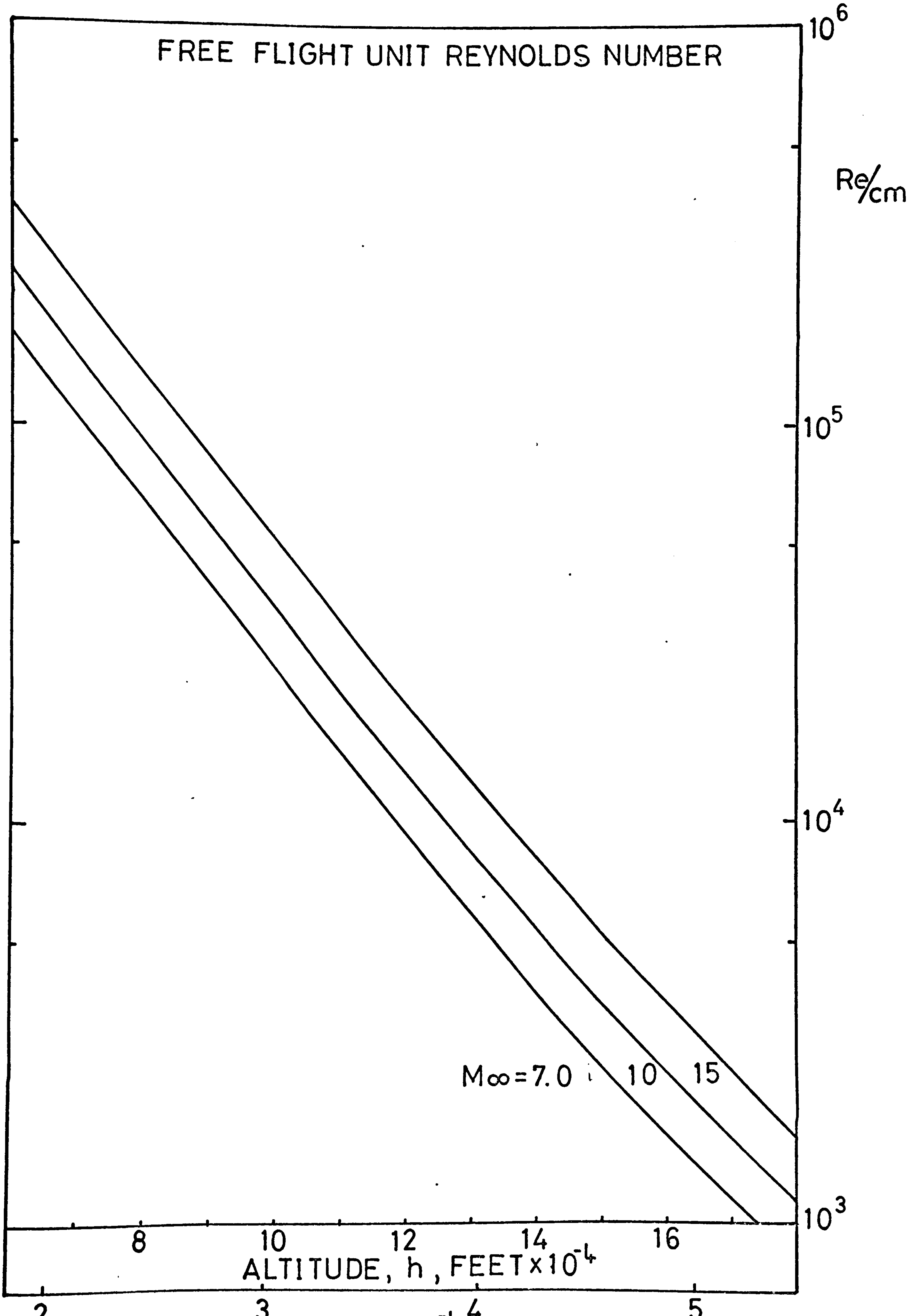
FREE FLIGHT UNIT REYNOLDS NUMBER
10^6
Re/cm
10^5
10^4
10^3
M∞=7.0
10
15
8
10
12
14
16
ALTITUDE, h, FEET × 10^{-4}
2
3
4
5
METERS × 10^{-4}

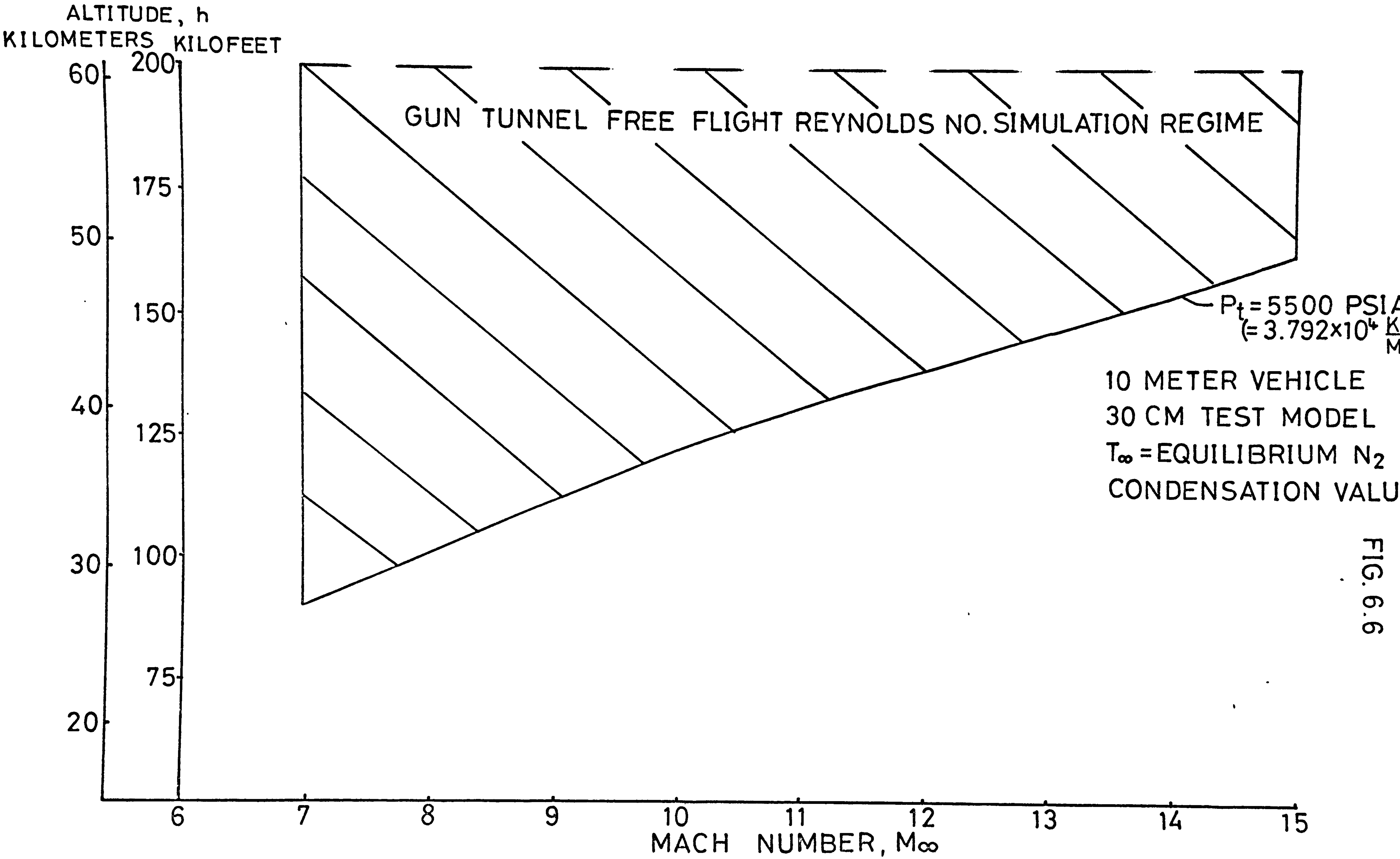
ALTITUDE, h
KILOMETERS KILOFEET
60
50
40
30
20
200
175
150
125
100
75
GUN TUNNEL FREE FLIGHT REYNOLDS NO. SIMULATION REGIME
$P_t = 5500$ PSIA
$(= 3.792 \times 10^4 \frac{KN}{M^2}$
10 METER VEHICLE
30 CM TEST MODEL
T_∞ = EQUILIBRIUM N_2
CONDENSATION VALUE
6
7
8
9
10
11
12
13
14
15
MACH NUMBER, M_∞

FIG. 6.6

CHAPTER SEVEN

CONCLUSIONS-PART ONE

Tests have verified the operational reliability of the Oxford Gun Tunnel up to 200 atmospheres driver pressure. The run to run repeatability of barrel end wall conditions was found to be very good with the diaphragm and pistons developed during these tests. The shock wave and piston trajectories in the barrel were found to be reasonably well predicted by an ideal shock tube analysis.

The Mach 7 contoured nozzle designed for the Gun Tunnel produced quite uniform flow conditions in the working section with the calibrated Mach Number distribution being close to the nominal design value for the nozzle. Axial Mach Number gradients of less than .007/cm were measured. The total temperature of the flow was directly measured up to a value of 1000°K and appeared to be some 10-15% below the temperature predicted by a semi-empirical analysis of barrel shock wave strengths. Running times of about 30-40 msec. were observed in the total temperature range below 1000°K. About one half of this time was considered quasi-steady state for most applications because of the pressure fluctuations from the multiple shock wave reflections.

The total temperature at which the onset of condensation in the nozzle occurs was determined from tests. This information allowed operation at low total temperatures (but above the condensation point) and therefore at higher unit Reynolds Numbers. It was found that in this way a wide range of free flight Reynolds Number conditions could be duplicated in the Gun Tunnel at Mach 7.

A wide range of special instrumentation and instrumentation techniques were developed for Gun Tunnel use during the course of these tests. Many of these techniques, including multi-channel data acquisition capabilities, would be of quite general usefulness in many Gun Tunnel applications. Twelve channels of direct reading heat transfer instrumentation were developed for use in the experiments described in Chapter 10.

PART II

PART II - HYPERSONIC BOUNDARY LAYER TRANSITION

CHAPTER EIGHT

INTRODUCTION

The early work of L. Prandtl (circa 1904) in developing the concept of the thin layer near the surface of solids in fluid flows where viscosity effects were important soon led to the observation that this thin 'boundary layer' could exist in either the laminar or turbulent state. In much the same manner as O. Reynolds' earlier (circa 1883) observations in circular pipe flow, it was found that the boundary layer flow changed from the laminar state to the turbulent state when a certain critical value of the Reynolds Number was attained. The large increase in skin friction of the turbulent boundary layer and its increased ability to sustain a larger adverse pressure gradient before separation made knowledge of the location of the transition point between laminar and turbulent flow vitally important from a design point of view.

For many years all attempts to predict the transition point by the application of very elegant mathematical theories of laminar layer stability were unsuccessful. It was not until the classic experiments of Schubauer and Skramstad (Ref. 74) in the early 1940's in a low turbulence wind tunnel that the theoretical predictions of the existence and properties of two-dimensional 'Tollmien-Schlichting' oscillations in laminar boundary layers were verified in every respect. This successful prediction, however, was only for the initial instability and linear amplification region and did not predict the location at which the flow became wholly turbulent. Much experimental (and some theoretical) evidence since the original work of Ref. 74 has added to the understanding of the important region between the initial instability and final fully developed turbulence (see Section 11.3) although the picture is still far from complete even for the low speed incompressible case.

In the supersonic/hypersonic flow regime, the confusion surrounding the mechanisms and location of transition is complete. This situation is due, at least in part, to the great scarcity of <u>detailed</u> measurements <u>within</u> the transitional boundary layer at supersonic speeds. (A review of existing detailed measurements is made in Section 11.3). Great quantities of high speed transition data have been accumulated and correlated in the past twenty years quite independently of stability considerations. These measurements have yielded neither a consistent transition theory nor any even moderately reliable means of predicting transition (as opposed to linear instability) critical Reynolds Numbers in wind tunnel facilities. The extension of these measurements to full scale free flight conditions has been even less successful.

The bulk of these supersonic transition experiments have involved the measurement of changing <u>surface</u> effects resulting from the changing <u>mean</u> diffusion characteristics between the laminar and the turbulent state. These measurements include changes in surface recovery temperature, surface skin friction, surface heat transfer rate, surface pitot pressure levels, as well as actual measurements of velocity (or pitot) profiles. The changing density profiles of the two states of the boundary layer also makes the observation by shadowgraph/schlieren techniques possible. Some recent experiments have also shown that measurements of rms surface fluctuations of pressure (Ref. 75) or heat transfer (Ref. 76) provide a sensitive indication of the state of the boundary layer. The measurement techniques listed above (with the possible exception of the optical method) generally provided a consistent definition of the bounds of the transition region and were mutually consistent on tests on a single model in a particular wind tunnel.

The definition of the transition location becomes very important especially at high speeds where the length of the region where surface changes are observed becomes appreciable and the idea of a single transition point ambiguous. The ambiguity in the definition of the transition region was increased still further when detailed anemometer measurements within the boundary layer (Refs. 77, 78 and 79) revealed unsteady 'transitional' behavior upstream of the point where changes first appeared on the surface. This phenomenon is investigated in much more detail in the discussion of the experimental results of Chapter 11 where hot wire probes were used in an attempt to discover the source and nature of fluctuations present within the quasi-laminar boundary layer in the early stages of transition. For the sake of clarity in the chapters which follow, the unqualified terms 'transition region' or 'begin transition' refer to areas defined on the basis of surface pitot pressure (Chapter 9) or surface heat transfer (Chapter 10) measurements and are not intended to suggest that transitional behavior does not exist upstream of the surface-defined transition region.

Very recently, the results of two extremely important studies have been presented which shed much new light on the whole field of supersonic/hypersonic boundary layer transition. One of these studies represented a theoretical breakthrough while the other presented experimental evidence which raised very pertinent questions about the validity of nearly all high speed transition data previously reported in the literature. Mack's numerical solutions (Ref. 80) of the complete (viscous) compressible stability equations led to the discovery of unstable 'skew' disturbances which propagate at some angle to the local free stream direction and also demonstrated the existence of higher modes of instability. In fact, the second mode can quite easily be less stable than the primary mode for many frequencies over a wide range of Mach Numbers, especially for cooled wall conditions.

The experimental paper referred to, by Pate and Schueler (Ref. 81), demonstrated that measured boundary layer transition in supersonic/hypersonic wind tunnels was systematically dominated by the level of free stream turbulence (in the form of sound radiation from the turbulent side walls) in the working section. This correlation accounted for observed Mach Number and unit Reynolds Number effects in wind tunnel tests quite independent of stability criteria.. The implications of this finding was that 1) meaningful stability experiments could not be performed in the presence of this strong radiation and 2) that comparison of transition results from various facilities could only be made in a meaningful way if information on the level of free stream disturbances was also known, a condition seldom met in practice.

A growing awareness of the significance of the new developments listed above has resulted in a few new more closely controlled experiments and analyses which, if they are indicative of a new trend in high speed transition work, are likely to produce a more consistent picture of the transition process in the future. Kendall's stability experiments (see discussion in Ref. 82) with laminar side walls has yielded supporting evidence to Mack's stability analysis. Reshotko's (Ref. 83) application of Mack's multi-mode results has explained the apparent inconsistency of much wall cooling effects on transition in published data. More recently, Wagner, et. al. (Ref. 84), has presented measured free stream fluctuation levels simultaneously with transition measurements.

Although the existence of dominant free stream sound radiation has made comparative measurements of transition location uncertain, there remains a considerable quantity of useful parametric studies of transition in particular wind tunnels which are meaningful. These include studies of wall cooling effects, leading edge bluntness, surface roughness, angle of attack, and sweep angle. Because of the uncertainty of the environment, it was not considered of value to review comprehensively existing high speed transition literature. A detailed survey of relevant literature was made, however, for the aspects of transition investigated in this thesis and are found in the appropriate chapters.

The aspects of hypersonic boundary layer transition investigated in some detail in the following chapters can be broadly divided into three main areas. The first (Chapter 9) involved an extension of earlier work on the effects of the varying free stream environment on transition location. This involved the testing of a common model in various wind tunnel facilities under cold wall conditions with open jet nozzle configurations which were not included in the original Pate and Schueler correlation. The second aspect studied (Chapter 10) was basically an investigation of model spanwise curvature effects on transition. Since heat transfer measurements were also involved in these tests, some comparisons with existing heat transfer theories was also possible. The third area investigated (Chapter 11) involved a study of the origin, scale, and character of transitional fluctuations existing within the boundary layer upstream of the surface-observed transition region using hot wire anemometry.

CHAPTER NINE

HOLLOW CYLINDER TRANSITION

A hollow cylinder model configuration was selected for the initial series of Gun Tunnel tests investigating boundary layer transition. The model was selected for its relative simplicity of design and for the ease and accuracy with which a sharp leading edge could be produced and maintained. The leading edge thickness has been shown to be one of the important parameters to be controlled in hypersonic transition experiments (e.g. Ref. 77). The hollow cylinder design also simplified the application of the surface pitot technique for the detection of boundary layer transition. This technique has been shown to provide a sensitive indication of the location of the transition region by detecting the effects of the changes in the mean velocity profile of the boundary layer as it undergoes transition to a fully developed turbulent condition (e.g. Ref. 85). The hollow cylinder of course also offers the advantage that it represents the simple flat plate type of flow situation on which the vast bulk of experimental and theoretical boundary layer stability and transition research has been performed.

A concurrent consideration which influenced the final configuration of the model was the knowledge that this model was intended to serve as the standard model for transition tests to be performed in various aerodynamic testing facilities in Europe. These tests were intended to reveal any influence on the transition region which may be attributed to factors unique to the facility itself. The results of these tests are described in Section 9.3. The final details of the model design were fixed after a preliminary drawing had been circulated to several prospective testing groups for comment. The surface pitot technique had the advantage here of simplicity of operation in both shock driven and long duration wind tunnels. The ease of maintenance of the hollow cylinder leading edge on a model being handled by different personnel at the various installations also offered an obvious advantage.

9.1 The Model

The hollow cylinder model was constructed from 3 inch (7.62 cm) diameter stainless steel tubing with a removable high carbon steel (EN 26) leading edge section. The overall length of the model was $15\frac{3}{8}$ inches (39 cm). A photograph of the model is shown in Fig. 9.1 and a detail drawing of the model is given in Fig. 9.2. The two pieces of the cylinder were rough machined and then the leading edge section hardened and tempered before the two sections were joined and given the final grinding on the outside surface. The final surface finish was measured at less than 10 microinch roughness. The surface roughness stylus was also taken over the joint between the two cylinder sections. This step was found to be of the order of .0001 inch and rearward facing after repeated removal and rejoining of the two parts. The leading edge was examined with a precision travelling microscope and found to be of the order of .0003 inches (± .0001") thickness uniformly around the circumference. This figure was also repeatable after regrinding operations.

The pitot probe and transducer were mounted in a sliding brass collar which could be moved the entire length of the model. The transducer was a Kistler Type 7031 acceleration compensated piezo-electric gauge and was calibrated for low pressure operation by the method outlined in Section 3.4.1. Stainless steel tubing (.064" o.d.) was brazed into the collar in the approximate configuration shown in Fig. 9.2 to form the pitot probe. The tip

FIG. 9.1

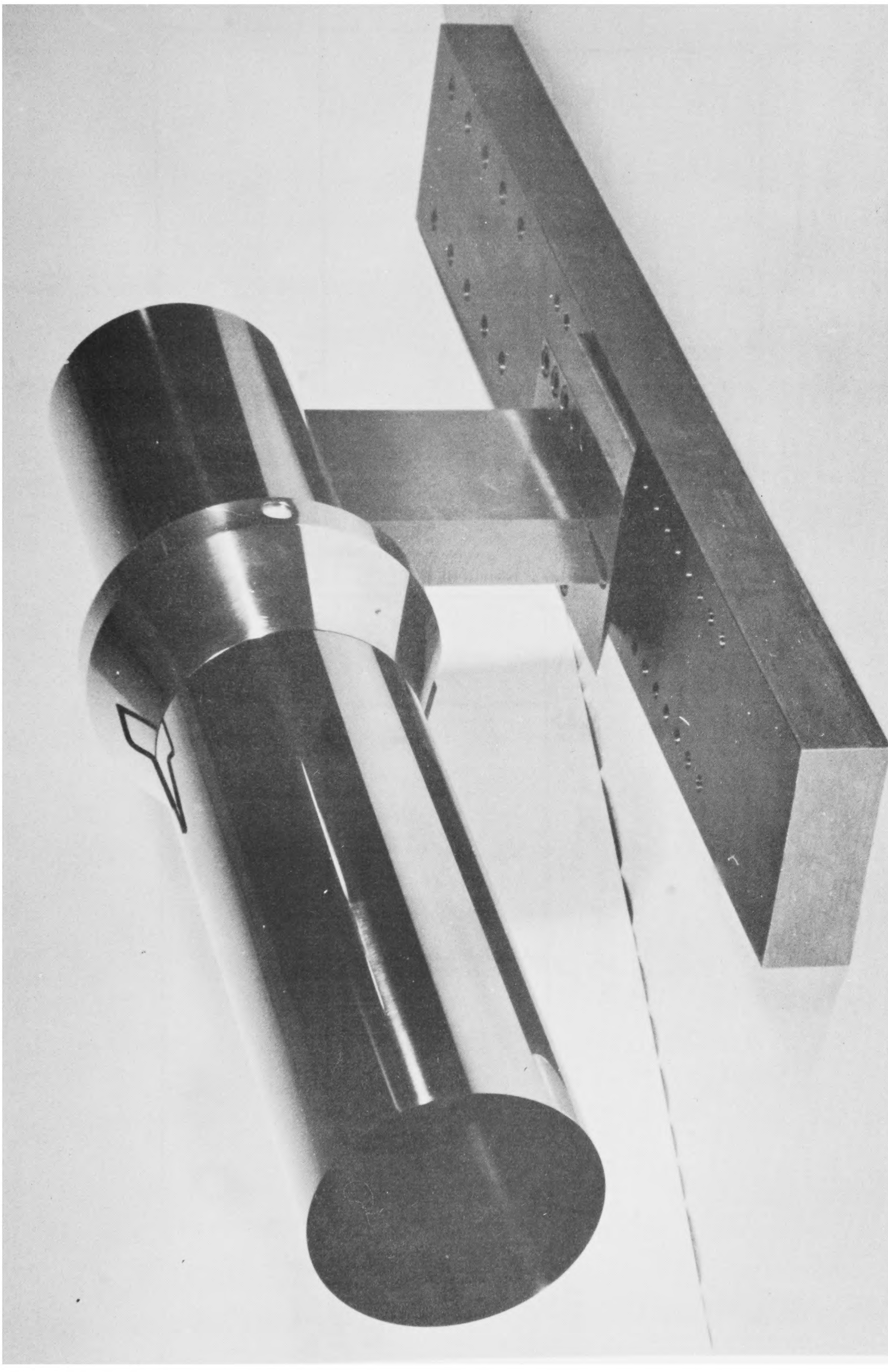

3" HOLLOW CYLINDER MODEL

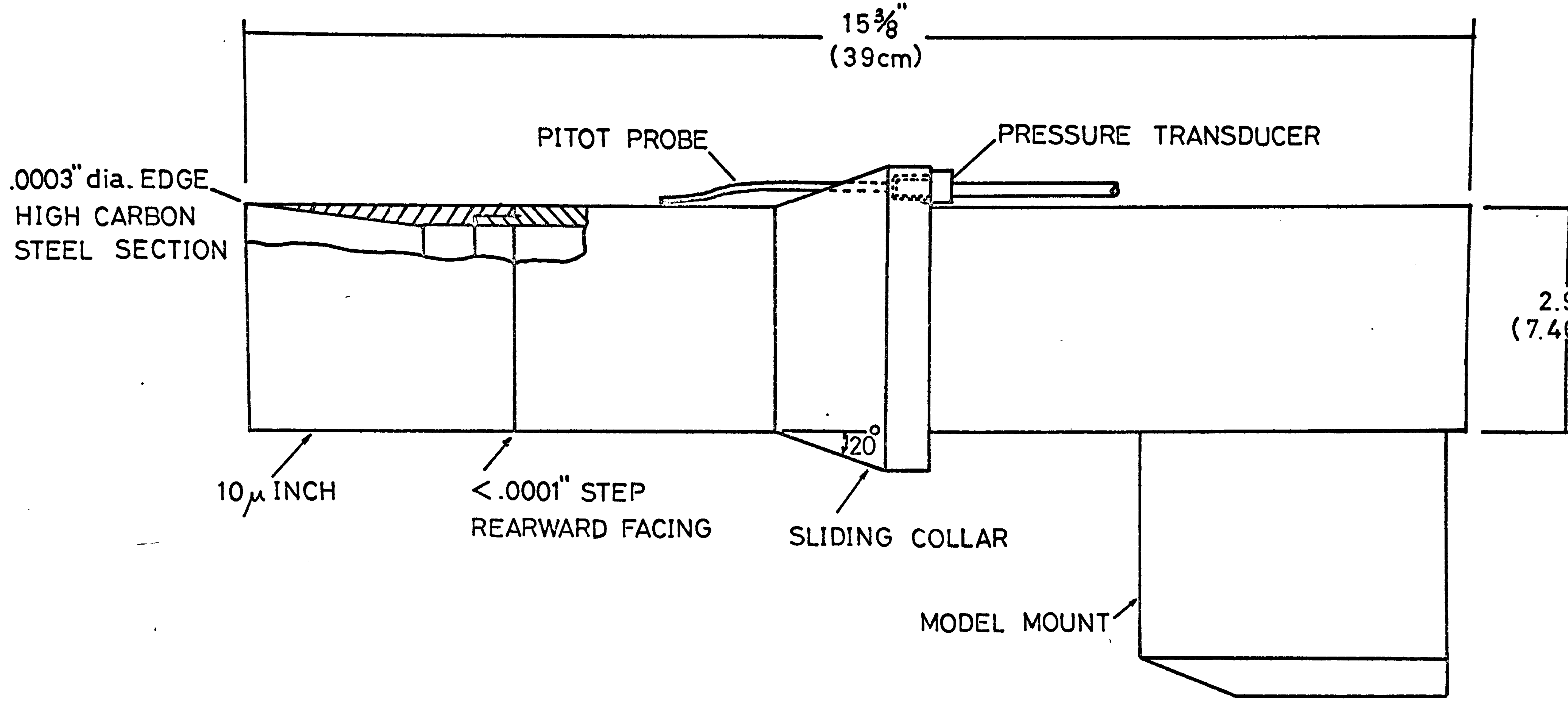

FIG. 9.2

STANDARD HOLLOW CYLINDER TRANSITION MODEL of the probe was flattened in a precision vice into a nearly rectangular shape with a height of about .016". The leading edges of the probe were honed to less than .002" thickness. The probe tip extended at least 1½" ahead of the compression corner of the 20° wedge on the collar. This distance was judged to be sufficient to avoid the region of incipient separation based on the measurements of Needham (Ref. 86).

The model was mounted on a slender support (½" thick) at bottom-dead-center at the downstream end. The brass collar was slotted to permit its movement to the rearmost end of the model. Pitot measurements were confined to the top of the model to avoid possible upstream influence of the model support.

9.2 Gun Tunnel Transition Results

The hollow cylinder model was mounted in the Gun Tunnel working section on the nozzle centerline. The model leading edge was located at or near the exit plane of the free jet nozzle. When it was necessary to move the model axially during a series of tests, some measurements were repeated to assure that they had not been affected by the move. All tests were performed in the Mach 7 contoured nozzle at a total temperature of 720°K. The total pressure was varied to provide a range of unit Reynolds Numbers for the tests.

9.2.1 Shadowgraph Tests

The initial series of transition tests were conducted with the pitot collar off the model to provide an undisturbed flow field over the length of the cylinder. A range of unit Reynolds Numbers from 1.75 - 6.15 x 10^5 per cm was investigated using schlieren and shadowgraph techniques to estimate the state of the boundary layer and to determine what flow conditions were likely to produce a naturally turbulent boundary layer. The shadowgraph pictures were found to present more detail within the boundary layer compared with the schlierens and were therefore used on the majority of the tests. Well defined dark and light bands were observed near the model surface beginning near the leading edge. Further from the leading edge these sharp bands became first intermittently less well defined then gradually more diffused until all regular definition was lost and the flow took on the apparent characteristics of random turbulence. The definition of the extent of the transition region from flow photography alone is somewhat ambiguous and is likely to depend as much on individual opinion as on variations in photographic quality due to changes in flow conditions or exposure. The onset of the transition region was taken for the purpose of this investigation as the point where the first lack of sharpness appeared in the optical bands near the model surface The end of all band structure in the shadowgraphs was assumed to indicate the end of the transition region. The photographic evidence indicated that natural transition would occur on the hollow cylinder over the entire range of the test conditions.

A typical shadowgraph is shown in Fig. 9.3. The extent of the transition region defined by the surface pitot experiments (for identical flow conditions and described below) is indicated in the figure. Disturbances appeared in the laminar boundary layer before mean changes in the velocity distribution became appreciable enough to affect the pitot pressure. The end of transition determined from the shadowgraph is very near the beginning of transition found from the pitot record. This discrepancy is more clearly illustrated in Fig. 9.4 where the shadowgraph determined transition Reynolds Number is compared with the surface pitot results. The pitot results, of course, offer a more precisely defined determination of the transition

FLOW DIRECTION

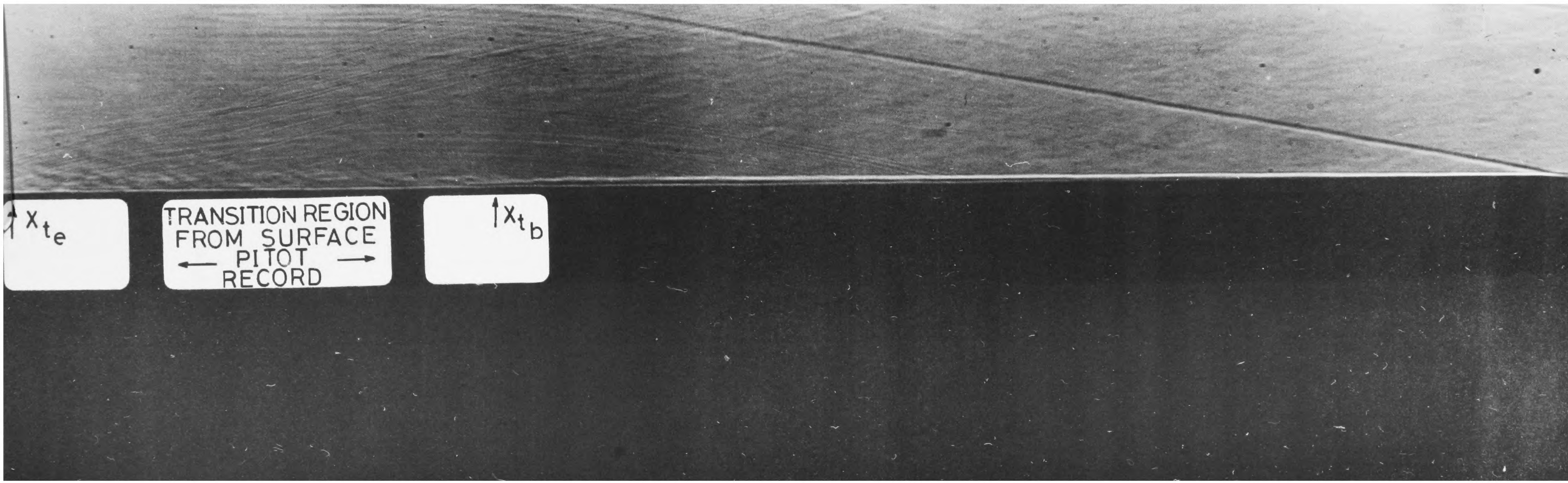

HOLLOW CYLINDER SHADOWGRAPH
$M=7$, $Re/cm = 3.42 \times 10^5$, $T_t = 720°K$

FIG. 9.3

FIG. 9.4

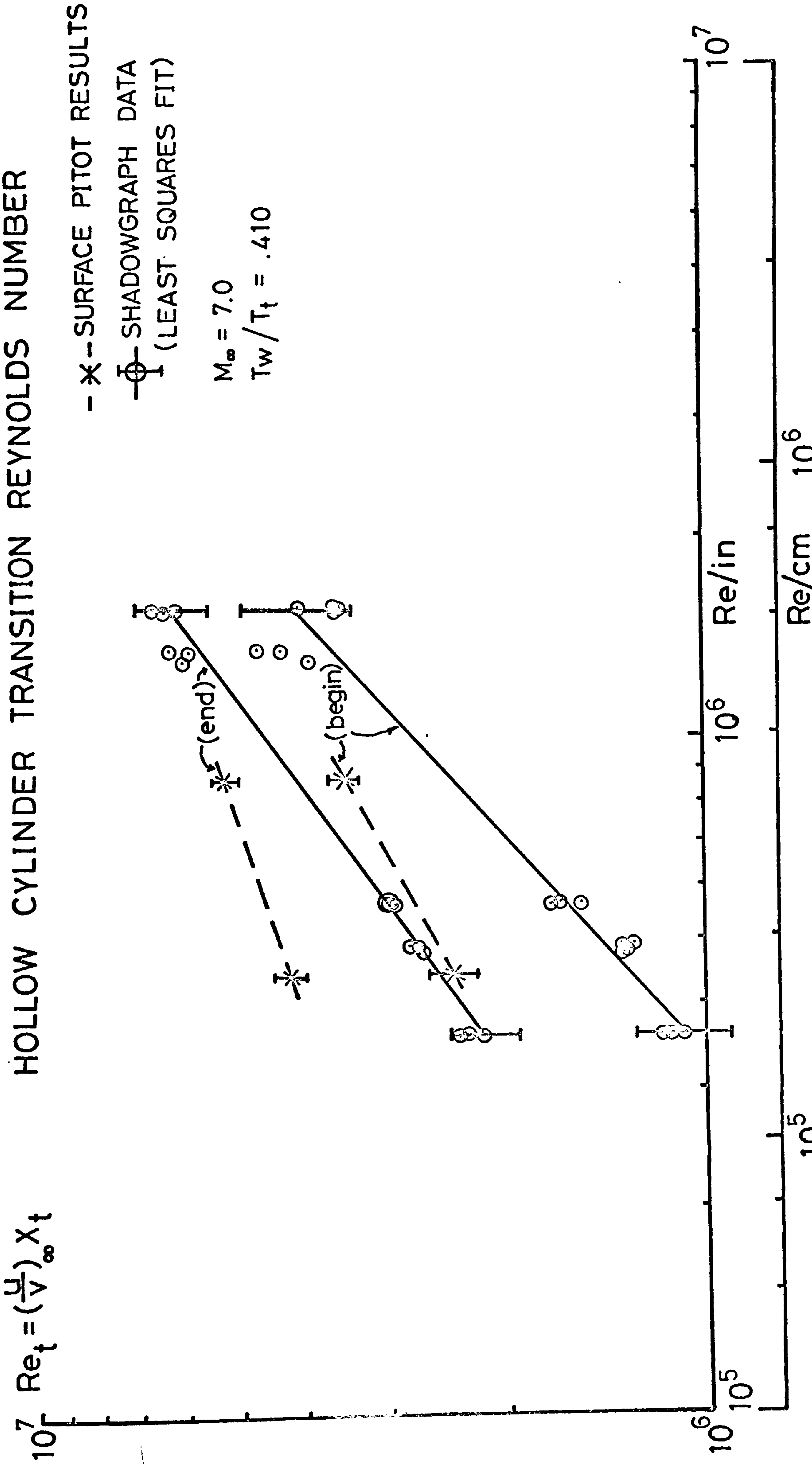

HOLLOW CYLINDER TRANSITION REYNOLDS NUMBER
-✱- SURFACE PITOT RESULTS
SHADOWGRAPH DATA (LEAST SQUARES FIT)
$M_\infty = 7.0$
$T_w/T_t = .410$
$Re_t = (\frac{u}{\nu})_\infty X_t$
(end)
(begin)
Re/in
Re/cm
10^5
10^6
10^7

region and are therefore used in the remainder of the chapter to define this region.

The interpretation of shadowgraph information can be aided somewhat if quantitative measurements of the photograph optical density are made. Fig. 9.5 shows several profile traces of the boundary layer region on the negative plate of Fig. 9.3. These profiles were obtained with a Joyce-Loebl optical microdensitometer. This instrument produces a graph of the plate emulsion optical density as its narrow rectangular beam traverses the boundary layer perpendicular to the wall. It is interesting to compare the changing pattern of the profiles with the location of the transition region from the surface pitot results. Near the pitot-determined beginning of transition a secondary peak has begun to develop near the model surface. Immediately after the end of transition, the profile has settled down to one similar to the no-flow profile shown for comparison. There are thus seen to be real differences existing in the shadowgraph records for some distance downstream after they have ceased to be apparent to the unaided eye.

9.2.2 Surface Pitot Tests

Tests were then performed with the pressure probe collar in place on the hollow cylinder to determine more precisely the location of the transition region than was possible from flow visualization tests alone. It was first necessary to determine the pitot pressure levels which would be encountered within the model boundary layer and to find the best location for the probe to detect the changing mean velocity profile. Pitot profiles normal to the surface at three different x locations were measured for the lowest unit Reynolds Number conveniently tested on the Gun Tunnel (at a constant total temperature). The low Reynolds

FIG. 9.5

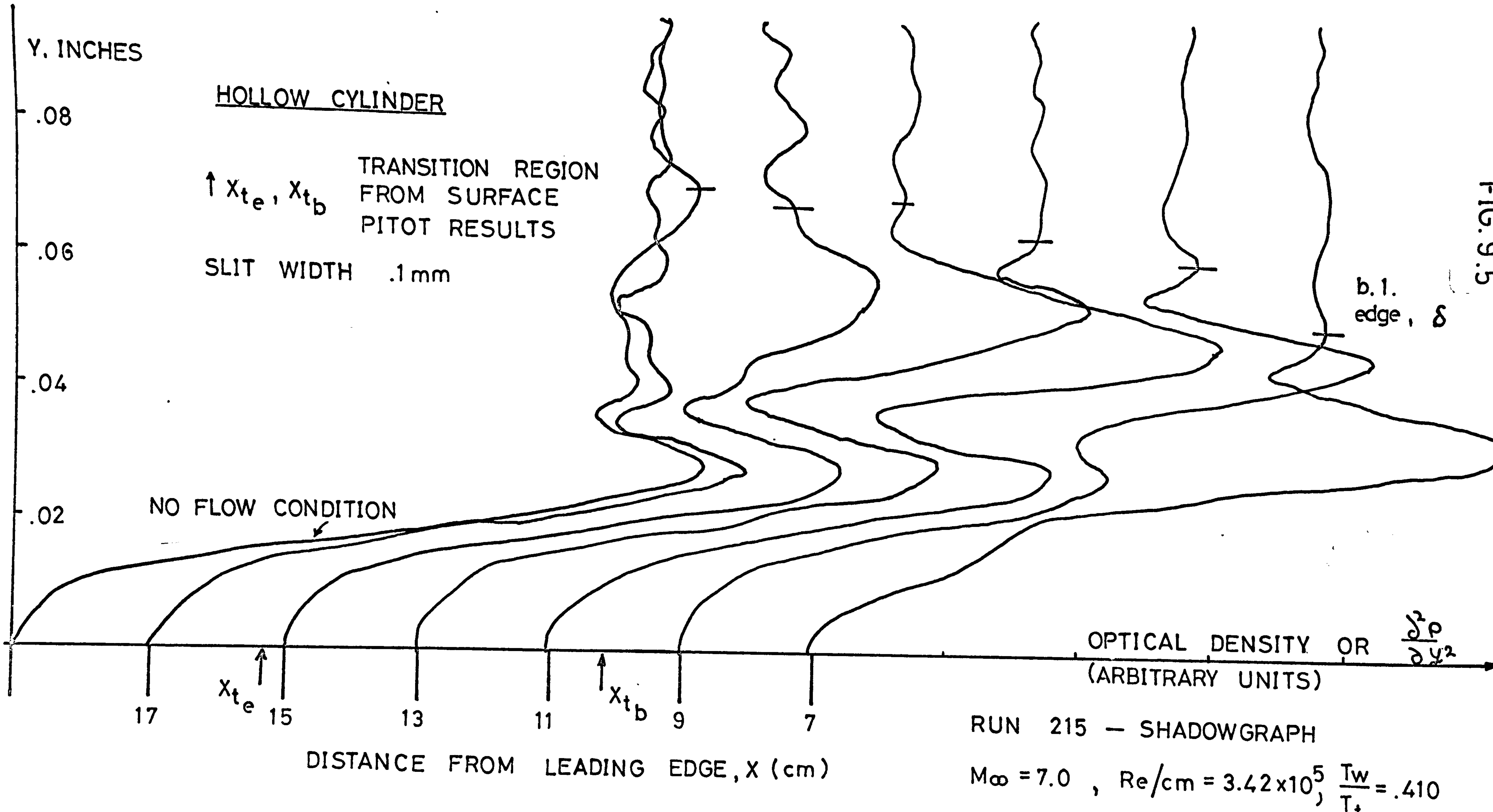

MICRODENSITOMETER BOUNDARY LAYER PROFILES

Number case was selected because the resulting increase in boundary layer thickness improved the pitot traverse accuracy. The three pitot traverses are shown in Fig. 9.6 with y normalized against the boundary layer thickness (δ) estimated from the pitot pressure record. The pitot pressure is normalized against its free stream value. The rapid changes in the mean pitot profiles are apparent as the boundary layer undergoes transition. It was later determined in the surface pitot experiments described below that the x = 2", 5.5" and 8" profiles corresponded to a laminar, early transitional, and late transitional condition respectively. It would appear from Fig. 9.6 that appreciable changes in pressure would be measured in a surface pitot 'x' traverse experiment with the probe at a constant y/δ of the order of 0.3 to 0.6.

It is, of course, not convenient to maintain a constant y/δ for the probe as it is translated along the model. Several tests were conducted with the probe at a constant y. It was found that a probe centerline height above the surface of about .020" produced an adequate signal to noise ratio (for a rigidly mounted Kistler 7031 transducer) and pressure change between laminar and turbulent profiles to be useful in defining the limits of the transition region for the flow conditions of interest. The surface pitot record for two unit Reynolds Number cases is shown in Fig. 9.7 plotted against Reynolds Number from the leading edge. There is up to a factor of five change in pitot pressure as the probe is traversed along the model, thus making the limits of the transition region quite well defined. There is still some uncertainty in locating the beginning and end of transition because of the finite number of data points which are necessarily obtained in a short duration facility. The limits of uncertainty are indicated in the figure with the pitot-

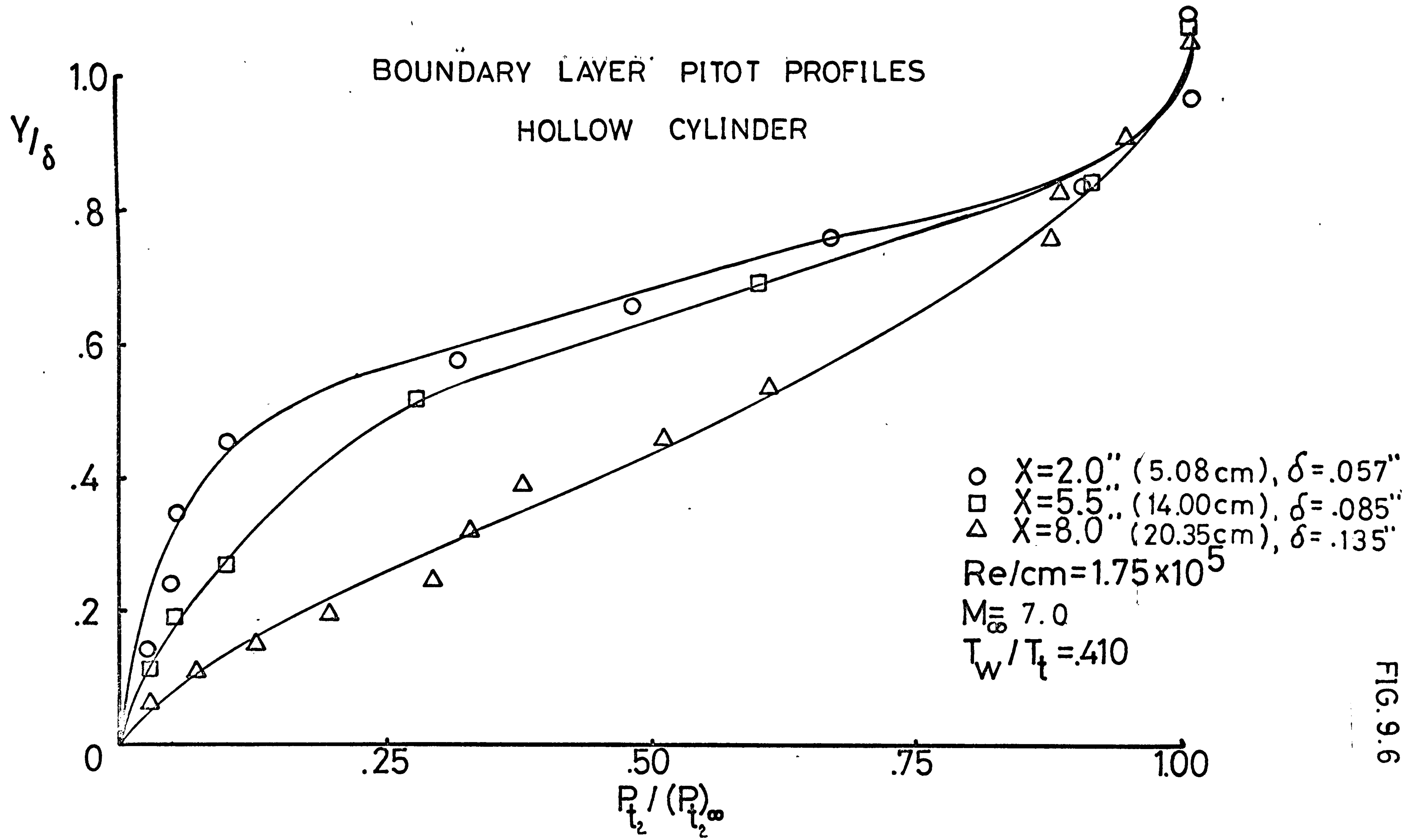
BOUNDARY LAYER PITOT PROFILES
HOLLOW CYLINDER
Y/δ
1.0
.8
.6
.4
.2
0
.25
.50
.75
1.00
$P_{t_2}/(P_{t_2})_\infty$
○ X=2.0" (5.08 cm), δ=.057"
□ X=5.5" (14.00 cm), δ=.085"
△ X=8.0" (20.35 cm), δ=.135"
Re/cm=1.75×10^5
M_∞= 7.0
T_w/T_t=.410

FIG. 9.6

FIG.9.7

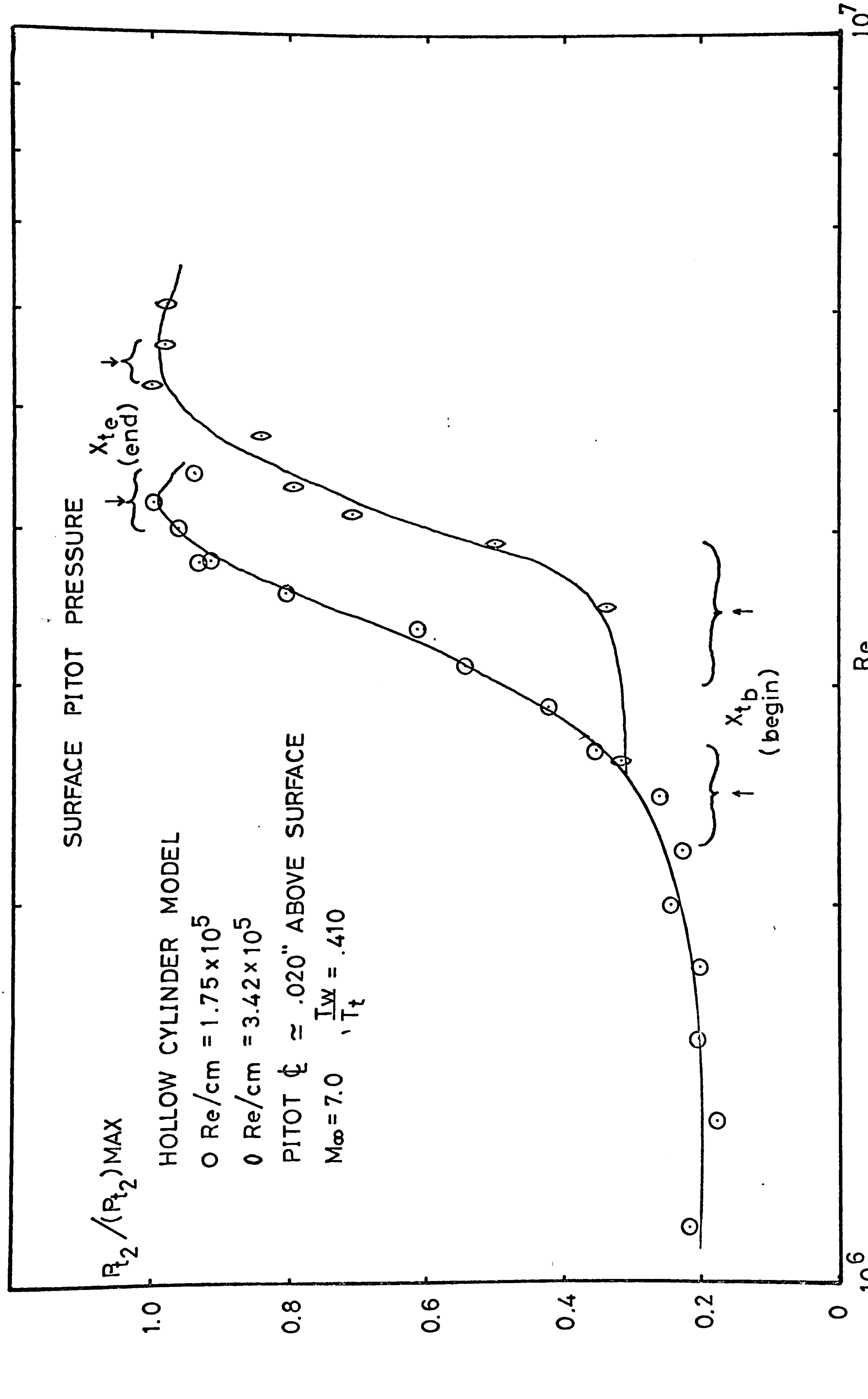
SURFACE PITOT PRESSURE
$P_{t_2}/(P_{t_2})_{MAX}$
HOLLOW CYLINDER MODEL
O Re/cm = 1.75 x 10^5
ʘ Re/cm = 3.42 x 10^5
PITOT ℄ ≃ .020" ABOVE SURFACE
M∞ = 7.0 , Tw/Tt = .410
X_{t_e} (end)
X_{t_b} (begin)
Re_x
10^6
10^7
0
0.2
0.4
0.6
0.8
1.0

defined beginning and end of transition. Richards (Ref. 87) made surface heat transfer measurements on a hypersonic flat plate both with and without a surface pitot probe in place and found that presence of the probe did not affect the heat-transfer-determined transition location. Richards also concluded that the surface pitot method gave essentially the same transition region location as the surface heat transfer results.

The data of Fig. 9.7 was replotted in Fig. 9.4 as transition Reynolds Number (Re_t) against unit Reynolds Number. The unit Re effect on Re_t is apparent in both Figs. 9.4 and 9.7. The slope of the end-of-transition points in Fig. 9.4 gives the following expression

$$Re_t \sim (Re/cm)^{.38}$$

for the power dependence on unit Re. Nagel (Ref. 88) has summarized a wide range of published supersonic transition data and found that a unit Re to the 0.4 power slope described much of the data. Nagel offered some suggestions as to the origins of this so-called unit Reynolds Number effect. His comments and some other work describing this effect will be discussed in Section 9.4.

Returning briefly now to the pitot 'y' profiles of Fig. 9.6 in view of the surface pitot results of Fig. 9.7, it is seen that the profile at x = 8 inches is slightly before the peak in the surface pitot record. It would be expected, therefore, that the boundary layer profile should be nearly fully turbulent by this stage. This pitot profile is compared with a nozzle wall turbulent pitot profile from Wallace (Ref. 89) and a turbulent profile on a hollow cylinder model from Samuels, et. al. (Ref. 90) in Fig. 9.8. Also included is a pitot profile on the hollow cylinder at a location past the peak in the surface pitot

FIG. 9.8

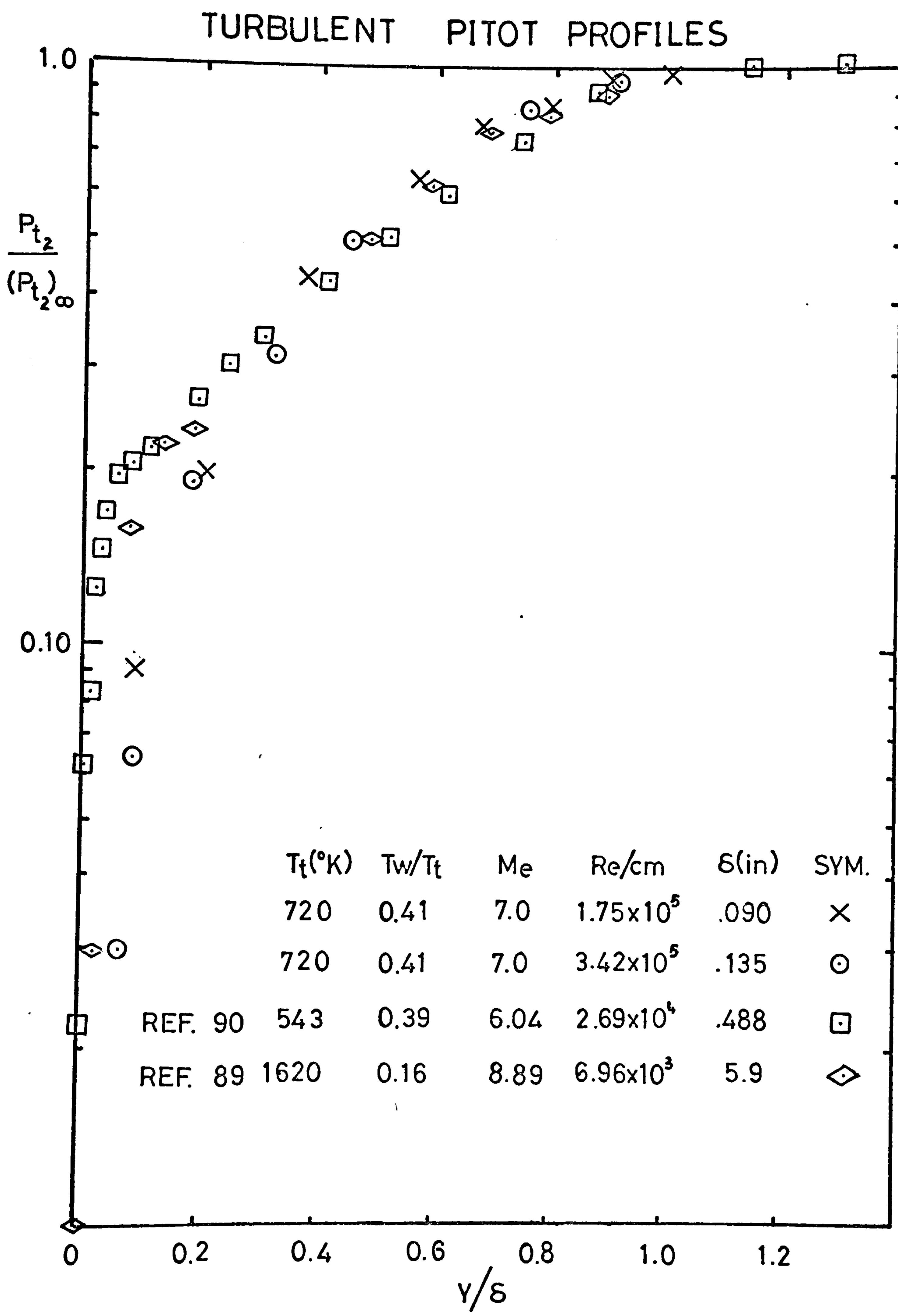
TURBULENT PITOT PROFILES
1.0
0.10
$\frac{P_{t_2}}{(P_{t_2})_\infty}$
0
0.2
0.4
0.6
0.8
1.0
1.2
Y/δ
Tt(°K) Tw/Tt Me Re/cm δ(in) SYM.
720 0.41 7.0 1.75x10^5 .090 ×
720 0.41 7.0 3.42x10^5 .135 ⊙
REF. 90 543 0.39 6.04 2.69x10^4 .488 ⊡
REF. 89 1620 0.16 8.89 6.96x10^3 5.9 ◇

record in a different series of tests. All test conditions were for similar hypersonic, cold wall conditions. The profiles are very similar, especially at distances from the wall greater than $y/\delta = 0.2$. At points closer to the wall, errors are introduced by the effects of a probe which is 15-20% of the boundary layer thickness working in the region of strong velocity gradients.

The laminar pitot profile (x = 2") in Fig. 9.6 gives an estimate of boundary layer velocity thickness which can be compared with a suitable theory to verify the laminar state of the boundary layer. Smith (Ref. 30) derived an expression based on an analysis due to Stewartson for the thickness of a compressible, laminar, cold wall, flat plate boundary layer. A linear viscosity-temperature relationship was assumed along with a unity Prandtl Number. The expression is given as

$$\frac{\delta}{x} = \frac{1}{\sqrt{Re_x}}\left[\eta^* + .332(\gamma-1)M_\infty^2 + 1.73\left\{\frac{T_w}{T_\infty} - 1\right\}\right] \qquad (9.2.1)$$

where η^* is the constant from the Blasius incompressible solution. For a velocity thickness based on $(u/u_\infty) = 0.99$, $\eta^* = 5.0$. The flow conditions of the laminar profile of Fig. 9.6 then gives $\delta = 0.0526"$ using (9.2.1). The measured value is given as 0.057" and represents a reasonable agreement considering the assumptions of the theory and the use of a pitot pressure profile ($\sim\rho u^2$) to estimate the velocity thickness.

The laminar characteristic of the pitot profile is further verified by comparison with other experimentally observed laminar, hypersonic, cold wall profiles. Fig. 9.9 contains the laminar pitot profile data as compared with the average profiles observed by three other research groups. Two of these tests were on sharp slender cones (Refs.91 and 92), and one on a flat plate (Ref. 56).

FIG. 9.9

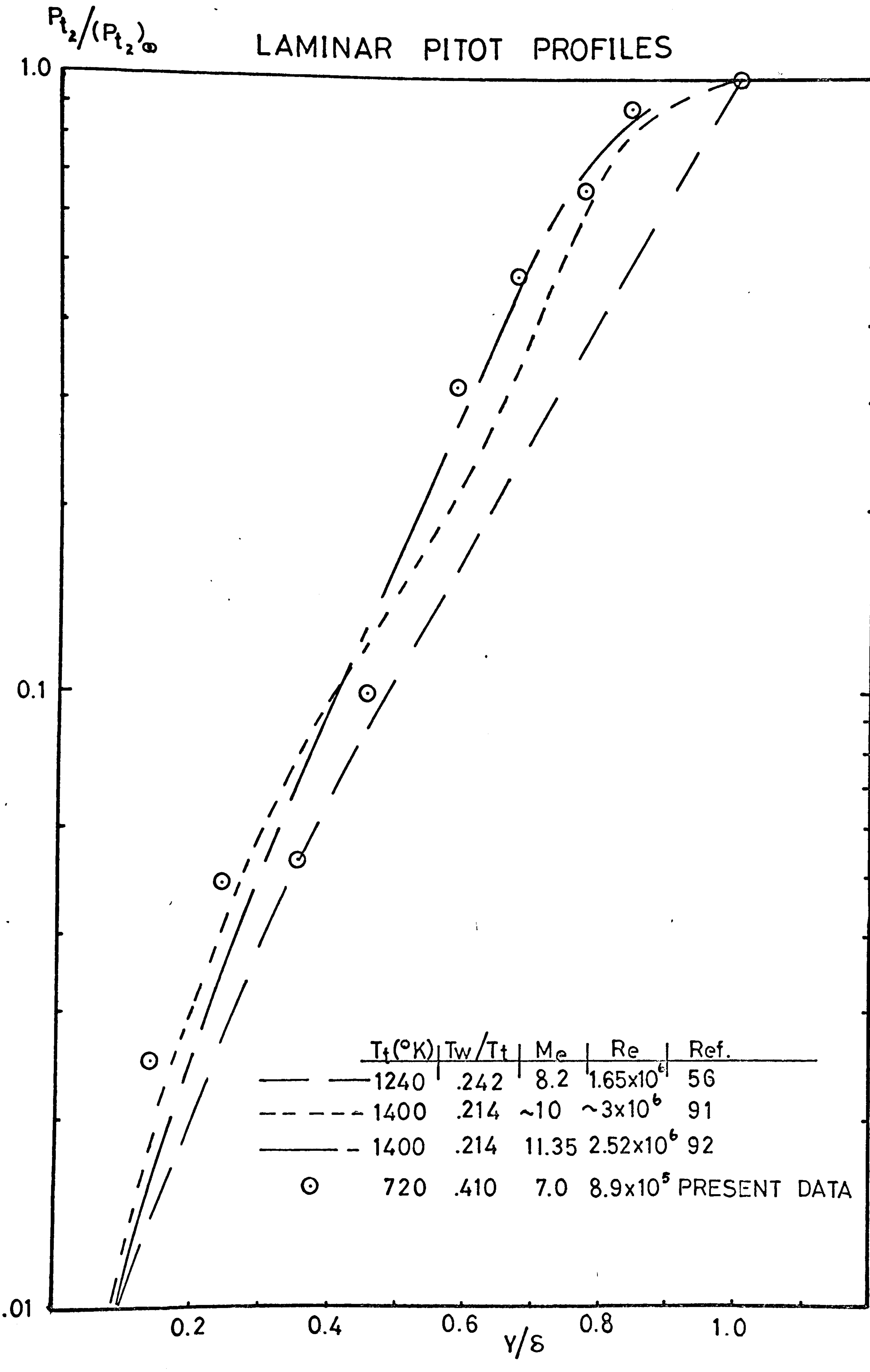

T_t(°K)	T_w/T_t	M_e	Re	Ref.
1240	.242	8.2	1.65×10^6	56
1400	.214	~10	$\sim 3 \times 10^6$	91
1400	.214	11.35	2.52×10^6	92
720	.410	7.0	8.9×10^5	PRESENT DATA

9.3 Transition Tests in Other Facilities

Despite the quantity of supersonic transition data which has become available in recent years, there are still many aspects of the problem where conflicting experimental evidence makes the unambiguous description of events and trends somewhat difficult. One of the most troublesome areas of uncertainty has been the apparent inability to match results on very similar transition tests made in two different wind tunnels. Very often, however, there were very real differences in model detail, wind tunnel configuration, and transition detection methods which, although assumed to have no effect, could well have had some unknown influence on the observed transition phenomena. Much interest was created by the recent paper of Pate and Schueler (Ref. 81) in which they presented considerable experimental evidence which indicated the strong influence of the intensity of the aerodynamic acoustic energy radiated from the tunnel wall turbulent boundary layer on the model boundary layer transition process. Pate and Schueler went on to correlate many transition measurements from various wind tunnels in terms of the nozzle boundary layer parameters which were known to scale the radiated sound intensity. The findings of their paper are discussed in more detail in Section 9.4.

In order to further examine this dependence of boundary layer transition on test facility, a program was initiated in which the hollow cylinder described in this chapter was tested in several other hypersonic aerodynamic facilities. In this way, any uncertainties due to model configuration and transition detection method would be eliminated. Flow parameters which were known to affect transition behavior were controlled within narrow limits. This included the Mach Number and the wall to total temperature ratio. Each facility test program was run at two unit Reynolds Number conditions, where possible, to provide a comparative indication of the influence of this parameter. The test conditions and working section-nozzle configuration are listed below in Table 9. Three of the facilities were gun tunnels and the other was a blowdown tunnel to provide a useful comparison of the quasi-continuous hypersonic tunnel with the short duration, shock heated type.

TABLE 9

TRANSITION TEST FACILITIES

Organization	Facility	M_∞	Re/cm of tests 10^{-5}	$\frac{T_w}{T_t}$	Working Section and nozzle
Oxford University Dept. Eng. Science (O.U.)	Gun Tunnel	7.0	1.75 3.42	.410	Open Jet 6.1" dia. (15.5 cm) contoured
Imperial College Aero. Dept. (I.C.)	Gun Tunnel	8.2	1.50 2.68	.378	Open Jet 7.5" dia. (19.1 cm) contoured
Rolls Royce Bristol Engines Div. (R.R.)	Gun Tunnel	7.75	1.49 2.80	.369	Open Jet 11.1" dia. (28.2 cm) contoured
Aero. Research Inst. of Sweden F.F.A.)	HYP.500 Blowdown Tunnel	7.15 4.0 4.0	4.12 2.34 5.59	.454 .631 .705	Open Jet 19.7" dia. (50 cm) contoured

The transition region location was defined from the surface pitot x traverse record as outlined in Section 9.2. The beginning of transition was taken as the point where the pitot pressure first began to rise whereas the end of the transition process was at the peak in the pitot pressure. The resultant transition Reynolds Numbers are plotted (from Refs. 93-95) against unit Reynolds Number in Fig.

9.10 along with the hollow cylinder results from Section 9.2. There appear to be some real differences in the observed transition Reynolds Numbers despite the close similarity in test conditions for most of the data. (The M = 4 data can be ignored for this comparison because the existence of a Mach Number effect on transition is well dominated [e.g. see Ref. 81] and will be discussed in the next section). The data also show the much observed 'unit Reynolds Number effect' although the power law dependence on this factor seems to vary slightly in different facilities (see comparative 0.4 slope in Fig. 9.10). The apparent differences in Re_t must be attributed to factors in the various wind tunnel facilities which are not normally accounted for in most research programs. The possible origins of some of these factors are discussed in the next section.

9.4 Correlation Theories

9.4.1 Aerodynamic Noise

The presence of free stream disturbances in wind tunnels and their possible effects on laminar boundary layer stability and transition has long been appreciated by workers in the field. In fact, it was not until the character and source of this 'noise' was determined and finally controlled that it was possible to conduct uncontaminated experiments relating the two-dimensional Tollmien-Schlichting mechanism with observed laminar boundary layer oscillations on a flat plate in low speed wind tunnels (Ref. 74). In the low speed case it was found that the dominant disturbances were pure velocity fluctuations due to grid-induced vorticity from the settling chamber.

When data began to become available from supersonic tunnels, it soon became apparent that the character and source of the

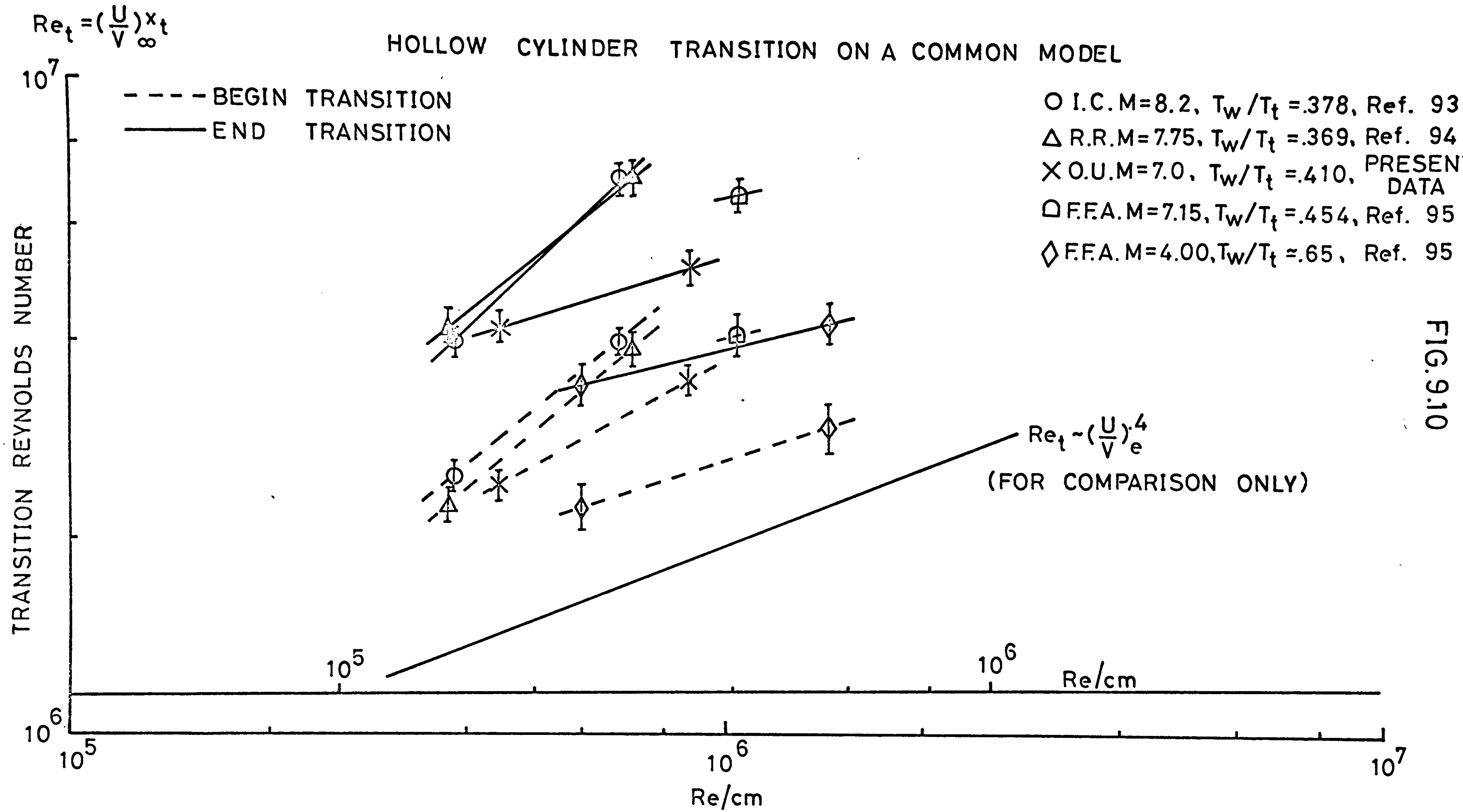

HOLLOW CYLINDER TRANSITION ON A COMMON MODEL
$Re_t = (\frac{U}{V})_\infty x_t$
BEGIN TRANSITION
END TRANSITION
O I.C. M=8.2, T_w/T_t =.378, Ref. 93
Δ R.R. M=7.75, T_w/T_t =.369, Ref. 94
X O.U. M=7.0, T_w/T_t =.410, PRESEN DATA
F.F.A. M=7.15, T_w/T_t =.454, Ref. 95
◊ F.F.A. M=4.00, T_w/T_t ≈.65, Ref. 95
$Re_t \sim (\frac{U}{V})_e^{.4}$
(FOR COMPARISON ONLY)
TRANSITION REYNOLDS NUMBER
Re/cm

FIG. 9.10

working section disturbances was different from the low speed case. Laufer (Ref. 96) found that changing the rms velocity fluctuations in the stagnation chamber by an order of magnitude had no effect on transition on a working section model for $M > 2.5$. Morkovin (Ref. 97) found no transition change at $M = 1.77$ for settling chamber velocity fluctuation changes of the same order of magnitude as Laufer's. Yet at the same time, Morkovin was reporting 'noise' levels of the order of 130 dB in the working section free stream (see Ref. 82). This lack of influence of velocity fluctuation was attributed to the large expansion ratios of supersonic nozzles. Laufer (Ref. 98) carried out the first quantitative series of measurements of the nature and source of these strong fluctuations using hot wire techniques in the JPL supersonic tunnel. Laufer was able to show by analysis of the hot wire mode diagrams that the measured disturbances could not be attributed to either pure velocity fluctuations associated with vorticity or to pure temperature (or entropy) fluctuations. By elimination, he then concluded that the disturbances must be due to a pure sound field. The fact that the mass flow fluctuations and temperature fluctuations exhibit a high degree of correlation strengthened the assumption of sound waves. He was able to show that these sound waves must have a preferred orientation angle which was greater than the Mach angle. This in turn implied a sound source velocity moving with respect to the free stream and the wall. From the sound orientation angle, the source velocity was estimated to be of the order of one half the free stream velocity for the Mach Number range of the tests ($M = 3$-5).

Laufer then suggested that the most probable source of this sound radiation was from the nozzle wall turbulent boundary layers. He presented some convincing evidence that this was indeed the case. The free stream fluctuation level was reduced by 20% when the wire probe was shielded from one of the tunnel wall's direct radiation by a flat plate in the working section. The order of magnitude decrease in mass flow fluctuation level when all the nozzle walls were made laminar was equally dramatic. Laufer was also able to show in a later paper (Ref. 99) that the radiated pressure field from the wall boundary layer scaled as the square of the mean wall shear stress (τ_w) for a given Mach Number and that the pressure fluctuation nondimensionalized by the wall shear increased with Mach Number.

A relation between the sound dominated free stream fluctuations and the vorticity and entropy dominated turbulent boundary layer fluctuations was considered theoretically by Phillips (Ref. 100) for high Mach Numbers. Conceptually, Phillips' approach consisted of a consideration of the turbulent eddies within the shear layer which are convected downstream at a mean velocity which is supersonic with respect to the free stream. These spatially random eddy patterns act as source generators of Mach waves which are radiated toward the free stream in a direction depending on the relative velocity between the mean eddy velocity and the free stream.

Laufer commented on Phillips' analysis in another paper (Ref. 101) in view of his own earlier experimental data. Laufer found the theory was qualitatively consistent with the main features of the experimentally observed free stream sound field. An explicit solution for finite Mach Numbers was not possible, however, and Laufer found the asymptotic $M \to \infty$ solution of Phillips to be inadequate to describe the functional behavior of the sound field intensity with M in the range below $M = 5$. The general observed features of a homogeneous sound field outside of the boundary layer with a preferred propagation direction which becomes more coherent with increasing Mach Number were, however, predicted by Phillips' asymptotic 'eddy Mach wave' model.

In summary then it is apparent that no adequate theoretical model exists which can predict the intensity and gross characteristics of the radiated pressure fluctuation field observed in supersonic wind tunnel working sections. The evidence associating this pressure field with the nozzle wall turbulent boundary layer is unmistakable. The strong increase of fluctuation intensity with Mach Number and its scaling with wall shear stress is also well established.

9.4.2 Noise-Transition Correlations

The interaction of a free stream pressure fluctuation field with a compressible laminar boundary layer and its effects on stability and transition has not been treated theoretically. Some experimental evidence exists, however, which qualitatively exhibits that a relation exists between the sound fluctuation level and the transition Reynolds Number on a model in the working section of a supersonic tunnel.

Some unpublished findings by Kendall of JPL were reported by Morkovin (Ref. 82) which indicated that the transition Reynolds Number (Re_t) was increased by a factor, > 2, when the tunnel wall boundary layer was changed from turbulent to laminar flow at $M = 4.5$. This test was performed in the same tunnel and at the same conditions at which Laufer (Ref. 98) reported an order of magnitude decrease in free stream mass flow fluctuations when the nozzle boundary layer was made laminar.

A new comprehensive series of experiments establishing in a more positive way the causal relationship between fluctuation levels and transition was reported by Pate and Schueler (Ref. 81).

These tests were performed at M = 3 and 5 in the AEDC tunnel A. The variation of the transition point with unit Re on a 3 inch hollow cylinder model was measured as the boundary layer on the inside of a 12 inch cylindrical shroud (mounted concentrically around the 3 inch model) was altered from laminar to turbulent. A small flat plate with a microphone flush mounted on the surface was also placed within the shroud near the test model. It was found that when the unit Reynolds Number of the flow was increased and the transition 'point' on the inside shroud surface moved forward past the point of the 3 inch test model, that the rms radiated pressure fluctuation level began to go up at the same time as the 3 inch cylinder transition Reynolds Number began to decrease. In fact, throughout the unit Re range of the tests the variation of Re_t was observed to follow the pressure fluctuation level as its approximate mirror image when plotted on the same abscissa (unit Re). Pate and Schueler were also able to substantiate Laufer's observation (Ref. 99) that the free stream pressure fluctuations (measured with the shroud off) scaled as the wall shear stress for a fully developed turbulent boundary layer on the wall.

Some recent data has been reported by Wagner, et. al. (Ref. 84) concerning free stream fluctuation measurements and transition behavior in a Mach 20 helium tunnel at NASA-Langley. The results of this important experiment strongly reinforced the findings discussed earlier in this section. This includes the observation that the free stream disturbances of a high speed wind tunnel are dominated by sound radiation from moving sources within the nozzle wall turbulent boundary layer and that there exists a strong correlation between the movement of the transition point on a model and the free stream pressure fluctuation level.

9.4.3 Correlation of Multi-Source Data

A. Pate & Schueler Correlation

A major effort to correlate empirically the relationship between nozzle wall boundary layer radiated sound and model transition was reported by Pate and Schueler (Ref. 81). They assembled a wide range of hypersonic transition data from several facilities and corrected the data for leading edge bluntness effects ($b \to o$) and for any differences in defining the transition (end) point. Since the scaling relation between free stream sound levels and wall shear stress had been established by earlier experiments, Pate and Schueler proposed correlating the transition data in terms of the mean nozzle wall skin friction coefficient up to the model location, $\bar{c}_f$, and displacement thickness, δ^*. They also proposed to include another length, c, the working section circumference, to account for the radiating area (per unit length). The parameter $Re_t \sqrt{\delta^*/c}$ correlated all the data for a particular tunnel size as a function of $\bar{c}_f$. The remarkable results of the correlation indicated that for a particular tunnel, Mach Number and unit Re effects on transition were systematically dominated by parameters which scaled the sidewall sound radiation, quite independent of any boundary layer stability considerations. The Mach Number range included was from M = 3 to M = 8 and unit Re variations by a factor of 20. Pate and Schueler then brought all the data onto one curve by the use of another factor containing a tunnel dimension. The final expression is given as

$$Re_t = \frac{0.0141(\bar{c}_f)^{-2.55}[0.56 + 0.44\ c_1/c]}{\sqrt{\delta^*/c}} \qquad (9.4.1)$$

where c_1 is a reference dimension (48 inches).

The correlation expressed in (9.4.1) is based on adiabatic wall transition experiments in closed working section, continuous running wind tunnels with adiabatic (or nearly adiabatic) sidewalls. It is not obvious why local conditions were used for δ^* and c while a mean value was used for skin friction. The choice must be related to the geometry of the radiated sound field with respect to the model location yet this cannot be predicted by present theoretical or experimental evidence. This perhaps explains why the correlation relies on arbitrary constants to effect some agreement even among very similar tunnels. The correlation used by Pate and Schueler for δ^* was based on considerable experimental evidence over the Mach Number range of the tests and were thus judged reliable. The case for their prediction method of $\bar{c}_f$ was less precise. In the internal report version of Ref. 81 they presented experimental evidence of $\bar{c}_f$ compared with the flat plate, zero pressure gradient theory of Van Driest (Ref. 102) on supersonic tunnel walls up to only M = 3. The general two-dimensional compressible momentum integral equation for arbitrary pressure gradient is given by Schlichting (Ref. 85) as

$$\frac{d\theta}{dx} + \frac{\theta}{u_\infty}\frac{du_\infty}{dx}\left[2 + \frac{\delta^*}{\theta} - M^2\right] = \frac{\tau_w}{\rho_\infty u^2_\infty} \equiv \frac{c_f}{2} \qquad (9.4.2.)$$

where momentum thickness (θ) and displacement thickness (δ^*) are defined in the standard (2-D) compressible form,

$$\theta = \int_0^\delta \frac{\rho u}{\rho_\infty u_\infty}\left(1 - \frac{u}{u_\infty}\right) dy \qquad (9.4.3)$$

and

$$\delta^* = \int_0^\delta \left(1 - \frac{\rho u}{\rho_\infty u_\infty}\right) dy \quad . \qquad (9.4.4)$$

It is apparent from an examination of (9.4.2) that there are conditions on nozzle walls where the second term on the left cannot be ignored locally, especially at high M. The success of the Pate and Schueler correlation may have been due to the use of closed working section tunnels with long straight walls in the test section where the pressure gradient term vanished locally. The mean skin friction coefficient may then have been dominated by the zero pressure gradient value. In fact, the use of this approximate $\bar{c}_f$ expression implied that the correlation probably could have been produced using local c_f with only the constants in (9.4.1) being changed.

The direct comparison of equa. (9.4.1) with the results on the Oxford Gun Tunnel would require some assumptions. The first factor to be considered was δ^*. An estimate for velocity thickness (δ) was obtained from Fig. 5.3 for $M \approx 7$, Re/cm = 1.75×10^5, and $T_w/T_t = 0.41$. The ratios δ^*/δ and θ/δ were obtained from the results summarized by Wallace (Ref. 65) for hypersonic cold wall conditions. Wallace obtained the integrated expressions for θ and δ^* from pitot profiles and an assumption of a Crocco (Pr = 1) relation between velocity and temperature. The values of δ^*/δ and θ/δ computed by Wallace compared favorably with other cold nozzle wall data he cited including some where temperature profiles were also measured. He concluded that the integrated values of δ^* and θ were relatively insensitive to the assumption of the Crocco relation, to pressure gradients, and to high total temperatures. The values of Wallace were computed for axi-symmetric nozzles and were found to differ from the two-dimensional case by less than 10% for δ/D values (D = nozzle diameter) greater than those of the Gun Tunnel test described above. The value of δ^* computed from the measured δ and the Wallace δ^*/δ value also compares with the faired mean δ^* correlation presented by Pate and Schueler in their report for the cold wall, M = 7 case.

An accurate value for the mean skin friction coefficient,

$\bar{c}_f$, would be difficult to determine from equa. (9.4.2) for the cold wall, hypersonic, contoured nozzle of the Gun Tunnel. The flat plate approximation to (9.4.2) is given as

$$c_f = 2 \frac{d\theta}{dx} \tag{9.4.5}$$

and the mean c_f follows as

$$\bar{c}_f = \frac{2\ \theta(L)}{L} \tag{9.4.6}$$

where L is the length from the origin of the boundary layer to the point where θ is measured. Using the measured value of θ at the exit plane and the length L = 34 inches for the Gun Tunnel nozzle, a rough estimate of $\bar{c}_f$ was obtained to calculate the transition Reynolds Number from (9.4.1). The value calculated ($Re_t \approx 3.7 \times 10^6$) compared favorably with the observed end of transition ($Re_t \approx 4.2 \times 10^6$). (No correction was made for leading edge bluntness effects on Re_t since for the conditions of the model and the tests, Potter and Whitfield's data [Ref. 77] shows this to be a negligible correction). This apparent reasonable agreement between predicted and measured Re_t should be treated with caution, however, in view of the strong dependence of the Re_t prediction on $\bar{c}_f$ and the many assumptions made to estimate $\bar{c}_f$ in the Gun Tunnel. As an example of the sensitivity of Re_t to the choice of $\bar{c}_f$, the mean skin friction coefficient was calculated by the method of Van Driest (Ref. 102) for the flow conditions of the Gun Tunnel test stated above. Using this new value, the predicted Re_t was increased by nearly 50% (to 5.25×10^6). In addition, it should be remembered that the Pate and Schueler correlation did not include any transition data with heat transfer. This was another factor present in the hollow cylinder experiments described in this chapter which would make a direct comparison with the Pate and

Schueler method uncertain.

Insufficient information concerning the wall boundary layer was available from the other facilities in which the hollow cylinder was tested to allow a meaningful approximate comparison of the data with the Pate and Schueler correlation. The general validity of the functional form of the correlation can be evaluated by a simple scaling analysis, however. A scaling approximation was possible because of the similarity of the nozzle conditions for the four sets of data reported in Sections 9.2 and 9.3. They were all open jet contoured nozzles operating under cold (or cooled) wall conditions and were roughly of the same slenderness ratio (length/diameter). In fact, the three gun tunnels tested used nozzles made from the same family of coordinates (see Section 2.2.2). The FFA-HYP-500 nozzle wall was water-cooled with wall temperature claimed not to exceed 500°K (Ref. 103). Since all tests in this tunnel were run 5-10 seconds after the flow started, it was likely that the wall temperature was below this value at the time of the tests. Ignoring the effects of changing Mach Number and nozzle wall T_w/T_t, the following scaling relationships were assumed to hold for the parameters appearing in equa. (9.4.1).

$$\left.\begin{array}{l} c_f \sim \bar{c}_f \sim Re_D^{-.2} \\ \delta^* \sim D\, Re_D^{-.2} \\ c \sim D \end{array}\right\} \qquad (9.4.7)$$

Substituting the scaling expressions of (9.4.7) into (9.4.1) yields the Re_t scaling expression

$$Re_t \sim (Re_D)^{.61}\left[.56 + \frac{6.72}{D}\right] \frac{1}{\phi[M, T_w/T_e]} \qquad (9.4.8)$$

where D is the nozzle exit diameter in inches and $\phi(M,T_w/T_e)$ is a function to account for Mach number and T_w/T_e effects not considered in the relations of (9.4.7).

Examining the M dependence of δ^* alone we can write

$$\delta^* = K_1 f_1(M) \tag{9.4.9}$$

or, $$(\delta^*)^{\frac{1}{2}} = [K_1 f_1(M)]^{\frac{1}{2}} = K_2 f_2(M) \tag{9.4.10}$$

where K_1 and K_2 are constants. Variations of δ^* with T_w/T_e are not considered in this analysis and are judged to be small compared with the M dependence for the temperatures encountered in these tests. Experimental evidence concerning δ^* growth with M for turbulent nozzle walls (at constant unit Re) has been presented by Laufer (Ref. 98). His data suggests a relation

$$\delta^* \sim (M)^{1.8} = f_1(M) \tag{9.4.11}$$

which gives in turn

$$f_2(M) = (M)^{.9} \tag{9.4.12}$$

Turning then to the M and T_w/T_e dependence of $\bar{c}_f$ we can write

$$\bar{c}_f = B_1 f_3(F_c, F_{Re_\theta}) = B_2 f_4(M, T_w/T_e) \tag{9.4.13}$$

and, $$[\bar{c}_f]^{2.55} = B_3 f_5(M, T_w/T_e) \tag{9.4.14}$$

where B_1 and B_2 are constants (for constant Re) and F_c and F_{Re_θ} are the factors defined by Spalding and Chi (Ref. 104) for reducing the compressible skin friction relation to the incompressible case. (The general validity of Ref. 104 for hypersonic cold wall experiments will be discussed in Chapter 10). The terms F_c and F_{Re_θ} cannot be expressed in a convenient explicit form but were found to be a function of M and T_w/T_e alone and have been tabulated in Ref. 104. The function f_5

can be computed from Ref. 104 for discrete cases for comparison of the effects of M and T_w/T_e on $\bar{c}_f$ at constant Re.

The final comparison of the scaling relation (9.4.8) would require the observed Re_t values to be normalized to a single M and T_w/T_e condition. The hollow cylinder results were normalized to the case of M = 8.2 and T_w/T_e = 5.47 by the following expression,

$$Re_t(8.2) = \frac{Re_t(M)}{\frac{f_5(8.2)}{f_5(M)} \cdot \frac{f_2(8.2)}{f_2(M)}} \tag{9.4.15}$$

$$= Re_t(M)\phi(M,T_w/T_e)$$

$$\text{where } \phi(M,T_w/T_e) = \frac{f_5(M)}{f_5(8.2)} \cdot \frac{f_2(M)}{f_2(8.2)} \ . \tag{9.4.16}$$

The second part of the r.h.s. of (9.4.16) is given from (9.4.12) as

$$\frac{f_2(M)}{f_2(8.2)} = \left(\frac{M}{8.2}\right)^{0.9} \tag{9.4.17}$$

whereas the first part is computed from Spalding and Chi (Ref. 104) as described in Appendix I.

The end-of-transition Reynolds Numbers determined from the hollow cylinder data in the various facilities are plotted [as corrected by equations (9.4.8) and (9.4.16)] against Reynolds Number based on nozzle exit diameter in Fig. 9.11. The results show a significant improvement of the correlation of the data when compared with the 'raw' data of Fig. 9.10. The results give added support to the central approach of the Pate and Schueler paper, viz. that supersonic and hypersonic transition experiments are dominated by factors scaling the nozzle wall turbulent boundary layer sound radiation intensity.

B. Emmons' Turbulent Spot Theory

The concept of the transition region of a boundary layer

FIG. 9.11

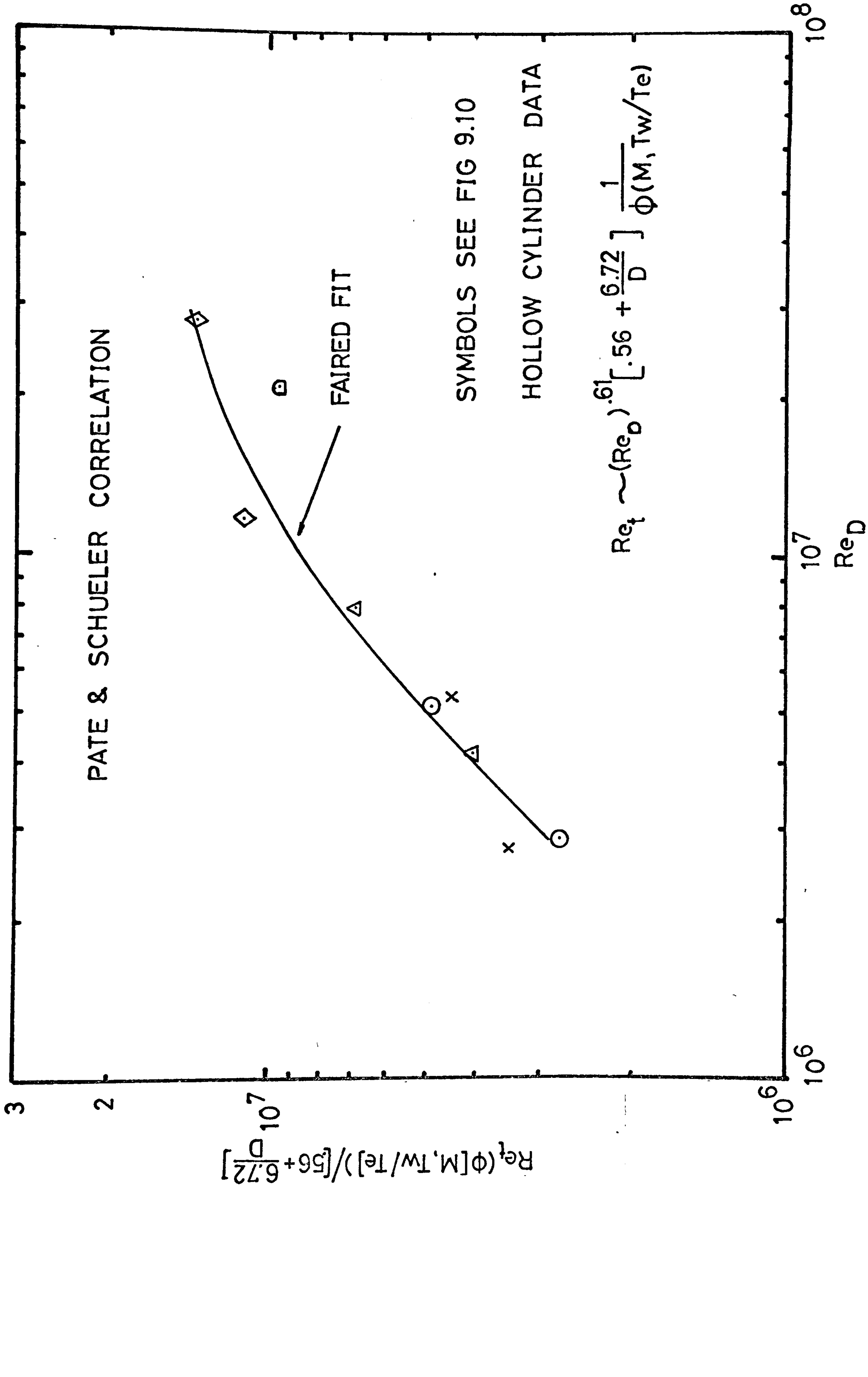

PATE & SCHUELER CORRELATION
FAIRED FIT
SYMBOLS SEE FIG 9.10
HOLLOW CYLINDER DATA
$Re_t \sim (Re_D)^{.61}[.56 + \frac{6.72}{D}]\frac{1}{\phi(M, Tw/Te)}$
$Re_t(\phi[M,Tw/Te])/[.56+\frac{6.72}{D}]$
Re_D
10^6
10^7
10^8
2
3

being composed of randomly mixed portions of turbulent and laminar flow was first observed and treated theoretically by Emmons (Ref. 105) for an incompressible fluid. Turbulent 'spots', produced randomly in the laminar boundary layer, grew three dimensionally as they travelled downstream until they merged and the flow was fully turbulent (or the probability of a turbulent spot being present approached unity). Subsequent work by other groups confirmed Emmons' observations and added much information concerning the shape and growth rates of the turbulent spots (see Refs. 106 and 107).

In a recent paper, Nagel (Ref. 88) has extended Emmons' theory to hypersonic conditions. The interesting result of the paper was the author's suggestion that the mean lateral spacing of the spot formation sites was impressed on the boundary layer by the free stream sound field produced by the wind tunnel wall turbulent boundary layer. The final expression for Re_t obtained by Nagel was given as

$$Re \sim \left[\left(\frac{u_\infty \sigma}{\nu_\infty}\right)\left(\frac{u_s}{u_\infty}\right)\frac{1}{\alpha^2 \lambda f}\right]^{\frac{1}{2}} \qquad (9.4.17)$$

where σ was the mean lateral spacing of the spot formation sites, u_s the mean spot velocity, α the growth angle of the spot, λ a factor related to the spot shape, and f a dimensionless frequency related to the mean spot formation rate. Although the details of the analysis can be found in the original paper (Ref. 88) the primary assumptions were 1) all spots were formed at a particular value of x at or near the leading edge, 2) all spots grew independently of other spots, and 3) the spot velocity and shape were independent of time. Relying primarily on the observations of supersonic turbulent spot details reported by James (Ref. 108), Nagel concluded that Re_t was determined mainly by σ and f in equa. (9.4.17) in addition to the unit Re, (u_e/ν_e). He then presented considerable circumstantial evidence that the spot spacing term, σ, was determined by the scale of the free stream disturbances at the boundary layer edge. Then following Laufer's observations (Ref. 98) that supersonic tunnel free stream disturbances were primarily sound radiation from the wall boundary layers, Nagel suggested that the scale of the disturbances must be proportional to the wall boundary layer thickness,

$$\sigma \sim \delta \sim D \, Re_D^{-.2} \qquad (9.4.18)$$

Equation (9.4.17) then becomes

$$Re_t \sim \left(\frac{u_\infty D}{\nu_\infty}\right)^{.4} \left[\frac{u_s}{u_\infty} \frac{1}{\alpha^2 \lambda f}\right]^{.5} \qquad (9.4.19)$$

Following James' (Ref. 108) high speed observations, Nagel claimed that u_s, α, λ and f were independent of unit Re with only f having a strong M dependence. From stability theory analysis, the most highly amplified disturbance frequency's M dependence gives

$$f \sim \frac{1}{M^{1.75}} \qquad (9.4.20)$$

Equation (9.4.19) then is given as

$$Re_t \sim Re_D^{.4} \, M^{.875} \qquad (9.4.21)$$

Equation (9.4.21) illustrates in a qualitative way the existence of a unit Re effect for a particular tunnel (D = constant) and the Mach number dependence of much high speed transition data. This expression also suggested a possible method of comparing transition data from similar tunnels of different size if both model wall and tunnel wall cooling ratios are comparable. It is interesting to note that Nagel's approach combines elements of stability theory with the concept of free stream disturbances imposing its <u>scale</u> as a boundary condition whereas the Pate and Schueler correlation considered only the <u>amplitude</u> of the free stream sound disturbances as the dominant effect in the transition process.

The hollow cylinder data from Sections 9.2 and 9.3 was plotted in Fig. 9.12 against Re_D with Re_t normalized to M = 8.2 by the $(M)^{.875}$ relation. The results indicate somewhat of an improvement over the original data especially with respect to Mach Number effects but still clearly did not account for all the 'facility effects' present in the tests. It is clear that a true test of the basic approach cannot be made until more experimental evidence is produced concerning the variation of the parameters in equa. (9.4.17) with M, unit Re and the tunnel free stream disturbance field at high Mach numbers. Based on experimental evidence to date, the purely empirical approach of Pate and Schueler holds more promise in correlating the effects of facility environment on transition measurements at high speeds.

FIG.9.12

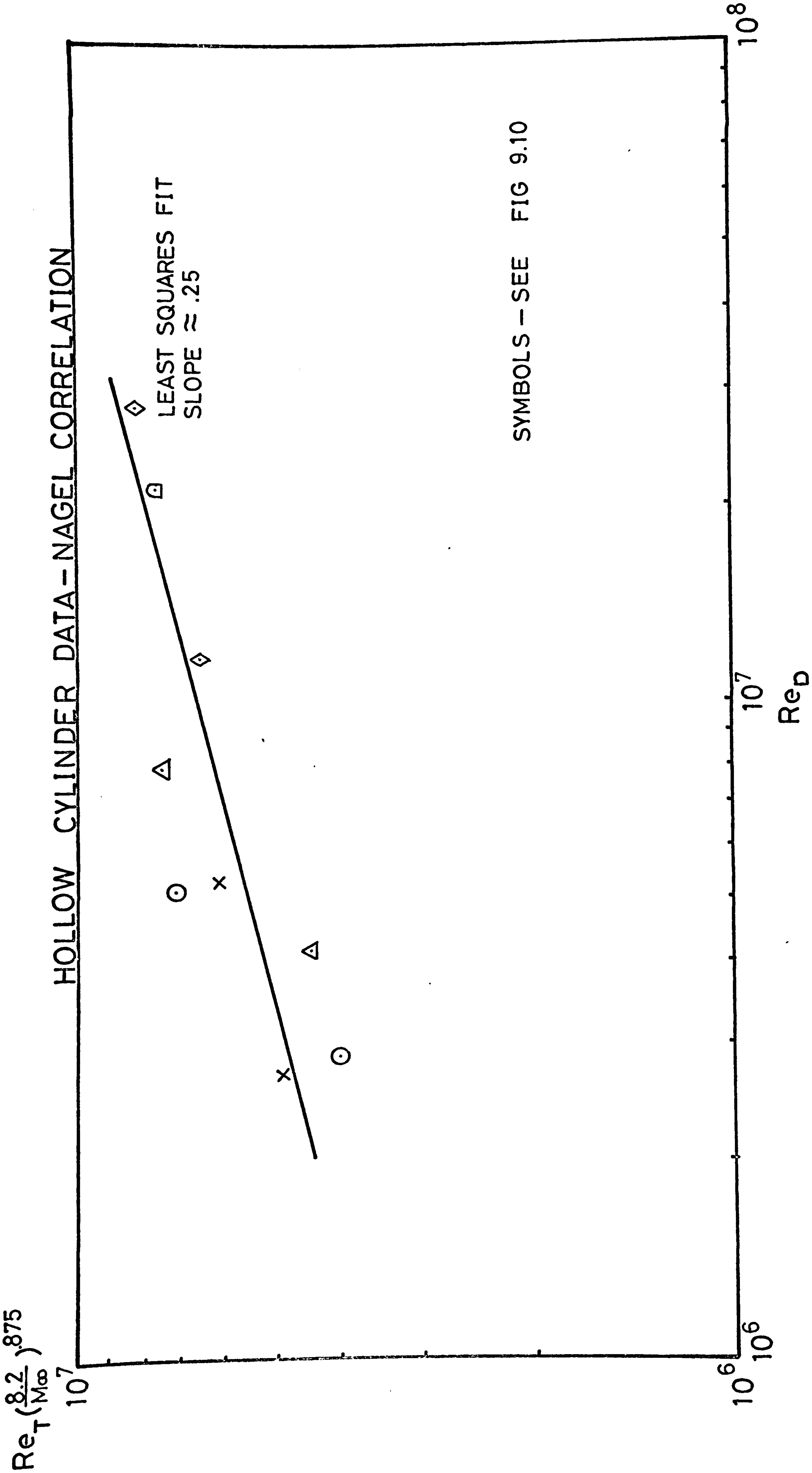
HOLLOW CYLINDER DATA - NAGEL CORRELATION
LEAST SQUARES FIT
SLOPE ≈ .25
SYMBOLS - SEE FIG 9.10
$Re_T (\frac{8.2}{M_\infty})^{.875}$
10^7
10^6
10^6
10^7
10^8
Re_D

CHAPTER TEN

HEAT TRANSFER MEASUREMENTS

To provide further insight into the behavior of hypersonic transitional boundary layers, two models were constructed and instrumented with heat transfer gauges for use in the Gun Tunnel. The model configurations selected were a sharp leading edge flat plate and a 10° total angle cone. The measurement of mean surface heat transfer rates has been shown to provide a very sensitive indication of the location of the transition region in hypersonic boundary layers (see Ref. 109). Richards (Ref. 87) has shown that the transition region defined by surface heat transfer measurements is essentially the same as that defined by surface pitot experiments. The thin film heat transfer gauges used in the experiments of this chapter also offered the advantage of increased frequency response over the surface pitot method and therefore made the observation of transient events in the transitional region possible.

The model configurations selected also made possible the determination of any transverse curvature effects on transition when compared with the hollow cylinder results of the previous chapter.

10.1 The Models

10.1.1 Sharp Leading Edge Flat Plate

A photograph of the flat plate heat transfer model is shown in Fig. 10.1. The overall length of the model was 13.7 inches and the width was 3.37 inches. The material used was 0.5 inch stainless steel and was ground to a surface finish of the order of 10 microinches. The leading edge had a 15° bevel angle on the underside and was ground and honed to a 'sharp' edge after

FIG. 10.1

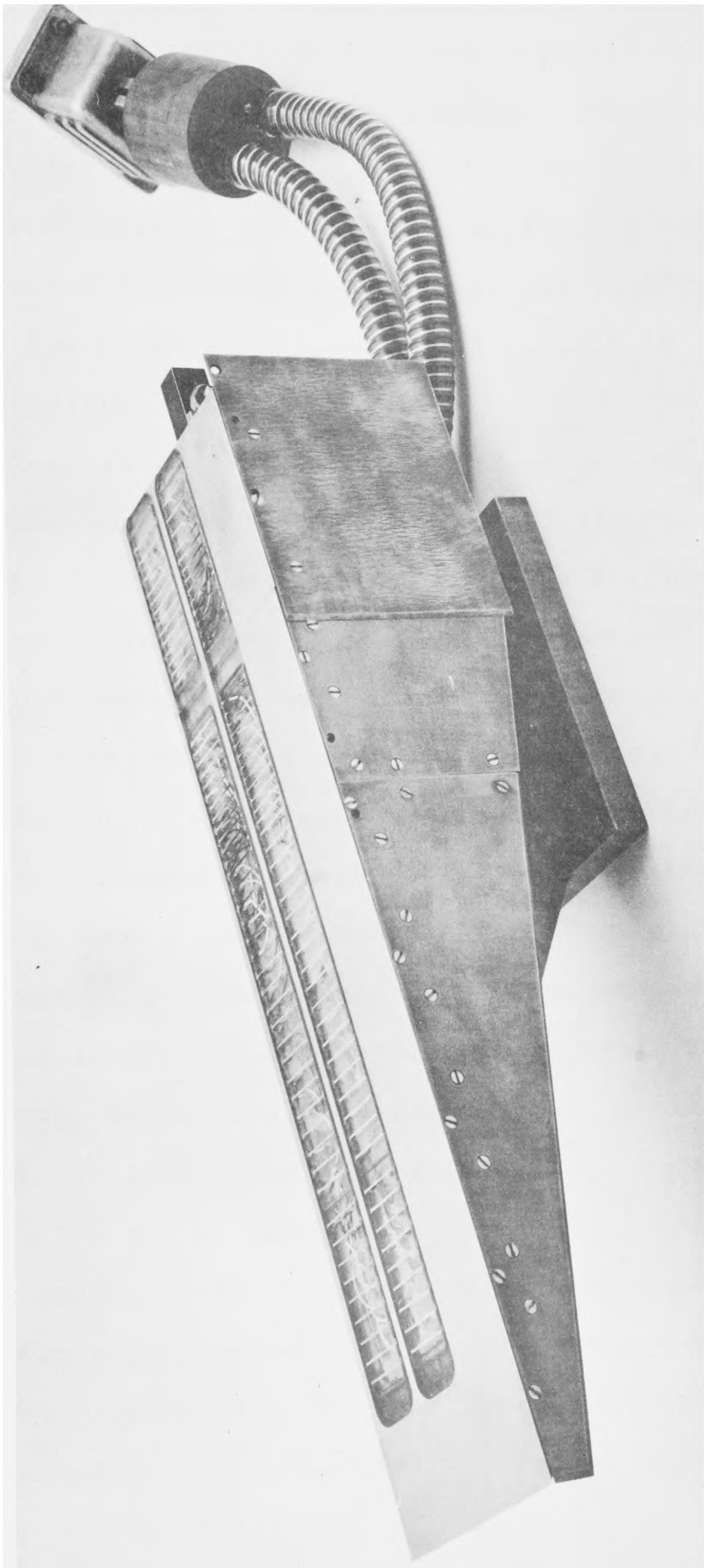

FLAT PLATE HEAT TRANSFER MODEL (No.1)

heat treatment and oil quenching. A precision travelling microscope measured the leading edge diameter as less than .0006 inches. Although the leading edge suffered occasional minor damage due to secondary diaphragm particle impact, the edge was easily returned to its original dimensions with a fine lapping stone. Mounting the model 0.45 inches above the nozzle centerline seemed to decrease the incidence of particle impact. The model leading edge was located $4\frac{1}{2}$ inches upstream of the nozzle exit plane.

Platinum thin film heat transfer gauges fabricated according to the procedures outlined in Section 3.2.1 were painted on fused quartz substrates using Hanovia 05-X platinum alloy suspension. The gauges were about 0.03 inches wide and 0.75 inches long and were mounted along the model top surface centerline at $\frac{1}{4}$ inch intervals starting at $1\frac{3}{4}$ inches from the leading edge. Between $8\frac{3}{4}$ inches and $10\frac{1}{2}$ inches from the leading edge the gauge spacing was $\frac{1}{8}$ inches. Beyond this, the gauges were not used in these experiments. A row of gauges of identical spacing was placed down one side of the model between the centerline gauges and the model edge to check the two dimensionality of the flow. (The sharp edged side plates shown in place in Fig. 10.1 were designed to prevent 'spillage' of the high pressure flow on the underside of the model to the test surface). The heat gauge substrates were set in the model into machined Araldite recesses and affixed with adhesive Araldite. Molten beeswax was poured into the remaining gaps between the quartz substrate and the Araldite with the excess scraped by hand to the model surface level.

It was difficult to measure quantitatively the effective roughness of the joints between the quartz and the model using a conventional profile stylus instrument. An estimate of this roughness was made by visual and tactile comparison with shim stock of known thickness. The roughness was estimated to be no greater than .001-.002 inches. High speed observations of the effect of roughness on transition (Ref. 87) indicated that roughness of this order of magnitude would have no effect on transition except perhaps very near the leading edge where the laminar layer is thinnest. Since the first non-machined joint on the model surface was $1\frac{1}{2}$ inches from the leading edge, this roughness was not expected to influence the experiments.

The platinum thin film gauges were calibrated for α, the thermal coefficient of resistivity, in a heated distilled water bath using a Norma precision bridge for resistance measurements. The substrate properties ρ, c and k were taken as the bulk values supplied by the manufacturer for quartz. During the actual heat transfer experiments, the gauges were run at a constant current and were connected to analogue circuits to convert the gauge surface temperature response directly to heat transfer rate to the surface. The details of the circuitry and methods used were described in Section 3.2. The final expression relating heat transfer and analogue output was given in equation (3.2.14) with β taken as

$$\beta = (\rho c k)^{\frac{1}{2}} = .0398 \text{ cal}/(\text{cm})^2 {}^{\circ}\text{C}(\text{sec})^{\frac{1}{2}}.$$

10.1.2 The 10° Cone Model

A photograph of the 10° cone model is shown in Fig. 10.2. The conical portion of the model has an axial length of $17\frac{1}{4}$ inches and a base diameter of 2.97 inches. A 3 inch long nylon cylindrical section has been fitted to the base as physical protection for the wiring to the gauges. The stainless steel nose section of the model had a tip diameter of .012 inches as

FIG. 10.2

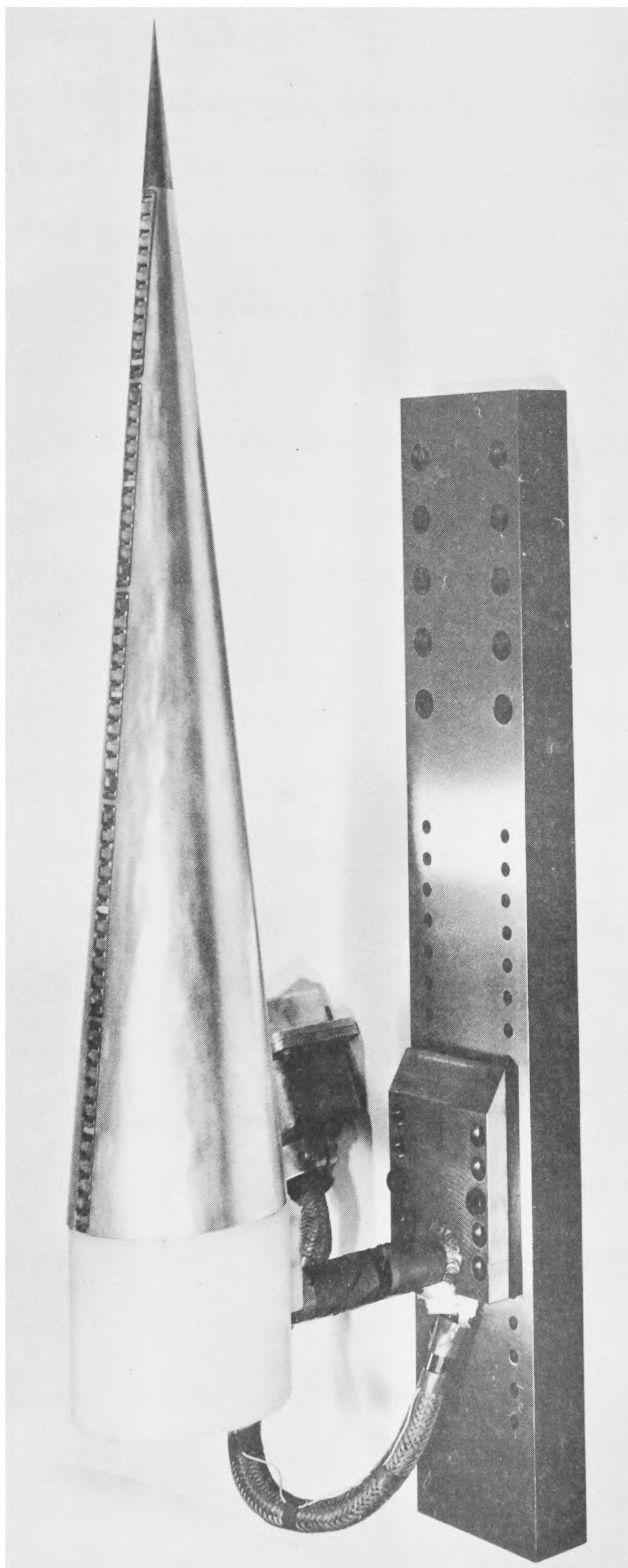

10° CONE HEAT TRANSFER MODEL

determined by a travelling microscope. Platinum thin film gauges, 0.05 inches wide and 0.32 inches long were mounted along the top generator of the cone at $\frac{1}{4}$ inch intervals starting $2\frac{1}{2}$ inches from the tip. The gauges were hand painted on quartz substrates which had been ground to the contour of the model. The model surface roughness was estimated to be less than 20 microinch and the roughness associated with model-substrate joints estimated to be less than .002 inches. As with the flat plate, the gauge section roughness was not considered to have any influence on transition because of its distance from the model tip.

The gauge α's were determined by distilled water hot bath experiments and the substrate properties taken as the value determined by the National Physical Laboratory who were responsible for the fabrication of the gauges and the model (see Section 3.2.5). The circuitry for the gauges with the analogue networks is the same as for the flat plate and was described in detail in Section 3.2.

The model was mounted $\frac{1}{4}$ inch above the nozzle centerline to avoid damage to the thin film gauges from diaphragm particles. The tip of the model was located 7 inches upstream of the nozzle exit plane. In this position the entire model was within the test rhombus defined by the Mach angle ($\sin^{-1} \frac{1}{M}$) and the useful test core diameter (∿ 5 inches) with the exception of the last 4 inches at the base of the model. All surface measurements reported in this chapter were made within the test rhombus.

10.2 Heat Transfer Results and Theoretical Comparisons

10.2.1 Test Conditions

The models were tested with the Mach 7 contoured nozzle in place. The Mach Number was assumed to be 7.0 for calculation purposes (see Section 5.2). All tests with the exception of one were run with a diaphragm pressure ratio of 20 yielding a total temperature of 720°K ± 10°K (Section 5.3). The model wall temperature was assumed to be at room temperature for the duration of all the tests giving a wall/total temperature ratio of 0.41. One test condition on the cone was performed at 985°K ± 15°K total temperature giving a wall/total temperature ratio of 0.30. The driving pressure was varied from 41 to 137 atmospheres to vary the free stream unit Reynolds Number from 1.75×10^5 to 5.55×10^5 per cm.

10.2.2 <u>Heat Transfer Results</u>

The measured heat transfer results on the flat plate and 10° cone model are presented in Figs. 10.3-10.9. The heat transfer values are presented in terms of the non-dimensional heat transfer coefficient, St_e, defined as

$$St_e = \frac{\dot{q}}{\rho_e u_e (c_p)_e (T_r - T_w)} . \tag{10.2.1}$$

The surface heat transfer rate per unit area, $\dot{q}$, was the value measured from the calibrated output of the analogue circuits. The gas properties were evaluated at the free stream conditions at the outer edge of the boundary layer. The specific heat, c_p, was considered constant throughout the boundary layer, an assumption in error by less than 10% for the temperature conditions of the tests. The recovery temperature (T_r) was defined by the relation

$$T_r = T_e + r\frac{(\gamma-1)}{2}(M_e^2)T_e . \tag{10.2.2}$$

where the recovery factor, r, was defined by

$$\begin{aligned} r &= (Pr^*)^{1/2} \quad \text{(laminar)} \\ r &= (Pr^*)^{1/3} \quad \text{(turbulent)} . \end{aligned} \tag{10.2.3}$$

The Prandtl Number, Pr*, was evaluated at a reference temper-

FLAT PLATE
SURFACE HEAT TRANSFER - I

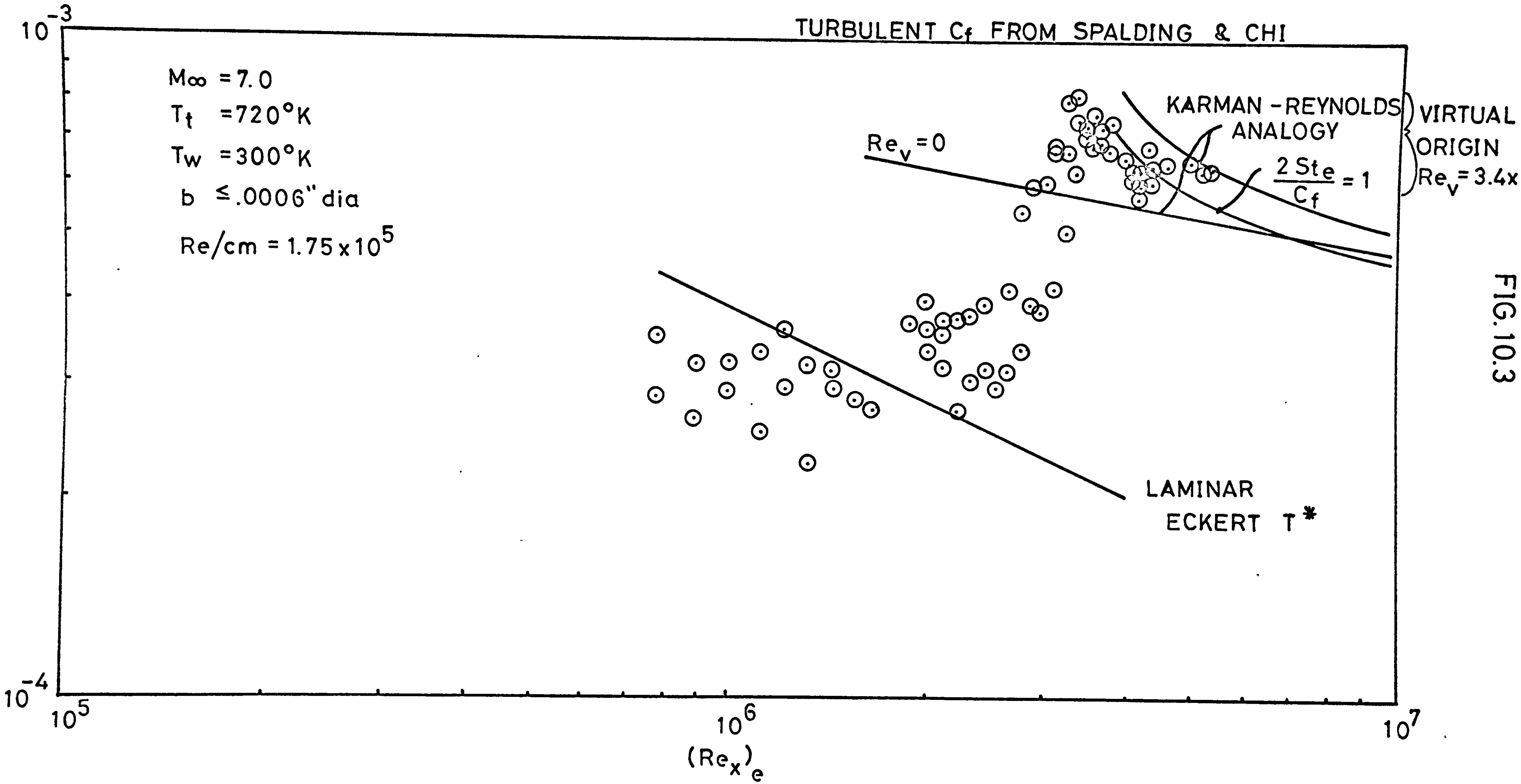

FIG. 10.3

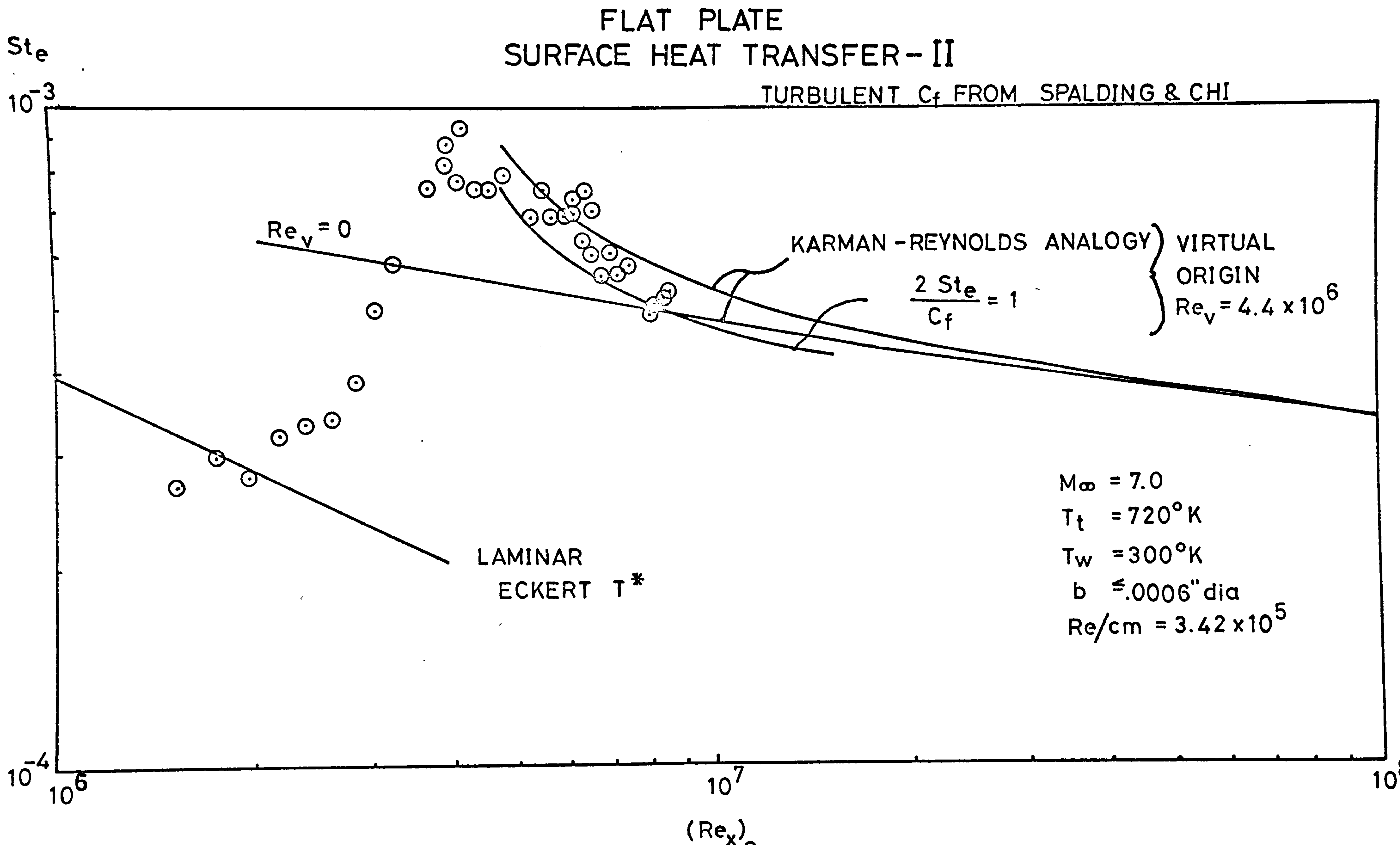
FLAT PLATE
SURFACE HEAT TRANSFER - II
TURBULENT C_f FROM SPALDING & CHI
St_e
10^{-3}
10^{-4}
10^6
10^7
10^8
$(Re_x)_e$
$Re_v = 0$
KARMAN - REYNOLDS ANALOGY
$\frac{2\,St_e}{C_f} = 1$
VIRTUAL ORIGIN
$Re_v = 4.4 \times 10^6$
LAMINAR
ECKERT T^*
$M_\infty = 7.0$
$T_t = 720°K$
$T_w = 300°K$
b $\leq .0006''$ dia
$Re/cm = 3.42 \times 10^5$

FIG.10.4

FIG.10.5

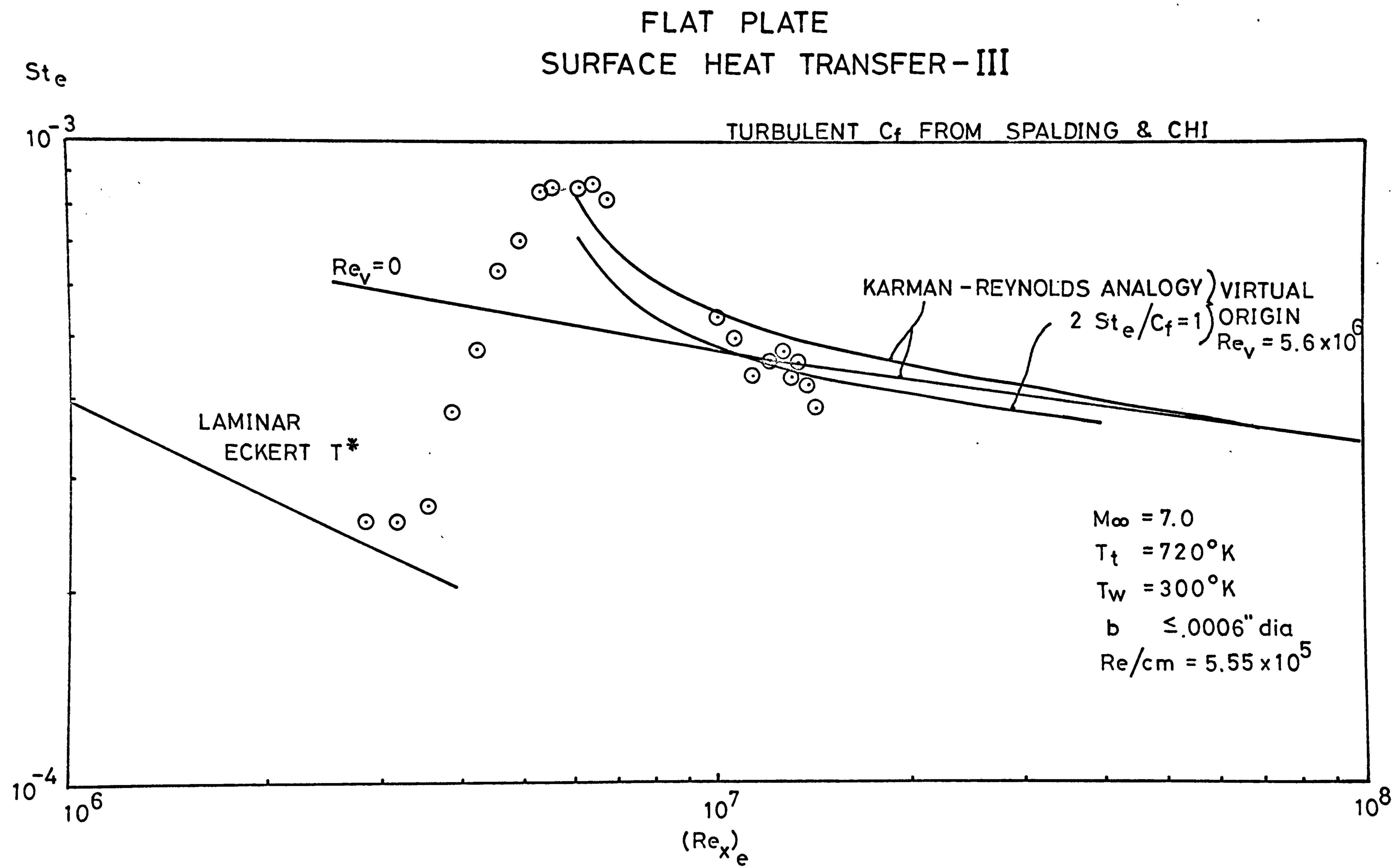

FLAT PLATE
SURFACE HEAT TRANSFER - III
TURBULENT Cf FROM SPALDING & CHI
St_e
10^-3
10^-4
10^6
10^7
10^8
(Re_x)_e
Re_v = 0
LAMINAR ECKERT T*
KARMAN - REYNOLDS ANALOGY
2 St_e/C_f = 1
VIRTUAL ORIGIN Re_v = 5.6 x 10^6
M∞ = 7.0
T_t = 720°K
T_w = 300°K
b ≤ .0006" dia
Re/cm = 5.55 x 10^5

FIG.10.6

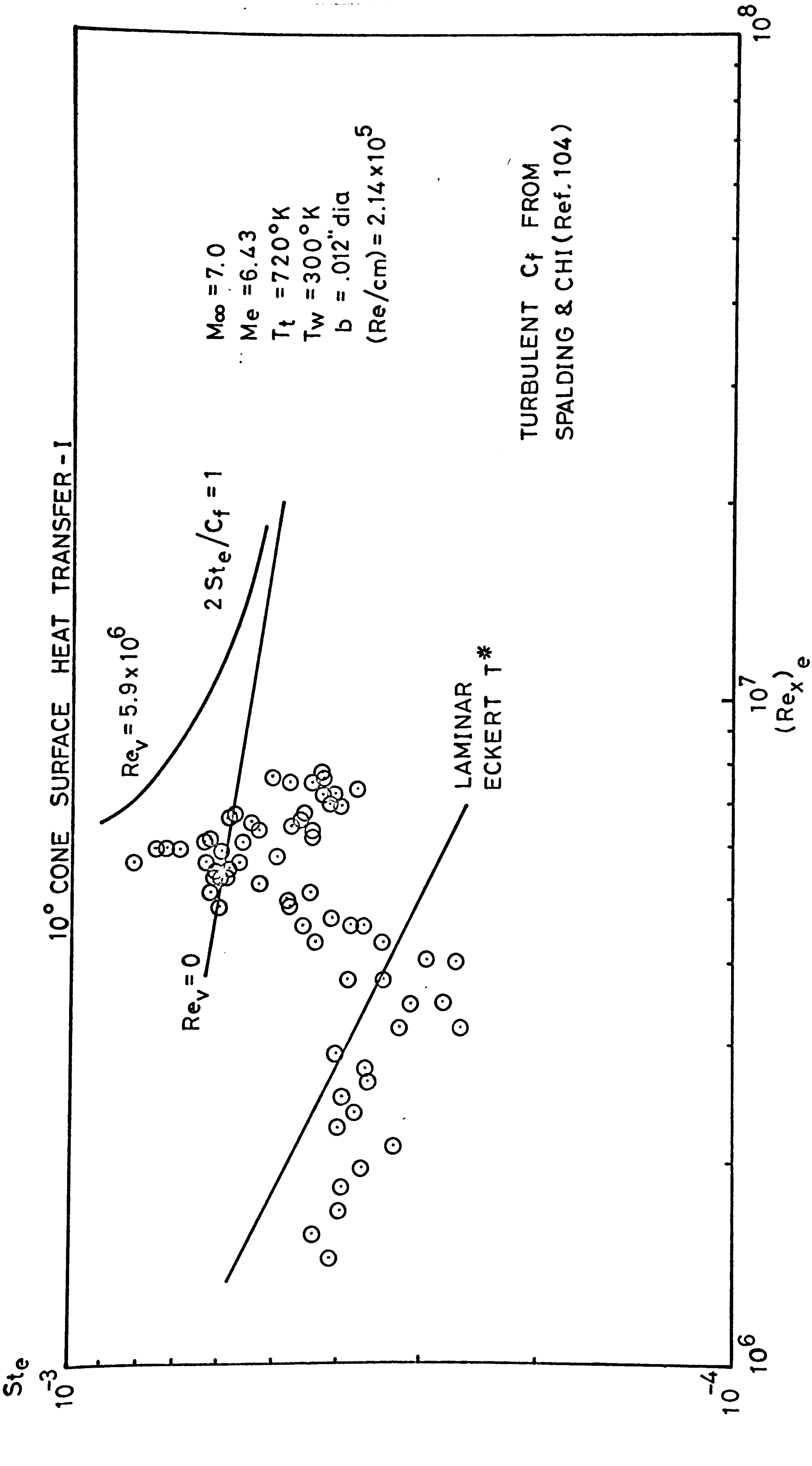

10° CONE SURFACE HEAT TRANSFER - I
$Re_v = 5.9 \times 10^6$
$2\,St_e/C_f = 1$
$Re_v = 0$
LAMINAR
ECKERT T*
$M_\infty = 7.0$
$Me = 6.43$
$T_t = 720°K$
$T_w = 300°K$
$b = .012''$ dia
$(Re/cm) = 2.14 \times 10^5$
TURBULENT C_f FROM
SPALDING & CHI (Ref. 104)
St_e
10^{-3}
10^{-4}
10^6
10^7
10^8
$(Re_x)_e$

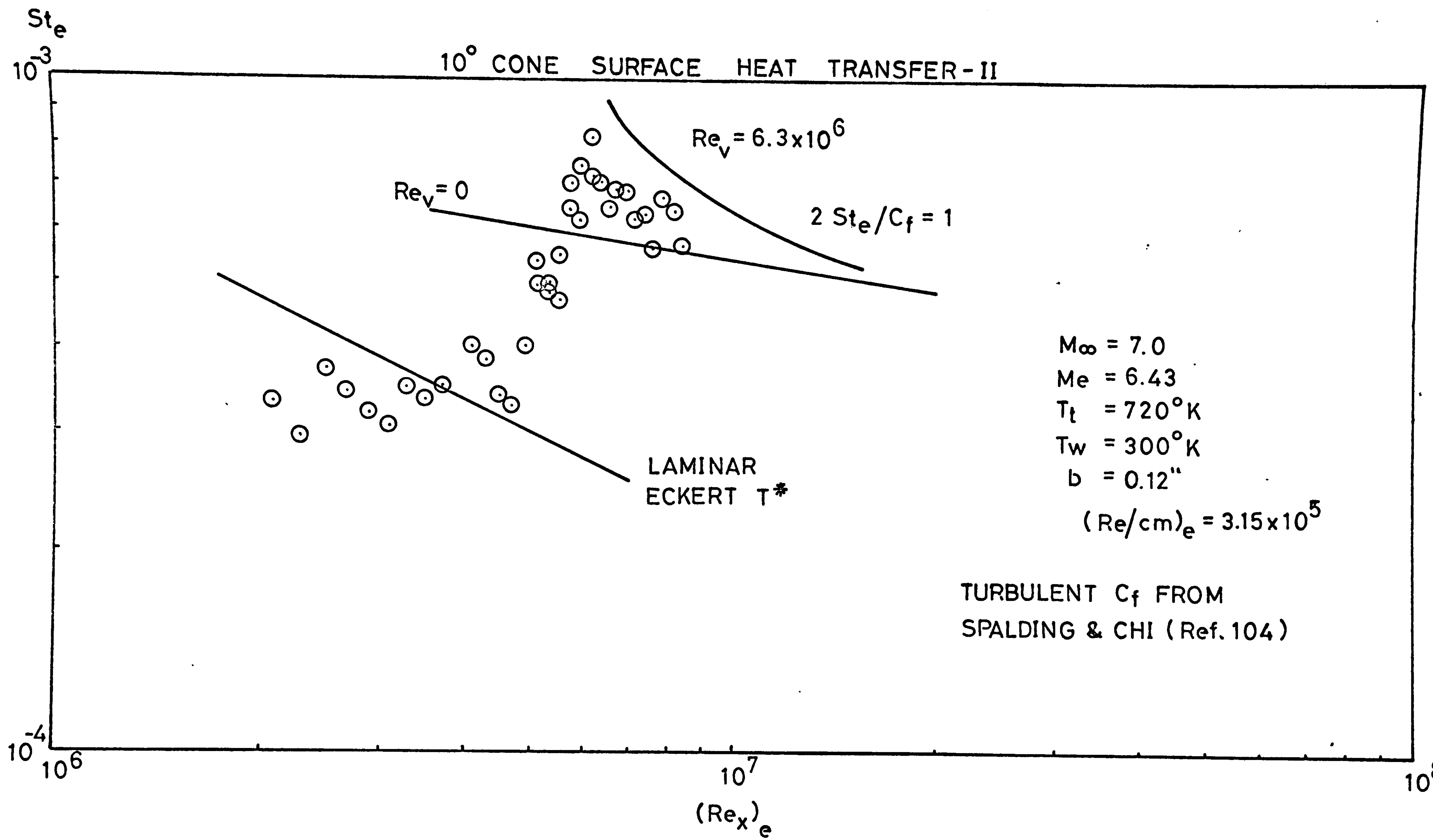

10° CONE SURFACE HEAT TRANSFER - II
St_e
10^{-3}
10^{-4}
$Re_v = 6.3\times10^6$
$Re_v = 0$
$2\,St_e/C_f = 1$
LAMINAR
ECKERT T^*
$M_\infty = 7.0$
$Me = 6.43$
$T_t = 720°K$
$Tw = 300°K$
$b = 0.12''$
$(Re/cm)_e = 3.15\times10^5$
TURBULENT C_f FROM
SPALDING & CHI (Ref. 104)
10^6
10^7
10^8
$(Re_x)_e$

FIG.10.7

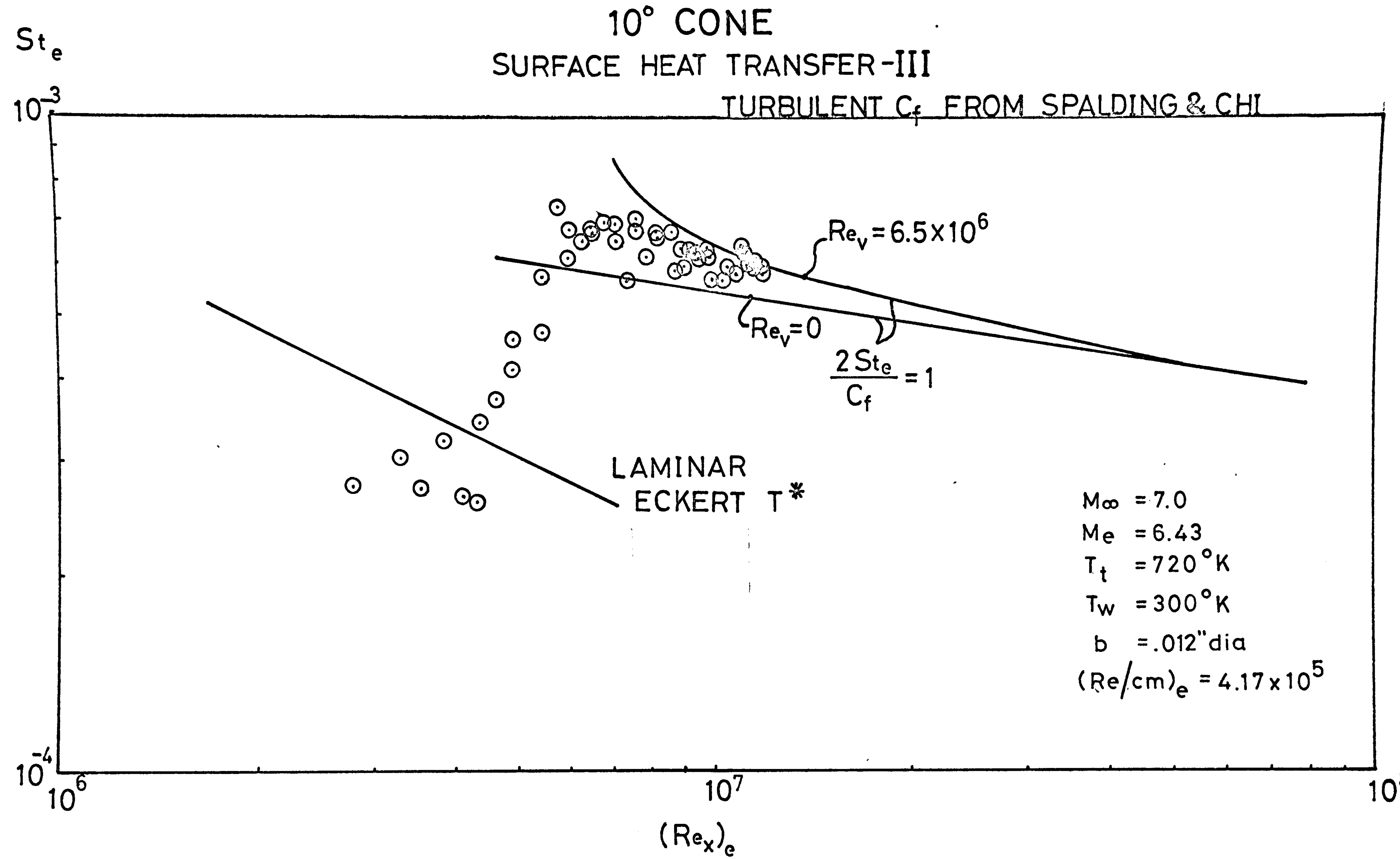

10° CONE
SURFACE HEAT TRANSFER-III
TURBULENT C_f FROM SPALDING & CHI
St_e
10^{-3}
10^{-4}
10^6
10^7
10^8
$(Re_x)_e$
$Re_v = 6.5 \times 10^6$
$Re_v = 0$
$\frac{2St_e}{C_f} = 1$
LAMINAR
ECKERT T*
$M_\infty = 7.0$
$M_e = 6.43$
$T_t = 720°K$
$T_w = 300°K$
$b = .012"$ dia
$(Re/cm)_e = 4.17 \times 10^5$

FIG. 10.8

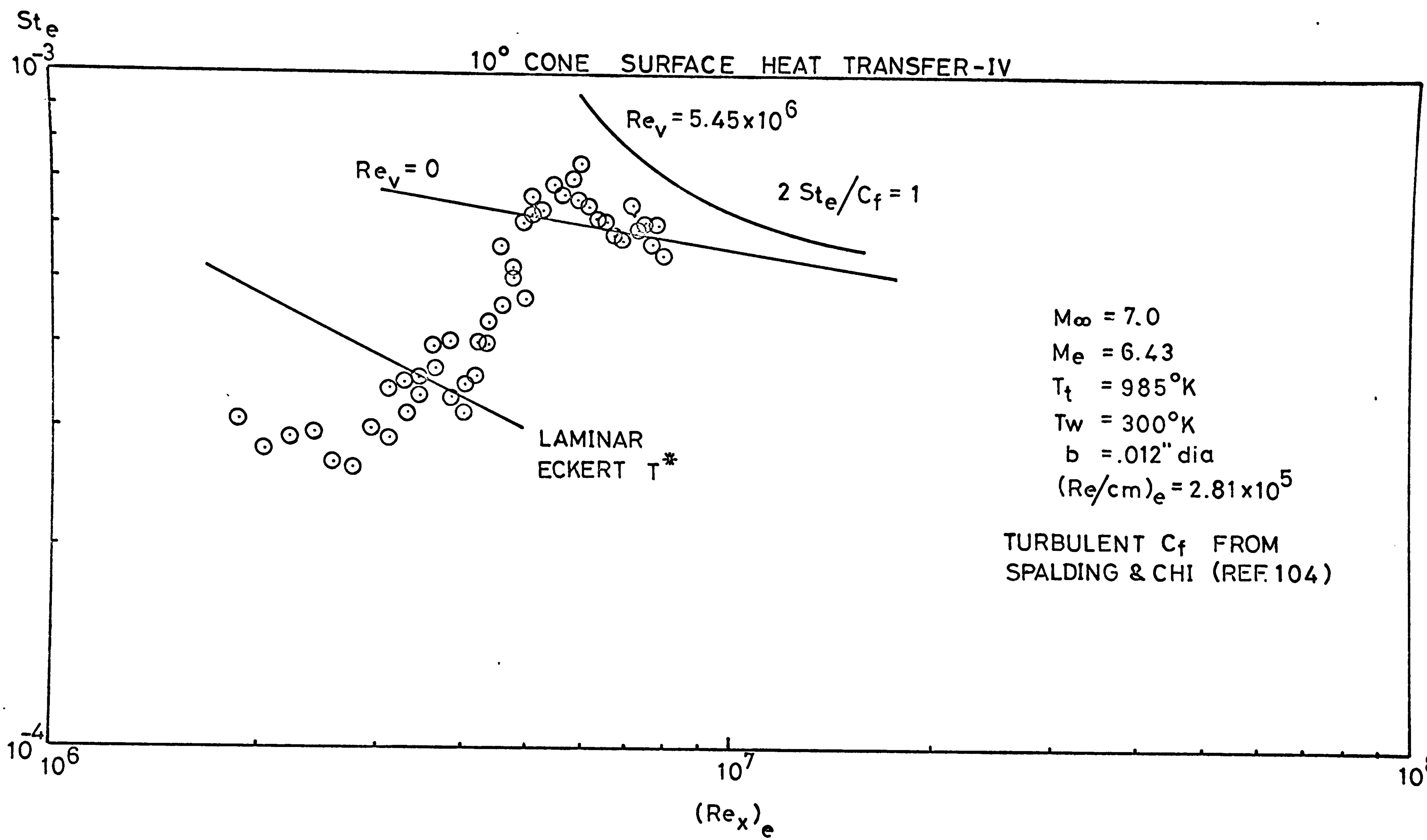
10° CONE SURFACE HEAT TRANSFER-IV
St_e
10^{-3}
10^{-4}
$Re_v = 5.45 \times 10^6$
$Re_v = 0$
$2\,St_e/C_f = 1$
LAMINAR
ECKERT T^*
$M_\infty = 7.0$
$M_e = 6.43$
$T_t = 985°K$
$T_w = 300°K$
b = .012" dia
$(Re/cm)_e = 2.81 \times 10^5$
TURBULENT C_f FROM
SPALDING & CHI (REF. 104)
10^6
10^7
10^8
$(Re_x)_e$

FIG.10.9

ature, T*, defined by Eckert (Ref. 110) as

$$T^* = T_e + 0.5(T_w - T_e) + 0.22(T_r - T_e). \qquad (10.2.4)$$

It is obvious from the inter-relationship of equations (10.2.2)-(10.2.4) that an iteration is needed to determine the recovery temperature. This is easily accomplished because of the weak variation of Pr with temperature and due to the fact that T* is very near room temperature for the conditions of the Gun Tunnel tests. The Stanton Number for transitional data is expressed in terms of a recovery temperature linearly interpolated between the laminar value and the turbulent value, depending on the x location of the data point between the beginning and end of transition location.

The Reynolds Numbers in Figs. 10.3-10.9 were evaluated at free stream conditions at the outer edge of the boundary layer and based on the distance from the model leading edge (or tip).

10.2.3 Theoretical Comparisons

A. The Laminar Case

The Eckert reference temperature method for predicting compressible laminar heat transfer (Ref. 110) was used as a comparison with the heat transfer values measured. The Eckert method is based on an empirically determined equivalence between the incompressible and compressible case if an intermediate (reference) temperature (or enthalpy) is used to evaluate fluid properties in the latter. The compressible Stanton Number is then, for a flat plate, given as

$$St^* = 0.332(Pr^*)^{-2/3}(Re_x^*)^{-1/2} \qquad (10.2.5)$$

where

$$Re_x^* \equiv \frac{\rho^* u_e x}{\mu^*} = (Re_x)_e \frac{T_e}{T^*} \frac{\mu_e}{\mu^*} \qquad (10.2.6)$$

and

$$St^* \equiv \frac{\dot{q}}{\rho^* u_e (c_p)_e (T_r - T_w)} = St_e \frac{T^*}{T_e} \qquad (10.2.7)$$

with all starred (*) properties evaluated at the reference temperature given by equa. (10.2.4). The Prandtl Number was evaluated from the curves of Ref. 49. The Stanton Number on a cone surface is $\sqrt{3}$ times the flat plate expression at the same local conditions as determined from the Mangler transformation to the boundary layer equations.

The predicted laminar values of St_e are shown on the figures (10.3)-(10.9) and are seen to generally overpredict the values measured except in the region very close to where the heat transfer begins to rise with the onset of transition. The reason for this discrepancy is not clear. Richards (Ref. 87) and Softley (Ref. 92) have reported good agreement with the Eckert T* prediction for hypersonic, cold wall flat plates and slender cones respectively. Viscous interaction could not account for the observed effects on the flat plate because of the distance from the leading edge of the measurements. Some of the scatter could be attributed to the ± 3% variation in total pressure from run to run which was not corrected for in the measurements. The films were cleaned with ether and pure grade acetone between runs to eliminate scatter due to surface contamination. The scatter was generally greatest for the lowest unit Re cases where the signal levels were very low.

Another interesting aspect of the laminar data was that the heat transfer trend with Re appeared to have a lesser slope than that predicted by theory. Instead of decreasing in proportion to the increasing boundary layer thickness ($\sim \sqrt{x}$), the heat transfer drop appeared to be at least partially offset by some process which increased the rate of heat conduction through the boundary layer. This mechanism could be related to the strong fluctuation levels observed to develop and grow within the laminar region by the hot wire analysis described in Chapter 11. Assuming the fluctuations to be associated with intermittent turbulent spot formation, a simple model would then exist to explain qualitatively the increased efficiency of energy transport with the approach toward transition. The fluctuation observations will be discussed more completely in Chapter 11.

B. The Turbulent Case

The prediction of compressible turbulent heat transfer rates involves several basic assumptions. Generally the only analytically feasible approach is to obtain a reasonable expression relating the wall skin friction coefficient to the Reynolds Number and then in turn proposing a suitable form of the relation between the skin friction coefficient and the non-dimensional heat transfer coefficient (Reynolds analogy). This approach in the present case is complicated by the scarcity of data available concerning the skin friction coefficient and the Reynolds analogy appropriate to hypersonic cold wall conditions. The situation is further complicated when applying a theory to models where the turbulent boundary layer does not originate at the leading edge. The definition of the virtual origin of the turbulent boundary layer then becomes important. These areas of uncertainty will now be discussed in view of existing experimental evidence at or near the flow conditions of the present tests.

Neal (Ref. 111) has reported direct skin friction measurements at $M = 6.8$ and $T_w/T_e = 0.5$ on a flat plate. Neal found that the best overall correlation of skin friction coefficient was given by the Spalding and Chi (Ref. 104) transformation between the compressible and incompressible skin friction expression when the virtual origin was taken as the location of the peak of the surface heat transfer rate (end of transition). Spalding and Chi had suggested that a unique relation exists between $F_c c_f$ and $F_R Re_x$ (or $F_{R_\theta} Re_\theta$) where c_f is the compressible skin friction coefficient and the factors F_c and F_R (or F_{R_θ}) were functions of Mach Number and the wall/total temperature alone. Spalding and Chi derived an expression for F_c from mixing length theory and deduced F_R semi-empirically.

The only other direct measurement of turbulent skin friction reported for hypersonic, cold wall conditions was the work of Wallace (Ref. 65) on a flat plate and shock tunnel wall. The nozzle wall tests were in a Mach Number range of 6.6-8.0, and a wall/total temperature range of about 0.1-0.3. Combining the wall c_f measurements with boundary layer momentum thickness calculations, Wallace was able to compare skin friction with the momentum thickness Reynolds Number, thus eliminating the uncertainties of selecting a virtual origin of the turbulent boundary layer. His analysis then showed that the data was best correlated by the method of Spalding and Chi when compared with several other compressible skin friction predictions. Wallace also obtained reasonable agreement with Spalding and Chi for his flat plate data assuming a virtual origin calculated by momentum thickness matching in the transition region.

Another recent experimental work which suggested Spalding and Chi as the most consistent correlation method for hypersonic, cold wall skin friction was that reported by Perry and East (Ref. 112). These measurements were made on a hypersonic gun tunnel nozzle wall and were less direct in that skin friction was inferred from velocity profile measurements.

The above cited reports of Wallace (Ref. 65), Neal (Ref. 111) and Perry and East (Ref. 112) also included direct measurements of heat transfer to the wall. This information provided a direct means of evaluating the Reynolds analogy factor ($2\ St_e/c_f$) when combined with the skin friction measurements. Neal found that the Reynolds analogy factor was predicted quite closely by a modified form of the Kármán incompressible three zone turbulent boundary layer analysis (see Ref. 85, p. 496). The Kármán expression is given as

$$\frac{2St_e}{c_f} = \left\{1 + 5\left(\frac{c_{f_i}}{2}\right)^{\frac{1}{2}}\left[(Pr-1) + \ln\left(\frac{5Pr + 1}{6}\right)\right]\right\}^{-1} \tag{10.2.8}$$

and was transformed to the compressible plane by evaluating Pr at a reference temperature and by converting the skin friction term on the r.h.s. to the Spalding and Chi incompressible value ($= F_c c_f$). (also see Ref. 113).

Wallace found that while the Kármán expression (10.2.8) was within the scatter of his data, the Reynolds analogy factor could equally well be given simply by unity. Wallace re-examined Neal's data and found that it could also be well described by assuming a value of unity for the factor $2\ St_e/c_f$. Perry and East also confirmed these observations by suggesting that the unmodified Reynolds analogy resulted in the best comparisons with their data.

Based on this limited experimental evidence, values of turbulent heat transfer were then calculated using the Spalding and Chi method for predicting the skin friction coefficient at the conditions of the present tests. Both the unity Reynolds analogy factor and the modified Kármán expression (equation 10.2.8) were used to compare the flat plate results in Figs. 10.3-10.5. Because of the closeness of the two methods, only the case $2\ St_e = c_f$ was used for the cone predictions (Figs.

10.6-10.9).

The degree of uncertainty introduced by the selection of the virtual origin point of the turbulent boundary layer is displayed in the figures. Two virtual origins were selected to represent the widest possible range of reasonable choices, viz. the model leading edge or tip ($Re_v = 0$), and the location of the peak surface heat transfer rate (end of transition). It is seen that in the region of peak heat transfer, the prediction is improved by selecting the origin at the end of transition. The two methods rapidly converge, however, at Reynolds Numbers not far downstream of the peak and the data (where it was measured sufficiently far downstream) was adequately described by either method. Some authors have attempted to correlate flat plate turbulent heat transfer based on some theoretically more reasonable virtual origin. These include the extrapolation of the turbulent momentum thickness to zero (Ref. 87) and the intersection of the laminar momentum thickness growth with the turbulent momentum thickness (Ref. 65). These locations fall between the two extremes plotted here and could only offer some marginal improvement in the region of the peak heating if at all. It does not seem unreasonable that in view of the complicated non-linear transition process which precedes the turbulent boundary layer, that the virtual origin is best selected by empirical methods rather than theoretical extrapolation methods.

The anomalous behavior of the 10° cone turbulent heat transfer data at the lowest unit Re case (Fig. 10.6) could possibly be attributed to model interaction with the Mach wave defining the test rhombus. The data at a Re above 6.5 million was taken at a 'x' location within one inch of the expected interaction location. The unusual drop in the heat transfer level could have been due to either the interaction region being further upstream than expected or to upstream influence effects through the boundary layer.

10.3 Transition Results

The measured heat transfer distributions of Figs. 10.3-10.9 provided a very convenient means of defining the location and extent of the transition region on the models. Defining the beginning of transition as the location at which the surface heat transfer rate first started to increase and defining the end of the transition process as coincident with the peak of the heat transfer rate, the transition Reynolds Numbers were plotted in Fig. 10.10 against the unit Re for the two models. Also included in the figure for comparison were the hollow cylinder results from the Gun Tunnel tests described in Chapter 9. A direct comparison is realistic in this case because of the consistency of the method of transition definition and because the tests were all conducted in the same facility. All the models tested could be considered to be at a sharp leading edge configuration based on Potter and Whitefield's (Ref. 77) findings for flat plates (and hollow cylinders) and Stetson and Rushton's (Ref. 109) observations on cone bluntness effects. The transition results in Fig. 10.10 are also tabulated in Table 10 below.

Before discussing the general trends of Fig. 10.10, the nature of the heat transfer gauge outputs will be discussed in view of what detail they may add to an improved understanding of the relationship between the actual transition process and the convenient definitions of transition assumed above. The analogue circuit heat transfer output traces are shown in Fig. 10.11 for a few characteristic positions on the 10° cone model.

TABLE 10

TRANSITION RESULTS SUMMARY

$M_\infty = 7.0$

$T_w = 300^\circ K$

Model	$(\times 10^{-5})$ $(Re/cm)_e$	T_t (°K)	T_e (°K)	$(\times 10^{-6})$ Re_{t_b}	$(\times 10^{-6})$ Re_{t_e}	(cm) X_{t_b}	(cm) X_{t_e}	(cm) ΔX_t
H.Cylinder	1.75	720	66.5	2.45	4.25	14.00	24.30	10.30
"	3.42	"	"	3.50	5.25	10.20	15.35	5.15
Flat Plate	1.75	"	"	2.25	3.40	12.83	19.45	6.63
" "	3.42	"	"	2.40	4.40	7.02	12.87	5.85
" "	5.55	"	"	3.00	5.60	5.40	10.10	4.70
10° Cone	2.14	"	77.8	3.50	5.90	16.36	27.60	11.24
" "	3.15	"	"	4.00	6.30	12.70	20.00	7.30
" "	4.17	"	"	4.10	6.50	9.82	15.60	5.78
" "	2.81	985	109	3.50	5.45	12.45	19.40	6.95

FIG.10.10

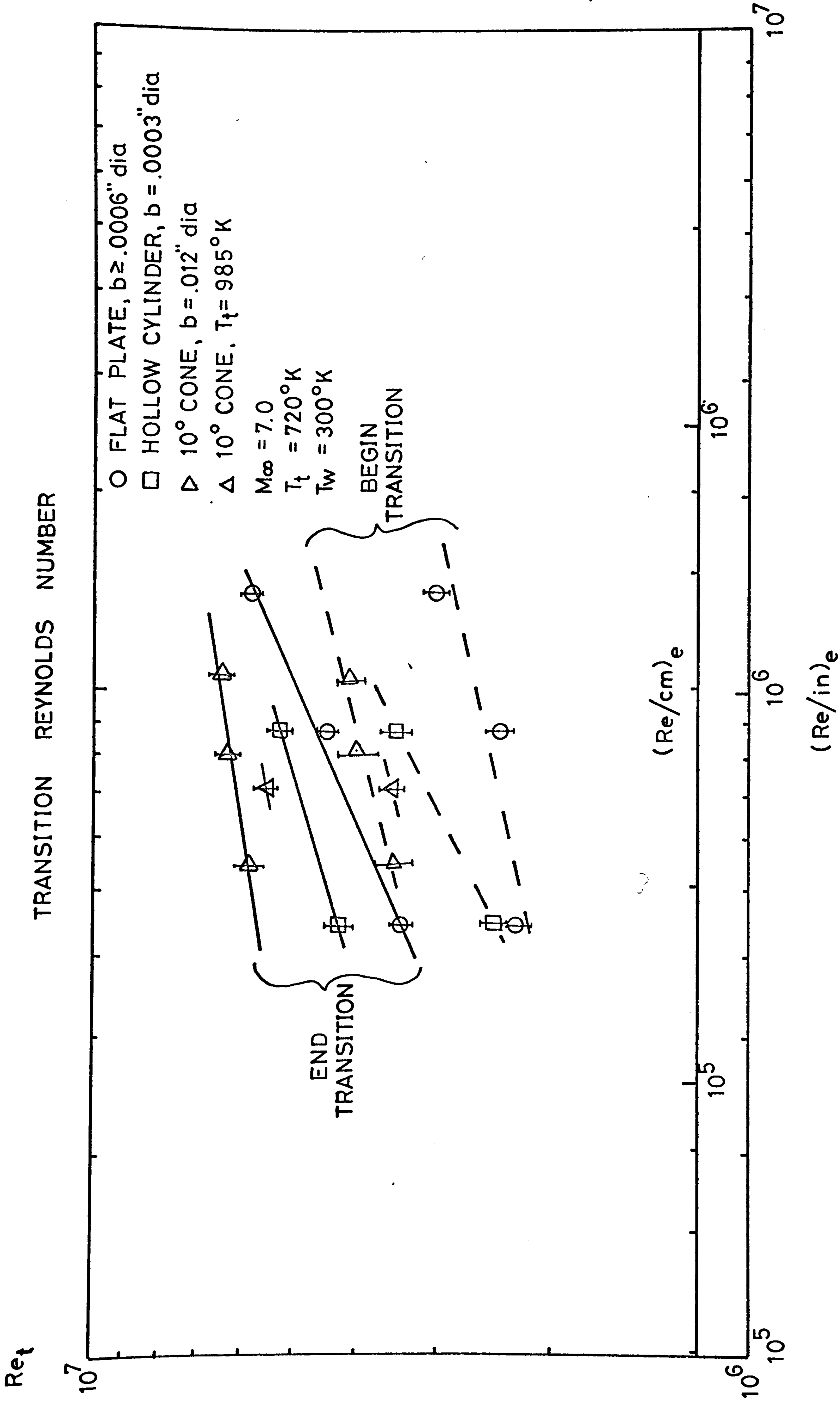
TRANSITION REYNOLDS NUMBER
O FLAT PLATE, b≥.0006" dia
□ HOLLOW CYLINDER, b = .0003" dia
▷ 10° CONE, b = .012" dia
△ 10° CONE, T_t = 985°K
M_∞ = 7.0
T_t = 720°K
T_W = 300°K
BEGIN TRANSITION
END TRANSITION
Re_t
10^7
10^6
10^5
$(Re/cm)_e$
$(Re/in)_e$

It will be remembered from Section 3.2 that the heat transfer instrumentation included low pass filters which attenuated components of the signal at frequencies above about 3 KHz. Thus only relatively large scale disturbances to the surface heat transfer rate will be observed. It is interesting to observe Figs. 10.7 and 10.11 concurrently to appreciate why the definition of the beginning of transition is somewhat arbitrary.

FIG.10.11
10° CONE HEAT TRANSFER TRACES

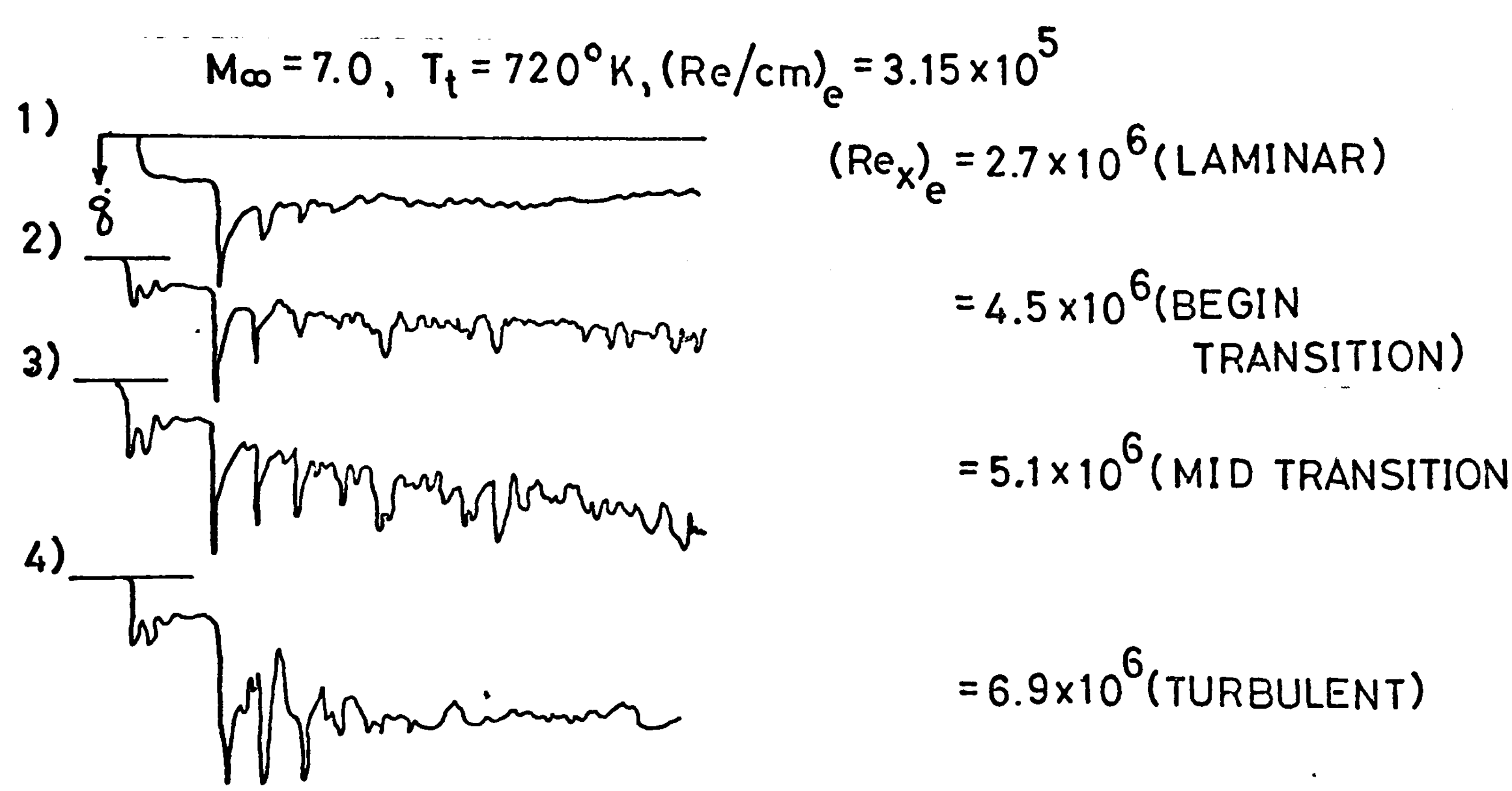

The first trace is well forward of the position where the mean heat transfer begins to rise and is seen to be relatively steady (aside from the pressure induced fluctuations due to the shock reflections) as would be expected of laminar flow. The next few gauges downstream usually begin to display one or two isolated narrow 'spikes' of increased heat transfer superimposed on the steady laminar trace without affecting the mean level. These fluctuations are probably due to the presence of 'turbulent spots' produced within the unstable region of the laminar boundary layer and propagating to the vicinity of the surface. Such heat transfer 'spikes' have been observed by other workers at cold wall hypersonic conditions (see Refs. 87 and 91). By the gauge position of the second trace in Fig. 10.11, the number of 'spikes' has become much more numerous and are beginning to influence the mean heat transfer level. This is the position defined as the beginning of transition from mean surface heat transfer measurements and yet it is clearly downstream of the point where 'non-laminar' phenomenon first appear at the surface. The arbitrary nature of the begin-transition definition will be discussed in more detail when fluctuation measurements within the boundary layer upstream of transition are discussed in Chapter 11.

The mid-transition trace in Fig. 10.11 is seen to be quite 'noisy' with the mean $\dot{q}$ increasing rapidly. The slight upward trend with time of the trace can be attributed to the slight drift upward of unit Re with time (increasing P_t, decreasing T_t) during the run. This has the effect of moving the transition point forward over the gauge during the run and since the gauge location is in the high slope portion of Fig. 10.7, the $\dot{q}$ will increase with time. (In all time variant cases, the measurement was taken at 30 msec. after the start of the flow). The final trace (No. 4) is just past the peak in the surface heat transfer rate and is seen to be quite steady and much like the laminar case although higher. The micro-structure fluctuations due to the turbulence of the fully developed turbulent boundary layer are not discernible because of the frequency limitations of the system. A detailed examination of the heat transfer traces is thus seen to qualitatively substantiate the subsonic 'turbulent spot' transition model of Emmons (Ref. 105) with the final stages of the transition process being dominated by the formation, growth, and merger of discrete turbulent 'spots'.

Returning to the transition results plotted in Fig. 10.10, several trends are immediately apparent. One is the existence of a 'unit Reynolds Number effect' in common with most supersonic transition tests and attributed to the nozzle wall boundary layer noise radiation by Pate and Schueler (Ref. 81). The concept of the sound field-unit Re relationship has been subject to some minor counter-evidence in three recent reports on sharp slender cone studies. Mateer and Larson (Ref. 114) reported no unit Re effect on transition for a 10° cone at $M_e = 6.8$ and cold wall conditions. This data, however, was taken in a tunnel which had cold helium injected in the nozzle sidewalls with the resulting possibility that the wall sound radiation may have been affected. A paper by Softley (Ref. 115) has recently reported no unit Re effect on a 10° cone at $M_e = 8.8$ and cold wall conditions in a shock tunnel. This observation would be difficult to account for using the Pate and Schueler approach. Equally difficult to explain would be results reported by Potter (Ref. 116) on 20° cones at $M_e = 4.34$ in the AEDC ballistic range. Potter found the existence of a unit Re effect despite a measured free stream noise level three orders of magnitude lower than corresponding wind tunnel conditions. The unit Re effect observed in the present data for the cone in Fig. 10.10 is seen to be weaker than the cylinder and plate data. This may represent a case which differs only in degree from the zero unit Re dependence findings of Refs. 114 and 115 where a unique combination of model and flow conditions may have resulted in a further weakening of the unit Re dependence to zero.

The data of Fig. 10.10 also illustrates the importance of precise definitions when discussing hypersonic transition results. The extensive length of the transition region even by the restricted definition of this chapter, makes any reference to a single transition 'point' quite ambiguous. The length of transition (ΔX_t) from Table 10 is seen to increase very rapidly with the introduction of some transverse curvature to the model being considered, especially for the lower unit Re cases. This effect contributes to the delay in the end of transition measured on the models with curvature. The effect of model transverse curvature on hypersonic boundary layer stability (or transition) has not been considered theoretically but is most likely related to the three-dimensional nature of the turbulent spot breakdown model. The most important parameter when considering curvature effects on boundary layers is the relation between the boundary layer thickness and the local radius of curvature. The movement of the end of transition Reynolds Number on the three models tested in the Gun Tunnel is compared in Fig. 10.12 with the parameter δ_b/r_m for two unit Re cases. The boundary layer thickness at the beginning of transition (δ_b) was calculated from the laminar growth expression

$$\frac{\delta}{x} \sim Re_x^{-\frac{1}{2}}$$

and the known condition from Chapter 9 of δ = .057" at x = 2 inches for Re/in. = 4.45×10^5. The cone value was obtained from the relation

$$\delta_{PLATE} = \sqrt{3}\ \delta_{CONE}$$

at identical boundary layer edge flow conditions. The local radius of curvature (r_m) was taken as the model value midway between the model leading edge (or tip) and the beginning of

FIG.10.12

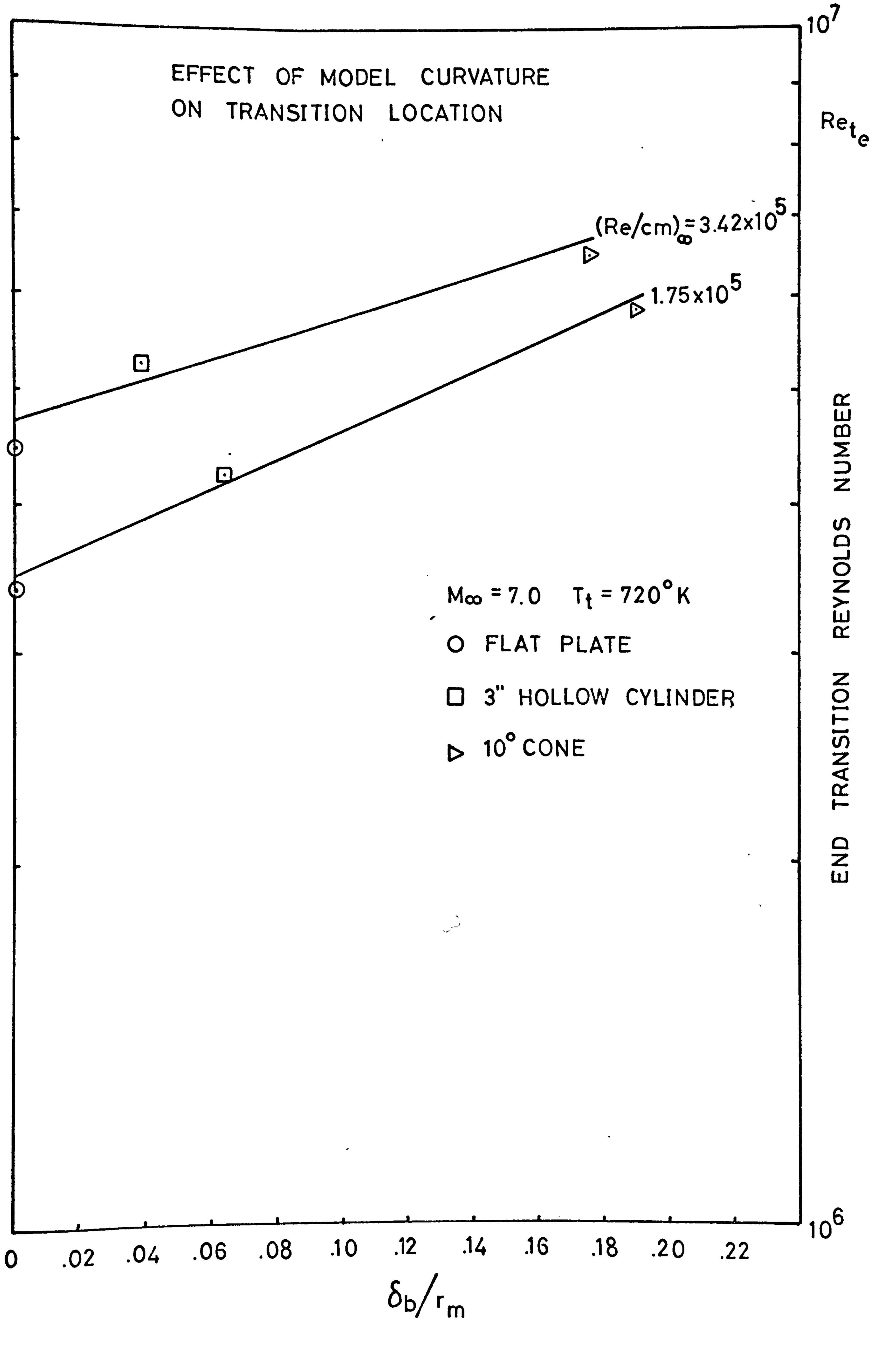

EFFECT OF MODEL CURVATURE
ON TRANSITION LOCATION
$(Re/cm)_\infty = 3.42 \times 10^5$
1.75×10^5
$M_\infty = 7.0 \quad T_t = 720^\circ K$
O FLAT PLATE
□ 3" HOLLOW CYLINDER
▷ 10° CONE
10^7
Re_{t_e}
END TRANSITION REYNOLDS NUMBER
10^6
0
.02
.04
.06
.08
.10
.12
.14
.16
.18
.20
.22
δ_b/r_m

transition. This location was considered appropriate to account for curvature effects on the important turbulent spot induction region ahead of the beginning of transition. The curvature effects seem to be reasonably well described by this parameter.

The delay of transition in hypersonic boundary layers on cones compared with flat plates at similar flow conditions was first reported by Potter and Whitefield (Ref. 117). They reported a decreasing ratio of cone/flat plate transition Reynolds Number from about 3 at $M_e = 3$ to near unity at $M_e = 8$. Very little of this comparative data was recorded on models in the same facility and, as such, the ratios should be treated with caution in view of the facility sound radiation effect discussed earlier. More recent data from AEDC has been reported, however, by Pate (Ref. 118) which substantiate these earlier trends using comparative models in the same facilities. Both studies, however, suffer from the ambiguity of using flat plate and hollow cylinder data interchangeably, a condition not necessarily valid in view of the findings of the present data. The delay in transition of the hollow cylinder configuration has not been reported previously and clearly must be considered when making curvature comparisons of this sort unless the parameter δ_b/r_m is very much smaller than encountered in the tests reported here.

In the correlation of cone data, Pate (Ref. 118) was able to produce an expression similar to that reported by Pate and Schueler to account for Mach Number, unit Re and tunnel size effects based on the tunnel wall turbulent boundary layer sound radiation parameters. The empirical equation derived was given as

$$(Re_t)_e = \frac{10.5(\bar{c}_f)^{-1.66}}{(\delta^*/c)^{.5}}[0.56 + 0.44\ c_1/c] \qquad (10.3.1)$$

where the terms are defined in the same way as for equa. (9.4.1). Although the same uncertainties are involved in applying (10.3.1) to the present data for the open jet, cold wall nozzle configuration as was present for the flat plate correlation discussed in Chapter 9, some points of interest do arise from the form of the equation. In the case of data from a single source at identical Mach Numbers and temperatures, the Reynolds Number dependence of $\bar{c}_f$ and δ^* can be given by the incompressible expression (e.g. equa. [9.4.7]). The unit Re dependence of the transition Reynolds Number is then

$$(Re_t)_e \sim (Re/x)^{.43} \tag{10.3.2}$$

for cones. This is, however, a considerably stronger dependence than that observed.

A more interesting comparison which can be made from the correlation expression for cones and plates is the ratio of cone to flat plate transition Reynolds Number. Dividing equation (10.3.1) by (9.4.1) for a common tunnel gives

$$\Psi \equiv \frac{(Re_t)_e^{CONE}}{(Re_t)_e^{PLATE}} = 745(\bar{c}_f)^{0.89} \tag{10.3.3}$$

Pate (Ref. 118) analysed this expression for the AEDC tunnels used in his tests and found that Ψ decreased monotonically from values around 2-3 at $M_\infty = 3$ to values approaching unity at $M_\infty = 8$ confirming the trends of his data. There was; moreover, a unit Re and tunnel size effect remaining in the ratio Ψ at a given Mach Number precluding the determination of a unique value of Ψ for different tunnels even at identical flow conditions. Pate was only marginally successful in correlating actual Ψ measurements with predicted values from equa. (10.3.3).

Equation (10.3.3) can be compared with the measured Ψ for the present data using the approximate value of $\bar{c}_f$ = 1.4×10^{-3} at a Re/cm of 1.75×10^5 determined in Section 9.4 for the Gun Tunnel conditions. This gave a value $\Psi = 2.15$ which overpredicted the observed value of $\Psi = 1.675$ at the same unit Re. The uncertainty of the value for $\bar{c}_f$ can be eliminated if the theoretical and experimental dependence of Ψ on unit Re are compared. Defining a new ratio, η, given by

$$\eta = \frac{\Psi_1}{\Psi_2} = \left[\left(\frac{Re_2}{Re_1}\right)^{1/5}\right]^{.89}$$

for similar Mach Number and temperature conditions, a value of $\eta = 1.192$ is given for $(Re/cm)_1 = 1.75 \times 10^5$ and $(Re/cm)_2 = 4.72 \times 10^5$. The experimentally observed value of η at the same two unit Re is $\eta = 1.345$. It is interesting to observe that if the experimental comparisons are made between the cone and the hollow cylinder data, then the value of η was found to be $\eta = 1.15$, a much closer approach to the theory. This point emphasizes again the importance of differentiating between hollow cylinder and flat plate data in transition experiments (at least at some flow condition-model combinations).

The theoretical and measured values of the cone/planar transition ratio, Ψ, are summarized in Fig. 10.13. The theory was extended from the one calculated point by an assumed variation of $(Re/x)^{-.18}$. The data from the two planar cases (cylinder and plate) were plotted separately. It should be noted that in view of the nature of the theory (equa. 10.3.3), the measured ratios, Ψ, were determined at constant free stream (∞) conditions rather than boundary layer edge (e) conditions. The data of Fig. 10.13 would suggest that the hollow cylinder and flat plate ratios would cross at some higher unit Re and

FIG.10.13

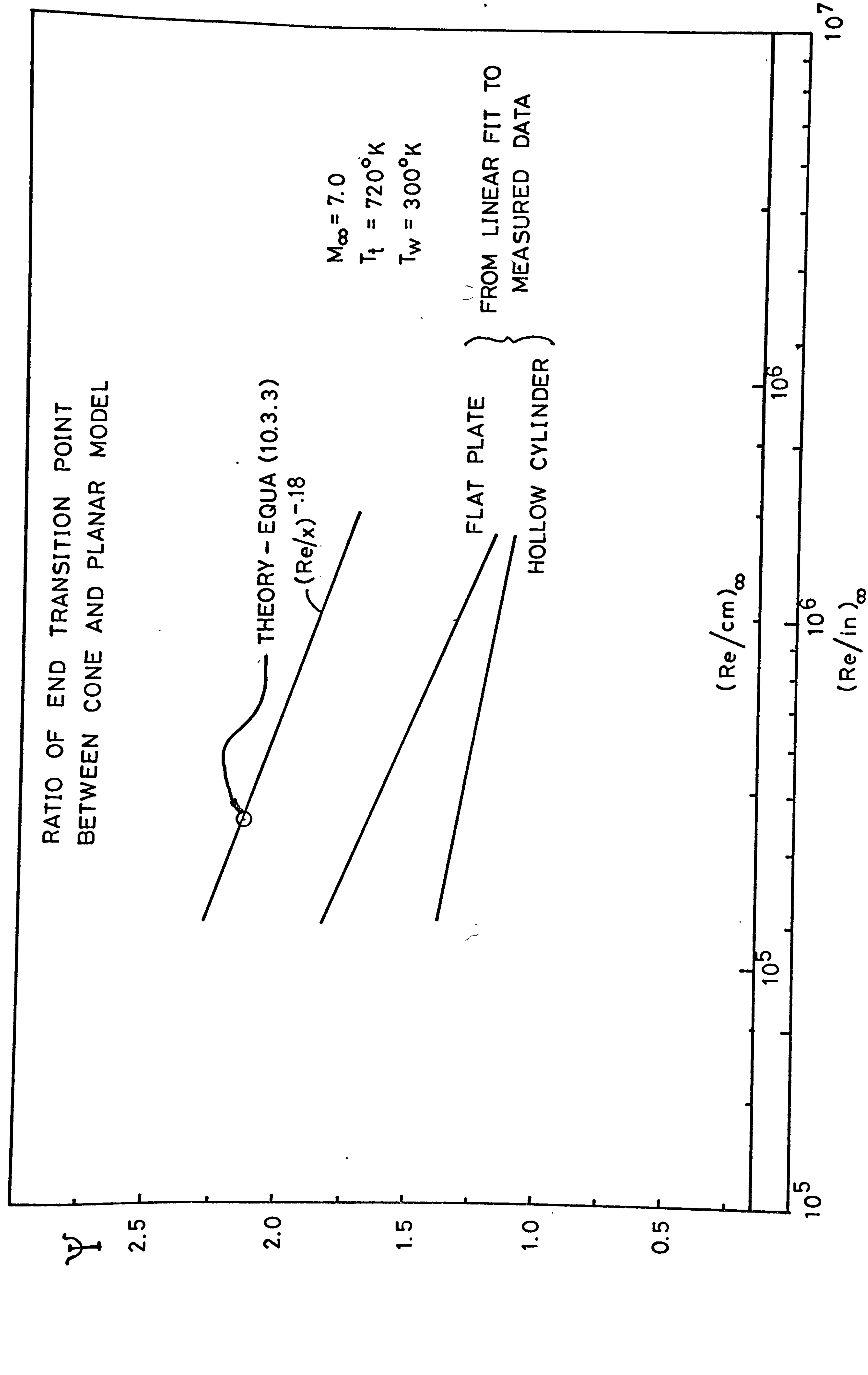
RATIO OF END TRANSITION POINT
BETWEEN CONE AND PLANAR MODEL
THEORY - EQUA (10.3.3)
$(Re/x)^{-.18}$
$M_\infty = 7.0$
$T_t = 720°K$
$T_w = 300°K$
FLAT PLATE
HOLLOW CYLINDER
FROM LINEAR FIT TO
MEASURED DATA
Ψ
2.5
2.0
1.5
1.0
0.5
10^5
10^6
10^5
10^6
10^7
$(Re/cm)_\infty$
$(Re/in)_\infty$

that both would drop below unity, i.e. the cone model boundary layer would become less stable than the planar case at a sufficiently high unit Re. Such an observation remains to be substantiated experimentally.

CHAPTER ELEVEN

BOUNDARY LAYER FLUCTUATIONS

It was mentioned briefly during the discussion of the heat transfer and transition results in the previous chapter that certain transient phenomenon becomes apparent on the surface thin film gauge outputs before mean changes were measured. These transient 'spikes' in the heat transfer records were attributed to the presence of turbulent eddies generated within the unstable upper regions of the upstream laminar boundary layer. By implication it was suggested that since the surface-observed events were probably the late stages of the turbulent spot growth history, measurements at y/δ greater than zero may indicate transitional behavior upstream of the surface beginning-of-transition point.

In order to investigate in more detail the existing ambiguity in defining the beginning of transitional breakdown in hypersonic laminar boundary layers, a program was initiated to probe the boundary layer upstream of the surface transition region. It was required that the probe should be sensitive to high frequency transient events such as turbulent spot development and at the same time be physically small to permit adequate spatial resolution within the thin laminar boundary layers encountered in the typical Gun Tunnel tests with minimal flow disturbance. A hot wire anemometer probe was judged most likely to meet the requirements set out above. Although very little hypersonic experience with hot wires has been reported in the literature (see Section 11.2), the potential usefulness of such a probe made an extensive effort to develop some hot wire instrumentation capability a worthwhile endeavour.

This chapter describes some of the experience which has been gained in the construction and use of fine wire probes in the Gun Tunnel including the development of electronic instrumentation for the analysis of hot wire signals in the short running times available. A discussion of some extensive boundary layer surveys with fine wires operated at constant temperature is then presented and compared with the transition results presented in earlier chapters.

11.1 Experimental Apparatus

11.1.1 The Model

A flat plate model was constructed with similar overall dimensions to the flat plate heat transfer model described in Chapter 10. This was to provide a direct comparison between the hot wire probe surveys and the surface heat transfer information when discussing the extent of the transition region. The model was made from stainless steel $\frac{1}{2}$ inch thick, 14 inches long and $3\frac{5}{16}$ inches wide. The leading edge was ground to a measured thickness of 0.0006 (± 0.0001) inches. Sharp edged side curtains were provided in a similar configuration as those shown on the model in Fig. 10.1. The model was supported on a slender stand on the underside near the trailing edge.

Instrumentation ports $\frac{3}{8}$ inches in diameter were located along the model surface centerline at 1 inch intervals starting $2\frac{1}{2}$ inches from the model leading edge. Stainless steel solid inserts which fit into these ports from the underside of the model (see Fig. 11.1) were in place when the model top surface was ground to better than a 15 μ inch rms finish. The resulting vertical step due to the insert was less than the rms roughness and the horizontal gap between the model and the insert was of the order of 0.001 inches. The sequence and orientation of the inserts were marked to allow their removal and replacement

FIG. 11.1

FLAT PLATE HOT WIRE TRAVERSING MECHANISM

SIDE VIEW

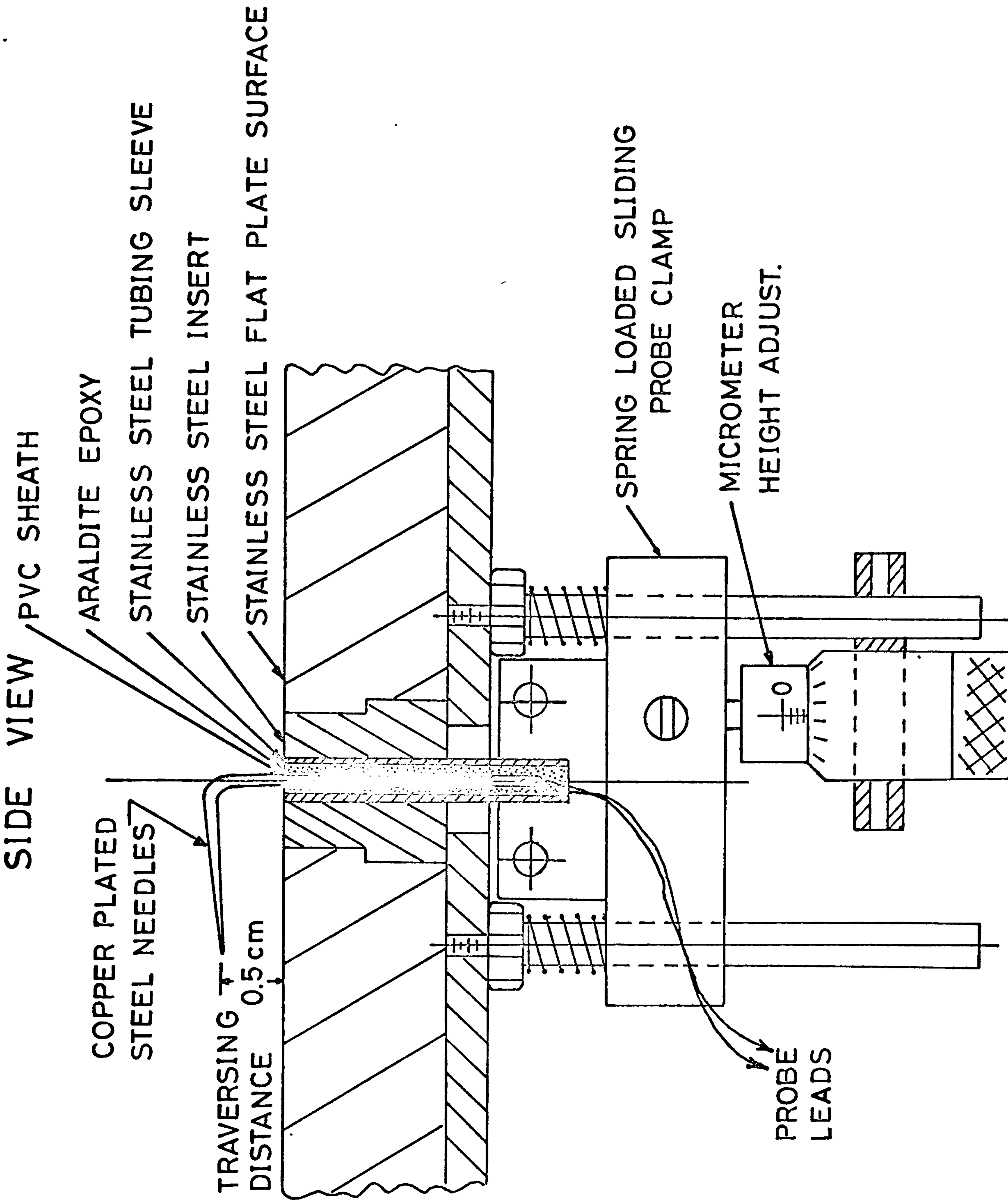

without affecting the surface smoothness.

A micrometer driven traversing mechanism was designed to be mounted on the underside of the plate and was capable of being easily moved between the various instrumentation ports. A detail drawing of the traversing mechanism,in place,together with a probe in position on the model is shown in Fig. 11.1. (The details of probe construction are discussed in Section 11.1.2). The probe was constrained in height and yaw by the spring loaded clamp of the traversing mechanism. Vertical displacement over a range of 0.5 cm was controlled by the micrometer. Probe movement in pitch was constrained by both the clamp and by the precision fit between the probe tubing sleeve and the insert guide. The probe height above the model surface was set at a reference position using a 10X cathetometer aligned with the plate along with a scribed surface set near the probe tip. Movement from this reference position was read from the micrometer scale (and checked by the cathetometer). The reference position was checked at both flow and no-flow conditions with a direct shadowgraph picture. Microdensitometer analysis of the probe position in the shadowgraph indicated that the probe was within ± 0.001 inch of its expected position.

11.1.2 Fine Wire Probes

A. Needle Probe Supports

The fine wire supporting probes were of essentially identical configuration for all the wires tested and will therefore be described first. The supports were selected from a large batch of commercial grade steel sewing needles for a diameter of 0.024 inches and a total length of $1\frac{3}{8}$-$1\frac{1}{2}$ inches. The needle tips were blunted to a diameter approximately equal to the diameter of the wire to be used. Blunting was done on a fine stone or emery paper by a very light single stroke. The blunting was necessary to improve the strength of the soldered joint between the wire and the support. Two needles were held side by side with their tips aligned and then bent to the configuration shown in Fig. 11.1 using a fine gas torch to soften the needles at the desired location of the bend. The tips of the needles were protected from excess heating by a pair of small pliers acting as a heat sink. This was to prevent oxidation of the needle surface near the tips and the resulting copper plating difficulties.

Shrinkable PVC insulating tubing was slipped over each needle from about $\frac{1}{4}$ inch below the bend to near the needle 'eye' and contracted into position with a hot air blower. Stranded conductor leads (4/.007) were soldered to the 'eye' of each needle before placing the two needles into a short length ($\frac{3}{4}$ inch) of 10 gauge stainless steel tubing (0.10 inch i.d.) as shown in Fig. 11.1. When the probes were positioned to the proper alignment and tip spacing, 'Araldite' epoxy resin was injected into the steel tubing to secure the probe position. The tips of the needles were then copper plated over a $\frac{1}{2}$ inch length using a 'Zonax' copper cyanide commercial electroplating solution. A plating current of 3 ma/needle for about 8 minutes produced a very smooth copper surface on the needles if they were thoroughly cleaned beforehand with reagent grade acetone and distilled water.

After a second distilled water cleaning, the needles were 'tinned' using a resin core solder in conjunction with 'Ween' liquid soldering flux and a 15 watt iron with a 1 mm tip. A thin bridge of clear lacquer (finger nail polish) was then applied between the needles from the bend up to about 3/16 inch from the tips to increase the relative separation stiffness of the needle probes. The probes were then ready for the application of the wire. A microphotograph of the needle tip arrangement is shown in Fig. 11.2 with a wire in place and the supporting lacquer in place on the right of the picture.

B. Wire Application

The selection of wires suitable for the present application was primarily a matter of empirical trial and error guided by very general wire performance criterion. The scarcity of published accounts of experience at the present flow conditions made such an approach almost mandatory. Basically, a hot wire's sensitivity to fluctuations in the flow is related to the changes in heat transfer to the wire produced by the flow fluctuation. Although details of hot wire response will be discussed in Section 11.2, a first analysis gives the wire's sensitivity as being proportional to the wire thermal coefficient of resistivity (α), the wire length to diameter ratio (L/D), and the temperature difference between the wire mean temperature ($\bar{T}_w$) and the flow recovery temperature (T_r). In addition to the above sensitivity parameters there is the mechanical requirement for the probe to survive the distributed aerodynamic loading as well as the starting and breakdown shock wave loading. This, of course, required wires of high tensile strength (σ) and low L/D ratios. The choice of material and diameter then reduces to a problem of compromise. A 'figure of merit' has been suggested by Kovaznay in Ref. 53 of the form

$$\text{'figure of merit'} = \alpha^{3/2}(\bar{T}_w - T_r)^{3/2} r^{\frac{1}{2}} \sigma \qquad (11.1.1)$$

where r is the wire specific resistivity and $\bar{T}_w$ is taken at the maximum operating temperature of the material. Tungsten and platinum-iridium alloys were found to be comparable and an order of magnitude 'better' than pure platinum. Tungsten's

FIG. 11.2

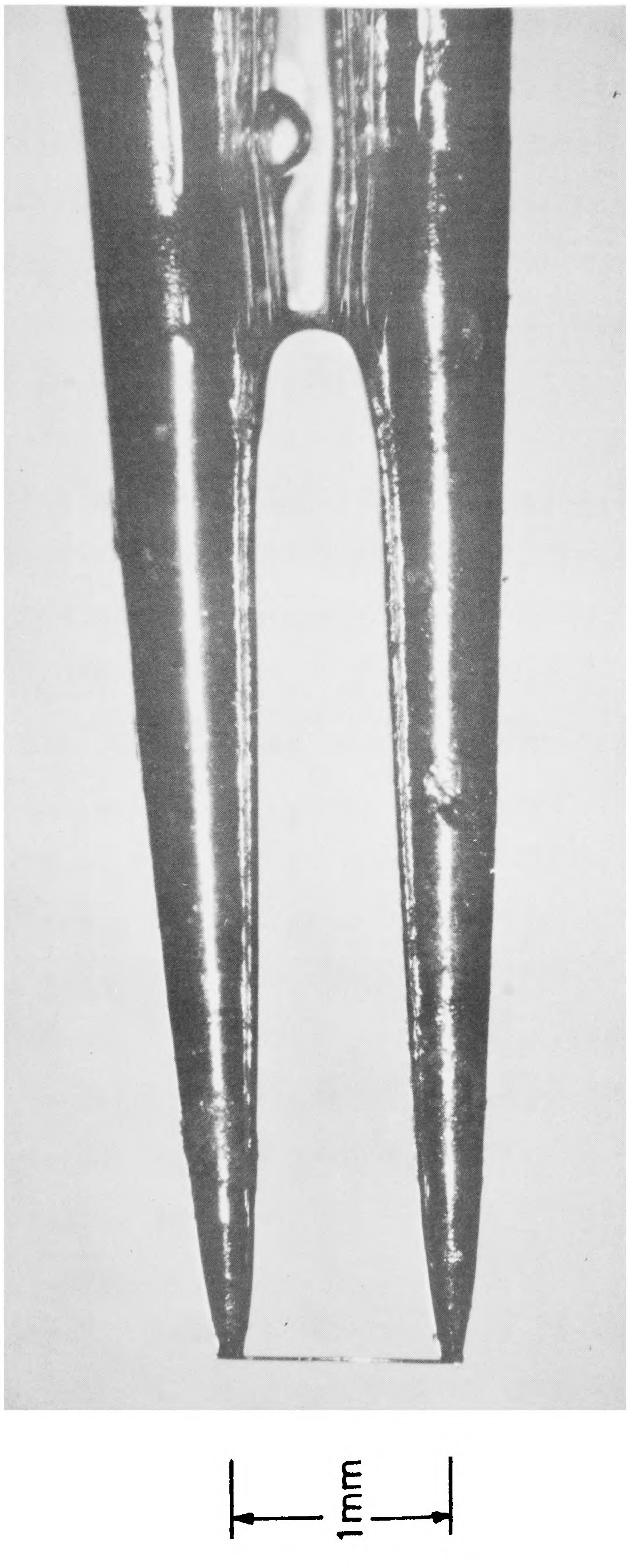

HOT WIRE PROBE TIP

disadvantage in the present situation, however, is the low maximum $\bar{T}_w$ that can be operated. Oxidation problems limit peak T_w to about 650°K. Since the wire recovery temperature T_r was probably close to 95-100% of the total temperature for the present conditions (see Ref. 119), tungsten could not be operated at positive overheats $(\bar{T}_w - T_r) > 0$. This was not a problem with platinum alloys. In addition platinum alloys could be soft soldered directly to the needles, unlike tungsten.

Another consideration on wire dimension limits was the frequency response of the wire itself. The wire frequency response is dependent mainly on its finite thermal capacity and thus an additional consideration for high bandwidth requirements was the desirability to reduce both wire length and diameter. Frequency response will be discussed with the description of the electronics in Section 11.1.3.

A range of wire lengths and diameters were evaluated on probes mounted above the flat plate and exposed to free stream conditions ($M = 7.0$, $T_t = 720°K$, $Re/cm = 1.75 \times 10^5$). The materials used were a 80% platinum-20% iridium alloy and platinum plates tungsten. The plated tungsten was tried because it was though that the oxidation problem would be reduced with a resultant increase in the upper temperature limits. A comprehensive test program evaluating all (or even many) of the possible combinations of wire material, length and diameter was not considered possible. The final probe-wire configuration thought best for the purposes of the present series of tests did not necessarily represent an optimization of design. The results therefore did not necessarily represent an upper limit of hot wire capabilities in the present Gun Tunnel flow environment.

The tungsten wires could not be direct soldered to the tinned needle supports even though the wires were platinum plated. It was necessary to copper plate the wires using the same copper cyanide solution as used on the needles. A special 'perspex' container was made with 0.01 inch holes drilled on opposite sides to hold the plating solution and to allow a wire to be fed into the solution and plated in $\frac{3}{4}$ inch lengths. The plating current used was 20 amps/ft^2 (or about 100-200 μ amps for the wires used) for about 4 minutes. One inch lengths of plated wire were then affixed with black sealing wax between two posts, one of which was a 2 inch length of 0.005 inch stainless steel shim. The separation of the posts could be adjusted until the shim began to deflect, placing a slight tension on the wire (see sketch below). This whole assembly

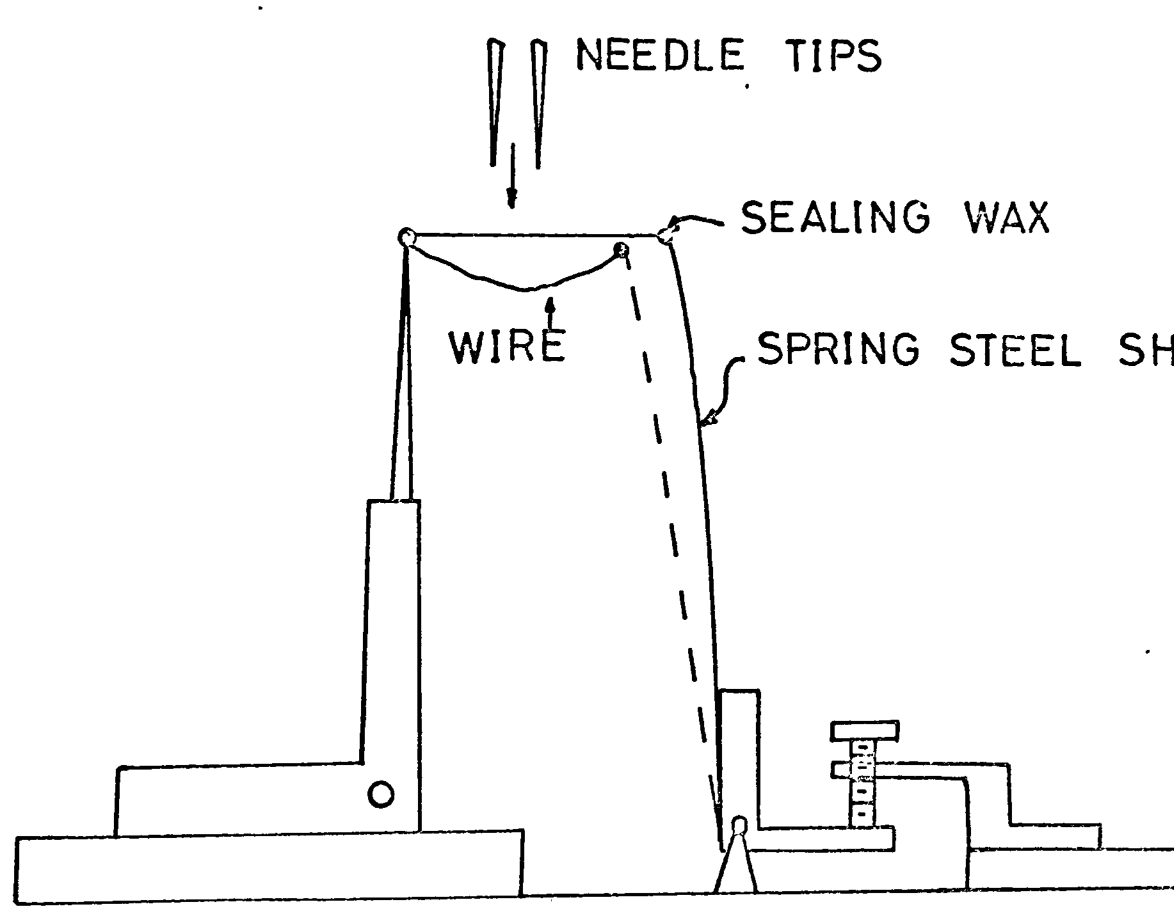

WIRE TENSION MECHANISM

was then placed in a three degree of freedom micromanipulator. A completed needle probe support was placed in another micromanipulator and both units were adjusted under a 20X stereo microscope until both needles came into contact with the wire. The wire and needles were cleaned with distilled water before a drop of liquid soldering flux was applied to each. The 15 watt soldering iron, operating at $\frac{3}{4}$ power and well tinned, was brought into contact with the tip of each needle, in turn, making a solid connection between the wire and the needle. The excess wire was broken off and the copper plating on the central span of wire was removed with a drop of 60% nitric acid on the end of a glass rod. Both 5μ and 9μ Pt. plated tungsten were handled in this way in addition to some 8.7μ unplated tungsten which was used to check out procedures. The platinum alloy wires used were of 15μ and 0.00025 inch diameter. They were handled in much the same way as the tungsten except that copper plating was not necessary for soldering to be effective. The photograph in Fig. 11.2 shows a completed assembly with a 15μ Pt. alloy wire in place.

Details of the electrical connections to the probe and the supporting electronics equipment will be discussed in Section 11.1.3. Basically, the wire was placed in a bridge circuit with the bridge kept in balance for any set value of probe resistance by a high gain feedback amplifier. The wire 'cold' resistance (R_o) was measured and then a value of hot resistance (R_w) was set and maintained by the bridge. The ratio R_w/R_o is a measure of the mean wire operating temperature ($\bar{T}_w$) and can be expressed for a linear temperature-resistance relation as

$$R_w = R_o[1 + \alpha(\bar{T}_w - T_o)] \quad . \tag{11.1.2}$$

Knowledge of the wire α was required to estimate the $\bar{T}_w$ from the resistance ratio. It should be emphasized, however, that the actual distribution of temperature levels along the wire will deviate considerably from the mean value obtained from (11.1.2). This is due to the relatively massive needle supports which remain at essentially room temperature even during the run time in the Gun Tunnel flow. Heat conduction along the wire extended the support influence for many wire diameters. A given mean temperature could only be obtained then by having the central portion of the wire at temperatures considerably above $\bar{T}_w$. In fact, for wires with low L/D (say < 100), it was observed that roughly the middle 1/3 of the wire was radiating in the visible spectrum ranging from dull red up to 'blue-white' near the center. Since the $\bar{T}_w$ in this case was about 1100°K, the central portion of the wire was clearly in excess of $\bar{T}_w$.

The tungsten wires (plated and unplated) operated satisfactorily at L/D ratios of 100-300 at low resistance ratios ($R_w/R_o < 2$) from a mechanical point of view. At $R_w/R_o \approx 2.5$ most of the probes failed in the middle of the span. Evidence of oxidation on the wire surface indicated that this was the probable cause of the failure at the hottest point in the wire. Observations of the sign of the mean heat transfer to the wire during the run indicated that the mean wire temperature was only just approaching the recovery temperature for a R_w/R_o of 2.5. Assuming a tungsten α value of 0.004/°C gives $R_w \cong 675$°K, confirming the heat transfer observation. Tungsten wire would clearly be inadequate for the present test conditions from sensitivity considerations since positive values of $(\bar{T}_w - T_r)$ are needed for successful operation of constant temperature anemometers.

The 15μ platinum alloy wire was run up to a L/D value of 200 with a R_w/R_o of 1.8. Because of the relatively low α for platinum alloys ($\sim$ 0.00075/°C) this resistance ratio corresponded to a $\bar{T}_w$ of about 1370°K. Shorter probes (L/D < 100) at R_w/R_o values over 1.6 developed some permanent physical distortion near the center of the wire, probably due to operation near the material's softening temperature. The final operating configuration of the wires used in the tests of Section 11.3 was determined primarily from the electrical performance of the probe described in Section 11.1.3.

11.1.3 Electronic Instrumentation

All the probes tested in the Gun Tunnel were run in the constant temperature mode in a DISA 55D01 universal anemometer. The basic circuit diagram of the anemometer bridge connections are shown in Fig. 11.3. The probe connections from the working section to the bridge input terminal must generally be kept to a minimum length with stray inductance sources avoided where possible to keep the probe bridge arm electrical characteristics within the compensating range of the anemometer unit. With careful adjustments of bridge balance, the feed-back amplifier gain could be taken to its maximum gain setting allowing a maximum system upper frequency limit of 100-135 KHz (for the 1:20 bridge arm ratio used in the tests). In practice, the overall frequency response of the system depended on both the amplifier and the probe. For a given probe, the bandwidth increased with flow velocity and probe temperature in theory.

Ideally, the system bandwidth should be measured by applying a step change in velocity to the probe. In practice, this is not practical but can be approached indirectly by applying a sudden step change of electrical power to the probe and observing the system response. This procedure was followed for each of the probes used in the Gun Tunnel tests with the probes in place in the working section. The resulting system bandwidth probably represented a lower limit as the tests were necessarily run with zero flow velocity. The maximum frequency response of the system was defined by $f = 1/2\pi\tau$, where τ was the square wave response rise time (1/e). The 15μ platinum alloy gave a frequency response of 20-30 KHz depending on length but with very little

FIG.11.3

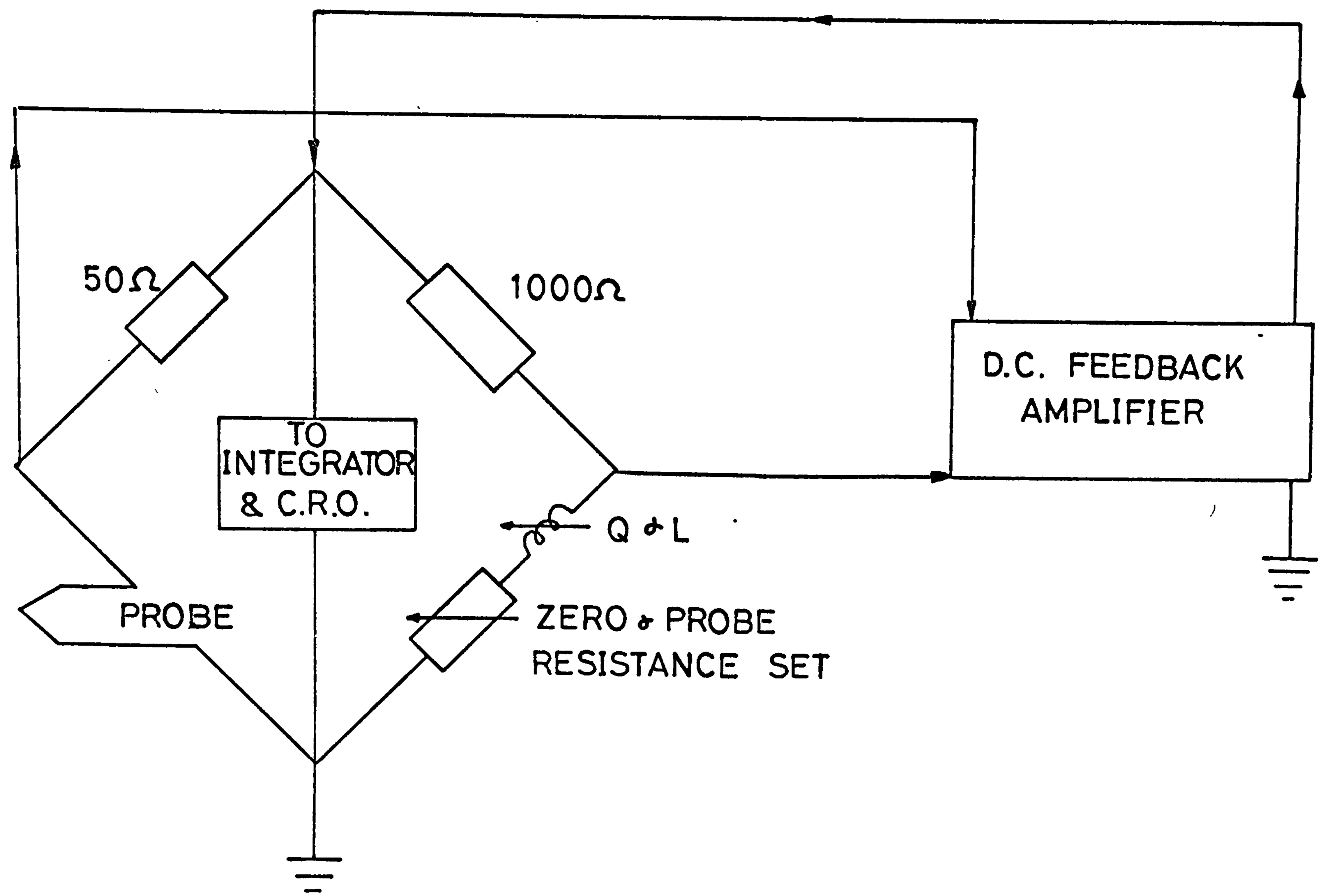

HOT WIRE ANEMOMETER BRIDGE CONNECTIONS

dependence on R_w/R_o. The 0.00025 inch platinum alloy probes produced a system bandwidth of between 50-65 KH_z for wire lengths in the range between .010-.020 inches. Because of their superior frequency characteristics, the 0.00025 inch platinum-20% iridium wires were used exclusively in the boundary layer surveys described in Section 11.3. It was also found in practice that a visible amount of slack had to be left in the wire when mounted to eliminate high frequency oscillations on the bridge amplifier output signal. This was probably due to 'strain gauging' effects for the wire with tension left in. Similar experience was reported by Wagner et. al. (Ref. 84) for hot wires operated in a hypersonic helium tunnel.

The output of the anemometer is actually the signal produced by the feedback amplifier to maintain bridge balance. The typical output signal produced when the wire is subjected to a sudden change in flow velocity is composed of a step change in d.c. voltage needed to balance the change in mean convected heat transfer from the probe with a fluctuating voltage level superimposed corresponding to instantaneous heat transfer changes produced by flow irregularities. It is the fluctuating component which is usually of primary interest in most hot wire applications in turbulent flow. In order to quantify a fluctuating signal that is usually random in frequency and amplitude, most theoretical analysis and experimental measurements of hot wire signals deal with the signal rms values. Although the measurement of rms values are routine in continuous wind tunnel facilities, their measurement in short duration facilities is a more formidable problem and has not been reported in the literature to date.

A slightly different approach was adopted in the present tests to provide a quantitative measure of wire fluctuation levels. The total voltage fluctuation signal was half-wave rectified and the resultant signal was then integrated by an active integrator circuit. This system thus provided an accurate value for the integrated signal level (half-wave) during any time interval during the Gun Tunnel running time. Quantitative comparisons of fluctuation levels at different probe locations were then possible.

After considerable developmental efforts, the final circuit arrangement selected was that shown in Fig. 11.4. This shows the complete rectifier-integrator combination. Some gain was built into the rectifier to increase the signal levels the integrator had to deal with, thereby reducing integrator drift problems. The use of an FET operational amplifier in the integrator also eased drift problems because of its low input bias current. To prevent integration of the hot wire noise level immediately before the test run, the hold switch (Fig. 11.4) was kept closed until the Gun Tunnel diaphragms were burst. This ensured that the integrator base line kept on the oscilloscope screen.

The diagram in Fig. 11.5 shows how various aspects of the hot wire signal were analyzed. A low pass filter enabled the d.c. component of the signal to be accurately measured. A high pass filter allowed the a.c. component of the signal to be monitored on an oscilloscope during the test run. The amplifier-rectifier part of the circuit shown in Fig. 11.4 included a high pass filter to remove the d.c. component. Details of the signal as it was analyzed by the half wave integrator are shown in Fig. 11.6. The signal was monitored on an oscilloscope after it had passed the rectification stage. This part of the signal was displayed on a time sweep that covered the whole test run and also on an extended sweep that covered 1 msec. of the test

FIG.11.4

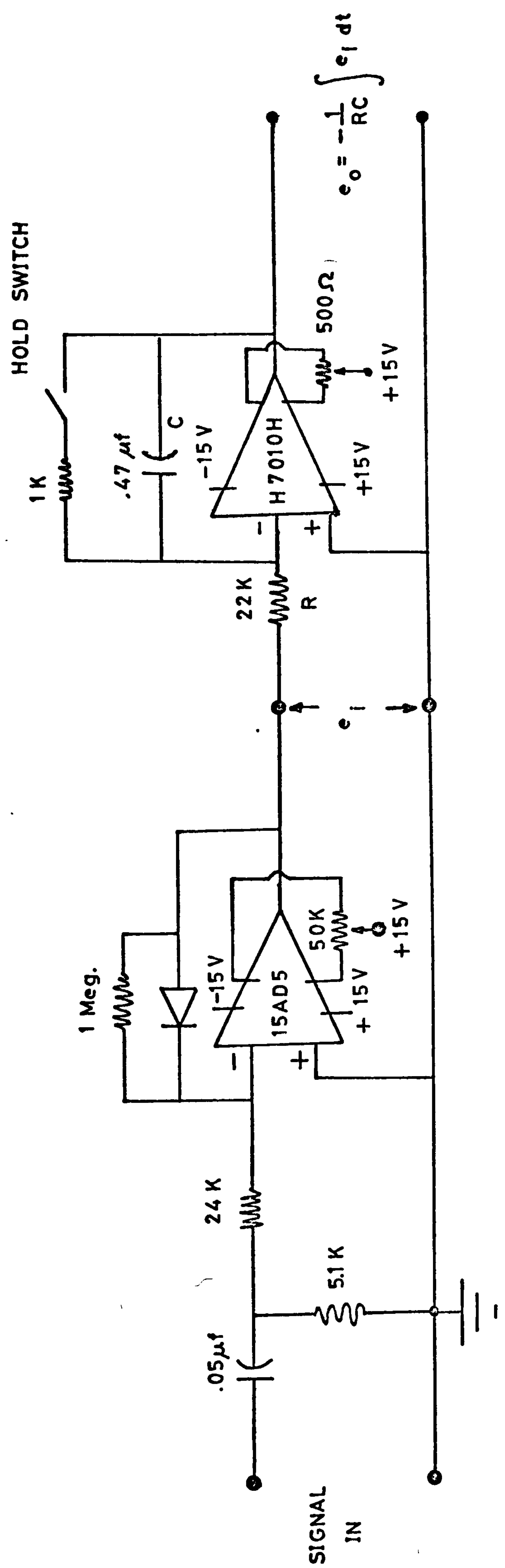

HALF WAVE INTEGRATOR

FIG.11.5

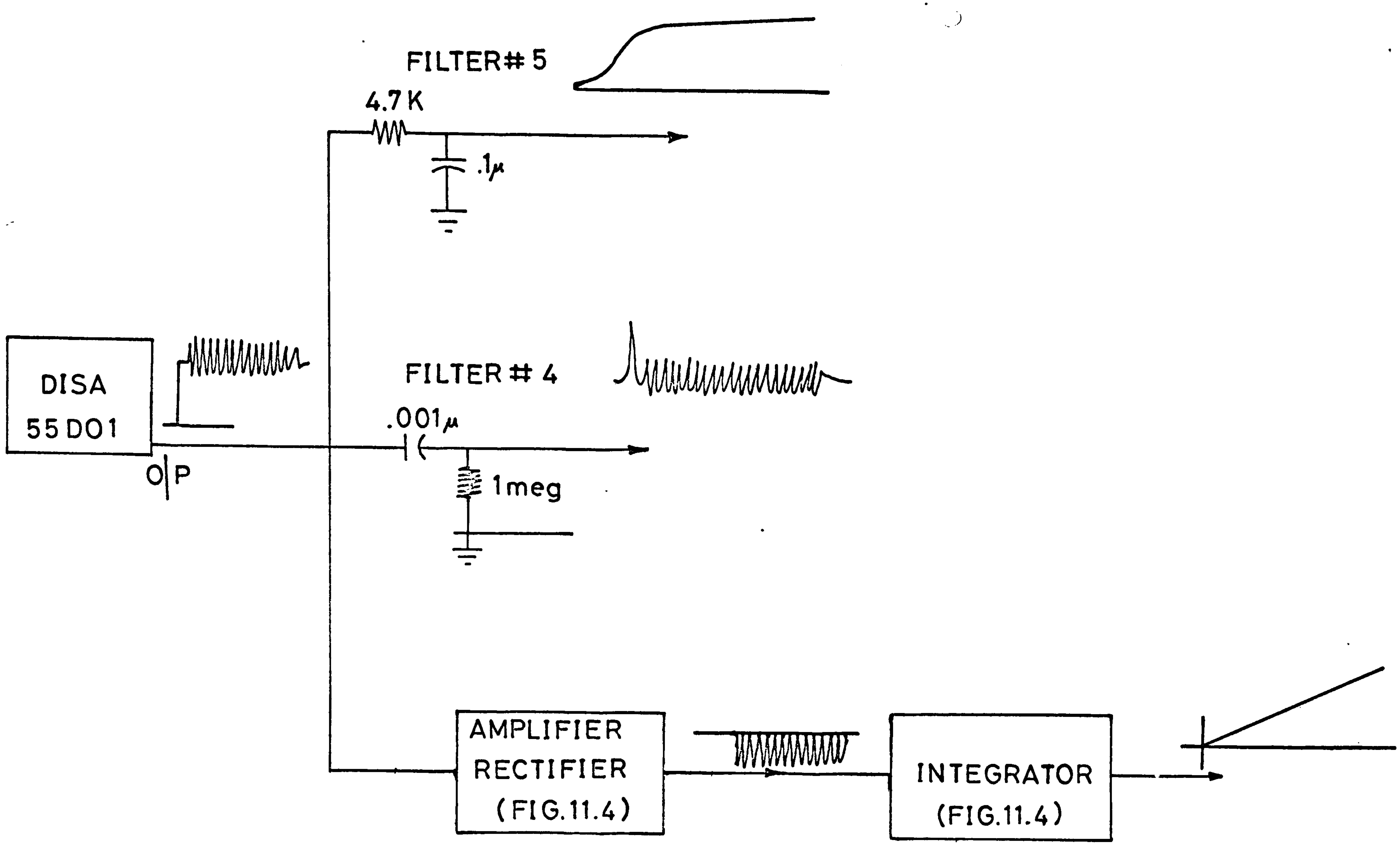

HOT WIRE SIGNAL ANALYSIS — I

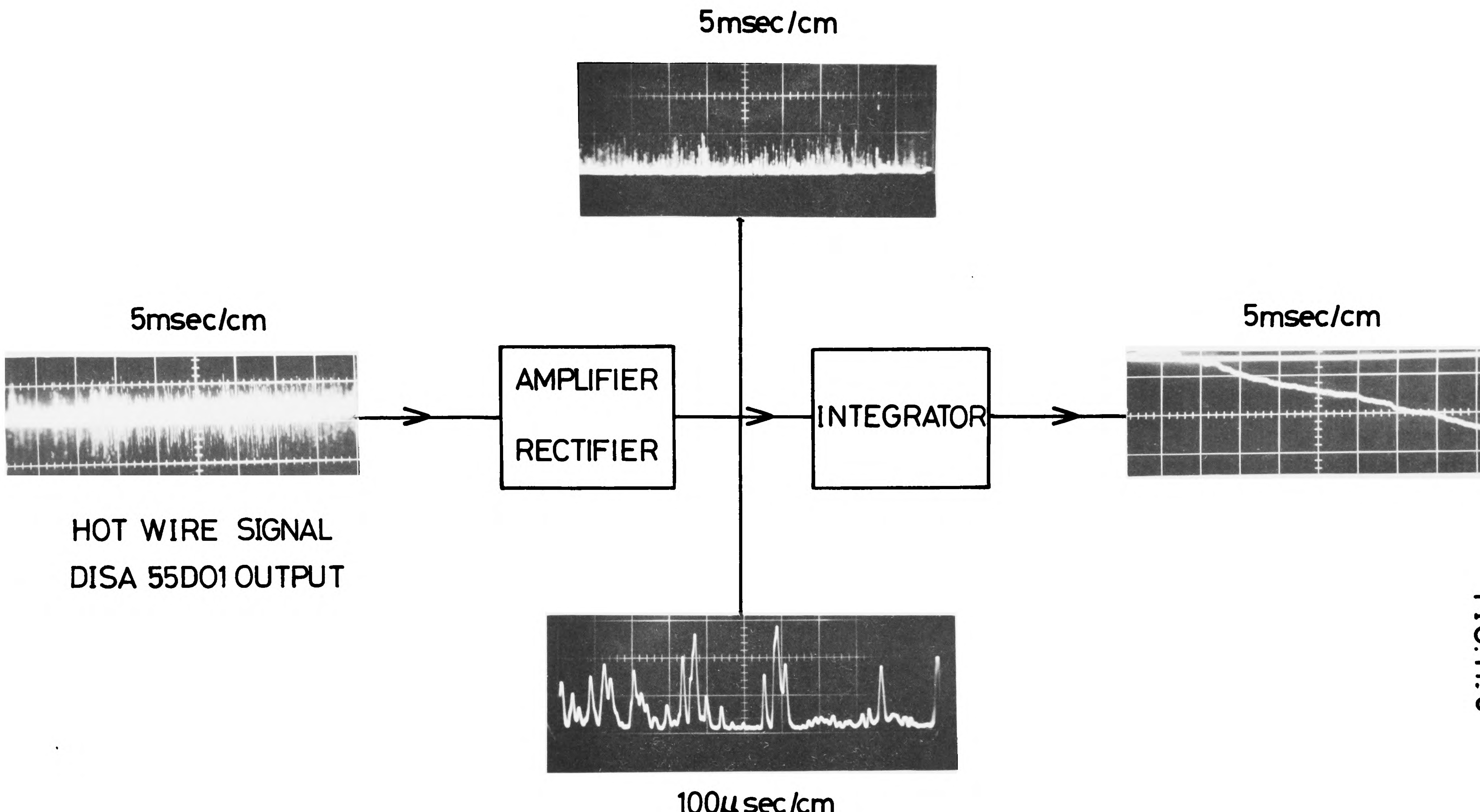
5msec/cm
5msec/cm
5msec/cm
AMPLIFIER
RECTIFIER
INTEGRATOR
HOT WIRE SIGNAL
DISA 55D01 OUTPUT
100μsec/cm

FIG. 11.6

starting near the 30 msec. point after flow establishment. This extended sweep provided great detail of the flow fluctuation structure within the boundary layer. These detailed observations of the fluctuations would normally be lost by the conventional approach of rms averaging in continuous tunnels. The final step of signal integration is also shown in Fig. 11.6 with a typical integrator output signal presented. Although either positive or negative fluctuations could be integrated by reversing the diode in Fig. 11.4, the fluctuation measurements described in Section 11.3 all involved negative fluctuations from the mean wire output level for reasons that will be described in that section.

11.2 Hot Wires in Supersonic Flow

The sensitivity of hot wire anemometers in supersonic flow has been extensively discussed in papers by Kovasznay (Ref. 120) and Morkovin (Ref. 121). The single piece of statistical information available from hot wire measurements is the fluctuating voltage level (e'). This fluctuating voltage is produced by instantaneous changes in wire heat transfer produced by fluctuations in the flow properties, ρ, u, and T_t. In supersonic flows the effects of ρ and u are usually combined into mass flow fluctuations (ρu). The wire sensitivity is then given as

$$e' = -\Delta e_m \frac{(\rho u)'}{\overline{\rho u}} + \Delta e_T \frac{(T_t)'}{\overline{T_t}} \qquad (11.2.1)$$

where primed terms are instantaneous fluctuations and bar terms ($\overline{}$) refer to mean values. The sensitivity coefficients Δe_m and Δe_T have been derived by Morkovin (Ref. 121) and depend on several empirically determined relationships including 1) wire resistance-temperature relation, 2) wire overheat parameter $(R_w-R_r)/R_r$, and

3) wire Nusselt Number (corrected for end loss effects) and recovery factor variation with flow Mach Number and Reynolds Number. It is also assumed in the expression (11.2.1) that the measured value of e' has been corrected for probe time constant effects (thermal lag).

The extensive experimental hot wire measurements of Laufer and McClellan (Ref. 119) has led to universal wire calibrations for Nu and recovery factor in the near supersonic ($M < 4.5$) flow regime. This information has allowed the routine calculation of the wire sensitivity coefficients (Δe_m, Δe_T) in supersonic flow. The fluctuation components $(\rho u)'$ and $(T)'$ and the cross-correlation parameter of the two can be extracted from the basic information, e', if the wires are run at several (at least three) different overheat values. This method takes advantage of the different sensitivities to overheat of the sensitivity coefficients (Δe_m, Δe_T) as proposed by Kovasznay (Ref. 122) and Wise and Schultz (Ref. 123).

The extension of hot wire anemometry to hypersonic conditions would require extensive additional wire calibration procedures if quantitative fluctuation information is to be extracted. As a result, very little published information on wire performance exists for hypersonic conditions. Demetriades (Ref. 124) has used hot wires at $M = 5.8$ to measure the amplification of natural and artificial disturbances in a laminar boundary layer. An absolute wire calibration was not attempted as relative e' measurements were all that were required for his tests. Wire sensitivity variations across the boundary layer were minimized by taking all x variation measurements at constant y/δ values and by using high L/D values to keep end loss corrections below 10%. Potter and Whitfield (Ref. 77) made comparative e' (rms) measurements in a flat plate boundary layer up to $M = 8$ with no sensitivity corrections attempted. Staylor and Morrisette (Ref. 78) presented a calibration procedure for finite length wire end loss corrections at M = 6. This allowed e' and mean mass flow profiles to be determined in a flat plate laminar boundary layer although no attempt to separate the e' components was made.

The problems in wire calibration procedures at the high total temperature conditions of hypersonic wind tunnels was avoided in some very recent wire measurements made in a M = 20 helium tunnel by Wagner, et. al. (Ref. 84). In their important work, a unique calibration of each separate wire's Nusselt Number, recovery factor and time constant variation with Reynolds Number was obtained (at constant M). In this way, end loss effects were accounted for in the calibration. With accurate calibration data, Wagner, et. al. were able to separate the mass flow and total temperature fluctuations (and their cross-correlation) in the tunnel free stream.

The calibration of hot wires for the Gun Tunnel flow conditions is further complicated by several factors. The short running times ($\sim$ 40 msec) make a direct in situ calibration of wire heat transfer, recovery factor and time constant variation with Re quite difficult. The use of a universal wire calibration procedure (e.g. Ref. 125) would (even if one existed) also lead to uncertainties in the end loss corrections. Unlike the continuous facility experiments described in the previous two paragraphs, the probe supports will remain at room temperature during the tests in the Gun Tunnel. Since the wire mean temperature must operate above the wire recovery temperature to obtain reasonable sensitivity, the end loss correction term (Ref. 125) would become of the order of 50% for typical operating conditions for the wire in the Gun Tunnel (at T_t = 720°K). At such high operating temperatures, even the normally straightforward measurement of the wire resistance-temperature relationship also becomes non-trivial.

No attempt to calibrate the wire was made because of the difficulties mentioned above. Only factors which were likely to affect probe sensitivity were controlled within reasonable limits. All tests described in the next section were with probes of the same material, diameter, L/D (approximately), and mean temperature (R_w/R_o). Relative fluctuation level comparisons may then be meaningful at different x positions if y/δ is constant and then only before the boundary layer mean flow property profiles begin to change. The actual fluctuation y profiles are probably somewhat distorted by changes in wire sensitivity with flow properties. There is no reason to suspect, however, that the location of a maximum in the fluctuation profiles would be affected by this sensitivity distortion.

The final wire voltage fluctuation expression is thus not reduced beyond the form given in (11.2.1). That is to say, the measured fluctuating voltage term, e', is proportional to the sum of the local mass flow and total temperature fluctuation effects. As a further approximation, Laufer and Vrebalovich (Ref. 126) suggested that since vorticity fluctuations dominate in unsteady laminar and transitional boundary layers, the voltage fluctuation is proportional to mass flow fluctuations only. Thus the time integrated e' measured in the present tests can be given as approximately

$$\int_{t_1}^{t_2} (e')dt = \frac{-\Delta e_m}{2(\overline{\rho u})} \int_{t_1}^{t_2} (\rho u)' \, dt \qquad (11.2.2)$$

from (11.2.1).

11.3 Experimental Results and Discussion

11.3.1 Fluctuation Profiles

Boundary layer fluctuation level surveys were made along the flat plate model described in Section 11.1.1. The model was mounted ½ inch above the nozzle centerline with its leading edge 2 inches upstream of the nozzle exit. The flow conditions for all the tests were $M = 7.0$, $T_t = 720^{\circ}K$, $T_w = 300^{\circ}K$, and $Re/cm = 1.75 \times 10^5$ ($P_t \approx 50$ atm.). The wire probes used were all the 80% platinum-20% iridium alloy (.00025 inch dia.) operated at L/D between 50 and 100, approximately. The probes were all operated in a DISA type 55D01 constant temperature bridge at $R_w/R_o = 1.5$-1.6. The probe surveys were run at x intervals of 1 inch starting at a distance of x = 2 inches from the leading edge to the probe tip. The y traverses were performed at 0.010 inch intervals starting at y = 0.010 inches from the surface. In some cases where the rate of change of fluctuation level (with y) was greatest, the y interval was reduced to 0.0025 inches.

Some typical anemometer amplifier fluctuation outputs are shown in Fig. 11.7 for a single x position (x = 3 inches) at various y/δ values. The signals are the total (unrectified) probe outputs (feedback amplifier output) with the d.c. component removed. The most striking aspect of the oscillograms in Fig. 11.7 is the strong increase in fluctuation levels apparent in the central regions of the boundary layer even though the Reynolds Number is nearly a factor of two less than the beginning of transition defined by the surface $\dot{q}$ experiments. The distribution of fluctuation levels is illustrated more clearly in the integrated profiles presented in Figs. 11.8 and 11.9. In these figures the fluctuation intensity is given in arbitrary units obtained from the integrator output measured

FIG. 11.7

HOT WIRE TOTAL OUTPUT

Re $= 1.33 \times 10^6$

Y/δ

a) 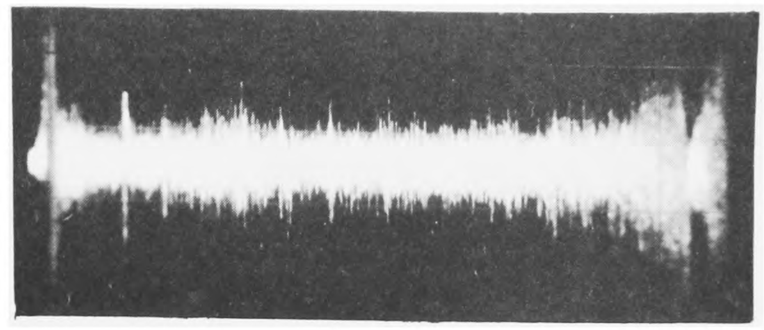 .92

5 msec/cm →

b) 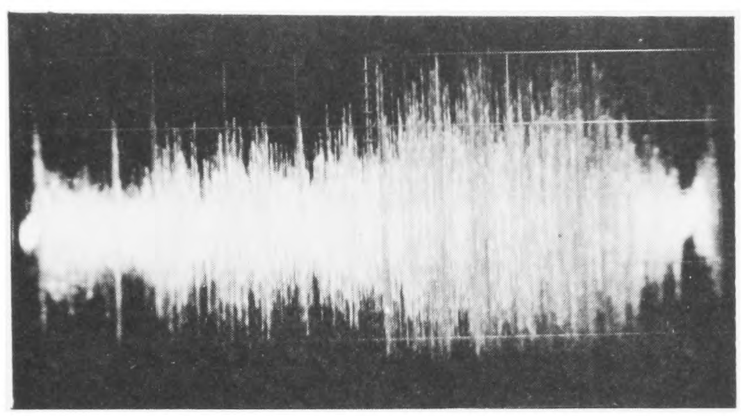 .77

c) 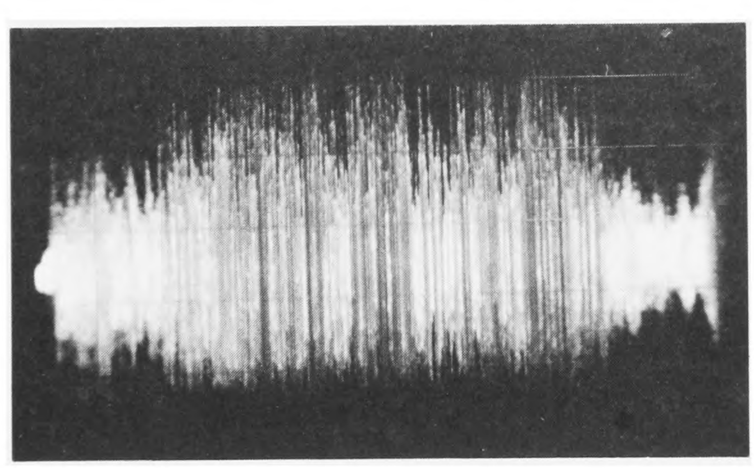 .69

d) 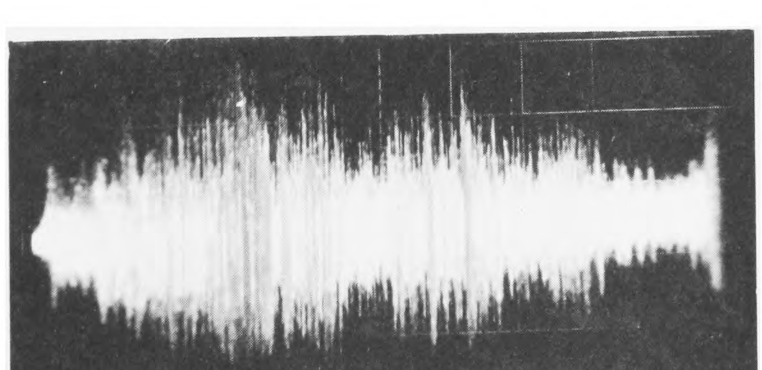 .54

e) 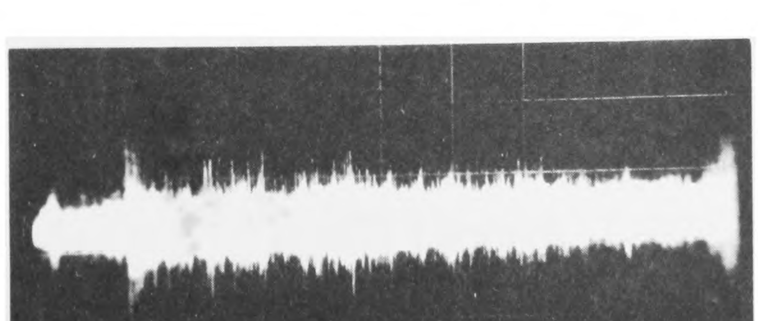 .31

FIG.11.8

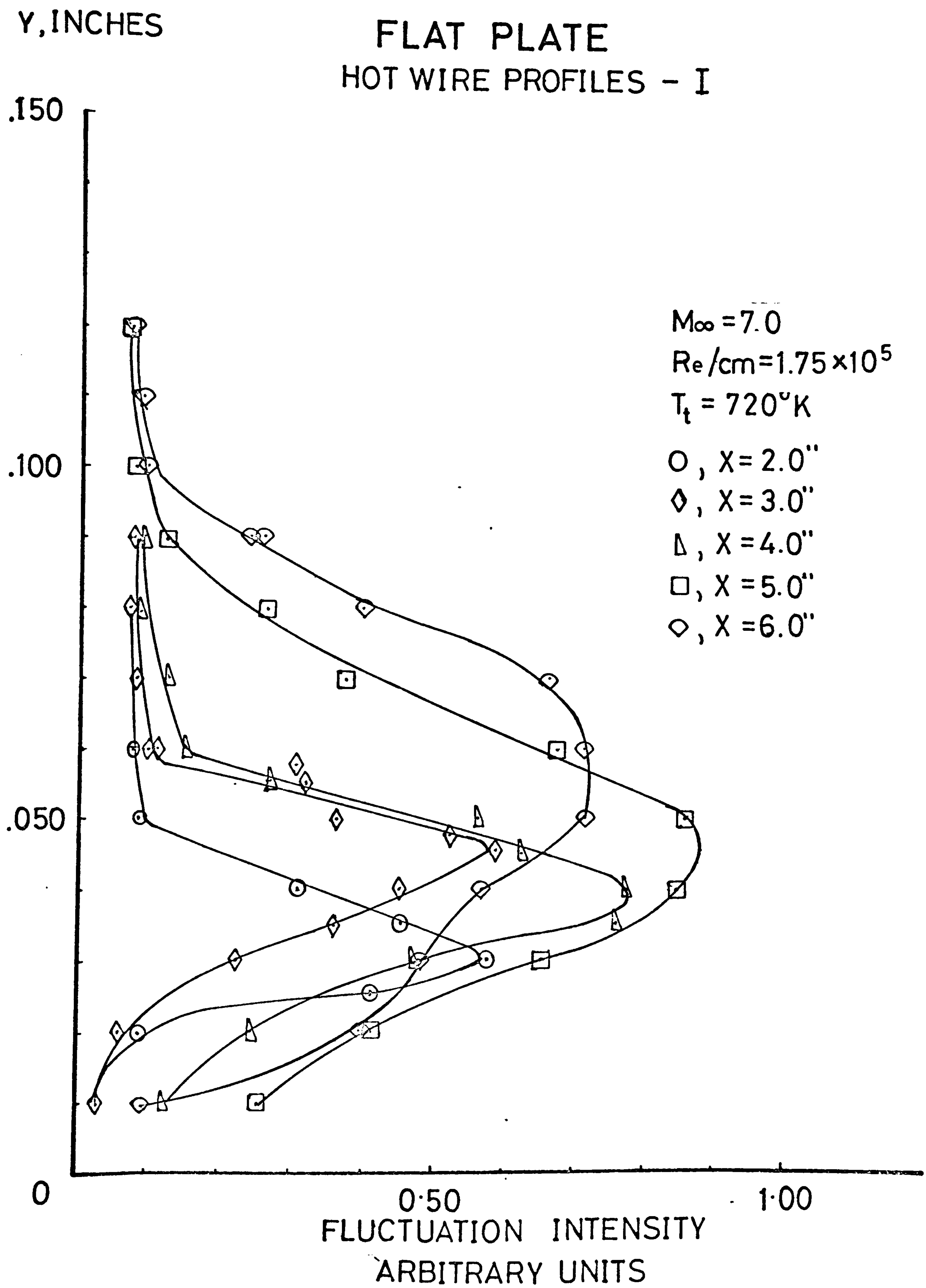
Y, INCHES
FLAT PLATE
HOT WIRE PROFILES - I
.150
.100
.050
0
0·50
1·00
FLUCTUATION INTENSITY
ARBITRARY UNITS
M∞ = 7.0
Re/cm = 1.75 ×10^5
T_t = 720°K
○, X = 2.0"
◊, X = 3.0"
Δ, X = 4.0"
□, X = 5.0"
◇, X = 6.0"

FIG. 11.9

FLAT PLATE

HOT WIRE PROFILES – II

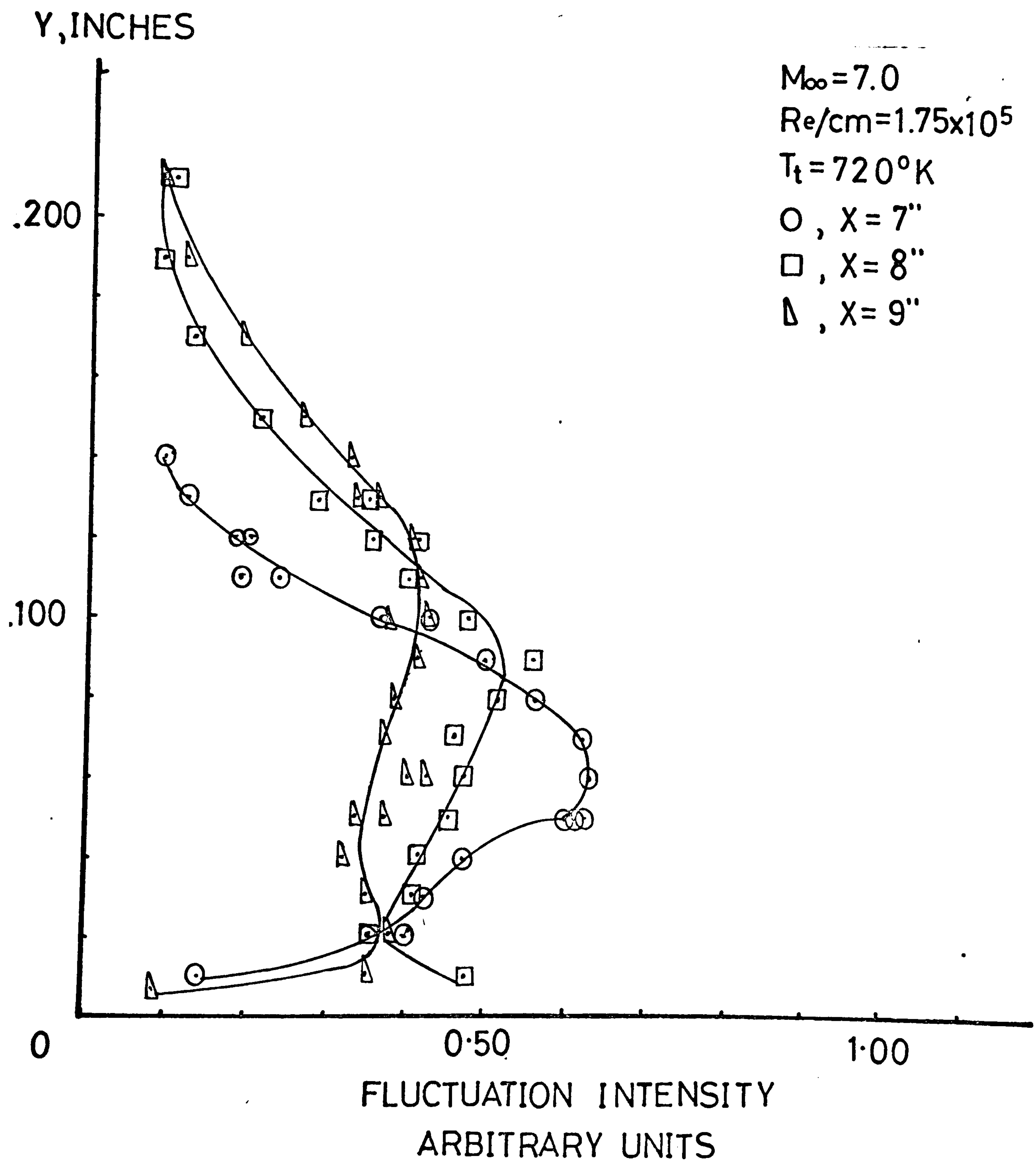

over a fixed time interval during each run. The integrated e' output had to be normalized at only one position (x = 3 inches) to match the free stream values of fluctuation levels. This was attributed to the use of a longer (and therefore more sensitive) probe in this position compared with the others.

Examining the profiles in succession, it is seen that even the lowest Re case (x = 2 inches) contains very considerable fluctuation intensities within the boundary layer which start to increase from the free stream level near the outer edge of the boundary layer then rise to a very sharply defined peak before falling off very rapidly below the peak to levels near or below the free stream level near the wall. At the x = 3 inch position, the profile has widened somewhat with the level falling off from the peak less rapidly and with the peak location itself moving away from the wall. The peak levels were about equal for these first two x position profiles. The next profile (x = 4 inches) remained similar in shape although the peak level has increased substantially and the profile has continued to broaden on the wall side of the peak. The fluctuation level at the position closest to the wall has started to increase also. Substantial changes in the profile shape first become apparent at x = 5 inches where rapid broadening of the profile toward the free stream has begun. The profile broadening toward the wall has continued and the level at the y = .010 inch position has increased further. The observations at this x position take on special significance when it is remembered (Fig. 10.3) that the transition region defined by the surface heat transfer results on the flat plate in Chapter 10 is located approximately between x = 5 and x = 8 inches. It thus appears that surface heat transfer measurements do not detect a change in laminar conditions until the laminar breakdown which begins in the outer regions of the boundary layer has spread to the proximity of the wall. This conclusion has also been observed at adiabatic supersonic conditions by Potter and Whitfield (Ref. 77) and at hypersonic adiabatic conditions in a helium tunnel by Maddalon and Henderson (Ref. 79). The nature of the breakdown process will be discussed further in Section 11.3.3.

Beyond the x = 5 inch point, the profiles continue to broaden substantially with the peak level decreasing and becoming less well defined. The profile at the surface-defined end of transition (x = 8 inches) indicates a greatly increased boundary layer thickness and a much flatter fluctuation level distribution extending over the inner half of the boundary layer to the proximity of the surface. There is some further slight readjustment in the profile at the x = 9 inch position. A few measurements below y = 0.10 inches at the x = 10 inch position indicated no further decrease in fluctuation level. The flat distribution profile in the inner portion of the boundary layer is characteristic of the uniformly distributed vorticity of the inner core of a turbulent shear layer. In fact, the entire fluctuation profile shape for the fully developed turbulent case (x = 9 inches) is remarkably similar to the intermittency factor distribution measured by Klebanoff (Ref. 127) for a flat plate incompressible turbulent boundary layer. With the intermittency factor defined as the fraction of time the flow is turbulent, Klebanoff found that the factor decreases from unity in the inner core of the boundary layer to zero near the outer edge. This variation took place between $y/\delta = .5$ and 1.2 in a similar way to the fluctuation distribution for the turbulent case of Fig. 11.9 which also began to decrease at $y/\delta \simeq 0.5$. Klebanoff demonstrated that the position of the fairly sharp boundaries between the highly turbulent flow in the boundary layer and the nearly turbulence-free external stream fluctuates strongly with time. Detailed examination of the probe output signal (before integration) in the present tests revealed that the drop-off in integrated output was due to the intermittent nature of the wavy outer edge of the turbulent boundary layer when viewed by a probe fixed with respect to the wall.

The boundary layer thickness growth can be estimated from the fluctuation profiles of Figs. 11.8 and 11.9. With the thickness defined as where the fluctuation level approached the free stream level (say within 1%) the x growth of δ is given in Fig. 11.10. Values of δ estimated from pitot probe profiles on the hollow cylinder and flat plate are also included for comparison. It should be remembered, however, from the discussion in Chapter 10, that the hollow cylinder transition was delayed compared to the flat plate case and that δ measurements would therefore not be comparable after transition had begun on the plate. The laminar measurements can be compared though and are seen to agree closely with a growth law approximately proportional to $(x)^{\frac{1}{2}}$. Deviation from a laminar growth rate does not begin until the x = 5 inch position where the fluctuation profile was first observed to change appreciably and the surface $\dot{q}$ first began to increase. The growth from this point is quite rapid as is typical of transitional boundary layers. The growth rate approaches $\sim x^{4/5}$ past the peak in the surface $\dot{q}$ point (x = 8 inches, from Chapter 10) as is characteristic of turbulent boundary layers.

The mean (d.c.) probe output was also measured during each run as shown in Fig. 11.5. With radiation losses, free convection, and heat conduction to the probes balanced by the bridge before the run, the increase in bridge voltage (squared) required

FLAT PLATE
BOUNDARY LAYER THICKNESS

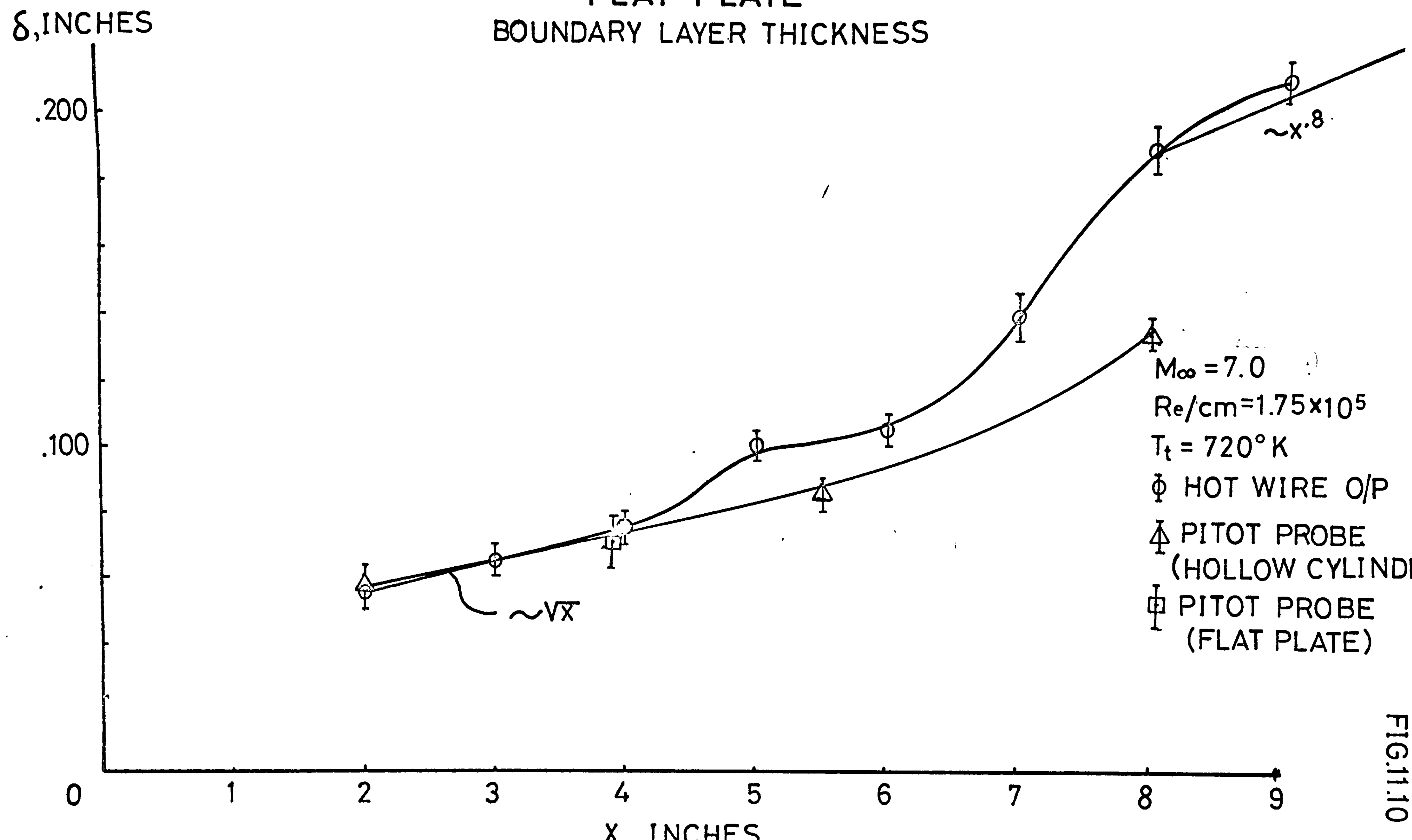

FIG.11.10

to maintain bridge balance during the run was proportional to the forced convection heat transfer from the wire due to the flow. The variation of wire mean convected heat transfer through the boundary layer is shown in Fig. 11.11 for two x positions (3 and 9 inches) corresponding to laminar and turbulent conditions respectively. The relative shape of the two profiles is qualitatively very similar to the mass flow (ρu) profiles measured by Staylor and Morrisette (Ref. 78) with calibrated hot wires at M = 6 and adiabatic wall conditions. The present heat transfer data could not be converted directly to mass flow profiles without knowledge of the wire's Nusselt Number dependence on Re and M.

11.3.2 The Critical Layer

Measurements of the streamwise velocity fluctuation distribution through a flat plate laminar boundary layer in low speed flow by Schubauer and Klebanoff (Ref. 107) showed a very well defined region of maximum activity similar to the sharply defined peaks found in the present hypersonic tests (see Fig. 11.8). The main readily apparent difference between the two sets of profiles was that for the incompressible results the fluctuation peak location was very near the wall whereas in the hypersonic results the peak had moved out a considerable distance from the wall. The location of the peak (y_c) in the present tests is shown in Fig. 11.12 for all the x positions measured. As mentioned earlier, the sharpness of the peaks tended to decrease as the Re increased and thus the definition of the peak location became more ambiguous as transition progressed until, at the fully turbulent condition, the 'peak' extended over most of the lower half of the boundary layer. The location of the peak fluctuation level in the earliest stages of development is, however, the most interesting from a

FIG.11.11

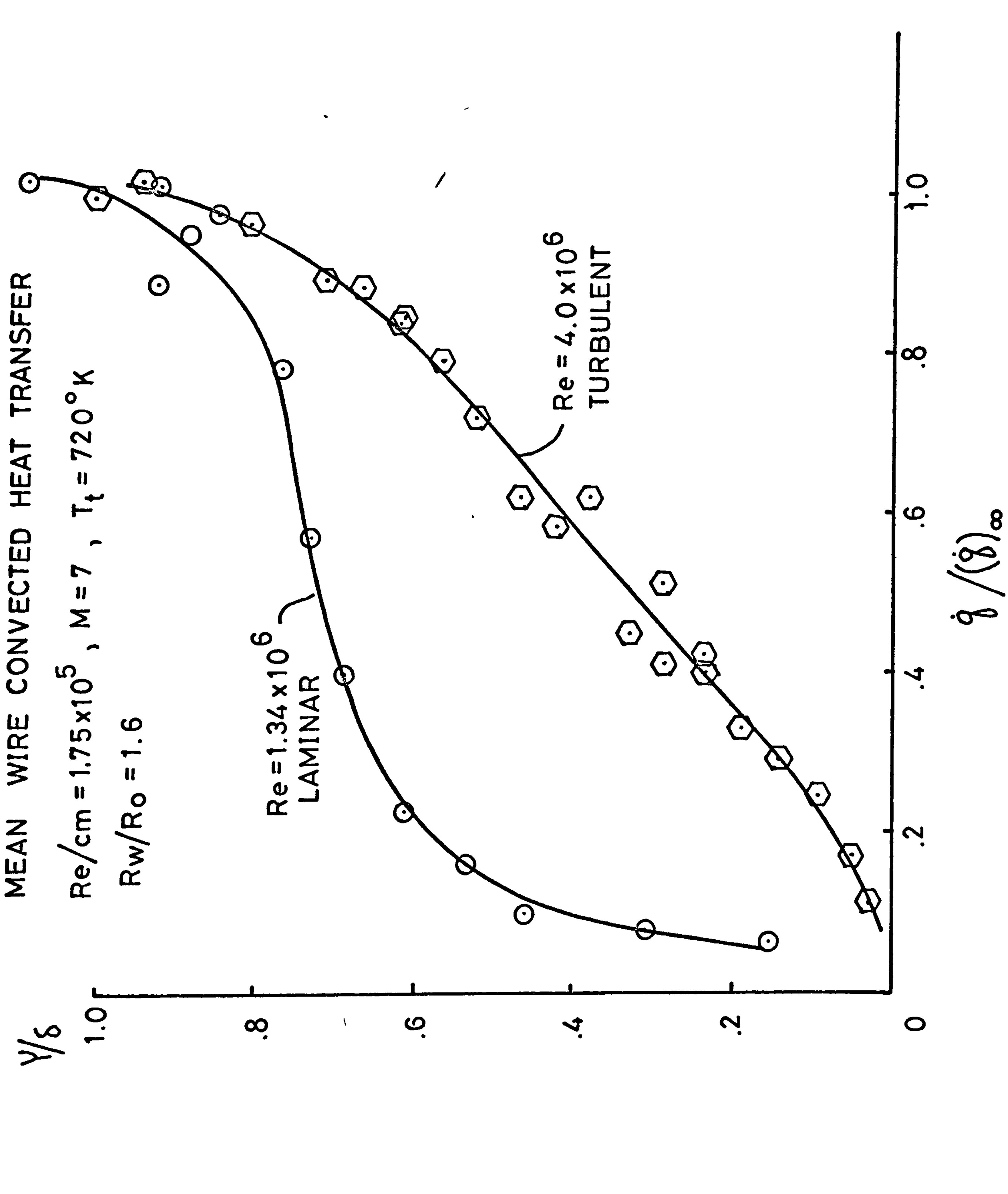
MEAN WIRE CONVECTED HEAT TRANSFER
Re/cm = 1.75x10^5 , M = 7 , T_t = 720°K
Rw/Ro = 1.6
Re = 1.34 x 10^6
LAMINAR
Re = 4.0 x 10^6
TURBULENT
y/δ
1.0
.8
.6
.4
.2
0
.2
.4
.6
.8
1.0
q̇/(q̇)∞

FIG.11.12

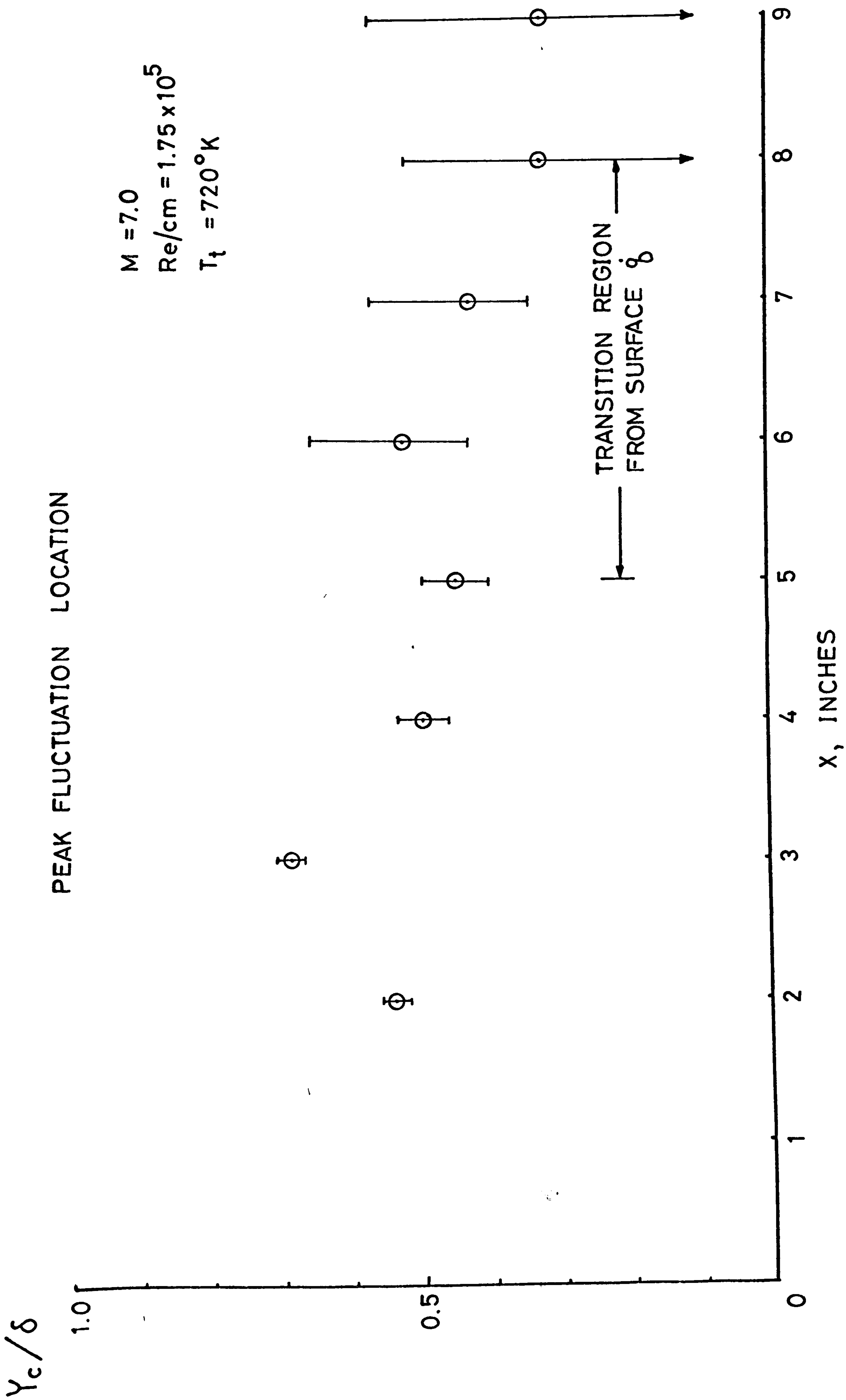

PEAK FLUCTUATION LOCATION
M =7.0
Re/cm = 1.75 x 10^5
T_t =720°K
TRANSITION REGION
FROM SURFACE q̇
Y_c/δ
1.0
0.5
0
1
2
3
4
5
6
7
8
9
X, INCHES

stability point of view, and thus this will be the profile considered exclusively in the discussion which follows.

The outward displacement of the peak fluctuation point at supersonic conditions was first observed by Laufer and Vrebalovich (Ref. 126) at M = 1.6 and 2.2 and by Demetriades (Ref. 124) at M = 5.8 on an adiabatic flat plate. By direct comparison with the characteristic peaks which were a feature of the self-excited instability oscillations observed in incompressible laminar boundary layers, Laufer and Vrebalovich inferred that the peak fluctuations were a result of the strong vorticity concentrations at points in the flow where the phase velocity (propagation speed) of the oscillations were equal to the local mean velocity, i.e. at the critical layer.

The concept of a critical layer arose from the existence of an apparent mathematical singularity in the inviscid form of the stability equation (Orr-Sommerfeld equation). This equation was derived by superimposing a two-dimensional disturbance which was a function of time and space on the mean flow before substitution into the Navier-Stokes equations. Solutions of the form given by the stream function

$$\Psi(x,y,t) = \phi(y)e^{i(\alpha x-\beta t)} \tag{11.3.1}$$

were sought, where α is the wave number of the disturbance related to its wave length λ by

$$\lambda = 2\pi/\alpha \ . \tag{11.3.2}$$

The quantity β is complex and given by

$$\beta = \beta_r + i\beta_i \tag{11.3.3}$$

where β_r in the circular frequency of the partial oscillation and β_i determines the amount of amplification (if positive) or damping (if negative). The ratio of α and β defines a more useful quantity given as

$$c = \frac{\beta}{\alpha} = c_r + ic_i \qquad (11.3.4)$$

where c_r is now the phase velocity (propagation velocity) of the disturbance and c_i, like β_i, is the amplification factor giving the amount of amplification or damping of the disturbance depending on its sign. In its inviscid incompressible form, the resulting Orr-Sommerfeld differential stability equation is given as

$$(u-c)(\phi''-\alpha^2\phi) - u''\phi = 0 \qquad (11.3.5)$$

where u is the local mean velocity and the primed terms represent differentiation w.r.t. the y variable.

Lin (Ref. 128) has shown that for self-excited disturbances to exist, u'' must vanish within the boundaries of the flow considered. This inflection point criterion for instability was first proposed by Lord Rayleigh in 1880. To avoid the singularity in (11.3.5) where the phase velocity equals the local flow velocity $(u-c) = 0$, either u'' must vanish simultaneously or, more generally, viscosity terms must be considered in the full stability equations in the region of the critical layer. Schlichting (Ref. 85) has shown that the inclusion of viscosity terms near the critical layer introduces a phase change in the fluctuating velocity component, u, which has important consequences for the mechanism of propagation of disturbances and the interchange of angular momentum (vorticity) across the critical layer. A more comprehensive discussion of the derivation and particular solutions of the stability equations can be found in Lin's book (Ref. 128).

Lees and Lin (Ref. 129) have suggested a generalized inflection point criterion for compressible fluids which is both a necessary and sufficient condition for the existence of a neutral disturbance. This is of the form

$$\frac{\partial}{\partial y}(\rho\frac{\partial u}{\partial y}) \sim \frac{\partial}{\partial y}(\frac{u'}{T}) = 0 \ . \qquad (11.3.6)$$

The phase velocity of this disturbance is equal to the mean velocity where (11.3.6) is satisfied. Lees and Lin also postulated that only disturbances which propagate subsonically compared with the free stream velocity need be considered although this was not proved rigorously. Mack's (Ref. 80) numerical solutions of the full compressible stability equation indicated that although amplified supersonic disturbances do exist, the most unstable are always subsonic w.r.t. the free stream. This places an important restriction on the location of the unstable disturbances in a supersonic boundary layer. The phase velocity, c_r, then must be given as

$$c_r > u_e - a_e \qquad (11.3.7)$$

or

$$\frac{c_r}{u_e} > 1 - \frac{1}{M_e} \ . \qquad (11.3.8)$$

Thus the phase velocity takes on a higher fraction of the free stream velocity with increasing M. Mack's calculations in fact showed that the location of the generalized inflection point (11.3.6) satisfied (11.3.8) for an adiabatic flat plate (to M = 6) and moved toward the outer regions of the boundary layer with increasing M in much the same way as c_r/u_e.

Returning now to the measured values of peak fluctuation location and assuming that this corresponds to the critical layer location, Demetriades (Ref. 124) found that his critical layer height of $y/\delta = 0.9$ corresponded to $c_r/u_e = .98u_e$ which easily satisfied (11.3.8) at M = 5.8. Potter and Whitfield (Ref. 77) measured critical layer location on an insulated flat plate between M = 3 and 8 and found that the peak fluctuation location increased monotonically with M and agreed with the measurements of Refs. 124 and 126. Owen (Ref. 130) recently confirmed these earlier measurements at M = 2.5-4.5 on an insulated flat plate. The only other adiabatic measurements reported were on cones by Maddalon and Henderson (Ref. 79) in a helium tunnel between M_e = 7.5 and 15.6. They found the critical layer height approximately constant over the M range tested although there was some downward movement of the peak when the boundary layer became transitional (from surface measurements). In all the measurements listed above, the critical layer location was determined from the very intense peaks in the fluctuation distribution across the boundary layer as detected by hot wire or film anemometers. The data is summarized in Fig. 11.13.

Also included in Fig. 11.13 is the peak fluctuation height location of the present tests (for x = 2 inches, Re = 8.9 x 10^5) and the only two other cold wall measurements recently reported by Nagamatsu, et. al. (Ref. 131) and Softley, et. al. (Ref. 92). The data from Refs. 92 and 131 were measured on 10^o total angle cones in shock tunnels. Both measurements were admitted by the authors to be very tentative, preliminary estimates of peak fluctuation location. In both tests flat wedge shaped probes with a platinum thin film gauge mounted near the leading edge were used. These probes had dimensions of the order of 10-20% of the boundary layer thickness and only 5 or 6 positions were investigated. Nagamatsu, et. al. estimated the peak location by the degree of scatter in the wedge probe mean surface heat transfer level. Softley, et. al. estimated the peak location by visually measuring the approximate peak-to-peak signal fluctuations from his probe. The error bars on this data in Fig. 11.13 give reasonable estimates of the uncertainty in the measurements. Additional uncertainty in the interpretation of

PEAK FLUCTUATION HEIGHT IN LAMINAR BOUNDARY LAYERS

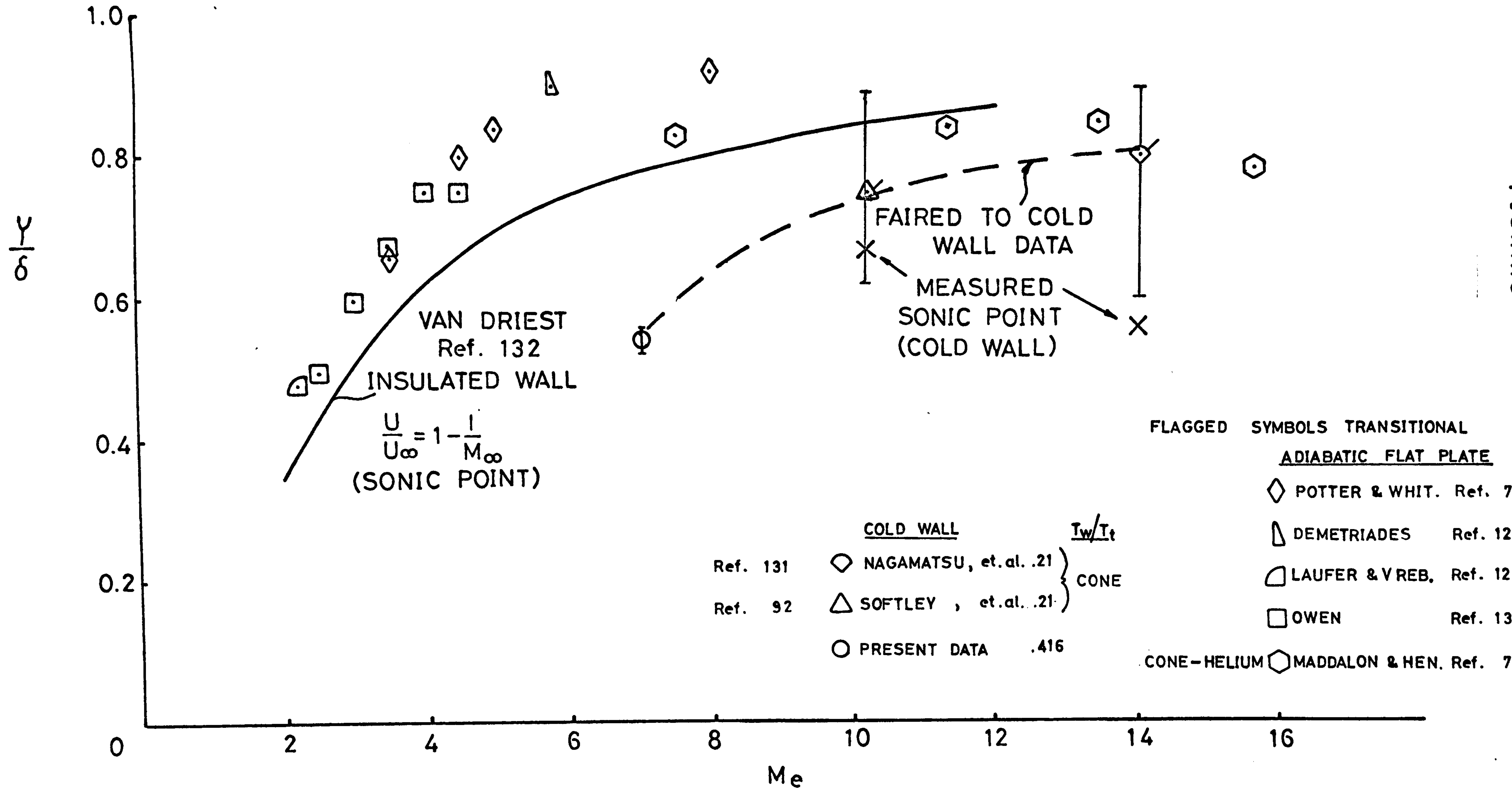

FIG.11.13

their data may be caused by the fact that the measurements were made at the beginning of transition (defined by surface measurements) and thus were not strictly laminar although Fig. 11.12 suggests that this may not be too important. In addition, the data of Nagamatsu was obtained on a long model in a conical nozzle with the resulting strong favorable pressure gradients along the model having a possible effect on velocity profiles and thus stability.

Nagamatsu, et. al. (Ref. 131), summarized existing supersonic critical layer data at the time of their report (1966) and calculated the sonic point location (y/δ where $u/u_e = 1-1/M_e$) for an insulated plate using the analysis of Van Driest (Ref. 132). They found that the adiabatic data was well above the sonic point or, in other words, the disturbances associated with the critical layer were subsonic w.r.t. the free stream. Owen (Ref. 130) made a similar comparison with the adiabatic data also using the Van Driest paper and found that the peak disturbance location was very <u>near</u> the sonic point up to M = 8. There appears, however, to have been a numerical error in Owen's calculation of the Van Driest profiles. The helium data of Ref. 79 cannot be compared directly with the air calculations of Van Driest. The authors of Ref. 79, however, presented velocity profile measurements of their tests and a close examination of these reveals that their peak locations were well above the sonic disturbance point.

The cold wall laminar profile calculations of Van Driest are not appropriate for the temperature levels of the shock tunnel and Gun Tunnel data. Both Nagamatsu (Ref. 131) and Softley, et. al. (in Ref. 133), however, have reported velocity profile measurements for the conditions of their fluctuation tests. The sonic disturbance location can be estimated from these results and are shown in Fig. 11.13. It is seen that the peak fluctuation location is also above the sonic point for this cold wall data.

Although velocity profiles were not measured for the present Gun Tunnel tests, it seems reasonable that the criterion of disturbances subsonic w.r.t. the free stream dominating the stability of the laminar boundary layer will be satisfied for the M = 7 cold wall case. The important observation is that although this criterion is still satisfied for the cold wall case, the actual location of the critical layer need not be confined to the outer edge of the boundary layer at hypersonic conditions when strong heat transfer to the walls is present.

A very recent note has been published by Stainback (Ref. 134) in which an attempt to predict the critical layer height in laminar boundary layers has been made. The calculation of the location of the maximum value of a stability parameter proposed by Rouse has been made. This parameter has the form

$$R = (\rho y^2/\mu)\partial u/\partial y \tag{11.3.9}$$

and is presumed to give the location where instability is most likely to occur. Its form is similar to (11.3.6) although it is obviously functionally different. Stainback found a reasonable prediction of existing adiabatic data between M = 3 and 8. The helium, cold wall, and lower M predictions were less successful although the upward trend with M and downward trend with wall cooling were qualitatively predicted. No attempt to substantiate the use of this parameter on compressible stability theory grounds was made.

11.3.3 Boundary Layer Breakdown and Transition

In the discussion of the integrated wire output fluctuations for the present tests in Sections 11.3.1 and 11.3.2, details of the nature of the individual fluctuations were not examined. This is also true of all the references cited in the preceding section in which supersonic laminar boundary layer fluctuations were measured. In all cases, fluctuation details were lost in some average measurement such as rms voltage. Schubauer and Klebanoff (Ref. 135) in their study of low speed laminar boundary layer transition, concluded that "while certain mean quantities, such as the rms value of the fluctuations, were useful, records of the actual wave form of the fluctuations turned out to be by far the more meaningful". The results of their detailed analysis led to a picture of the transition region as being composed of discrete 'spots' of turbulence which grew in size while travelling downstream to finally merge into fully turbulent flow and thus substantiating Emmons' turbulent spot model (Ref. 105). Schubauer and Klebanoff's wire output signals indicated low level periodic oscillations in the laminar layer followed by a sudden burst of turbulence which was in turn followed by laminar oscillations. As the wire was moved through the transition region, the flow consisted of periods of turbulence for an increasing fraction of time until the flow became completely turbulent. Following this important contribution, many increasingly sophisticated studies were reported by various workers which added important details to the understanding of at least the low speed transition phenomenon. The picture, however, is by no means complete conceptually and especially theoretically even for the incompressible case.

Stuart (Ref. 136) has reviewed the major theoretical work (up to 1965) relating to various phases of the region between the initial instability and the final fully turbulent condition in incompressible flows. Tani (Ref. 137) has reviewed some of the important incompressible experiments which have contributed to the general picture of the full transition process. Stuart defined six regions of interest in the incompressible flat plate boundary layer transition process. These were given, briefly, as:

1) Region of initial instability to small disturbances as predicted by linearized instability theory and confirmed by Schubauer and Skramstad (Ref. 74).

2) Region of three-dimensional spanwise periodicity due to irregular amplification of disturbances as a result of minor perturbations in the free stream. The initial experimental observation of this region was made by Klebanoff and Tidstrom (Ref. 138).

3) The strong development of the three-dimensional periodic structure with large 'peaks' in velocity fluctuation levels occurring at fixed spanwise positions. The result is visualized as a streamwise vortex system with the filaments parallel to the stream direction.

4) Region of vorticity concentration and the development of a region of large shear (inflection point) in the instantaneous streamwise velocity profile near the outer region of the boundary layer as observed by Kovasznay, et. al. (Ref. 139).

5) Region of breakdown when sufficiently strong shear has developed in the instantaneous velocity profile near the spanwise peaks. A strong high frequency velocity fluctuation develops quite rapidly which Klebanoff and Tidstrom (Ref. 138) have described as 'hairpin eddies' and assigned the role of embryo turbulent spots.

6) Region of turbulent spot growth spanwise and toward the wall until agglomeration of spots into a fully turbulent region is completed via the model proposed by Emmons (Ref. 105).

Of these six regions, only the first has received both theoretical and experimental attention at supersonic speeds and then with only limited success due to the strong influence of free stream disturbances in most tunnels. A notable exception is the unpublished work of Kendall reported by Morkovin (Ref. 82) in which partial verification of Mack's numerical stability predictions (Ref. 80) were made in a supersonic tunnel with laminar sidewall boundary layers.

The regions 2 → 5 have received no attention in compressible flows either experimentally or theoretically. In fact, it cannot be said with certainty whether the incompressible mechanisms will adequately describe the compressible case.

The only other region of the transition regime to receive attention at supersonic speeds is the final turbulent spot growth region and here only experimentally. Although the existence of supersonic turbulent spots is well established (e.g. Refs. 108 and 140), most experimental information about their behavior has been obtained from optical observations and these are, necessarily, somewhat limited. Wide bandwidth surface heat transfer instrumentation is capable of detecting the passage of turbulent spots, as was reported in Chapter 10 and in Refs. 131 and 76, but the detection is only after the spot has extended its influence to near the wall. The question of whether turbulent spots originate at or near the model leading edge (Ref. 108) or further downstream (Ref. 140) is by no means settled. The question of the y location of spot origin and subsequent growth rate perpendicular to the model surface is equally uncertain.

The detailed anemometer measurements of the supersonic adiabatic laminar boundary layer leading up to transition, which were discussed in the previous section, generally (where several x positions were probed) presented a picture of a gradual spreading of fluctuations from a very narrow region within the boundary layer toward the wall with increasing Re. A similar picture was presented for the cold wall measurements of the present study shown in Fig. 11.8. Yet, as mentioned in the opening paragraphs of this section, previous 'microscopic' measurements of supersonic laminar boundary layer transitional breakdown did not include detailed observations of the nature of the fluctuations. In fact, it was generally assumed by the various authors (Refs. 77, 124, 78, 126, 79, 130) that the fluctuations observed were synonymous with the laminar self-excited instability oscillations associated with the early stages of transition (region 1). This assumption may have been justified in some cases, although not conclusively substantiated.

Analysis of the data from those references where the growth of the fluctuations with Re was observed (Refs. 77, 78, 79), however, indicated a continuous growth in intensity up to the surface-observed beginning of transition starting from the lowest Re position (very near the leading edge in the case of Ref. 77). This observation contrasts sharply with the subsonic measurements of Schubauer and Klebanoff (Ref. 135) in which a very strong increase in fluctuation level was found between the purely laminar oscillation disturbances and that region where turbulent spots began to appear. This in turn suggests that the fluctuation measurements of Refs. 77, 78 and 79 were, in fact, observations of turbulent spot growth within the boundary layer. If this assumption is true, then it would seem that embryo turbulent spots are generated very early within the supersonic laminar boundary layer indeed, verifying James' (Ref. 108) observation that in supersonic/hypersonic boundary layers, turbulent spots originate very near the leading edge. This would mean that of the six regions of the transitional boundary layer outlined by Stuart (pg.149), the first five are compressed into a very short distance (if the same turbulence generation mechanism can be assumed to apply to compressible flows). It is possible that this shortened region of instability and three dimensional development is the region which is dominated by the strong free stream disturbances shown to control the transition process in supersonic wind tunnels.

The assumption of turbulent spot development near the leading edge (or at Reynolds Numbers very much less than the beginning of transition on the model surface) is consistent with detailed examination of the hot wire outputs in the present M = 7 tests. The method of anemometer output analysis shown in Fig. 11.6 permitted a fast sweep oscillogram of the signal to be obtained for each run. This sweep was usually made at 100 μsec/cm starting at 30 msec. after the start of the run. Typical oscillograms at five different x positions (all taken at values of y/δ near the peak in the profiles of Figs. 11.8 and 11.9) are shown in Fig. 11.14. The first trace (a), corresponding to x = 2 inches, contains very well defined, randomly distributed 'spikes' in the output. These are certainly more realistically attributed to discrete turbulent spots than to periodic oscillations of the laminar layer. The amplitude of some of the spikes represent a 30% fluctuation in mean wire output during the run. The amplitude variation is probably dependent on the size of the eddy swept past the wire and bandwidth limitations of the wire system. The low amplitude narrow spikes could be due to spots which have either formed later than the others (and thus are smaller when reaching the wire) or have originated at spanwise positions away from the wire and only partially intersect the probe. The pulse width of some of the larger spikes would indicate spots of appreciable size (of the order of 1 inch even assuming a spot velocity of only one half the free stream value [Ref. 140]). This in turn would indicate that the spot origin is much further upstream than the first test port (x = 2 inches) for the present test conditions.

FIG. 11.14

TYPICAL HOT WIRE OUTPUT NEAR PEAK Y/δ

$M = 7$, $Re/cm = 1.75 \times 10^5$, $T_t = 720^\circ K$

Re

a)

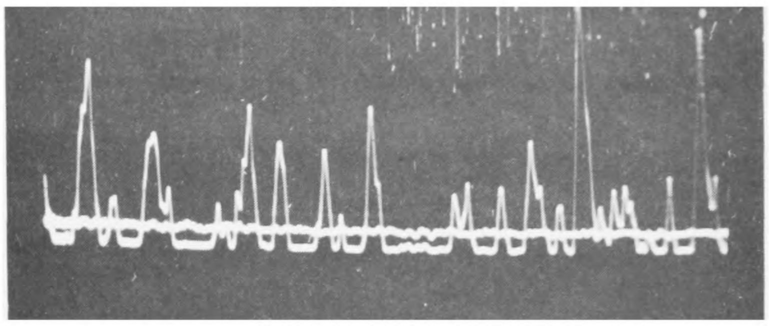

8.9×10^5

100 μsec/cm ⟶

b)

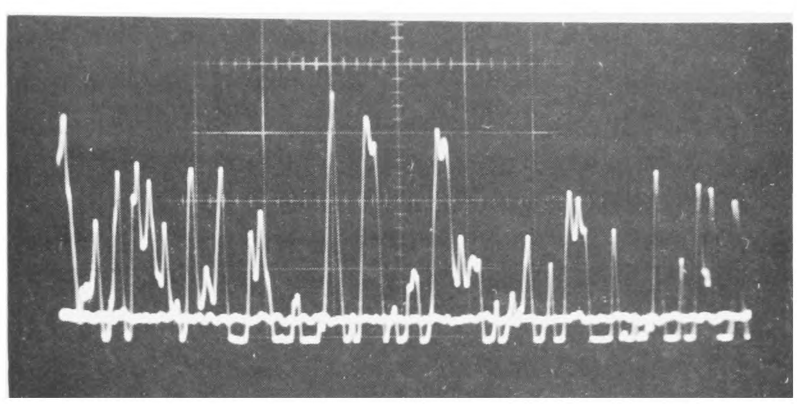

1.78×10^6

c)

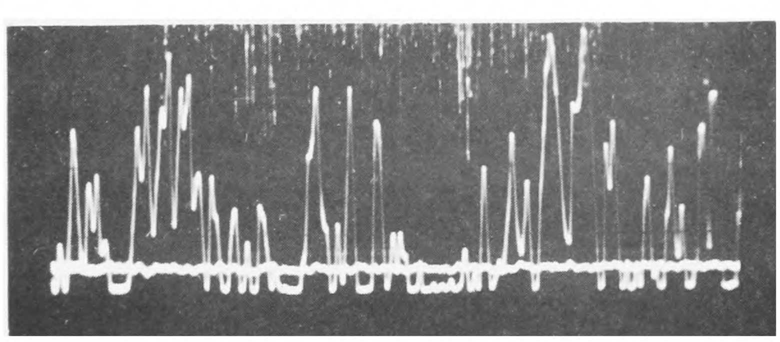

2.22×10^6

d)

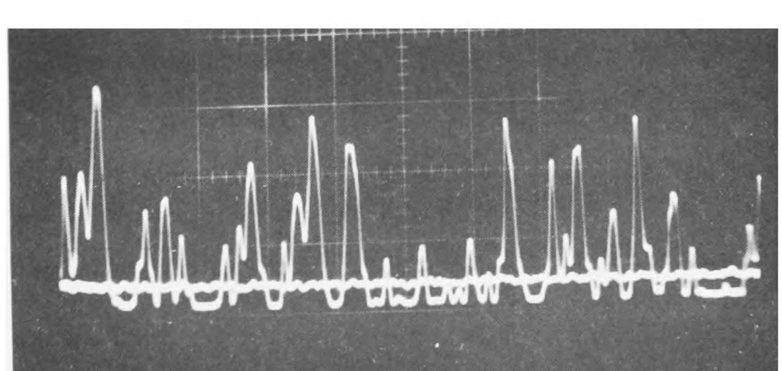

2.67×10^6

e)

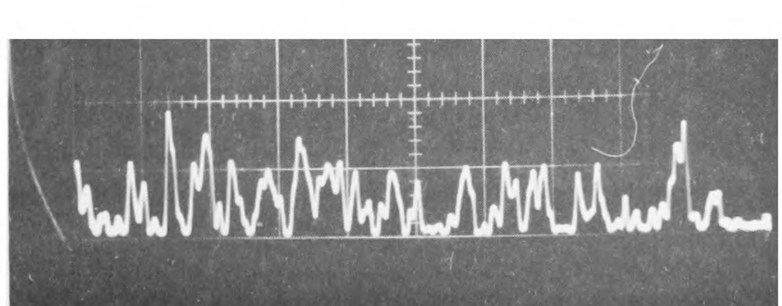

4.0×10^6

Another interesting aspect of the character of the sharp fluctuations in the probe output is their preferred direction (sign). Analysis of the complete a.c. bridge amplifier output signal indicated that all of the dominant fluctuations are negative, i.e. the fluctuations represent an instantaneous <u>decrease</u> in heat transfer from the wire. This is consistent with Klebanoff and Tidstrom's (Ref. 138) observations of turbulent eddy production in low speed laminar boundary layers. In fact, the wire outputs of Ref. 138 are remarkably similar to the observed spike pattern in the present tests even though the free stream velocities in the two tests differed by two orders of magnitude. The decrease in wire heat transfer during spot passage can be conceptually explained by visualizing the newly formed spot as a region of fluid moving at a velocity somewhat less than the local mean velocity for a purely laminar flow. This concept is consistent with the optical supersonic findings of Ref. 140 where the eddies were seen as erupting with a low mean velocity before accelerating to a velocity of about 0.7 free stream speed (at $M = 2$).

A qualitative estimate of the vertical growth rate of the spots can be made from the observation that the spots originate at $x < 2$ inches and are not observed by surface instrumentation (Chapter 10) until near the $x = 5$ inch position. This indicates a very gradual growth rate normal to the surface compared to the rapid stretching which must take place in the x direction. This slow growth (which was also clearly indicated in the integrated fluctuation profiles of Figs. 11.8 and 11.9) contrasts with the 'precipitous' growth rate suggested by Spangenberg and Rowland (Ref. 140) from optical studies at $M = 2$. This difference may be due to the method of observation or to real differences resulting from the widely different flow conditions. The gradual growth and spread of the fluctuation profiles reported in Refs. 77, 78 and 79 tends to support the 'slow growth' concept of high supersonic/hypersonic turbulent spot propagation.

An examination of the changes in the detailed probe output oscillograms with increasing x in Fig. 11.14a-e reveals a pattern at least qualitatively consistent with Emmons' (Ref. 105) turbulent spot model of boundary layer transition. The spike amplitude and frequency increased with x until many of the individual peaks had merged with adjoining peaks at the beginning of surface transition (Fig. 11.14c). The amplitude and frequency of strong fluctuations then began to decrease presumably because of the rearrangement of the large scale merged turbulent eddies into the smaller scale turbulence associated with turbulent boundary layers. The frequency of this turbulence rapidly exceeds the bandwidth of the system with a resulting drop in probe output. The final oscillogram (Fig. 11.14e) is in the fully turbulent region and has lost all trace of large scale discrete turbulent spots.

A plot of the integrated probe output level at a constant y position over the length of the model supports this general picture of spot growth. This is shown in Fig. 11.15 with the location of transition determined from the surface heat transfer experiments of Chapter 10 included. The nearly linear increase in integrated fluctuation intensity from the first upstream probe position until the surface beginning of transition corresponds to the region of linear growth of individual turbulent spots. At this point (x = 5 inches) the turbulence has reached the wall and much of the region consists of merged groups of spots (Fig. 11.14c). The fluctuation intensity is then at a peak and begins a linear decrease in a new region of

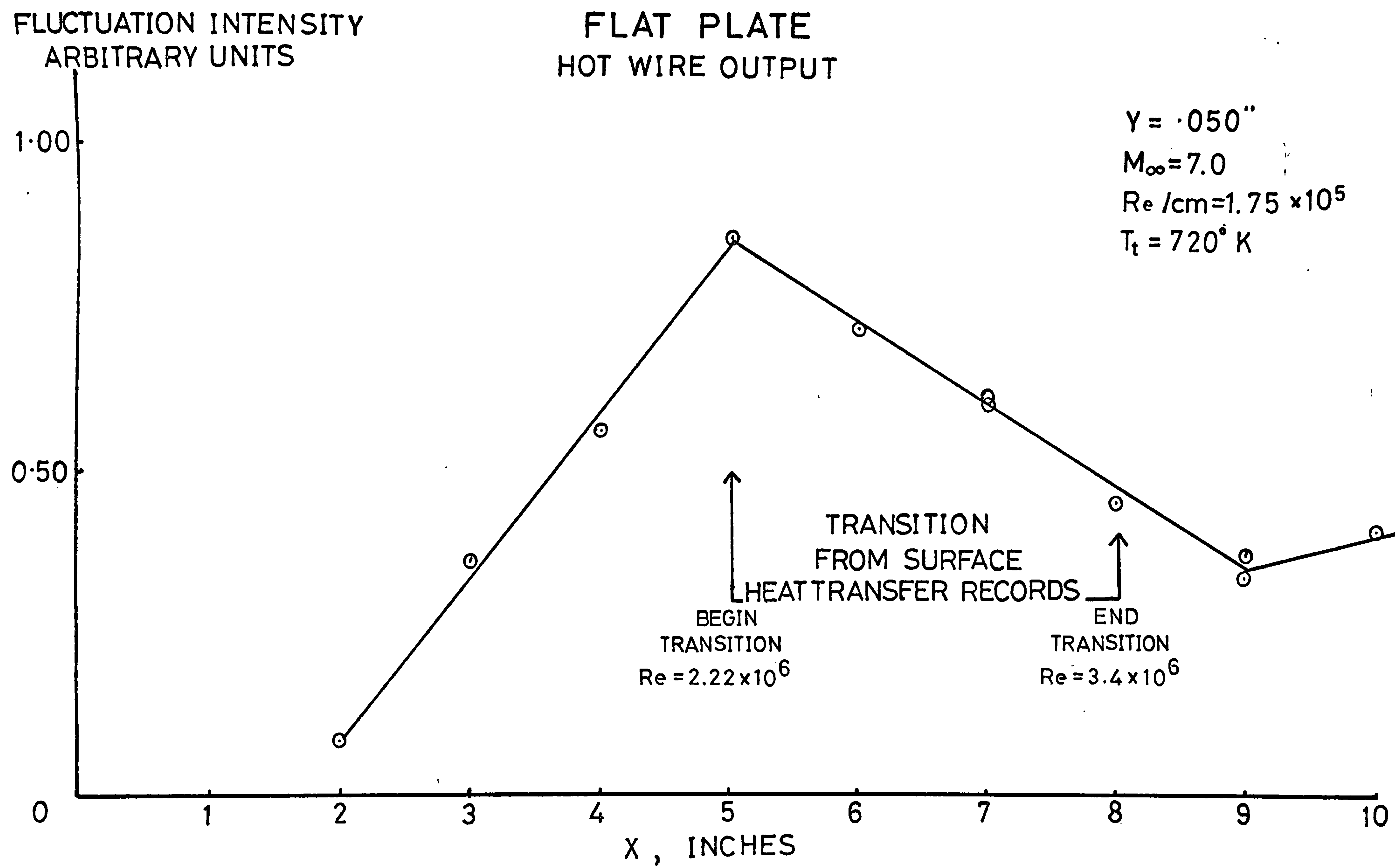
FLUCTUATION INTENSITY
ARBITRARY UNITS
FLAT PLATE
HOT WIRE OUTPUT
Y = ·050"
M_∞ = 7.0
Re /cm = 1.75 × 10^5
T_t = 720° K
1·00
0·50
0
TRANSITION
FROM SURFACE
HEAT TRANSFER RECORDS
BEGIN
TRANSITION
Re = 2.22 × 10^6
END
TRANSITION
Re = 3.4 × 10^6
1
2
3
4
5
6
7
8
9
10
X , INCHES

FIG.11.15

reorganization of the large groups of merged spots into smaller scale turbulent eddies. This continues until the breakdown is completed at or near the end of surface transition at which point the fluctuation intensity levels off in the fully turbulent boundary layer. It is the merger and breaking down of these large massed groupings of spots which are observed by the slower swept traces of surface film heat transfer outputs (e.g. see Fig. 10.11 for the case of a 10° cone).

It is interesting to recall the discussion of the critical layer concept in Section 11.3.2 in view of the strong evidence of this section that turbulent spot generation takes place very far upstream in supersonic laminar boundary layers. It was found in Section 11.3.2 that the location of the peak in the fluctuation y profiles was consistent with certain stability criteria for the location of the region of unstable disturbances. Since it is now suggested that the fluctuation measurements reported for the present tests and in the cited references were, in fact, fluctuations due to turbulent spots, a further property of the spot growth can be inferred. This is, namely, that the location of turbulent spot inception and initial linear growth must remain centered near the region in the boundary layer predicted by stability theory as the critical layer location.

CHAPTER TWELVE

CONCLUSIONS - PART II

Tests on a 3 inch hollow cylinder aligned with the flow direction have shown the surface pitot technique to provide a sensitive indication of the mean state of the boundary layer velocity profile. The location of the transition region defined by this measurement was seen to be a function of the free stream unit Reynolds Number. Transition tests made by the same technique on the same model in different hypersonic test facilities have shown the transition location to vary at similar free stream conditions. The transition correlation based on acoustic radiation from the turbulent boundary layer on the nozzle side walls given by Pate and Schueler (Ref. 81) appears to account for the variation in transition Reynolds Number between the facilities. This represents an extension of the functional validity of the Pate and Schueler correlation to open jet working section configuration and cold wall conditions. This test program is continuing under the sponsorship of the Ministry of Technology with tests planned in the supersonic tunnel at the NLR (Amsterdam), the gun tunnel at the National Physical Laboratory, and in the shock tunnel at the Technischen Hochschule, Aachen, in the near future.

It has been shown during comparative transition tests on a flat plate and a 10^{o} total angle cone in the Gun Tunnel, that a spanwise curvature effect is present. The flat plate transition location (defined by surface heat transfer variations) occurs earlier than the hollow cylinder results and the cone tests (based on heat transfer also) produce a transition location later than the hollow cylinder for the same boundary layer edge conditions. The movement of the transition Reynolds Number appears to be correlated by a function of the ratio of boundary layer thickness at the beginning of transition to the mean model curvature radius between the leading edge and beginning of transition point.

Surface heat transfer measurements on the flat plate and 10° cone models show a strong variation between the laminar and turbulent state and thus provide a sensitive indication of the transition location on the surface. The laminar heat transfer is generally slightly overpredicted by the Eckert reference temperature method (Ref. 110). The turbulent heat transfer is well predicted assuming the Spalding and Chi (Ref. 104) correlation for skin friction, a unity Reynolds analogy factor ($2\ St/c_f$), and a virtual origin of the turbulent boundary layer located at the peak in the surface heat transfer distribution.

Hot wire anemometer probes and instrumentation have been developed which are capable of operation in the environment and time scale of the Mach 7 Gun Tunnel. The use of these probes has led to the discovery of strong fluctuations within the boundary layer upstream of the point where transitional effects are first observed on the model surface. These fluctuations were observed to be initially confined to a very narrow region of the boundary layer but gradually spread normal to the surface with increasing distance downstream to cover the entire layer at the surface-observed beginning of transition. This initial region covers <u>at least</u> a factor of 2.5 in Reynolds Number. The fluctuation distribution then gradually adjusted to a characteristic turbulent profile by the surface-observed end of transition.

A detailed examination of the fluctuation wave forms revealed a discrete pattern which suggested the existence of turbulent spot breakdown down to the lowest Reynolds Number position tested on the model (8.9×10^5). This observation has an important bearing on theories of the onset of transitional instabilities in hypersonic boundary layers. The findings suggest that the three-dimensional development of small disturbances proceeds very rapidly to the production of large scale turbulent eddies (spots) which then grow gradually in the outer regions of the boundary layer before leading to the final fine scale breakup and redistribution of vorticity characteristic of turbulent boundary layers.

The experience gained in the use of hot wire anemometers in the Gun Tunnel brought to light many potential areas of future uses of the technique. An obvious first step would be the improvement of probe sensitivity and bandwidth. The sensitivity could be improved by using longer wires and/or different materials (with higher α's). The bandwidth could be improved by the use of more carefully designed probe connections and more refined adjustments of the bridge circuit (using perhaps a 1:1 bridge ratio). The use of a finer wire should not be disregarded either. This improved probe could be used to investigate the turbulent spot structure in more detail and to extend the measurements closer to the leading edge to investigate the origins of the spot growth. Attempts to partially shield the boundary layer from side wall radiation and to study the turbulent spot development and origin should also be made.

It should also be possible to make the probe response more quantitative by determining the system time constant (or thermal lag) with the flow on. End loss corrections could be calibrated out in free stream tests at various wire temperatures. The wire recovery factor and Nusselt Number variations with Reynolds Number could be calibrated in the Gun Tunnel free stream. The

Mach Number variation of these quantities could be determined on 2-D models. With a complete wire calibration available, the separation of mass flow and total temperature fluctuations could, in principle, be made by operation at various wire overheats. With sufficient improvement in bandwidth, the extension of fluctuation measurements to turbulent boundary layers and the free stream should also be possible. The use of the wires for mean measurements could yield useful information on boundary layer mean mass flow and total temperature profiles.

LIST OF REFERENCES

1. Cox, R.N. and Winter, D.F.T. "The Light Gas Hypersonic Gun Tunnel at A.R.D.E., Fort Halstead, Kent." AGARD Report 139, July, 1957.

2. Stollery, J.L. and Maull, D.J. "A Note on the Compression of Air Through Repeated Shock Waves." J.F.M., 3, 1958.

3. Bray, K.N.C., Pennelegion, L. and East, R.A. "Performance Studies for the University of Southampton Hypersonic Gun Tunnel". Proc. 11th Symp. Colston Research Soc., Univ. of Bristol, 1959, Butterworth, London.

4. Winter, D.F.T. "Multiple Shock Compression Using a Piston of Finite Weight". J.F.M., 8, 1960.

5. Stollery, J.L., Maull, D.J. and Belcher, B.J. "The Imperial College Hypersonic Gun Tunnel, August 1958-July 1959". J. Royal Aero. Soc. Vol. 64, 1960.

6. Needham, D.A. "Progress Report on the Imperial College Hypersonic Gun Tunnel". Imperial College, Department of Aeronautics, Report No. 118, August 1963.

7. East, R.A. "The Performance and Operation of the University of Southampton Gun Tunnel". A.R.C. 22878, Hyp. 188, 1960.

8. Bray, K.N.C. "An Evaluation of the Hypersonic Gun Tunnel". A.R.S., International Hypersonics Conference, Paper 1971-61, MIT, 1961.

9. Pennelegion, L. "Microwave Interferometry Studies in Free Piston Gun Tunnels". Proc. Second Symp. on Hypervelocity Techniques, Univ. of Denver, 1962.

10. Meyer, R.F., Campbell, W.F. and Jackson, K.P. "The NAE Hypersonic Gun Tunnel Part 1: The Compression Heater". NRC of Canada, Aeronautical Report LR-432, 1965.

11. Stalker, R.J. "Rebound of a High Speed Piston by Gas Compression in a Closed Tube". NRC of Canada, Report No. 6622, 1961.

12. Lemcke, B. "An Investigation of the Stagnation Conditions in the Shock-Compression Heater of a Gun Tunnel". FFA (Stockholm) Report No. 90, 1962.

13. Edney, B.E. "The Correlation of Measured and Predicted Temperatures in the Hypersonic Gun Tunnel". FFA (Stockholm) Report AU-II-209:2, 1965.

14. Edney, B.E. "Factors Limiting the Maximum Stagnation Temperatures in a Gun Tunnel". Paper presented at 26th Meeting of Supersonic Tunnel Association, 1966.

15. Davies, L. and Dolman, K.A. "On the Driver Reservoir Technique in Shock and Gun Tunnels". N.P.L. Aero Report 1226, ARC 28957, 1967.

16. Davies, L., Regan, J.D. and Dolman, K.A. "On the Equilibrium Piston Technique in Gun Tunnels". N.P.L. Aero Report 1240, ARC 29308, 1967.

17. Kamimoto, G., Mori, T., Kimura, T. and Kawachi, K. "Microwave Technique on Piston Motion Measurement in Hypersonic Gun Tunnel". Kyoto Univ., Dept. Aero. Eng., CP4, 1963.

18. Kamimoto, G., Mori, T. and Kimura, T. "An Analysis of the Piston Motion in a Hypersonic Gun Tunnel". Kyoto Univ.,Dept. Aero. Eng., CP5, 1964.

19. Merritt, G.E. "Velocity Measurements in the University of Southampton Hypersonic Gun Tunnel". A.A.S.U. Report No. 172, Univ. of Southampton, 1961.

20. East, R.A. and Perry, J.H. "A Study of the Characteristics of Gun Tunnel Operation at 10,000 lbs/in^2." Univ. of Southampton, A.A.S.U. Report No. 268, 1967.

21. Hurdle, C.V. "The Determination of Stagnation Temperature from Flow Velocity Measurements using a Spark Disturbance Method in a Hypersonic Gun Tunnel". RARDE Memo (B) 60/62, 1962.

22. Clayden, W.A. "Bulk Compressibility Effects in the RARDE No. 3 Hypersonic Gun Tunnel". RARDE Memo 21/65, 1965.

23. Bowman, J.E. "Determination of Stagnation Temperatures in the RARDE Hypersonic Gun Tunnel from Streak Camera Measurements of Flow Velocity". RARDE Memo. 2/66, 1966.

24. Vincent, C.R. "The Increase in Stagnation Temperature Produced by Pre-heating the Working Gas in a Hypersonic Gun Tunnel". RARDE Memo. 54/66, 1966.

25. LaGraff, J.E. "The Design, Instrumentation and Calibration of the Oxford University Hypersonic Gun Tunnel". Oxford University Department of Engineering Science, Report No. 1094,69, Dec. 1969.

26. Hawkins, R. Private Communication. Rolls Royce, Bristol Engines Division, Bristol.

27. Burke, A.F. and Bird, K.D. "The Use of Conical and Contoured Expansion Nozzles in Hypervelocity Facilities". Cornell Aeronautical Report No. 112, 1962.

28. Whitfield, J.D. and Norfleet, G.D. "Source Flow Effects in Conical Hypervelocity Nozzles". AEDC-TDR-62-116, 1962.

29. Stratford, B.S. and Beaver, G.S. "The Calculation of the Compressible Turbulent Boundary Layer in an Arbitrary Pressure Gradient - A Correlation of Certain Previous Methods". ARC R. & M. No. 3207 (1959).

30. Smith, C.E. "The Starting Process in a Hypersonic Nozzle". J.F.M., Vol. 24, Pt. 4, 1966.

31. Wright, J.K. "Shock Tubes" - Methuen and Co. Ltd., London,1961.

32. Bradley, J.N. "Shock Waves in Chemistry and Physics". Methuen and Co. Ltd., 1962.

33. Gaydon, A.G. and Hurle, I.R. "The Shock Tube in High-Temperature Chemical Physics". Reinhold Publishing Corp., New York, 1963.

34. Glass, I.I. and Hall, J.G. "Handbook of Supersonic Aerodynamics", Section 18 'Shock Tubes' NAVORD Report 1488 (Vol. 6), Dec. 1959.

35. Charlton, E. "Notes on the BSEL Gun Tunnel Diaphragms". Bristol Siddeley Engines, Advanced Propulsion Research Group, Research Memo. No. 474, October 1966.

36. Vidal, R.J. "Model Instrumentation Techniques for Heat Transfer and Force Measurements in a Hypersonic Shock Tunnel". Cornel Aeronautical Laboratory Report No. AD-917-A-1, 1956.

37. Schultz, D.L. "Thin Film Resistance Thermometers and Calorimeters". I.M.E. Symp. on Some Developments in Techniques for Temperature Measurement, April 1962.

38. Brown, H.K. "The Theoretical Response of Heat Transfer Gauges Employed in Shock Tubes". Avco Everett Research Note 58, 1958.

39. Forman, L. "Calibration and Data Reduction Techniques for Thin Film Resistance Thermometers". Avco RAD Technical Release 62-4, 1962.

40. Edney, B.E. "The Development of Thin Film Heat Transfer Gauges and Analogue Networks for Use in the FFA Gun Tunnel". FFA Report AU-209:1, Stockholm 1964.

41. Hunter, J.A. "Theory and Operation of the Equipment used at Imperial College to Measure Heat Transfer Rate in Hypersonic Flow". Imperial College, Department of Aeronautics Aero Report, July 1968.

42. Vidal, R.J. Private Communication, Cornell Aeronautical Laboratory.

43. Davies, L. Private Communication, N.P.L.

44. Somers, L.M. "The Variation of $(\rho ck)^{\frac{1}{2}}$ with Temperature in 'Pyrex'". Cornell Aeronautical Laboratory Report CAL-106, 1961.

45. Skinner, G.T. "A New Method of Calibrating Thin Film Gauge Backing Materials". Cornell Aeronautical Laboratory Report CAL-105, 1962.

46. Softley, E.J. and Graber, B.C. — "Techniques for Low Level Pressure and Heat Transfer Measurements and Their Application to Base Flows". General Electric MSD Report R67SD2, 1967.

47. Jones, T.V. — D. Phil. Thesis, Oxford University, 1966.

48. Fay, J.A. and Riddell, F.R. — "Theory of Stagnation Point Heat Transfer in Dissociated Air". J. Aero. Sci., Vol. 25, No. 2, 1958.

49. Crabtree, L.F., Dommett, R.L. and Woodley, J.G. — "Estimation of Heat Transfer to Flat Plates, Cones and Blunt Bodies". RAE Tech. Report No. 65137, 1965.

50. Meyer, R.F. — "A Heat Flux Meter for use with Thin-Film Surface Thermometers". NRC of Canada, Aero Report LR-279, 1960.

51. Meyer, R.F. — "Further Comments on Analogue Networks to Obtain Heat Flux from Surface Temperature Measurements". NRC of Canada, Aero Report LR-375, 1963.

52. Howarth, L. (edit.) — "Modern Developments in Fluid Dynamics", Vol. II, Oxford University Press, 1953.

53. Landenburg, R.W. et al. (editors) — "Physical Measurements in Gas Dynamics and Combustion". Volume IX, High Speed Aerodynamics and Jet Propulsion, Oxford University Press, 1955.

54. Holder, D.W. and North, R.J. — "Optical Methods for Examining the Flow in High Speed Wind Tunnels. Part I: Schlieren Methods". AGARDograph 23, November, 1956.

55. Barnes, N.F. and Bellinger, S.L. — "Schlieren and Shadowgraph Equipment for Air Flow Analysis". J. Op. Soc. of America, Vol. 35, No. 8, 1945.

56. Richards, B.E. and Stollery, J.L. — "Transition Reversal on a Flat Plate at Hypersonic Speeds". AGARDograph 97, Page 483, 1965.

57. Batham, P. — D. Phil. Thesis, Oxford University, 1969.

58. Manavalan, L. and Pennelegion, L. — "The Response Time of Connecting Pipes in Short Duration Wind Tunnel Pressure Measurement Systems" NPL Aerodynamics Report, Jan. 1970.

59. Harper, L.R. "Response of a Strain Gauge Pressure Transducer and Mounting to a Fast Rising Pressure Pulse". Rolls-Royce, Bristol Engines Division, Report AP5394, 1966.

60. Alpher, R.A. and White, E.R. "Flow in Shock Tubes with Area Change at the Diaphragm Section". JFM, Vol. 3, 1958.

61. Flagg, R.F. "Detailed Analysis of Shock Tube Tailored Conditions". AVCO-RAD-TM-63-64, 1963.

62. East, R.A. and Pennelegion, L. "The Equilibrium Piston Technique for Gun Tunnel Operation". A.R.C. 22, 852, Hyp. 186, 1961.

63. Cable, A.J. and Fuller, P.W.W. "The R.A.R.D.E. No. 3 Hypersonic Gun Tunnel". ARC 25614, R.A.R.D.E. Report (B) 14/63, Dec. 1963.

64. Ames Research Staff. "Equations, Tables and Charts for Compressible Flow". NACA Report 1135, 1953.

65. Wallace, J.E. "Hypersonic Turbulent Boundary Layer Studies at Cold Wall Conditions". Proceedings of 1967 Heat Transfer and Fluid Mechanics Institute, Stanford Univ. Press, 1967.

66. Liepmann, H.W. and Roshko, A. "Elements of Gasdynamics". John Wiley & Sons Inc., Pg. 105, New York, 1957.

67. Hurdle, C.V. "The Determination of Stagnation Temperature from Flow Velocity Measurements using a Spark Disturbance Method in a Hypersonic Gun Tunnel". R.A.R.D.E. Memorandum (B) 60/62, 1962.

68. Stollery, J.L. "Stagnation Temperature Measurements in a Hypersonic Wind-Tunnel using the Sodium Line Reversal Method". Nature, Vol. 190, May 27, 1961.

69. East, R.A. and Perry, J.H. "A Short Time Response Stagnation Temperature Probe". Univ. of Southampton Dept. of Aero & Astro. Report No. 264, March 1966.

70. Bowman, J.E. "Nitrogen Condensation in the RARDE Hypersonic Gun Tunnel". ARC28155, RARDE Memorandum 24/66, May 1966.

71. Chemical Rubber Publishing Co. "Handbook of Chemistry and Physics". Cleveland, 1964.

72. Hertzberg, A., Wittliff, C.E. and Hall, J.G. "Summary of Shock Tunnel Development and Application to Hypersonic Research". Cornell Aeronautical Lab. Report No. AD-1052-A-12, July, 1961.

73. U.S. Government Printing Office. "U.S. Standard Atmosphere Supplements, 1966". Washington, D.C., 1966.

74. Schubauer, G.B. and Skramstad, H.K. "Laminar Boundary Layer Oscillations and Transition on a Flat Plate." NACA-TR-909, 1947.

75. Heller, H.H. "Acoustic Technique for Detection of Flow Transition on Hypersonic Re-entry Vehicles." AIAA J.,Vol.7,No. 2, Dec. 1969.

76. Owen, F.K. "Transition Experiments on a Flat Plate at Subsonic and Supersonic Speeds." AIAA Paper No. 69-9, 7th Aerospace Sciences Meeting, Jan. 1969.

77. Potter, J.L. and Whitfield, J.D. "Effects of slight nose bluntness and roughness on boundary-layer transition in supersonic flows." J.F.M. Vol. 12, pg. 501, 1962.

78. Staylor, W.F. and Morrisette, E.L. "Use of Moderate-Length Hot Wires to Survey a Hypersonic Boundary Layer." AIAA J., Vol. 5, No. 9, 1967.

79. Maddalon, D.V. and Henderson, A., Jr. "Boundary Layer Transition at Hypersonic Mach Numbers." AIAA Preprint 67-130, 5th Aerospace Sciences Meeting, 1967.

80. Mack, L.M. "Boundary Layer Stability Theory in Incompressible and Compressible Flow." VKI Notes on Mechanics of Boundary Layer Transition, Jan. 1968. (Also available as a series of JPL internal reports).

81. Pate, S.R. and Schueler, C.J. "An Investigation of Radiated Aerodynamic Noise Effects on Boundary-Layer Transition in Supersonic and Hypersonic Wind Tunnels." Presented at AIAA 3rd Aerodynamic Testing Conference, Paper AIAA 68-375, April 1968. Also, AEDC-TR-67-236 and AIAA J., Vol. 7, No. 3, 1969.

82. Morkovin, M.V. "Critical Evaluation of Transition from Laminar Turbulent Shear Layers with Emphasis on Hypersonically Traveling Bodies." Air Force Flight Dynamics Laboratory, AFFDL-TR-68-149, 1968.

83. Reshotko, E. "Stability Theory as a Guide to the Evaluation of Transition Data." AIAA Paper No. 68-669, AIAA Fluid and Plasma Dynamics Conference, June 1968.

84. Wagner, R.D., Jr., Maddalon, D.V., Weinstein, L.M. and Henderson, A., Jr. "Influence of Measured Free-Stream Disturbances on Hypersonic Boundary-Layer Transition." AIAA Paper 69-704, AIAA Fluid and Plasma Dynamics Conference, June 1969.

85. Schichtling, H. "Boundary Layer Theory", McGraw Hill Co., Inc., New York, 1960.

86. Needham, D.A. "Laminar Separation in Hypersonic Flow." Ph.D. Thesis, Univ. of London, 1965.

87. Richards, B.E. Ph.D. Thesis, University of London, 1967.

88. Nagel, A.L. "Analysis of the Unit Reynolds Number Effect in Hypersonic Flat Plate Boundary Layer Transition." Proceedings 1968 Heat Transfer and Fluid Mechanics Institute, Stanford University Press, 1968. Also in U.S.A.F. Report No. BSD-TR-67-213, Vol.2, 1967.

89. Wallace, J.E. "Hypersonic Turbulent Boundary Layer Measurements Using an Electron Beam." Cornell Aero. Lab. Report CAL No. AN-2112-Y-1, August 1968.

90. Samuels, R.D., Peterson, J.B., Jr. and Adcock, J.B. "Experimental Investigation of the Turbulent Boundary Layer at a Mach Number of 6 with Heat Transfer at High Reynolds Numbers." NASA.TN-D.3858, March 1967.

91. Nagamatsu, H.T., Graber, B.C. and Sheer, R.E., Jr. "Transition of Hypersonic Boundary Layer." Physics of Fluids, Vol. 8, No. 2, 1965.

92. Softley, E.J., Graber, B.C. and Zempel, R.E. "Experimental Observation of Transition of the Hypersonic Boundary Layer." AIAA Paper 68-39, 6th Aerospace Sciences Meeting, Jan. 1968.

93. Hunter, J.A. Private communication, Imperial College, Department of Aeronautics, 1968.

94. Charlton, E. "Boundary Layer Transition on a Hollow Cylinder Model in the B.E.D. Gun Tunnel." Rolls - Royce Ltd., Bristol Engine Division, Contract Report No. A.P. 5598, 1969.

95. Lemcke, B. Private communication, FFA Stockholm, 1969.

96. Laufer, J. "Factors Affecting Transition Reynolds Numbers on Models in Supersonic Wind Tunnels." J. Aero.Sci., Vol.21, No.7, 1954.

97. Morkovin, M.V. "On Transition Experiments at Moderate Supersonic Speeds." J. Aero. Sci., Vol. 24, No.7, 1957.

98. Laufer, J. "Aerodynamic Noise in Supersonic Wind Tunnels." J. Aero. Sci., Vol. 28, No. 9, Sept. 1961.

99. Laufer, J. "Some Statistical Properties of the Pressure Field Radiated by a Turbulent Boundary Layer." Physics of Fluids, Vol.7, No.8, Aug. 1964.

100. Phillips, O.M. "On the Generation of Sound by Supersonic Turbulent Shear Layers" J.F.M., Vol.9, pg. 1, 1960.

101. Laufer, J. "Sound Radiation from a Turbulent Boundary Layer." JPL-TR No.32-119 Nov. 1961.

102. Van Driest, E.R. "Turbulent Boundary Layer in Compressible Fluids." J.Aero. Sci., 18, No.3, Pg.145, 1951.

103. ——————— "The FFA Aerodynamic Research and Test Facilities." FFA (Stockholm) Memorandum 33, 1964.

104. Spalding, D.B. and Chi, S.W. "The Drag of a Compressible Turbulent Boundary Layer on a Smooth Plate with and without Heat Transfer." J.F.M.,Vol.18, 1964.

105. Emmons, H.W. "The Laminar-Turbulent Transition in a Boundary Layer - Part I." J.Aero.Sci.,Vol.18,No.7,July 1951.

106. Elder, J.W. "An Experimental Investigation of Turbulent Spots and Breakdown to Turbulence." J.F.M.,Vol. 9, Pg. 235, 1960.

107. Schubauer, G.B. and Klebanoff, P.S. "Contributions to the Mechanics of Boundary Layer Transition." NACA-TN-3489, 1955.

108. James, C.S. "Observations of Turbulent Burst Geometry and Growth in Supersonic Flow." NACA-TN-4235, 1958.

109. Stetson, K.F. and Rushton, G.H. "A Shock Tunnel Investigation of the Effects of Nose Bluntness, Angle of Attack and Boundary Layer Cooling on Boundary Layer Transition at a Mach Number of 5.5." AIAA Paper No. 66-495, 4th Aerospace Sciences Meeting, June 1966.

110. Eckert, E.R.G. "Engineering Relations for Friction and Heat Transfer to Surfaces in High Velocity Flow." J. Aero. Sci., Vol. 22, No. 8, Pg. 585, 1955.

111. Neal, L., Jr. "A Study of the Pressure, Heat Transfer and Skin Friction on Sharp and Blunt Flat Plates at Mach 6.8. NASA TN-D-3312, April 1966.

112. Perry, J.H. and East, R.A. "Experimental Measurements of Cold Wall Turbulent Hypersonic Boundary Layers." AGARD CP No.30, Specialists meeting on Hypersonic Boundary Layers and Flow Fields, May 1968.

113. Bertram, M.H. and Neal, L., Jr. "Recent Experiments in Hypersonic Turbulent Boundary Layers." NASA-TMX-56335, 1965.

114. Mateer, G.G. and Larson, H.K. "Unusual Boundary-Layer Transition Results on Cones in Hypersonic Flow." AIAA Paper No.68-40, AIAA 6th Aerospace Sciences Meeting, Jan. 1968.

115. Softley, E.J. "Boundary Layer Transition on Hypersonic Blunt, Slender Cones." AIAA Paper No. 69-705, AIAA Fluid and Plasma Dynamics Conference, June 1969.

116. Potter, J.L. "Observations on the Influence of Ambient Pressure on Boundary-Layer Transition." AEDC-TR-68-36, March 1968.

117. Potter, J.L. and Whitfield, J.D. "Boundary Layer Transition under Hypersonic Conditions." AGARDograph 97, Pt. 3, May 1965.

118. Pate, S.R. "Measurements and Correlations of Transition Reynolds Numbers on Sharp Slender Cones at High Speeds." AEDC-TR-69-172, December 1969.

119. Laufer, J. and McClellan, R. "Measurements of Heat Transfer from Fine Wires in Supersonic Flows." J.F.M., Vol. 1, 1956.

120. Kovasznay, L.S.G. "The Hot Wire Anemometer in Supersonic Flow." J. Aero. Sci., Vol. 17, No. 9, 1950.

121. Morkovin, M.V. "Fluctuations and Hot Wire Anemometry in Compressible Flows." AGARDograph 24, Nov.1956.

122. Kovasznay, L.S.G. "Turbulence in Supersonic Flow." J. Aero. Sci., Vol. 20, No. 10, 1953.

123. Wise, B. and Schultz, D.L. "Turbulence Measurements in Supersonic Flow with the Hot-Wire Anemometer." ARC 18373, Dec. 1955.

124. Demetriades, A. "An Experiment on the Stability of Hypersonic Laminar Boundary Layers." J.F.M., Vol. 7, 1960.

125. Vrebalovich, T. "Application of Hot Wire Techniques in Unsteady Compressible Flows." Proc. ASME Hydraulic Div. Conf., Worcester, Mass., Pg. 61, May 1962.

126. Laufer, J. and Vrebalovich, T. "Stability and Transition of a Supersonic Laminar Boundary Layer on an Insulated Flat Plate." J.F.M., Vol. 9, Pt. 2, 1960.

127. Klebanoff, P.S. "Characteristics of Turbulence in a Boundary Layer with Zero Pressure Gradient." NACA Rep. No. 1247, 1955.

128. Lin, C.C. "Theory of Hydrodynamic Stability." Cambridge University Press, 1967.

129. Lees, L. and Lin, C.C. "Investigation of the Stability of the Laminar Boundary Layer in a Compressible Fluid." NACA TN 1115, 1946.

130. Owen, F.K. "Fluctuation Measurements in Compressible Boundary Layers." ARC 31228, Hyp. 751, 1969.

131. Nagamatsu, H.T., Graber, B.C. and Sheer, R.E., Jr. "Critical Layer Concept Relative to Hypersonic Boundary Layer Stability." General Electric Company, Research & Development Center Report No. 66-C-192, 1966.

132. Van Driest, E.R. "Investigation of Laminar Boundary Layer in Compressible Fluids Using the Crocco Method." NACA-TN-2597, 1952.

133. Softley, E.J. and Sullivan, R.J. "Theory and Experiment for the Structure of Some Hypersonic Boundary Layers." AGARD Conference Proceedings No. 30, Specialists Meeting on Hypersonic Boundary Layers and Flow Fields, London, May 1968.

134. Stainback, P.C. "Use of Rouse's Stability Parameter in Determining the Critical Layer Height of a Laminar Boundary Layer." AIAA J., Vol. 8, No. 1, 1970.

135. Schubauer, G.B. and Klebanoff, P.S. "Contributions on the Mechanics of Boundary Layer Transition." NACA Report 1289, 1956.

136. Stuart, J.T. "Hydrodynamic Stability." Applied Mech. Rev., Vol. 18, No. 7, 1965.

137. Tani, I. "Review of Some Experimental Results on Boundary-Layer Transition." Physics of Fluids Supplement, S11, 1967.

138. Klebanoff, P.S. and Tidstrom, K.D. "Evolution of Amplified Waves Leading to Transition in a Boundary Layer with Zero Pressure Gradient." NASA-TN-D-195, 1959.

139. Kovasznay, L.S.G., Komoda, H. and Vasudeva, B.R. "Detailed Flow Field in Transition." Proc. 1962 Heat Transfer and Fluid Mechanics Inst., Stanford Univ. Press, 1962.

140. Spangenberg, W.G. and Rowland, W.R. "Optical Study of Boundary-Layer Transition Processes in a Supersonic Air Stream." Physics of Fluids, Vol. 3, No. 5, 1960.

APPENDIX I

CALCULATION OF CORRECTION FACTORS FOR HOLLOW CYLINDER TRANSITION CORRELATION

The calculation of the term

$$\frac{f_5(M)}{f_5(8.2)}$$

from equa. (9.4.16) for use in normalizing Re_t for M and T_w/T_e effects will be described below for each of the test conditions encountered in the hollow cylinder tests of Sections 9.2 and 9.3. The tabulated results are listed first. (for $Re_\theta = 10^4$)

	M	Nozzle T_w/T_e	F_c	F_{Re_θ}	$\times 10^{-3}$ $F_{Re_\theta} Re_\theta$	$\times 10^3$ $F_c \bar{c}_f$	$\times 10^3$ $\bar{c}_f$	$\frac{\bar{c}_f(8.2)}{\bar{c}_f}$	$f_5(8.2)/f_5(M)$ $= \left[\frac{\bar{c}_f(8.2)}{\bar{c}_f}\right]^{2.55}$
FFA	4.0	~3.5	2.5	.45	4.5	3.7	1.48	.508	.178
O.U.	7.0	4.45	3.80	.65	6.5	3.42	.90	.836	.638
FFA	7.15	~7	4.67	.3	3	4.08	.873	.863	.687
R.R.	7.75	4.80	4.21	.67	6.7	3.4	.807	.933	.838
I.C.	8.2	5.47	4.65	.60	6.0	3.5	.753	1.0	1.0

The values in the columns are found as follows. Given M and T_w/T_e, F_c and F_{Re_θ} are determined from the charts of Ref. 104. Taking any reference Re_θ value (e.g. 10^4) as a constant, $F_{Re_\theta} Re_\theta$ is calculated. $F_c \bar{c}_f$ is a unique function of $F_{Re_\theta} Re_\theta$ and is tabulated in Ref. 104. The coefficient $\bar{c}_f$ is then determined for the arbitrary reference value of Re_θ. The changes observed in the values of $\bar{c}_f$ are due entirely to changes in M and T_w/T_e (since Re_θ = constant). The values of $\bar{c}_f$ are then normalized w.r.t. $\bar{c}_f$ at the M = 8.2 test conditions. The term we seek is then given as

$$\frac{f_2(8.2)}{f_2(M)} = \left[\frac{\bar{c}_f(8.2)}{\bar{c}_f}\right]^{2.55}$$